



REPORT 94003_1ONR

**STRONG BUBBLE / FLOW INTERACTIONS AND
CAVITATION INCEPTION**

G.L. Chahine,
K. Sarkar,
R. Duraiswami

March 6, 1997

DISSEMINATION STATEMENT A

Approved for public release
Distribution Unlimited

19970509 058



DYNAFLOW, INC.

Research & Development in Applied Sciences

7210 Pindell School Road, Fulton, Maryland 20759 USA Tel: (301) 604-3688 - Fax: (301) 604-3689

e-mail: info@dynaflo-w-inc.com <http://www.dynaflo-w-inc.com>

DTIC QUALITY INSPECTED 1

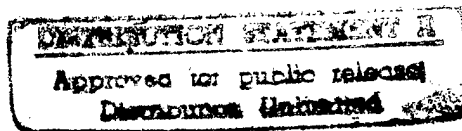
DISCLAIMER NOTICE



**THIS DOCUMENT IS BEST
QUALITY AVAILABLE. THE COPY
FURNISHED TO DTIC CONTAINED
A SIGNIFICANT NUMBER OF
COLOR PAGES WHICH DO NOT
REPRODUCE LEGIBLY ON BLACK
AND WHITE MICROFICHE.**

DYNAFLOW, INC.

REPORT 94003_1ONR



STRONG BUBBLE / FLOW INTERACTIONS AND CAVITATION INCEPTION

G.L. Chahine,
K. Sarkar,
R. Duraiswami

March 6, 1997

DYNAFLOW, INC.
7210 Pindell School Road
Fulton, MD 20759

This material is based work supported by the Office of Naval Research under
Contract number N00014-94-C-0093, monitored by Dr. Edwin Rood.

Contents

I INTRODUCTION	1
1 Overall summary	1
2 Summary of the approaches used	1
2.1 Axisymmetric bubble vortex interaction	2
2.2 3D two-way vortical flow field / bubble interaction	2
2.3 Modeling of unsteady sheet cavitation and cloud inception on an airfoil	3
II BUBBLE VORTEX ONE WAY INTERACTION¹	4
1 Introduction	4
1.1 Mechanistic Description	5
2 Order of magnitude considerations	6
3 Bubble capture by a vortex	9
3.1 Capture time	12
4 Numerical study	13
4.1 Bubble flow equations	14
4.2 Boundary integral method for three-dimensional bubble dynamics	15
4.3 Pressure / velocity potential relation	17
4.4 Specialization to axisymmetric problems	18
5 Numerical results and discussion	18
5.1 Validation of numerical codes	18
5.2 Bubble capture	19
5.3 Multiple bubbles	21
5.4 Bubble on vortex axis	25
5.5 Bubble on vortex axis perpendicular to a wall	29
6 3D Validation study: bubble/vortex ring interaction	30
6.1 Experimental study	30
6.2 Numerical Modeling	36
6.3 Numerical Results	36
III CAVITATION INCEPTION ON THE AXIS OF A LINE VORTEX —FULL VISCOUS INTERACTION	38
1 Introduction	38

¹This chapter is adapted directly from our publication in Reference [1].

2	Full Viscous Interaction Between a Cylindrical Bubble and a Line Vortex	38
2.1	Method of Solution	39
2.2	Initial and Boundary Conditions	40
2.3	Some Preliminary Results	40
3	Criteria for Cavitation Inception	43
3.1	Static Equilibrium	43
4	Two-dimensional Study of a Bubble on the Axis of a Line Vortex	47
4.1	Presentation of the problem	47
4.2	Matched asymptotic expansions approach	50
4.3	The outer problem.	51
4.4	The inner problem.	53
4.5	Resolution at order zero (ϵ^0).	55
4.6	Resolution at the following orders	62
IV THREE-DIMENSIONAL BUBBLE-VORTICAL FLOW INTERACTION — A NUMERICAL STUDY²		68
1	Introduction	68
2	Mathematical formulation	69
2.1	Kinematic Equations	69
2.2	Dynamic Equations	70
2.3	Boundary Conditions	72
3	Numerical Procedure	72
3.1	Vortex Element Method	72
3.2	Boundary Element Method	73
3.3	Time Integration	74
3.4	Solution of the Poisson Equation for Ψ	74
4	Numerical Examples	76
4.1	Bubble Dynamics in a Columnar Vortex	77
4.2	Bubble Dynamics in a Vortex Ring	81
5	Summary and Discussions	83
V SHEET CAVITATION INCEPTION		109
1	Introduction	109
2	Mathematical Formulation	109
2.1	Basic Equations and Boundary Conditions	109
2.2	Cavity Model	110
3	Implementation of the VEM	110
3.1	Vortex Elements	110
3.2	Generation of Vorticity at Solid Boundaries	111
3.3	Algorithm Summary	112
3.4	Free Surface Time Evolution	112
4	Boundary Element Method	113

²This chapter is adapted directly from our publication in Reference [64].

5	Axisymmetric Vortex Rings	113
6	Example	114
7	Conclusions	115
VI CONCLUSIONS		122
A INCLUSION OF NUCLEI DYNAMICS		124
1	Introduction	124
2	Problem considered	124
3	Nuclei local model	125
3.1	Evolution of the source term	126
3.2	Evolution of the dipole term	126
4	Code organization	127
5	Analytical Solutions to check the code	128

List of Figures

II.1	Practical examples of bubbles and vortices. a) Tip vortex cavitation on a propeller [2]. b) Vortex cavitation in the separated region behind a cylinder (courtesy cc. J.Y Billard, Ecole Navale, Brest, France [3]).	5
II.2	Sketch of the geometric quantities involved in the analytical description of bubble capture in a vortex line.	10
II.3	Comparison between Rayleigh-Plesset solution and the axisymmetric BEM code 2DYNAFS and the 3D BEM code 3DYNAFS. Computations started with an initial bubble pressure 584 times larger than the ambient pressure. a) Over bubble period. b) End of collapse.	19
II.4	3D bubble shapes at various times. Bubble initially at the origin of the cartesien coordinate system, and vortex at $X = 2R_{max}$. $\Omega = 0.474$, $p_i/p_\infty = 584.3$, $R_c/R_{max} = 4$. Projected view a) in the XOY plane; b) in the XOZ plane.	20
II.5	Motion of the two points initially on axis OX, A and B, and the mid point C between A and B, versus times. $\Omega = 0.474$, $p_i/p_\infty = 584.3$, $a_c/R_{max} = 4$. Vortex located at a) $X = 2R_{max}$; b) $X = R_{max}$.	21
II.6	Bubble contours at various times. $\Gamma = 0.1527m^2/s$, $p_i/p_\infty = 1$, $a_c = 2.2mm$, vortex located at $X = 3.2mm$, with a) $10\mu m$, b) $100\mu m$, c) $1000\mu m$.	22
II.7	Simulation of the dynamical interactions between a cloud of 21 bubbles using 3DYNAFS on a Cray. Two planes of symmetry are used. Each bubble has 102 nodes and 200 panels. a) Growth. b) Collapse.	22
II.8	Dynamical behavior of 5 bubbles in a vortex line flow - Bubble contours at various times. The vortex line is perpendicular to the page and centered on $Y = 1.5mm$. $R_c = 2.2mm$, $\Gamma = 0.1573m^2/s$. $\Omega = 0.872$. All bubbles have $a_0 = 100\mu m$.	24
II.9	3D bubble shapes in the vortex line flow field of Figure II.8 before collapse of bubble No. 1. View from a) OZ axis, b) OX axis.	24
II.10	Double exposure photo of a bubble in the viscous core of the trailing vortex of a NACA 66-209 hydrofoil (see [?]). Time of separation between two exposures =150 μs . Scale $190 \mu m/cm$. $R_e = 6.810^5$, $\Gamma = 0.232m^2/s$. Courtesy of Sheldon Green.	25
II.11	Comparison between the contours of an elongated bubble during its collapse in the absence and in the presence of swirl. Initial elongation ratio of 3. $p_\infty/p_i = 3.27$. a) No swirl. b) $\Omega = 0.56$. $R_c/R_{max} = 3$.	26

II.12 Bubble dynamics on the axis of a vortex line. Left side shows 3D shapes at selected times. Right side shows bubble contours at increasing times. $\Gamma = 0.005m^2/s$, $R_o = 100\mu m$. a) $p_i/p_\infty = 2$, $R_c/R_o = 1$, b) $p_i/p_\infty = 2$, $R_c/R_o = 1$, c) $p_i/p_\infty = 1$, $R_c/R_o = 0.57$.	27
II.13 Bubble collapse between two solid parallel plates resulting in the formation of an hourglass shaped bubble and a line vortex perpendicular to the two plates.	28
II.14 Cavitation bubble shapes observed at the exit of a vortex tube.	28
II.15 Influence of solid wall distance on bubble collapse in a line vortex. $\Omega = .475$, $p_i/p_\infty = 584$, $a_c = 1.18$. $L/R_{max} = $ a) 4; b) 3; c) 2.5.	30
II.16 Influence of Ω on the motion of bubble axial and longitudinal dimensions versus time for a bubble trapped in a line vortex perpendicular to a solid wall. Distances are normalized with R_{max} and times are normalized with Rayleigh time. $p_i/p_\infty = 584$, $a_c/R_{max} = 0.4$, $L/R_{max} = 4$.	31
II.17 Particle trajectory around the ring viscous core.	32
II.18 Bubble contours at various times from High Speed sequences of Figure 19.19. a) $\overline{D}_1 = 2.16$, $\overline{D}_2 = 0$, $V_{ring} = 0.28m/s$, b) $\overline{D}_1 = 2.38$, $\overline{D}_2 = 1.5$, $V_{ring} = 0.78m/s$, c) $\overline{D}_1 = 1.1$, $\overline{D}_2 = 0.37$, $V_{ring} = 0.82m/s$.	33
II.19 High Speed Movie sequences of bubble / vortex ring interaction. a) $\overline{D}_1 = 2.16$, $\overline{D}_2 = 0$, $V_{ring} = 0.28m/s$, b) $\overline{D}_1 = 2.38$, $\overline{D}_2 = 1.5$, $V_{ring} = 0.78m/s$, c) $\overline{D}_1 = 1.1$, $\overline{D}_2 = 0.37$, $V_{ring} = 0.82m/s$.	35
II.20 Numerical simulations of bubble / vortex ring interaction.. $\overline{D}_1 = 1.1$, $\overline{D}_2 = 0.37$, $V_{ring} = 0.82m/s$; $\Gamma = $ a) $0.025m^2/s$; b) $0.10m^2/s$; c) $0.12m^2/s$ which corresponds to Figure c.	37
III.1 Dynamics of the interaction between a cylindrical bubble and a line vortex. $\Gamma = 0.5 m^2/s$, $P_{go} = 5 \times 10^3 Pa$, $P_\infty = 1.3 \times 10^5 Pa$. a) Bubble radius, value of maximum azimuthal velocity $u_{\theta max}$, and position of $R_{\theta max}$. b) Bubble radius versus time with and without viscous interaction.	41
III.2 Dynamics of the interaction between a cylindrical bubble and a line vortex. $P_{axis} = 7 \times 10^5 Pa$. a) Influence of the initial bubble pressure, P_{go} , on bubble radius and position of $R_{\theta max}$. $R_c/a_o = 2$. b) Influence of R_c/a_o on the bubble radius and position of $R_{\theta max}$. $P_{go} = 1.5 \times 10^5 Pa$.	42
III.3 Cylindrical bubble static equilibrium in a line vortex. Relationship between ambient pressure and bubble radius for different values of a_o .	44
III.4 Influence of the circulation, Γ , on the critical pressure versus the initial bubble radius.	45
III.5 Bubble radius versus time for two values of the ambient pressure. $a_o = 60\mu m$, $P_{go} = 1e5 Pa$, $a_c = 1e - 2m$, $p_v = 2300 Pa$, $\Gamma = 0.1$, $\gamma = 0.7$.	46
III.6 Velocity of the bubble wall versus radius of the bubble for different values of P. $a_o = 60\mu m$, $P_{go} = 1e5 Pa$, $a_c = 1e - 2m$, $p_v = 2300 Pa$, $\Gamma = 0.05$, $\gamma = 0.7$.	46
III.7 The influence of the circulation Γ on the ambient pressure which results for a given bubble in an explosive growth. $a_o = 60\mu m$, $P_{go} = 1e5 Pa$, $a_c = 1e - 2m$, $p_v = 2300 Pa$, $\gamma = 0.7$.	47

III.8 The influence of the surface tension γ on the ambient pressure which results for a given bubble in an explosive growth. $a_o=60\mu m$, $P_{go}=1e5 Pa$, $a_c=1e-2m$, $p_v=2300 Pa$, $\Gamma = 0.05$	48
III.9 a)Bubble radius versus time. b) Core radius versus time. $a_o=60\mu m$, $P_{go}=1e5 Pa$, $a_c=1e-2m$, $p_v=2300 Pa$, $\Gamma = 0.05$, $\gamma = 0.1$	48
III.10Ratio between the core radius and the bubble radius. $a_o=60\mu m$, $P_{go}=1e5 Pa$, $a_c=1e-2m$, $p_v=2300 Pa$, $\Gamma = 0.05$, $\gamma = 0.1$	49
III.11Bubble radius versus time for an initial bubble volume much larger than the equilibrium volume. $\mathcal{V}_{eq}/\mathcal{V}_l = 0.063$, $t_0 = 100$, $a_o=500\mu m$, $P_{go}=5.10^5 Pa$, $a_c=0.025m$, $p_v=2300 Pa$, $\Gamma = 0.1$, $\gamma = 0.7$	60
III.12Bubble radius versus time for an initial bubble volume much larger than equilibrium volume. a. Full curve. b. Blow up of initial region. $\mathcal{V}_{eq}/\mathcal{V}_l = 0.63$, $t_0 = 100$, $a_o=500\mu m$, $P_{go}=5.10^5 Pa$, $t_0 = 100$, $a_c=0.025m$, $p_v=2300 Pa$, $\Gamma = 0.1$, $\gamma = 0.7$	60
III.13Bubble radius versus time in the case of bubble growth and collapse. $\mathcal{V}_{eq}/\mathcal{V}_l = 1.75$, $t_0 = 100$, $a_o=500\mu m$, $P_{go}=5.10^5 Pa$, $a_c=0.025m$, $p_v=2300 Pa$, $\Gamma = 0.1$, $\gamma = 0.7$	61
III.14Bubble radius versus time for various values of the initial bubble volume all smaller than the equilibrium volume. $t_0 = 100$, $a_o=500\mu m$, $P_{go}=5.10^5 Pa$, $a_c=0.025m$, $p_v=2300 Pa$, $\Gamma = 0.1$, $\gamma = 0.7$	61
III.15Bubble radius and viscous core radius versus time in the case of a strong bubble collapse. $\mathcal{V}_{eq}/\mathcal{V}_l = 0.063$, $t_0 = 100$, $a_o=500\mu m$, $P_{go}=5.10^5 Pa$, $P_\infty=1.10^4 Pa$, $a_c=0.025m$, $p_v=2300 Pa$, $\Gamma = 0.1$, $\gamma = 0.7$	62
III.16Bubble radius and maximum tangential velocity versus time in the case of a strong bubble collapse. $\mathcal{V}_{eq}/\mathcal{V}_l = 0.063$, $t_0 = 100$, $a_o=500\mu m$, $P_{go}=5.10^5 Pa$, $P_\infty=1.10^4 Pa$, $a_c=0.025m$, $p_v=2300 Pa$, $\Gamma = 0.1$, $\gamma = 0.7$	63
III.17Bubble radius and maximum vorticity versus time in the case of a strong bubble collapse. $\mathcal{V}_{eq}/\mathcal{V}_l = 0.063$, $t_0 = 100$, $a_o=500\mu m$, $P_{go}=5.10^5 Pa$, $P_\infty=1.10^4 Pa$, $a_c=0.025m$, $p_v=2300 Pa$, $\Gamma = 0.1$, $\gamma = 0.7$	63
III.18Bubble radius and viscous core radius versus time in the case of an explosive bubble growth. $\mathcal{V}_{eq}/\mathcal{V}_l = 145$, $t_0 = 100$, $a_o=500\mu m$, $P_{go}=7.10^4 Pa$, $P_\infty=1.10^4 Pa$, $a_c=0.025m$, $p_v=2300 Pa$, $\Gamma = 0.1$, $\gamma = 0.7$	64
III.19Bubble radius and maximum tangential velocity versus time in the case of an explosive bubble growth. $\mathcal{V}_{eq}/\mathcal{V}_l = 145$, $t_0 = 100$, $a_o=500\mu m$, $P_{go}=7.10^4 Pa$, $P_\infty=1.10^4 Pa$, $a_c=0.025m$, $p_v=2300 Pa$, $\Gamma = 0.1$, $\gamma = 0.7$	64
III.20Bubble radius and maximum vorticity versus time in the case of an explosive bubble growth. $\mathcal{V}_{eq}/\mathcal{V}_l = 145$, $t_0 = 100$, $a_o=500\mu m$, $P_{go}=7.10^4 Pa$, $P_\infty=1.10^4 Pa$, $a_c=0.025m$, $p_v=2300 Pa$, $\Gamma = 0.1$, $\gamma = 0.7$	65
IV.1 a) Geometry of the discretized bubble and column vortex. b) Plot at a cross-sectional plane through the bubble center, the dotted lines represent the core Δ of the cross-marked vortices. c) Geometry of the discretized bubble and column at a later time.	85

IV.2 Convergence study for different discretization of the core of the vortex column. Time evolution of the equivalent bubble radius R_{eq} for three discretization schemes with 1 line (dashed), 7 line vortices (dotted), 19 line vortices (solid). The curves for different number of elements along a vortex line (10,20 or 40) coincided with each other. Initial bubble radius: 10 μm , column core radius: 120 μm , $p_{g0}=5\times10^6 \text{ Pa}$, $P_\infty = 10^5 \text{ Pa}$, and $\Gamma=0.0015 \text{ m}^2/\text{sec}$	86
IV.3 Growth (a) and collapse (b) of the bubble in a columnar vortex for the conditions of Figure 2. Time evolution of bubble cross-sections and traces of the vortex lines in the plane of symmetry perpendicular to the vortex axis. The vortex lines move outward during growth, and inward during collapse in an anti-clockwise manner.	87
IV.4 The vorticity field ω normal to the plane and the induced vortical velocity vectors \mathbf{u}_ω , i.e., $\mathbf{u} - \mathbf{u}_b$ in a cross-sectional plane at six different times, three during growth at $t=1.03, 2.28, 4.79$, and three during collapse at $t=7.29, 9.78, 10.79$. The conditions are the same as in Figure 2 and 3.	88
IV.5 The difference in the normal component of the vorticity field ω and in the vortical velocity vectors \mathbf{u}_ω with and without the bubble at the same times and the same cross-sectional plane as in Figure 4.	89
IV.6 The normal component of the vorticity ω along a straight line going through the centers of the bubble and the column core at the same times as in Figure 4. The traces of the bubble at those times are also shown.	90
IV.7 The difference in the normal component of the vorticity field ω along the same line as in Figure 6 with and without the bubble.	91
IV.8 Study of the evolution of the non-dimensionalized equivalent bubble radius, R_{eq}/R_{\max} , for several values of the pressure drop parameter \mathcal{P} . In each case the bubble initial radius 10 μm , and the initial gas pressure is $4.742 \times 10^6 \text{ Pa}$, the pressure at infinity is 10^5 Pa , and the bubble is placed 60 μm away from the center of a vortex of core size 120 μm . The circulation, Γ , for the three cases is 0.0015, 0.003, and 0.0045 m^2/s respectively.	92
IV.9 Contours of bubble growth, and collapse, for four values of the pressure parameter \mathcal{P} . The top three cases correspond to the cases in Figure 8, while the last case is for a higher value of \mathcal{P}	93
IV.10 The out-of-plane vorticity (left column) and in-plane velocities (right column) along a line joining initial bubble and vortex centers, for the cases of Figure 9. The curves display the value at the initial time (dashed line), at bubble maximum (longer dashes) and at the instant of bubble collapse (solid line). In the velocity plots the component u_z is indicated with lines with circles.	94
IV.11 Study of the influence of the bubble over-pressure, $\bar{P}_g = P_g/P_\infty$, on the dynamics. The non-dimensionalized equivalent bubble radius, R_{eq}/R_{\max} , is plotted versus time for three values of \bar{P}_g . In each case the bubble initial radius is 10 μm , and is placed 30 μm away from the center of a vortex of core size 120 μm , and circulation 0.0015 m^2/s . The initial gas pressures are $1.2279 \times 10^6 \text{ Pa}$, $4.7417 \times 10^6 \text{ Pa}$, and $1.138 \times 10^7 \text{ Pa}$, and the pressure at infinity is 10^5 Pa	95

IV.12Contours of bubble growth (left column) and collapse (right column) for the cases of Figure 11. In the case with the smallest initial pressure, jet formation during rebound can be observed.	96
IV.13Geometry of the discretized bubble and the vortex ring.	97
IV.14A convergence study for the dynamics of a bubble in the flow field of a vortex ring. Four different discretizations, with 1 (dashed), 7 (dotted), 19 (solid), and 37 (dash-and-dotted) lines for the ring core are used. Time evolution of the bubble equivalent radius R_{eq}/R_0 is shown. Initial bubble radius: 10 μm , ring radius: 80 μm , ring core radius: 30 μm , $p_{g0}=5\times10^6 \text{ Pa}$, and $\Gamma=0.00045 \text{ m}^2/\text{sec}$	98
IV.15A convergence study with respect to the number of elements along a line in the core of the ring: 20 (dashed), 40 (dotted) and 100 (solid) elements are used to discretize a component ring and R_{eq}/R_0 is plotted.	99
IV.16Growth (a) and collapse (b) of the bubble in the ring vortex for the conditions of Figure 13. Time evolution of bubble cross-sections and traces of the vortex lines in a plane perpendicular to the column are shown. The scale is non-dimensionalized with the initial bubble radius. The ring is moving downward due to its own induced velocity.	100
IV.17Experimental observations of a bubble collapsing in the field of a vortex ring from Chahine (1995). The vortex ring is cavitating and is in the upper left corner of each frame.	101
IV.18The normal component of the vorticity field ω and the tangential components of the induced vortical velocity vectors \mathbf{u}_ω , i.e., $\mathbf{u} - \mathbf{u}_b$ in a cross-sectional plane at six different times, three during growth, $t=1.022, 2.27, 4.77$, and three during collapse, $t=7.27, 8.52, 10.92$. The conditions are the same as in Figure 13.	102
IV.19The difference in the normal component of the vorticity field ω and the tangential components of the vortical velocity vectors \mathbf{u}_ω with and without the bubble at the same times and the same cross-sectional plane as in Figure 18.	103
IV.20Modification of the bubble dynamics with varying vortex ring circulation, as shown by the variation of the bubble equivalent radius. R_{eq}/R_{\max} , with time t/τ_R . In each case the bubble initial radius is 10 μm , and is at an initial pressure of $4.6716\times10^6 \text{ Pa}$, and is placed 300 μm away from a vortex ring in its plane. The ring has a radius of 80 μm and a core radius of 30 μm . The circulations corresponding to the four cases are respectively 4.5×10^{-5} , 0.0009, 0.0025, and 0.0045 m^2/s	104
IV.21Modification of the bubble dynamics in a vortex ring flow field with varying initial bubble overpressure, as shown by the variation of the bubble equivalent radius. R_{eq}/R_{\max} , with time t/τ_R . In each case the bubble initial radius is 10 μm , and is placed 150 μm away from a vortex ring in its plane. The ring has a radius of 80 μm , a core radius of 30 μm , and a circulation of 0.00045 m^2/s . The initial bubble pressures are $1.2279\times10^6 \text{ Pa}$, $4.6716\times10^6 \text{ Pa}$, and $1.138\times10^7 \text{ Pa}$	105
IV.22Contours of bubble growth (left column) and bubble collapse (right column) for the cases of Figure 21.	106

IV.23 Growth (a) and collapse (b) of a bubble placed inside the core of the ring. $R_0 = 1\mu\text{m}$, the inside gas pressure $p_{g0} = 7 \times 10^6 \text{ Pa}$. The vortex parameters are ring radius: 80 μm , ring core radius: 30 μm , $p_{g0} = 5 \times 10^6 \text{ Pa}$, $P_\infty = 10^5 \text{ Pa}$ and $\Gamma = 0.00045 \text{ m}^2/\text{sec}$. The bubble is placed 5 μm away from the ring core center.	107
IV.24 The change in the vorticity and the vortical velocity field in the cross-sectional plane for the conditions of Figure 23 at six different times, $t=1.02, 2.27, 4.77$ during growth, and $t=7.27, 11.02, 12.27$ during collapse.	108
V.1 Pressure field around the sphere: sphere radius $R = 1 \text{ m}$, pressure at infinity = 101230 Pa, and vapor pressure $p_v = 2300 \text{ Pa}$, velocity $U = 19 \text{ m/sec}$	116
V.2 Dynamics of the cavity in a cross-sectional plane: Different curves represent the shape of the cavity at subsequent times.	117
V.3 Three dimensional discretization of the sphere and the cross-sections of cavity at the various times.	118
V.4 The vortex structure behind the spher: In the cross-sectional plane the contour of the spher and the time history of the traces of the vortex rings are presented.	119
V.5 The time history of the cavity with vortex emissin: The cavity computation is started after the vortical flow is developed. The subsequent cavity shapes and the traces of vortex rings are shown.	120
V.6 Near field of the sphere from Figure 6.5 showing detail of the cavity shape.	121

Abstract

The understanding of the fundamental mechanisms involved in the interaction between bubbles/free-surfaces and vortical flows is of relevance to many important naval applications. Classical assumptions of bubble sphericity and decoupling between bubble and flow behavior prevent one from capturing essential elements of the interaction, and might lead to incorrect conclusions with serious consequences. Bubble motion and deformation are seen to be of great importance for most bubbles in the size spectrum. In this report studies on various aspects of bubble interaction with vortical flows, and the appearance of sheet cavitation on hydrofoils in vortical flows are reported.

Chapter I

INTRODUCTION

1 Overall summary

This report summarizes work focused on the development, validation, and application of numerical and asymptotic methods for *the description of the microscale dynamics of bubbles in non-uniform flow, and the modelling of cloud cavitation inception*. Specific areas addressed include:

- The modeling of the dynamic behavior of a bubble in a vortex. This considers a one-way interaction model, with the large bubble deformation and dynamic behavior described numerically using a three dimensional boundary element method (Chapter 2).
- The inception of cavitation in line vortices using a fully viscous model (Chapter 3).
- The development of a new coupled Boundary Element/Vortex Element method for modeling the interaction of bubbles and vortical structures. This model is then used to study the two-way interaction between a bubble and a ring vortex, and between a bubble and a columnar vortex (Chapter 4).
- A model for the inclusion of the dynamics of cavitation nuclei in the liquid and their interaction with the flow-field and structures such as attached cavities on submerged structures (Chapter 5).
- The modeling of cavitation inception and cavity dynamics over hydrofoils or propeller blades (Chapter 6).

2 Summary of the approaches used

The following briefly summarizes the methods used. These methods are discussed in greater detail in the following chapters.

2.1 Axisymmetric bubble vortex interaction

The dynamics of a bubble centered on a line vortex was studied using successively two approaches. In a first approach the influence of the vortical flow field on the dynamics of the captured bubble was studied using an axisymmetric boundary element method. In this case the interaction considered was one-way in that the vortical flow field affected the bubble behavior while the basic vortex flow remained unaffected by the bubble dynamics which was not allowed to generate any additional vorticity. In a subsequent approach the influence of the dynamics of the captured bubble on the vortical flow field was studied using a singular perturbation technique, in which the influence of the axisymmetric bubble was modeled using the Navier-Stokes' equation under the assumption that the bubble radial dimension was much smaller than the vortex core characteristic size. Both approaches indicated that there was strong interaction, and pointed to the need for more sophisticated modeling of the complex dynamics. The two-way interaction can be used to generated engineering curves for cavitation inception in vortical field more adapted than the classical pressure / radius diagram for static spherical bubble equilibrium.

2.2 3D two-way vortical flow field / bubble interaction

To describe the two-way interaction between the bubble dynamics and a vortex field around it, a coupled boundary element/vortex element code was developed and implemented. DYNAFLOW's boundary element method code **3DynaFS** was coupled with our implementation of a vortex element method that models the evolving vorticity field.

- In the time stepping procedure, the coupling between the two methods is achieved through *the velocity and the pressure fields* which are used at each time step to update the positions of the vortices and the cavity free nodes.
- In our early approach we used a potential representation of the vorticity outside of the vortical region, which allowed us through application of a modified Bernoulli equation for the vortical field to compute the pressure field due to the vorticity and use only the BEM. Since such an approximation neglects any modification of the vorticity field by the bubble presence and behavior, the new coupled BEM/VEM formulation allows for a more precise description. In this formulation, the dynamic pressure at a field point is found to satisfy a Poisson type equation.
- This Poisson equation is solved with the same BEM method used for the velocity potential, with the right-hand-side handled by a so-called *dual reciprocity* method. The right hand side of the Poisson equation is represented by a sum of basis functions (here the same as those used to represent the vorticity field) which satisfy the Laplace equation and result in elimination of the volume integral terms in Green's equation. This results again in a boundary only formulation and a modified and still efficient boundary element method. Such complementary usage of the same methods results in a very efficient computational code which adds the advantages of both boundary element and the vortex element method.

- The model accounts for viscous effects through vorticity generation from a solid surface and vorticity decay with time. This allows us to model the interaction of bubbles and the vortical boundary layer of an airfoil.

Results to date show potential for significant effects of the bubbles on the vortex field and vice versa. The unsteady effects are not negligible and hence has significant implications on cavitation phenomena where the bubbles find themselves in intense time varying vortical regions.

2.3 Modeling of unsteady sheet cavitation and cloud inception on an airfoil

We have initiated a detailed investigation of cavity formation on an airfoil or propeller blade, which would include the interaction with the boundary layer, and a stream of travelling nuclei in the flow. The above mentioned BEM and coupled BEM/VEM codes are used to model this type of flow and the phenomena involved. The main components of our model are the following:

- The surface of the blade is discretized with surface panels. The potential flow around this geometry is found using the boundary element method.
- Panels are turned into free surface panels if the pressure on the corresponding nodes drop below the vapor pressure.
- These free panels then form the surface of a sheet cavity that is allowed to behave dynamically as a highly distorted bubble but these panels are prevented from penetrating the actual blade surface.
- The vorticity field, shear and boundary layer around the body are modeled by distributed vortex elements in the flow region. Their subsequent evolution is determined by solution of the vortex element method problem.
- The body with the attached cavity sheds vorticity into the flow which are subsequently modeled by vortex elements.
- Any freely travelling bubbles or nuclei are modeled by singularity distributions and by an asymptotic multipole expansion scheme.

This effort is our first attempt to model the unsteady three-dimensional flow around an airfoil with sheet and travelling bubble cavitation and the breakup of the sheet into bubble clouds at the end of the cavity.

Parts of the above described codes have been adapted to specialized super-computer architectures (CRAY and SGI power challenge).

Chapter II

BUBBLE VORTEX ONE WAY INTERACTION¹

1 Introduction

The simultaneous presence of bubbles and vortices is typical of many high velocity turbulent flows. Spectacular examples can be observed with propellers, where at high rotational speeds the helicoidal tip vortices formed at the tip of each blade 'cavitate' and become sites of bubble concentration and fluid vaporization into 'tip vortex cavities' (see photograph in Figure II.1 a). While for practical reasons engineers tend to superficially address the fundamental problem – by stating, for example, that cavity formation in the vortex will occur if the pressure on the center line drops in the monophase model below the liquid vapor pressure –, a closer look at the fundamental processes at work reveals that the actual phenomenon is rather very complex and very poorly understood. Questions such as how does a microscopic bubble behave in the presence of the vortex ..., or how and to what extent the presence of bubbles modifies the flow field of the vortex ... have, at this point, only preliminary answers or no answers at all.

The interaction between bubbles and vortex flows is in fact of relevance to several fluid engineering problems. Important examples include cavitation in shear layers, boundary layers, tip vortex cavitation, bubbles in the shear layer of submerged jets, cavitation behind orifices, bubbles in separated flow areas (see Figure II.1b), microbubbles in boundary layers, ...etc. In the above mentioned flows, bubbles are held responsible for dramatic effects such as noise generation, materials erosion, and bubble drag reduction. These effects, experimentally observed and widely accepted, are not yet completely understood. Therefore, a satisfactory control of the corresponding deleterious effects is not presently possible.

This chapter will try to model the problem and present some proposed explanations and methods for solution. Some of these methods of solution are reconsidered further in the following chapters.

¹This chapter is adapted directly from our publication in Reference [1].

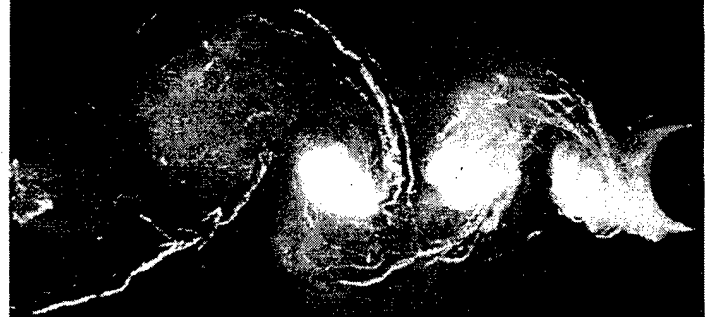


Figure II.1: Practical examples of bubbles and vortices. a) Tip vortex cavitation on a propeller [2]. b) Vortex cavitation in the separated region behind a cylinder (courtesy cc. J.Y Billard, Ecole Navale, Brest, France [3]).

1.1 Mechanistic Description

When a bubble approaches a region of high vorticity in a liquid, it is accelerated towards the center of the vortex. The asymmetric pressure field pushes the bubble towards the vortex axis while it is swirling. On its path the bubble experiences a decreasing ambient pressure which can lead to an increase in the bubble size. Simultaneously, since the non uniformity of the pressure field around the bubble increases with proximity to the vortex axis, bubble shape deformation increases. An explosive bubble growth is provoked if the pressure in the vortex field drops below the bubble '*critical pressure*', p_c . For a spherical bubble of equilibrium radius r_o when the ambient pressure is P_o , this pressure is defined as the pressure below which an equilibrium bubble radius does not exist. In cavitation studies within the assumption of an isothermal law of behavior of the gas included in the bubble this pressure is defined by²

$$p_c = P_v - \frac{4\sigma}{3r_c}, \quad (\text{II.1})$$

where σ is the surface tension parameter, and r_c is the '*critical radius*' given by

$$r_c = \left[\frac{3r_o^3}{2\sigma} \left(P_o - P_v + \frac{2\sigma}{r_o} \right) \right]^{1/2}, \quad (\text{II.2})$$

where P_v is the liquid vapor pressure (see for example [5]).

²This is obtained by considering Equation II.38, writing $V = \frac{4}{3}\pi r_b^3$ and $V_0 = \frac{4}{3}\pi r_0^3$, and solving for the minimum of the function $P_L(r)$.

Over the last decade several investigators have addressed the phenomenon of bubble capture by a vortex [6]-[10]. However, these studies made the strong simplifying assumption that the bubble, even though able to undergo volume changes, remains spherical. In addition, the type of interactions they considered was one-sided, since they did not consider vortex flow modification by the presence and behavior of the bubble. More recently, [11] considered a broader approach where bubble deformation and motion were coupled while neglecting flow field modification by the bubble presence. This study showed that the pressure gradient across the bubble can lead to significant departure from bubble sphericity, and led to the suggestion that the deformation and later splitting of the bubble during its motion towards the vortex center is, in addition to its volume change, the main source of noise in vortex cavitation. This appears to explain the reason for the location of tip vortex noise at cavitation inception very close to the blade [12], and is in agreement with recent observations by [13] about bubble capture in tip vortex cavitation. We will consider the details of such approaches in the following sections.

One can distinguish three phases in the interactive dynamics of bubbles and vortices:

- a) bubble capture by the vortex,
- b) interaction between the vortex and an initially quasi-spherical bubble on its axis, and
- c) dynamics of elongated bubbles on the vortex axis.

After some phenomenological and order of magnitude considerations of the phenomena at hand, we will consider each of the three phases and the method of solution proposed for their study.

2 Order of magnitude considerations

In order to analyze the problem of bubble capture and behavior in a line vortex let us consider as an example the Rankine vortex flow field. Let us denote as Γ the vortex circulation, R_c the radius of the viscous core, and u_θ the only non-zero velocity component. For distances r smaller than R_c the flow has a solid body rotation behavior (velocities vary as r), while for distances r larger than R_c the flow behaves as in an ideal inviscid irrotational vortex (velocities vary as $1/r$). For such a flow the pressure field is known. A key parameter which appears in the pressure expression is the "swirl parameter", Ω , defined as:

$$\Omega = \frac{\frac{1}{2}\rho(\frac{\Gamma}{2\pi R_c})^2}{p_\infty}, \quad (\text{II.3})$$

which characterizes the intensity of the pressure drop due to the rotation relative to the ambient pressure, p_∞ . To illustrate the importance of this parameter, we normalize the pressure with p_∞ , to obtain the following nondimensional expressions for the pressure and the pressure gradient:

$$\begin{aligned} \bar{p}(\bar{r}) &= 1 - \frac{\Omega}{\bar{r}^2}; & \frac{\partial \bar{p}}{\partial \bar{r}} &= \frac{2\Omega}{\bar{r}^3}; & \bar{r} &\geq 1, \\ \bar{p}(\bar{r}) &= 1 - \Omega(2 - \bar{r}^2); & \frac{\partial \bar{p}}{\partial \bar{r}} &= 2\Omega\bar{r}; & \bar{r} &\leq 1, \end{aligned} \quad (\text{II.4})$$

with

$$\bar{r} = \frac{r}{R_c}; \quad \bar{p}(\bar{r}) = \frac{p(r)}{p_\infty}. \quad (\text{II.5})$$

Note that the pressure on the vortex axis is $(1 - 2\Omega)$ and goes to zero when Ω approaches 1/2.

The pressure gradient steepens in the inviscid region when the viscous core is approached, achieves its maximum at $\bar{r} = 1$, and levels off in the viscous core close to the vortex axis. If a bubble is subjected to such a pressure field, it will experience a higher liquid pressure on its right side than on its left side, the difference being greater the larger the bubble is. Similarly, the bubble is ‘sheared’, since fluid particles on the bubble / liquid interface experience different velocities. The type of shearing action depends on the position of the bubble relative to the viscous core and inviscid fluid boundary, R_c . If the bubble is fully immersed in the inviscid region of the flow, fluid particles on its left side will experience larger velocities, while if it is fully immersed in the solid body rotation region of the flow fluid particles on its right side will experience larger velocities. The most complex situation is when the bubble is partly in the viscous core and partly in the inviscid region. In that case, it is expected that the bubble behavior will be vortex flow model dependent, since in fact the sharp separation between the two regions is purely mathematical, and is a very schematic representation of the physical reality.

Due to the pressure and velocity gradients the bubble is accelerated toward the axis while somewhat growing and deforming. Therefore, depending on its size and position, the bubble experiences a pressure variation along its surface and a slip velocity relative to the surrounding fluid. This results in some degree of bubble shape deviation from sphericity. The importance of this deviation is a function of the relative orders of magnitude of the pressure gradient, the bubble wall acceleration due to volume change, and surface tension forces.

An evaluation of the bubble wall acceleration can be obtained from a characteristic bubble radius, R_b , and from the Rayleigh time, τ_R , time needed for an empty bubble to collapse from its radius R_b to 0, under the influence of the pressure outside the bubble [14]. For the present problem let's take for characteristic outside local pressure the pressure at $r = R_c$, that is ($\bar{p} = 1 - \Omega$) as the typical local ambient pressure, the Rayleigh time is then:

$$\tau_R = R_b \sqrt{\frac{\rho}{p_\infty(1 - \Omega)}}. \quad (\text{II.6})$$

The characteristic bubble wall acceleration, γ_{growth} , at $r = R_c$ is then:

$$\gamma_{growth}|_{r=R_c} \simeq \frac{R_b}{\tau_R^2} \simeq \frac{p_\infty(1 - \Omega)}{\rho R_b} \quad (\text{II.7})$$

This value is to be compared with the acceleration force $\gamma_{gradient}$ due to the pressure gradients expressed in (IV.39):

$$\gamma_{gradient} \simeq \frac{1}{\rho} \frac{\partial P}{\partial r},$$

$$\gamma_{gradient}|_{r=R_c} \simeq \frac{2\Omega p_\infty}{\rho R_c}, \quad (\text{II.8})$$

The ratio between these two accelerations can be evaluated, for instance at $r = R_c$, to yield the simple expression:

$$\left. \frac{\gamma_{gradient}}{\gamma_{growth}} \right|_{r=R_c} = \frac{2R_b}{R_c} \cdot \frac{\Omega}{1 - \Omega} \quad (\text{II.9})$$

This expression underlines the relative importance between the characteristic bubble size R_b , and the viscous core size R_c . Keeping the surface tension parameter the same (see discussion on the Weber number below), the larger the ratio (II.9) is, the more important bubble deformation will be. *This remark has important implications concerning scale effects where R_b and R_c do not increase in the same proportion between scale and model*, since in most practical cases bubble distributions and sizes are uncontrolled and typically cannot be scaled much, while the size of the vortical regions depend on the selected geometry and velocity scales.

The ratio (II.9) is only an indication of the relative importance of bubble growth and slip forces at a given position. In fact the relative importance of these competing forces changes during the bubble capture process. For instance, the acceleration of the bubble toward the vortex axis increases with its proximity to the viscous core while the growth rate tends toward a constant value (decreasing pressure gradient). This indicates that strong deformation becomes predominant relative to volume change when either the bubble is very close to the axis or the vortex circulation (the “swirl parameter”, Ω) becomes large.

Another important physical factor which affects bubble shape is the surface tension. A normalized value of the corresponding pressure, a Weber number, can be constructed by combining the surface tension pressure (coefficient, σ) with either the pressure difference between the inside and the outside of the bubble, or the amplitude of the variations of the local pressures (pressure gradients) around the bubble. The first number, W_{e_1} , is given by:

$$W_{e_1} = \frac{p_i - p_\infty(1 - \Omega)}{\sigma/R_b}, \quad (\text{II.10})$$

where p_i is the pressure inside the bubble. The second number, W_{e_2} , is given by:

$$W_{e_2} = R_b \frac{\partial p / \partial r}{\sigma/R_b}, \quad (\text{II.11})$$

which can be written for $r = R_c$:

$$W_{e_2} = 2\Omega \left(\frac{p_\infty}{\sigma/R_b} \right) \left(\frac{R_b}{R_c} \right) = W_{e_1} \frac{2\Omega}{\bar{p}_i - (1 - \Omega)} \cdot \frac{R_b}{R_c}. \quad (\text{II.12})$$

For small values of either of these two numbers tension forces are predominant and prevent bubble distortion and deviation from sphericity. Expressions (II.12) shows that this is possible only if Ω is small and if R_b is much smaller than R_c . Therefore, as for the discussion on the acceleration forces, one should expect larger bubble deformations for stronger vortex circulations and larger bubbles.

3 Bubble capture by a vortex

Despite several significant contributions to the study of bubble capture in a vortex, to our knowledge, no complete approach has yet been undertaken. While the overall approach, in terms of the investigation of the bubble motion has several similarities to the problem of the interaction between vortices and solid particles, the bubbles, unlike solid particles, will deform and change volume while interacting with the vortex flow field. The complexity of the problem has led the various contributors to neglect one or several of the factors in play, and therefore to only investigate the influence of a limited set of parameters. The first approaches to the problem were attempted independently at about the same time by Bovis [6] and Latorre [15]. While both studies accounted for volume change during bubble motion, the basic assumptions and effects taken into account were quite different. Bovis [6, 7] considered the case where the flow velocities in the vortex flow are large enough to justify the assumptions of inviscid potential flow. This simplification, valid for instance in tip vortex cavitation where very large tangential velocities come into play, and when the bubble is not too close to the vortex axis, allows one to consider other important effects. For instance, one can then consider in a consistent fashion important phenomena such as the modification of the vortex flow by the presence of the bubble and the volume change and shape deformation of the bubble [16]. On the other hand, Latorre *et al.* in [15] and in following studies [10], in a more pragmatic approach, considered real fluid effects to determine the bubble motion equation, neglecting bubble shape deformation and modification of the flow by the bubble behavior. They coupled these equations with a spherical bubble dynamics model to deduce noise emission in tip vortex cavitation.

In the potential flow approach, the expression of the modified flow field due to the presence of a spherical bubble is based on Weiss' theorem [17]. In a spherical system of coordinates centered at the sphere center, if the undisturbed potential flow in absence of the sphere of radius a , is $\Phi_0(r, \theta, \phi)$, the velocity potential of the modified flow due to the presence of the fixed sphere is $\Phi(r, \theta, \phi)$ given by the equation:

$$\Phi(r, \theta, \phi) = \Phi_0(r, \theta, \phi) + \frac{1}{a} \int_0^{a^2/r^2} x \frac{\partial \Phi_0(x, \theta, \phi)}{\partial x} dx. \quad (\text{II.13})$$

Using the notations in Figure II.2, the expression of the velocity potential of the vortex flow is:

$$\Phi_0(r, \theta, \phi) = \frac{\Gamma}{2\pi} \tan^{-1} \frac{r \sin \theta \sin \phi}{\zeta(t) + r \sin \theta \cos \phi}, \quad (\text{II.14})$$

where Γ is the vortex circulation and $\zeta(t)$ is the instantaneous distance between the vortex and the bubble center.

Similarly, the expression of the velocity potential of the flow due to the bubble radius time variations, $\dot{a}(t)$, is

$$\Phi_b(r, \theta, \phi) = -\frac{a^2(t) \dot{a}(t)}{r}, \quad (\text{II.15})$$

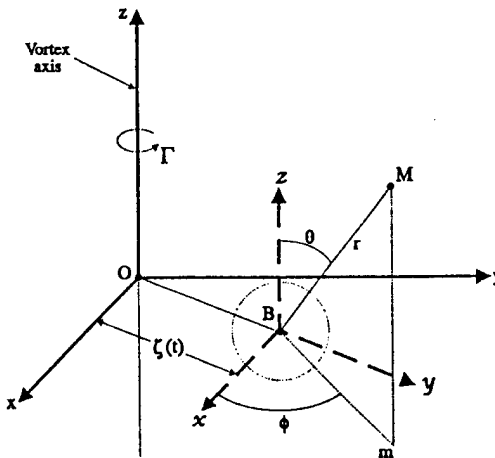


Figure II.2: Sketch of the geometric quantities involved in the analytical description of bubble capture in a vortex line.

where \circ indicates time differentiation. If we account for a relative velocity ($\mathbf{V} - \mathbf{V}_B$) between the spherical bubble and the fluid the modified bubble velocity potential becomes:

$$\Phi_b(r, \theta, \phi) = -\frac{a^2(t) \overset{\circ}{a}(t)}{r} - \frac{a^3(t)}{2r^3} \mathbf{r} \cdot (\mathbf{V} - \mathbf{V}_B), \quad (\text{II.16})$$

where $\mathbf{V}(t)$ and $\mathbf{V}_B(t)$ are the instantaneous fluid and bubble center velocities. The absolute velocity potential in the fixed coordinate system attached to the vortex, Φ_a , which accounts for bubble motion and radius variations is then:

$$\Phi_a = \Phi_0 - \frac{a^2 \overset{\circ}{a}}{r} - \frac{a^3(t)}{2r^3} \mathbf{r} \cdot (\mathbf{V} - \mathbf{V}_B) + \frac{1}{a} \int_0^{a^2/r^2} x \frac{\partial \Phi_0(x, \theta, \phi)}{\partial x} dx. \quad (\text{II.17})$$

The equation of motion of the sphere can now be obtained by using Bernoulli's equation and integrating the pressure over the surface of the sphere. The resulting force leads to the following dynamic equation:

$$\frac{4}{3}\pi a^3 \rho_b \frac{d\mathbf{V}_B}{dt} = \rho \iint_S \left[\frac{\partial \Phi_a}{\partial t} + \frac{|\nabla \Phi_a|^2}{2} \right] \mathbf{n} ds, \quad (\text{II.18})$$

where ρ and ρ_b are the liquid and bubble content density, a the bubble radius, \mathbf{n} the normal vector to the bubble surface, and $d\mathbf{V}_B/dt$ the bubble acceleration. The evaluation of the expression (II.18) in the general case is rather complex. A simplified asymptotic expression can however be obtained when the radius of the bubble is small relative to the distance from the vortex axis,

$$\epsilon = \frac{a_0}{\zeta_0} \ll 1. \quad (\text{II.19})$$

The expression of the two nondimensional components of the acceleration are then:

$$\left(\frac{\rho_b}{\rho} + \frac{1}{2} \right) \frac{d\bar{V}_{br}}{dt} = -\frac{3}{2\zeta^3} + \left(\frac{\rho_b}{\rho} + \frac{1}{2} \right) \frac{\bar{V}_{b\theta}^2}{\zeta} - \frac{\bar{V}_{br} \overset{\circ}{a}}{\bar{a}}, \quad (\text{II.20})$$

$$\frac{d\bar{V}_{b\theta}}{dt} = -\frac{\bar{V}_{b\theta}\bar{V}_{br}}{\bar{\zeta}} + \bar{\dot{a}} \left(\frac{3}{\bar{\zeta}} - \frac{2\bar{V}_{b\theta}}{\bar{a}} \right), \quad (\text{II.21})$$

where the velocities are normalized by the tangential velocity at the location ζ_o of the center of the bubble at $t = 0$, and time by the ratio between the distance ζ_o , and that characteristic velocity,

$$\bar{V}_i = V_i / \frac{\Gamma}{2\pi\zeta_o}, \quad \bar{t} = t / \frac{2\pi\zeta_o^2}{\Gamma}. \quad (\text{II.22})$$

Similarly, ζ is normalized with the initial position, $\bar{\zeta} = \zeta / \zeta_o$. Note that $V_{br} = d\zeta/dt$, and that for a bubble ρ_b/ρ is negligible. The third component along ϕ is obviously zero due to the symmetry of the problem (see [31], for further discussions and derivations of the above equations).

In the studies of [10] the bubble equation (II.18) is replaced by an empirical force balance equation first given by [18]:

$$\frac{d\mathbf{V}_B}{dt} = 3(\mathbf{V} - \mathbf{V}_B) \frac{\ddot{a}}{a} - \frac{3\nabla p}{\rho} + \frac{C_d}{4a} |\mathbf{V} - \mathbf{V}_B|, \quad (\text{II.23})$$

where C_d is a viscous drag coefficient. The first two terms on the right hand side come from inviscid flow considerations and are therefore included more formally and more accurately in Equation (II.18). The first term which results directly from the integration in (II.18) of the third term in Equation (II.17). It reflects the fact that any slip velocity between the bubble center and the surrounding fluid increases with an increase of the bubble wall velocity and a decrease of the bubble radius. Therefore, the bubble center decelerates during bubble growth and accelerates very much during the bubble collapse where both \ddot{a} and a^{-1} are very large. The second term is in fact an acceleration term of the relative or slip velocity, $(\mathbf{V} - \mathbf{V}_B)$, whose expression has been often debated in the multiphase flow community [19]. The third term is a viscous drag term where the drag coefficient C_d depends on the Reynolds number of the relative flow, \mathcal{R}_{eb} . [10] used the expression:

$$C_d = \frac{24}{\mathcal{R}_{eb}} [1 + 0.197\mathcal{R}_{eb}^{0.63} + 2.6 \times 10^{-4}\mathcal{R}_{eb}^{1.38}]; \quad \text{with} \quad \mathcal{R}_{eb} = \frac{2a|\mathbf{V} - \mathbf{V}_B|}{\nu} \quad (\text{II.24})$$

Other authors add a memory term (Basset term) which accounts for the full history of the slip velocity through an integration between 0 and t . Based on equation (II.23) the equations of motion of the bubble become for a Rankine vortex of viscous core radius, R_c :

$$\begin{aligned} \frac{dV_{br}}{dt} &= \zeta V_{b\theta}^2 - 3V_{br} \left[\frac{\ddot{a}}{a} + \frac{C_d |\delta V|}{4a} \right] - \frac{3\Gamma^2}{4\pi^2 R_c^2} f_1 \left(\frac{\zeta}{R_c} \right); \\ \zeta \frac{dV_{b\theta}}{dt} &= -2\zeta V_{b\theta} + 3\xi \left[\frac{\ddot{a}}{a} + \frac{C_d |\delta V|}{4a} \right]; \\ \frac{dV_{bz}}{dt} &= -3z \left[\frac{\ddot{a}}{a} + \frac{C_d |\delta V|}{4a} \right], \end{aligned} \quad (\text{II.25})$$

with

$$\begin{aligned} |\delta V| &= (V_{br}^2 + V_{b\theta}^2 + V_{bz}^2)^{\frac{1}{2}}, \\ f_1 &= \frac{\zeta}{R_c}, \quad \xi = \frac{\Gamma\zeta}{2\pi R_c^2} - \zeta \frac{dV_{b\theta}}{dt}; \quad \zeta \leq R_c, \\ f_1 &= \frac{\zeta^3}{R_c^3}, \quad \xi = \frac{\Gamma}{2\pi\zeta} - \zeta \frac{dV_{b\theta}}{dt}; \quad \zeta \geq R_c. \end{aligned} \quad (\text{II.26})$$

Both approaches of [6] and [15] used the spherical bubble dynamics equation – known as the Rayleigh Plesset Equation [20] – to determine the bubble radius variation with time:

$$\rho \left(a \ddot{a} + \frac{3}{2} \dot{a}^2 \right) - 4\mu \frac{\dot{a}}{a} = -P_\infty(t) + P_v - 2\frac{\gamma}{a} + P_{go} \left(\frac{a_o}{a} \right)^{3k}, \quad (\text{II.27})$$

where μ is the dynamic viscosity, P_{go} the initial gas pressure with k the polytropic gas constant, P_v the vapor pressure, and γ the surface tension coefficient. Assumptions leading to this equation are described further below.

3.1 Capture time

In order to get an idea about the characteristic time for bubble capture by the vortex let us consider equations (II.20) and (II.21). If one considers – for an order of magnitude evaluation– the case where the rate of change of the bubble volume is negligible relative to the other terms, then the two equations of motion degenerate to:

$$\begin{aligned} \mathcal{M} \frac{d\overline{V}_{br}}{dt} &= -\frac{3}{2\bar{\zeta}^3} + \mathcal{M} \frac{\overline{V}_{b\theta}^2}{\bar{\zeta}}, \\ \frac{d\overline{V}_{b\theta}}{dt} &= -\frac{\overline{V}_{b\theta}\overline{V}_{br}}{\bar{\zeta}}, \end{aligned} \quad (\text{II.28})$$

where

$$\mathcal{M} = \frac{\rho_b}{\rho} + \frac{1}{2}. \quad (\text{II.29})$$

Equations (II.28) can be integrated to give the position of the non deforming bubble relative to the vortex axis versus time. Using $d\zeta/dt$ as an intermediary variable to express d/dt as $d/d\zeta \cdot d\zeta/dt$, and assuming that the bubble center has no initial radial velocity ($v_{ro} = 0$), while the initial tangential velocity is $v_{\theta o}$, Equation (II.28) leads to:

$$\overline{V}_{b\theta}(t) = \frac{\overline{v}_{\theta o}}{\bar{\zeta}(t)}, \quad \text{and} \quad \bar{\zeta}(t) = \left[1 + \left(\overline{v}_{\theta o}^2 - \frac{3}{2\mathcal{M}} \right) \bar{t}^2 \right]^{1/2}. \quad (\text{II.30})$$

Equation (II.30) is very instructive in terms of the motion of a particle of density ρ_b in a vortex flow field. Depending on the sign of $(\overline{v}_{\theta o}^2 - \frac{3}{2\mathcal{M}})$ the particle will be attracted or repelled

by the vortex. This term in fact expresses a balance between inertial (centrifugal) and pressure forces. For bubbles entrained in the flow field of the vortex, $v_{\theta o}$ is between 0 and 1, and \mathcal{M} is very close to $\frac{1}{2}$, since $\rho_b/\rho \ll 1$. As a result,

$$\bar{\zeta}(\bar{t}) \simeq \sqrt{1 + (\bar{v}_{\theta o}^2 - 3)\bar{t}^2} \leq \sqrt{1 - 3\bar{t}^2}. \quad (\text{II.31})$$

The capture time, T_c , for a bubble initially at rest in the fluid ($\bar{v}_{\theta o}(0) = 0$) is therefore

$$\bar{t}_c = \sqrt{\frac{1}{3}}; \quad \text{or} \quad T_c = \frac{2\pi\zeta_o^2}{\Gamma\sqrt{3}}. \quad (\text{II.32})$$

In fact, for a sphere, only viscous effects can be responsible for bubble entrainment with the flow, since with the inviscid model Equations (II.18) clearly indicate that only radial forces on the sphere are non-zero. In the presence of viscosity friction forces enable entrainment of the bubble with the fluid. The characteristic time of viscous effects, or the order of magnitude of the time needed for the bubble to be entrained in the flow being

$$T_\nu = \frac{a_o^2}{\nu}, \quad (\text{II.33})$$

the qualitative nature of the capture depends on the relative size between T_c and T_ν .

If $T_c \gg T_\nu$, the capture time is too long, viscous effects are strong enough for the bubble to be entrained relatively rapidly by the liquid and it starts swirling around the vortex. It approaches the vortex axis little by little but very slowly.

If $T_c \ll T_\nu$, the opposite situation occurs: viscous effects are very slow to take effect and the bubble is practically sucked into the vortex moving towards its center almost in a purely radial fashion.

Finally, for $T_c \approx T_\nu$ entrainment by the liquid and attraction towards the center of the vortex occur on the same time scale. Therefore, the bubble approaches the axis in a spiral fashion. The above reasoning allows one to define a “violent capture radius” around the vortex which is bubble radius dependent. A bubble of radius a_o will be sucked in by the vortex if it is within the radial distance $R_{capture}$:

$$R_{capture} = a_o \sqrt{\frac{\Gamma\sqrt{3}}{2\pi\nu}}. \quad (\text{II.34})$$

4 Numerical study

Due to the difficulty of the problem at hand and to the improved performance of high speed computers, numerical methods offer presently the best hope for solutions. Coupled with guidance from analytical, experimental and order of magnitude or phenomenological studies, a numerical approach can enable minimization of the number of physical phenomena to take into account. One of the numerical methods that has proven to be very efficient in solving the type of free

boundary problem associated with bubble dynamics is the Boundary Element Method. Among others, Guerri *et al.* [33], Blake *et al.* [65, 34], and Wilkerson [74] used this method in the solution of axisymmetric problems of bubble growth and collapse near boundaries. This method was extended to three-dimensional bubble dynamics problems by Chahine *et al.* [26, 21]. We describe here the model, then apply it to the case of bubbles in a vortex flow.

4.1 Bubble flow equations

Let us consider the cases where the presence of a bubble in the flow has significant effects, that is cases where bubble volume time variations are not negligible. This implies large but subsonic bubble wall velocities. Therefore, one can neglect viscosity and compressibility effects on the bubble dynamics. These assumptions, classical in cavitation bubble dynamics studies, result in a flow that is potential, (velocity potential, Φ), and which satisfies the Laplace equation,

$$\nabla^2 \Phi = 0. \quad (\text{II.35})$$

The solution must in addition satisfy initial conditions and boundary conditions at infinity, at the bubble walls and at the boundaries of any nearby bodies.

At all moving or fixed surfaces (such as a bubble surface or a nearby boundary) an identity between fluid velocities normal to the boundary and the normal velocity of the boundary itself is to be satisfied:

$$\nabla \Phi \cdot \mathbf{n} = \mathbf{V}_s \cdot \mathbf{n}, \quad (\text{II.36})$$

where \mathbf{n} is the local unit vector normal to the bubble surface and \mathbf{V}_s is the local velocity vector of the moving surface.

The bubble is assumed to contain noncondensable gas as well as vapor of the surrounding liquid. The pressure within the bubble is considered to be the sum of the partial pressures of the noncondensable gases, P_g , and that of the liquid vapor, P_v . Vaporization of the liquid is assumed to occur at a fast enough rate so that the vapor pressure may be assumed to remain constant throughout the simulation and equal to the equilibrium vapor pressure at the liquid ambient temperature. In contrast, since time scales associated with gas diffusion are much larger, the amount of noncondensable gas inside the bubbles is assumed to remain constant and the gas is assumed to satisfy the polytropic relation,

$$P_g V^k = \text{constant}, \quad (\text{II.37})$$

where V is the bubble volume and k the polytropic constant, with $k = 1$ for isothermal behavior and $k = c_p/c_v$ for adiabatic conditions.

The pressure in the liquid at the bubble surface, P_L , is obtained at any time from the following pressure balance equation:

$$P_L = P_v + P_{g0} \left(\frac{V_0}{V} \right)^k - C\sigma, \quad (\text{II.38})$$

where P_{g0} and V_0 are the initial gas pressure and volume respectively, σ is the surface tension, C is the local curvature of the bubble, and V is the instantaneous value of the bubble volume. In the numerical procedure P_{g0} and V_0 are known quantities at $t = 0$.

4.2 Boundary integral method for three-dimensional bubble dynamics

In order to render possible the simulation of single or multiple bubble behavior in complex geometry and flow configurations including the full non-linear boundary conditions, a three-dimensional Boundary Element Method was developed and implemented by Chahine *et al.* [26, 67]. The Boundary Element Method was chosen here because of its computational efficiency. By considering only the boundaries of the fluid domain it reduces the dimension of the problem by one. This method is based on Green's equation which provides Φ anywhere in the domain of the fluid (field points P) if the velocity potential, Φ , and its normal derivatives are known on the fluid boundaries (points M), and if Φ satisfies the Laplace equation:

$$\int \int_s \left[-\frac{\partial \Phi}{\partial n} \frac{1}{|\mathbf{MP}|} + \Phi \frac{\partial}{\partial n} \left(\frac{1}{|\mathbf{MP}|} \right) \right] ds = a\pi\Phi(P), \quad (\text{II.39})$$

where $a\pi = \Omega$ is the solid angle under which P sees the fluid.

- $a = 4$, if P is a point in the fluid,
- $a = 2$, if P is a point on a smooth surface, and
- $a < 4$, if P is a point at a sharp corner of the surface.

If the field point is selected to be on the surface of any of the bubbles or on the surface of the nearby boundaries, then a closed set of equations can be obtained and used at each time step to solve for values of $\partial\Phi/\partial n$ (or Φ) assuming that all values of Φ (or $\partial\Phi/\partial n$) are known at the preceding step.

To solve Equation (II.39) numerically, it is necessary to discretize each bubble into panels, perform the integration over each panel, and then sum up the contributions to complete the integration over the entire bubble surface. To do this, the initially spherical bubbles are discretized into a geodesic shape using flat, triangular panels. This discretization of a bubble shape is described in Chahine *et al.* [26, ?]. Equation (II.39) then becomes a set of N equations (N is the number of discretization nodes) of index i of the type:

$$\sum_{j=1}^N \left(A_{ij} \frac{\partial \Phi_j}{\partial n} \right) = \sum_{j=1}^N (B_{ij}\Phi_j) - a\pi\Phi_i; \quad i = 1, \dots, N \quad (\text{II.40})$$

where A_{ij} and B_{ij} are elements of matrices which are the discrete equivalent of the integrals given in Equation (II.39).

To evaluate the integrals in (II.39) over any particular panel, a linear variation of the potential and its normal derivative over the panel is assumed. In this manner, both Φ and $\partial\Phi/\partial n$ are continuous over the bubble surface, and are expressed as a function of the values at the three nodes which delimit a particular panel. Obviously higher order descriptions are conceivable, and would probably improve accuracy at the expense of additional analytical effort and numerical computation time. The two integrals in (II.39) are then evaluated analytically. The resulting expressions, too long to present here, can be found in [26].

In order to proceed with the computation of the bubble dynamics several quantities appearing in the above boundary conditions need to be evaluated at each time step. The bubble volume

presents no particular difficulty, while the unit normal vector, the local surface curvature, and the local tangential velocity at the bubble interface need further development. In order to compute the curvature of the bubble surface a three-dimensional local bubble surface fit, $f(x, y, z) = 0$, is first computed. The unit normal at a node can then be expressed as:

$$\mathbf{n} = \pm \frac{\nabla f}{|\nabla f|}, \quad (\text{II.41})$$

with the appropriate sign chosen to insure that the normal is always directed towards the fluid. The local curvature is then computed using

$$\mathcal{C} = \nabla \cdot \mathbf{n}. \quad (\text{II.42})$$

To obtain the total fluid velocity at any point on the surface of the bubble, the tangential velocity, \mathbf{V}_t , must be computed at each node in addition to the normal velocity, $\mathbf{V}_n = \partial\Phi/\partial n$. This is also done using a local surface fit to the velocity potential, $\Phi_t = h(x, y, z)$. Taking the gradient of this function at the considered node, and eliminating any normal component of velocity appearing in this gradient gives a good approximation for the tangential velocity

$$\mathbf{V}_t = \mathbf{n} \times (\nabla \Phi_t \times \mathbf{n}). \quad (\text{II.43})$$

The basic procedure can then be summarized as follows. With the problem initialized and the velocity potential known over the surface of the bubble, an updated value of $\partial\Phi/\partial n$ can be obtained by performing the integrations in (II.39) and solving the corresponding matrix equation (II.40). $D\Phi/Dt$ is then computed using a “modified” Bernoulli equation (see Equation (II.51) below). Using an appropriate time step all values of Φ on the bubble surface can then be updated using Φ at the preceding time step and $D\Phi/Dt$,

$$\frac{D\Phi}{Dt} = \frac{\partial\Phi}{\partial t} + \left(\frac{\partial\Phi}{\partial n} \mathbf{n} + \mathbf{V}_t \right) \cdot \nabla \Phi. \quad (\text{II.44})$$

In the results presented below the time step, dt , was based on the ratio between the length of the smaller panel side, l_{min} and the highest node velocity, V_{max} . This choice limits the motion of any node to a fraction of the smallest panel side. It has the great advantage of constantly adapting the time step, by refining it at the end of the collapse – where l_{min} becomes very small and V_{max} very large – and by increasing it during the slow bubble size variation period. New coordinate positions of the nodes are then obtained using the displacement:

$$d\mathbf{M} = \left(\frac{\partial\Phi}{\partial n} \mathbf{n} + V_t \mathbf{e}_t + \mathbf{V}_o \right) dt, \quad (\text{II.45})$$

where \mathbf{n} and \mathbf{e}_t are the unit normal and tangential vectors. This time stepping procedure is repeated throughout the bubble growth and collapse, resulting in a shape history of the bubble.

4.3 Pressure / velocity potential relation

Let us consider the case of a bubble growing and collapsing in a nonuniform flow field ("basic flow") of velocity \mathbf{V}_0 that is known and satisfies the Navier Stokes equations:

$$\frac{\partial \mathbf{V}_0}{\partial t} + \mathbf{V}_0 \cdot \nabla \mathbf{V}_0 = -\frac{1}{\rho} \nabla P_0 + \nu \nabla^2 \mathbf{V}_0 . \quad (\text{II.46})$$

Also assume that in presence of the oscillating bubbles, the resulting velocity field, given by \mathbf{V} , also satisfies the incompressible Navier Stokes equation:

$$\frac{\partial \mathbf{V}}{\partial t} + \mathbf{V} \cdot \nabla \mathbf{V} = -\frac{1}{\rho} \nabla P + \nu \nabla^2 \mathbf{V} . \quad (\text{II.47})$$

Both \mathbf{V} and \mathbf{V}_0 also satisfy the continuity equation. We can now define bubble flow velocity and pressure variables, \mathbf{V}_b and P_b , as follows:

$$\mathbf{V}_b = \mathbf{V} - \mathbf{V}_0, \quad P_b = P - P_0. \quad (\text{II.48})$$

If we consider the case where "bubble flow" field is potential³ :

$$\mathbf{V}_b = \nabla \Phi_b, \quad \nabla^2 \Phi_b = 0, \quad (\text{II.49})$$

and subtract (II.46) from (II.47) accounting for (II.49) we obtain

$$\nabla \Psi = \nabla \left[\frac{\partial \Phi_b}{\partial t} + \frac{1}{2} |\mathbf{V}_b|^2 + \mathbf{V}_0 \cdot \mathbf{V}_b + \frac{P_b}{\rho} \right] = \mathbf{V}_b \times (\nabla \times \mathbf{V}_0). \quad (\text{II.50})$$

The assumption of potential "bubble flow" implies that, even though the basic flow is allowed to interact with the bubble dynamics and be modified by it, no new vorticity can be generated by the bubble behavior with the chosen model. Equation (II.50) can be integrated to obtain an equation similar to the classical unsteady Bernoulli equation. For the particular case of the Rankine vortex Equation (II.51) can be written in cylindrical coordinates, when the "bubble flow" does not have any e_θ components:

$$\frac{\partial \Psi}{\partial r} = 0, \quad \frac{1}{r} \frac{\partial \Psi}{\partial \theta} = 2V_b, \quad \frac{\partial \Psi}{\partial z} = 0.$$

In this case the Bernoulli equation is to be replaced by:

$$\frac{\partial \Phi_b}{\partial t} + \frac{1}{2} |\mathbf{V}_b|^2 + \frac{P - P_0}{\rho} = \text{constant in any radial direction.} \quad (\text{II.51})$$

Accounting for at-infinity conditions, the pressure in the liquid at the bubble wall, P_L , given by (II.51) is related to Φ_b and the pressure field in the Rankine vortex P_0 by:

$$\left[\frac{P_L}{\rho} = \frac{P_0}{\rho} - \frac{\partial \Phi_b}{\partial t} - \frac{1}{2} |\mathbf{V}_b|^2 \right]_{\text{at bubble wall}} . \quad (\text{II.52})$$

³This is obviously a simplifying assumption which is removed at the end of this chapter and in the following chapters.

4.4 Specialization to axisymmetric problems

In axisymmetric problems, the physical variables (velocity potential and pressure) are independent of the angular coordinate. Thus the angular coordinate only enters the formulation through the argument of the Green's function in Equation (II.39)

$$G(\mathbf{MP}) = 1 / |\mathbf{MP}|. \quad (\text{II.53})$$

The integration of these dependent quantities can be explicitly carried out. Let C represent the trace of the geometry under consideration in a meridian plane. Let (r, θ, z) be the cylindrical coordinates of point M , running point on the boundary, and without loss of generality we select the coordinates of P to be $(R, 0, Z)$. The integral equation (II.39) can then be written

$$\phi(R, 0, Z) = \int_C r\phi(r, z) \frac{\partial}{\partial n_M} \left(\int_0^{2\pi} G d\theta \right) ds_M - \int_C \frac{\partial \phi}{\partial n_M} r \int_0^{2\pi} G d\theta ds_M. \quad (\text{II.54})$$

In writing the above expression the fact that the normal to an axisymmetric surface is independent of the angular coordinate has been used. Thus, integration over the angular variable is reduced to evaluation of one integral

$$I = \int_0^{2\pi} G(r, \theta, z; R, Z) d\theta = -\frac{1}{4\pi} \int_0^{2\pi} \frac{d\theta}{\sqrt{R^2 + r^2 - 2rR \cos \theta + (Z - z)^2}}, \quad (\text{II.55})$$

which is nothing but the *complete elliptic integral of the first kind*, $K(m)$, with

$$m = \frac{4rR}{A}; \quad A = \sqrt{(R+r)^2 + (Z-z)^2}. \quad (\text{II.56})$$

The equation for the potential may then be written as:

$$2\pi\phi(R, Z) = - \int_C \phi(r, z) r \frac{\partial}{\partial n_M} \left(\frac{4K(m)}{\sqrt{A}} \right) ds_M + \int_C \frac{\partial \phi}{\partial n_M}(r, z) \frac{4K(m)}{\sqrt{A}} r ds_M. \quad (\text{II.57})$$

Further details of the method can be found in [73].

5 Numerical results and discussion

5.1 Validation of numerical codes

The use of the Boundary Element Method to study axisymmetric bubble dynamics has been validated by the various authors quoted earlier. This has included both comparisons with a quasi-analytical solution for spherical bubbles – Rayleigh-Plesset Equation (II.27) – and experimental validation for the relatively simple cases of spherical and axisymmetric bubble collapse near flat solid walls. Figures II.3a and II.3b show comparative results between the codes used below (axisymmetric 2DYNAFS and fully three-dimensional 3DYNAFS) and the semi-analytical results.

Comparison of the results of the 3D code used in the examples shown below against previously published and confirmed results in the literature for the relatively simple cases have been very

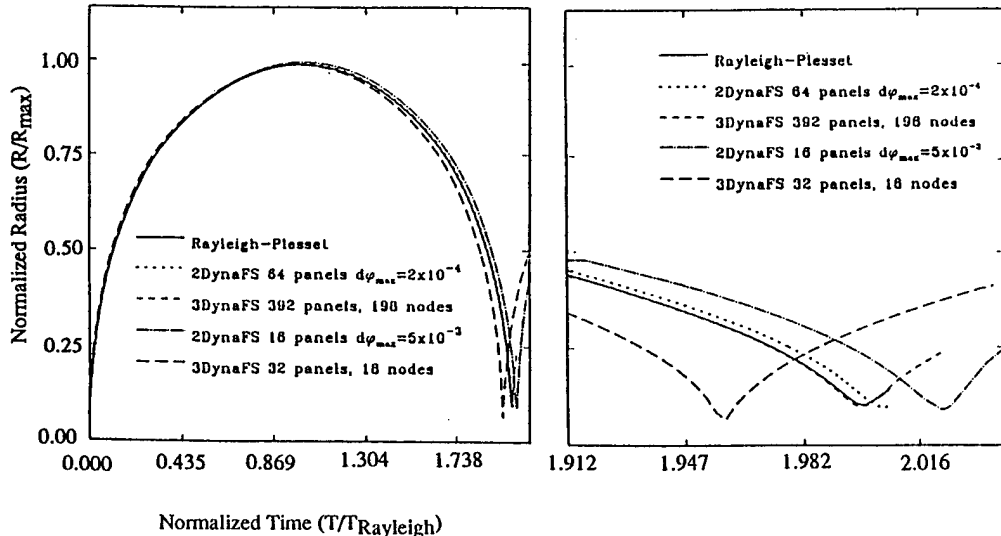


Figure II.3: Comparison between Rayleigh-Plesset solution and the axisymmetric BEM code 2DYNALFS and the 3D BEM code 3DYNALFS. Computations started with an initial bubble pressure 584 times larger than the ambient pressure. a) Over bubble period. b) End of collapse.

favorable. For spherical bubbles, comparison with the Rayleigh-Plesset “exact” solution revealed that numerical errors for a “coarse” discretization of a 102-node bubble (not shown in the above figures) was about 2 percent of the achieved maximum radius, but was very small, 0.03 percent, of the bubble period. The error on the maximum radius was less than 0.14 percent for a discretized bubble of 162 nodes (320 panels), and dropped to 0.05 percent for 252 nodes (500 panels). Comparisons were also made with studies of axisymmetric bubble collapse available in the literature [33, 65, 34], and have shown, for the coarse discretization, differences with these studies on the bubble period of the order of 1 percent. Finally, comparison with actual test results of the complex three-dimensional behavior of a large bubble collapse in a gravity field near a cylinder shows very satisfactory results [26, 67]. The observed difference in the period was shown to be related to the confinement of the experimental bubble in a cylindrical container.

5.2 Bubble capture

Large bubble growth rate, low surface tension case

As expected from the mechanistic considerations analysis presented in Sections II.1.1 and II.1.2 numerical simulations using the fully three-dimensional numerical approach reveal potential for strong bubble deformation during capture by a vortex. The numerical results indicate that this is the case for a very wide range of bubble sizes and initial values of the pressure difference between the inside and the outside of the bubble.

Figure II.4 shows three-dimensional bubble behavior in the case where the ratio between the pressure inside the bubble and the ambient pressure is significantly large, $p_i/p_\infty = 584.3$. This would be the case where the bubble in equilibrium in a high ambient pressure environment is suddenly subjected to the flow field of a vortex, as for instance when a propeller tip vortex suddenly captures a cavitation bubble (see [13, 70]). In a Cartesian system of coordinates, $OXYZ$,

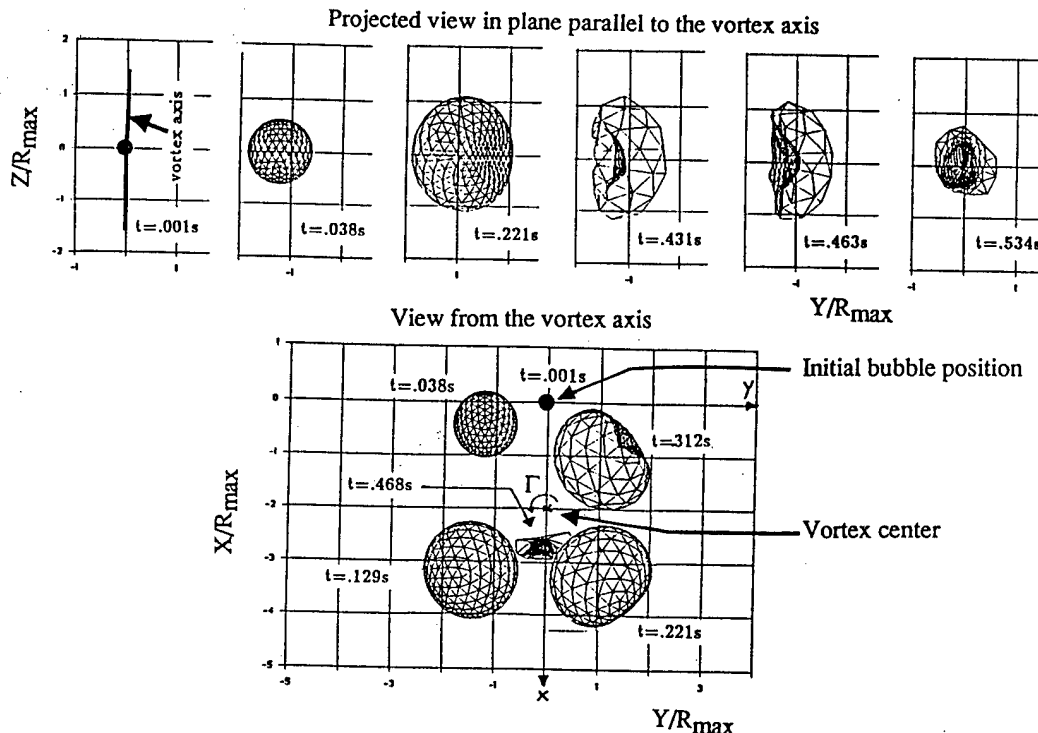


Figure II.4: 3D bubble shapes at various times. Bubble initially at the origin of the cartesian coordinate system, and vortex at $X = 2R_{max}$. $\Omega = 0.474$, $p_i/p_\infty = 584.3$, $R_c/R_{max} = 4$. Projected view a) in the XOY plane; b) in the XOZ plane.

the bubble is initially centered at $(0,0,0)$, and the line vortex is located parallel to the Z axis, at $\bar{X} = X/R_{max} = 2$ (two times the maximum size, R_{max} , the considered bubble would have if allowed to grow under the same pressure difference in an infinite medium). The core size considered here is $4R_{max}$. With this geometry the bubble center remains in the plane $Z = 0$.

Figure II.4a gives a projected view of the bubble in the XOY plane at different instants. The observer is looking down on the XOY plane from very far on the Z axis. The bubble is seen spiraling around the vortex axis (perpendicular to the figure) while approaching it. At the same time, due to the presence of the pressure gradient, the bubble strongly deforms and a reentrant jet is formed directed towards the axis of the vortex, thus indicating the presence of a much larger dynamic pressure on the bubble side opposite to the vortex axis.

Figure II.4b shows projected view of the same bubble in the YOZ plane seen from the OX axis. Here some moderate elongation of the bubble is observed along the axis of the vortex as well as a very distinct side view of the re-entrant jet. *This result is totally contrary to the usually held belief that bubbles constantly grow during their capture until they reach the axis and elongate along it.*

Figure II.5 shows in the XOY plane perpendicular to the vortex axis the motion of two particular points on the bubble, A and B , initially along OY . Also shown is the motion of the midpoint, C . While C seems to follow a path similar to the classical logarithmic spiral, A and B can follow more complicated paths, even moving away from the vortex axis at some point in time for case (b) where the vortex axis was initially at $X = 1$.

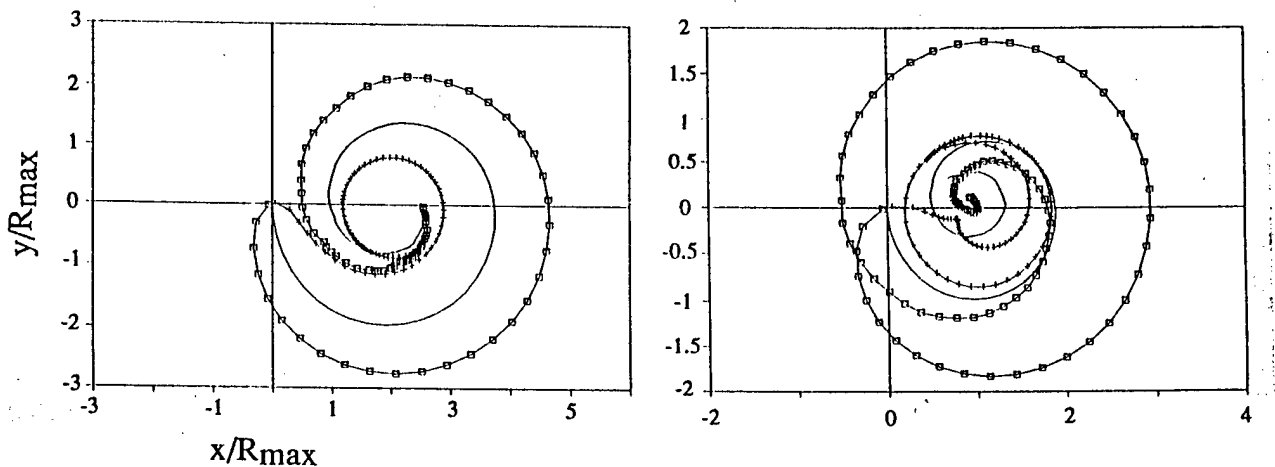


Figure II.5: Motion of the two points initially on axis OX, A and B, and the mid point C between A and B, versus times. $\Omega = 0.474$, $p_i/p_\infty = 584.3$, $a_c/R_{max} = 4$. Vortex located at a) $X = 2R_{max}$; b) $X = R_{max}$.

Small growth rate and surface tension

Figure II.6 considers the influence of bubble size on bubble behavior during the capture process. In all three cases shown in the figure a ratio between the pressures inside and outside the bubble equal to one is considered, $p_i/p_\infty = 1$. In all cases, the viscous core radius is chosen to be $R_c = 2.2$ mm, while the initial distance between the vortex center and the center of each bubble is chosen to be $\zeta_o \simeq 1.5R_c = 3.2$ mm. The dimensions shown are normalized values with the initial bubble radius for each case. The circulation in the vortex is chosen to correspond to a practical value for the case of a tip vortex behind a foil, such as that used in the experiments described by Maines and Arndt [13] and Green [70], $\Gamma = 0.152$ m²/s. Three bubble sizes are considered: 10 μ m, 100 μ m and 1000 μ m. As expected, bubble deformation increases with the bubble size. The deformation is small for $a_o=10$ μ m, becomes very significant for $a_o=100$ μ m, and is extremely important for $a_o=1000$ μ m. In all cases, the bubbles while remaining in the inviscid region, are seen to be sheared very strongly by the flow. The smaller bubbles appear to deform in the expected way in a shear flow. The computations were stopped when significant bubble shape deformations necessitated finer time steps. The larger bubble case ($a_o=1000$ μ m) shows extreme bubble elongation and wrapping around the viscous core region.

5.3 Multiple bubbles

One of the key question that one needs to address in bubble/vortex interaction practical studies is how does a distribution of bubbles modify the flow field in a vortex line. In order to address such a problem the program 3DYNAPS was modified for effective implementation on a supercomputer. Indeed one of the difficulties of such a study is the required large number of discretization points which prevents significant runs on typical memory and speed limited computers. Figure II.7 shows a case run in the case of a field of bubbles in absence of a vortex field on a Cray machine. In the figure case two planes of symmetry were assumed to minimize computation times. In the presence

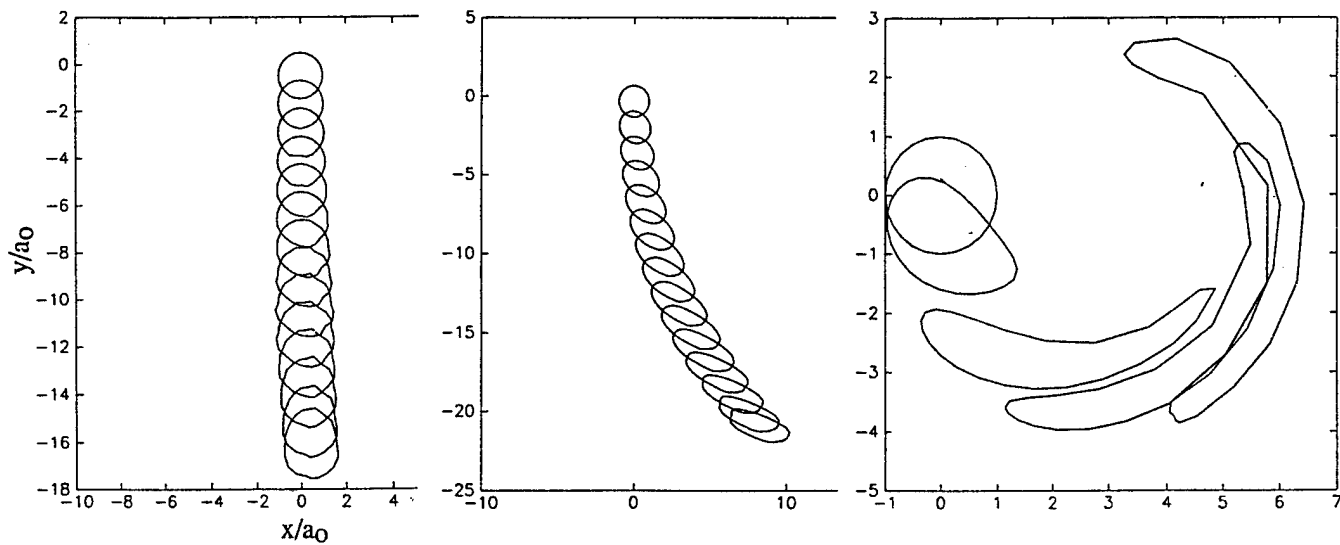


Figure II.6: Bubble contours at various times. $\Gamma = 0.1527 m^2/s$, $p_i/p_\infty = 1$, $a_c = 2.2 mm$, vortex located at $X = 3.2 mm$, with $a_o =$ a) $10\mu m$, b) $100\mu m$, c) $1000\mu m$.

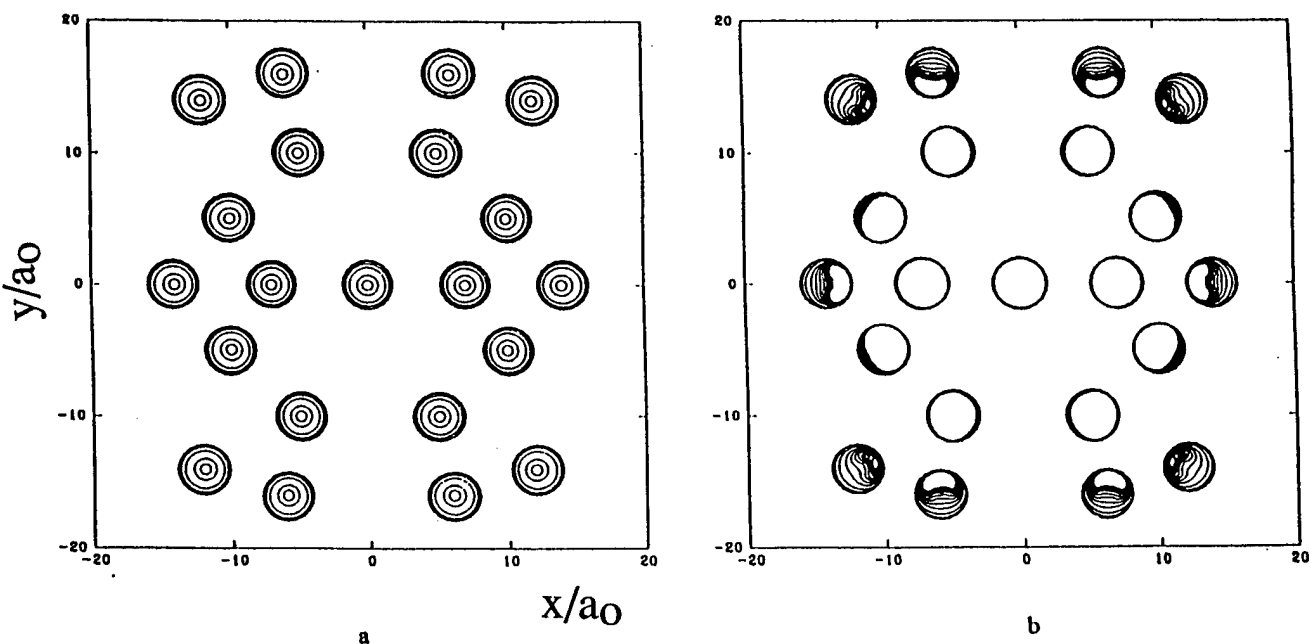


Figure II.7: Simulation of the dynamical interactions between a cloud of 21 bubbles using 3DYNAFS on a Cray. Two planes of symmetry are used. Each bubble has 102 nodes and 200 panels.
a) Growth. b) Collapse.

of a vortex line use of such a symmetry is not warranted since, due to various rates of rotation of each bubble in the vortex field, the symmetry is not preserved during the bubble motion. In addition, due to the high shear rates that bubbles can experience, a relatively large number of discretization points is needed to describe each bubble.

Figure II.8 shows the case of a 5-bubble configuration. This run has the advantage of including both vortex / bubble and bubble / bubble interactions. All five bubbles are chosen such that in absence of the vortex flow field, the pressures inside and outside each bubble are the same and equal to 0.74 atm, $p_i/p_\infty = 1$. The viscous core radius and the circulation are again chosen to be in the same ranges as those in the experiments described by Maines and Arndt [13] and Green [70]. The viscous core is chosen to be $R_c = 2.2\text{mm}$, while $\Gamma = 0.1573 \text{ m}^2/\text{s}$, $\Omega = 0.872$. The initial bubble centers are selected to be on OY axis at the coordinates: $Y = 0, 2, 3, 4$ and 5 mm . The vortex line is parallel to OX axis and is centered on $Y = 1.5\text{ mm}$. As a result, bubbles No. 1, 2 and 3 are initially located in the viscous core, while bubbles No. 4 and 5 are located in the inviscid flow region. All five bubbles considered have an initial radius of $100\text{ }\mu\text{m}$. Figure II.8 shows contours of the bubbles as they rotate around the vortex axis at various times. This figure clearly shows the presence of a nonuniform flow field. Indeed, Bubble No. 3 which is the closer to the region of highest angular velocity of the "basic flow" is seen to swirl around the vortex center at the fastest rate, while Bubble No. 2, which is the closest to the vortex center is seen to practically rotate around itself. Similarly, the highest shear is seen to occur close to the viscous core edge where the pressure gradients and their variations are steeper.

Since all bubbles were chosen to have the same initial radius and internal pressure, the natural period of oscillation of each of the selected bubbles increases with the proximity to the vortex axis. As a result, the farthest bubble from the axis, Bubble No. 5, collapses first while stretching and deforming. In order to be able to continue the computation following break up of a bubble, that bubble was removed and the computation was continued with the bubbles left.

Figure II.9 shows two three-dimensional views of the bubbles before the collapse of bubble No. 1. These views enable one to have a better idea of the bubble shape deformation and elongation during the capture phenomenon.

Figure II.10, courtesy of Sheldon Green, is an unpublished photo of a bubble in the viscous core of the trailing vortex of a NACA 66-209 hydrofoil (see [70], for details of the experiment). The photograph is a double exposure, the time of separation between the two pictures being $150\text{ }\mu\text{s}$. The three bubble shapes in the top of the figure are aligned along the axis of the vortex. The diameter of these shapes is of the order of $200\text{ }\mu\text{m}$. The bottom two shapes are those of the same bubble at two instants $150\text{ }\mu\text{s}$, and illustrate clearly the large deformations of the bubble during its capture by the vortex. As in the numerical simulations presented above, this behavior appears to be related to the large shear stresses experienced by the bubble while approaching the vortex axis. In the first of the two pictures the bubble is very elongated due to shear, while $150\text{ }\mu\text{s}$ later, it appears to have grown in size – due to the pressure drop in the vortex, – while conserving a strong deformation on its downstream surface.

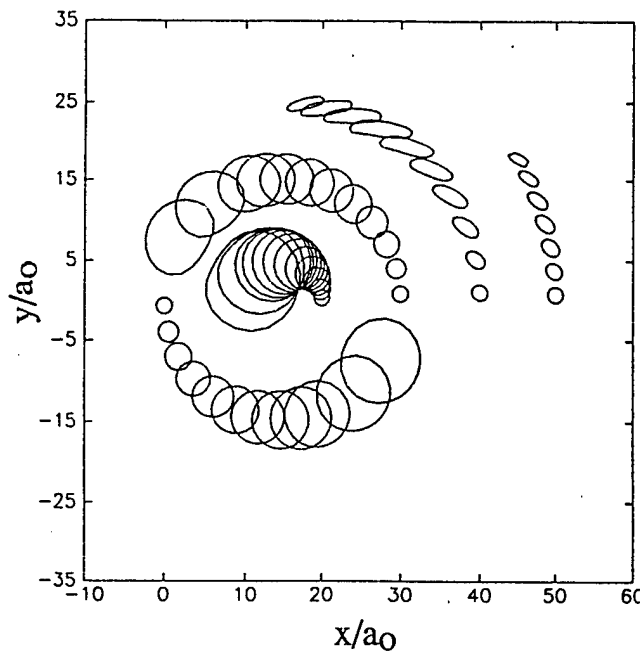


Figure II.8: Dynamical behavior of 5 bubbles in a vortex line flow - Bubble contours at various times. The vortex line is perpendicular to the page and centered on $Y = 1.5\text{mm}$. $R_c = 2.2\text{mm}$, $\Gamma = 0.1573\text{m}^2/\text{s}$. $\Omega = 0.872$. All bubbles have $a_0 = 100\mu\text{m}$.

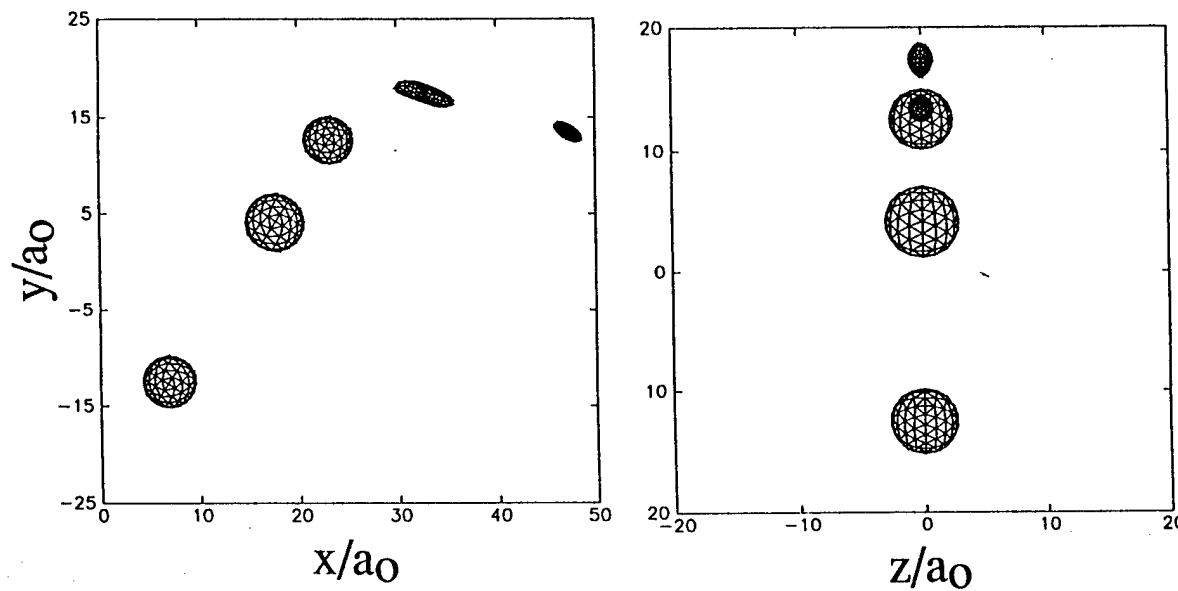


Figure II.9: 3D bubble shapes in the vortex line flow field of Figure II.8 before collapse of bubble No. 1. View from a) OZ axis, b) OX axis.

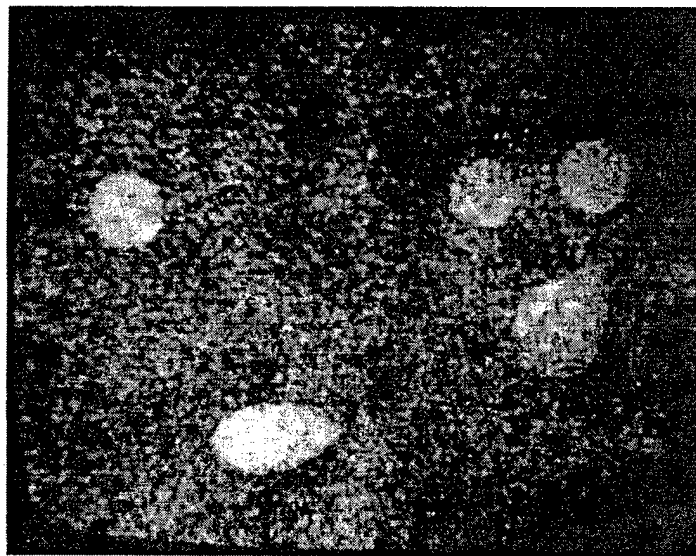


Figure II.10: Double exposure photo of a bubble in the viscous core of the trailing vortex of a NACA 66-209 hydrofoil (see [70]). Time of separation between two exposures = $150\ \mu s$. Scale $190\ \mu m./cm.$ $R_e = 6.810^5$, $\Gamma = 0.232m^2/s$. Courtesy of Sheldon Green.

5.4 Bubble on vortex axis

Let us consider now the case where the bubble is placed at the vortex axis at $t = 0$ and starts to grow due to the excess between the internal pressure and the local ambient pressure. Such a problem was considered earlier by Crespo *et al.* [69] who studied the dynamics of an elongated bubble. Unfortunately, his model neglected essential elements in the bubble / line vortex dynamics: i.e. the presence of an azimuthal velocity flow field, a rotational and viscous flow, and a pressure “well” on the axis. Crespo obtained a strong jet which initiated at both extreme points of the bubble along the axis of symmetry. As shown in Figure II.11a such a behavior is reproduced using the program 2DYNAPS when the vortex flow field is neglected. However, the opposite effect is in general obtained when the rotation in the vortex flow is included. Figure II.11b illustrates this for particular values of the circulation, Γ , (or the swirl parameter, Ω) and the normalized core radius, $\bar{R}_c = R_c/R_{max}$. Modifications in the results when Ω and \bar{R}_c are changed are discussed in the following paragraph.

In both cases shown in Figures II.11a and II.11b the initial bubble shape elongation ratio, bubble length to radius, was three. It is clear from the comparison that the swirl flow has a conclusive effect on the bubble dynamics. Bubble surface portions away from the vortex axis experience much higher pressures than bubble surface portions on and close to the vortex axis, and therefore move much faster during the collapse phase generating, instead of the sharp jets on the axis as in Figure II.10a, a constriction in the mid-section of the bubble. This generates an hourglass shaped bubble which then separates into two tear-shaped bubbles.

In the following figures II.12a – c, the dynamics of initially spherical bubble positioned at $t = 0$ on the vortex axis are studied. The initial internal pressures inside the bubbles are taken to be larger than the pressure on the vortex axis, and the bubbles are left free to adapt to this

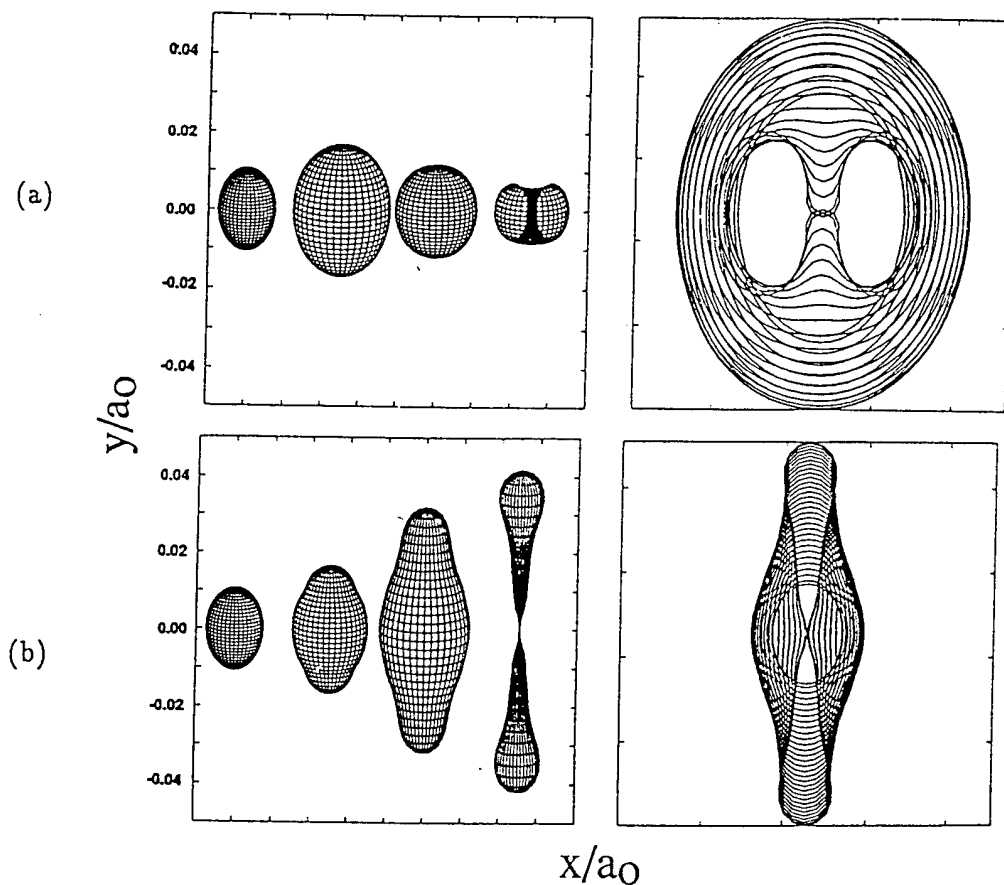


Figure II.11: Comparison between the contours of an elongated bubble during its collapse in the absence and in the presence of swirl. Initial elongation ratio of 3. $p_\infty/p_i = 3.27$. a) No swirl. b) $\Omega = 0.56$. $R_c/R_{max} = 3$.

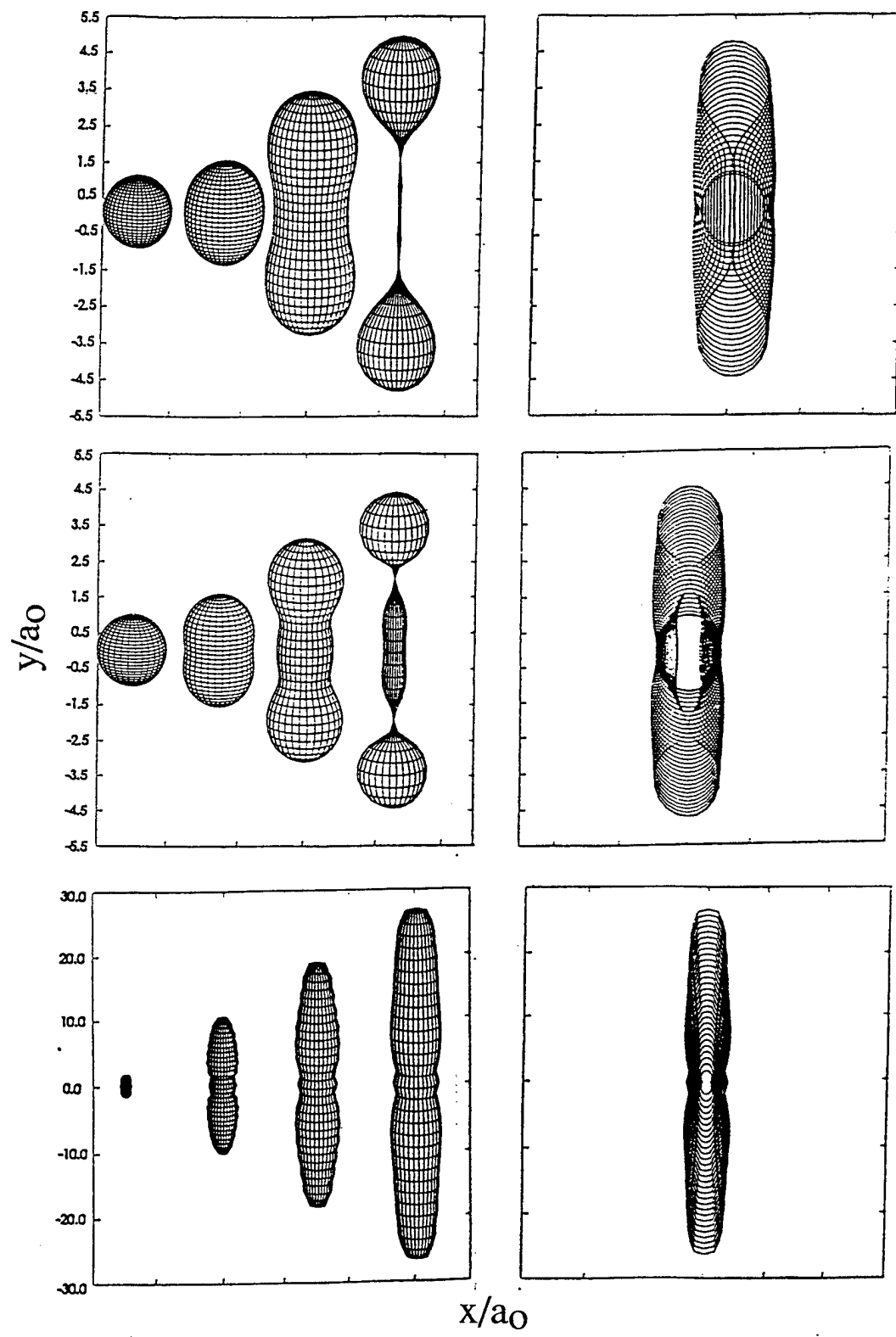


Figure II.12: Bubble dynamics on the axis of a vortex line. Left side shows 3D shapes at selected times. Right side shows bubble contours at increasing times. $\Gamma = 0.005m^2/s$, $R_o = 100\mu m$.
 a) $p_i/p_\infty = 2$, $R_c/R_o = 1$, b) $p_i/p_\infty = 2$, $R_c/R_o = 1$, c) $p_i/p_\infty = 1$, $R_c/R_o = 0.57$.

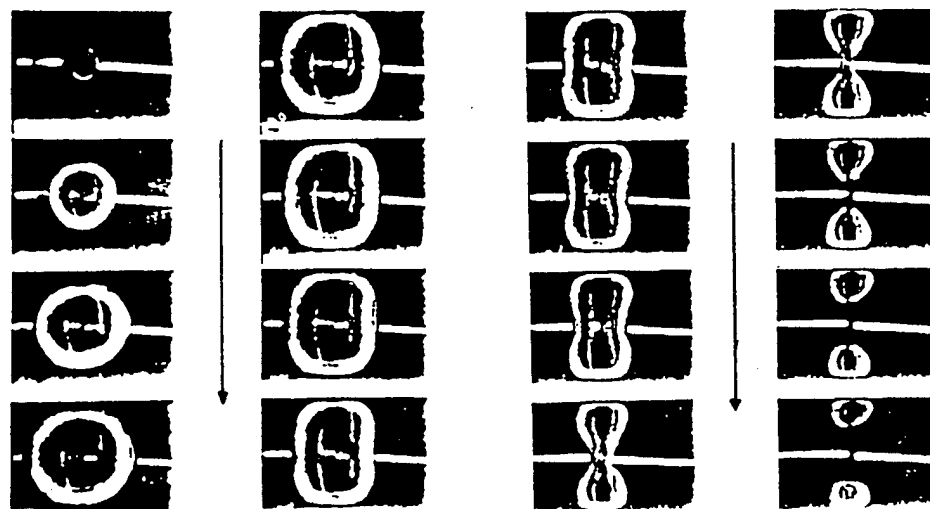


Figure II.13: Bubble collapse between two solid parallel plates resulting in the formation of an hourglass shaped bubble and a line vortex perpendicular to the two plates.

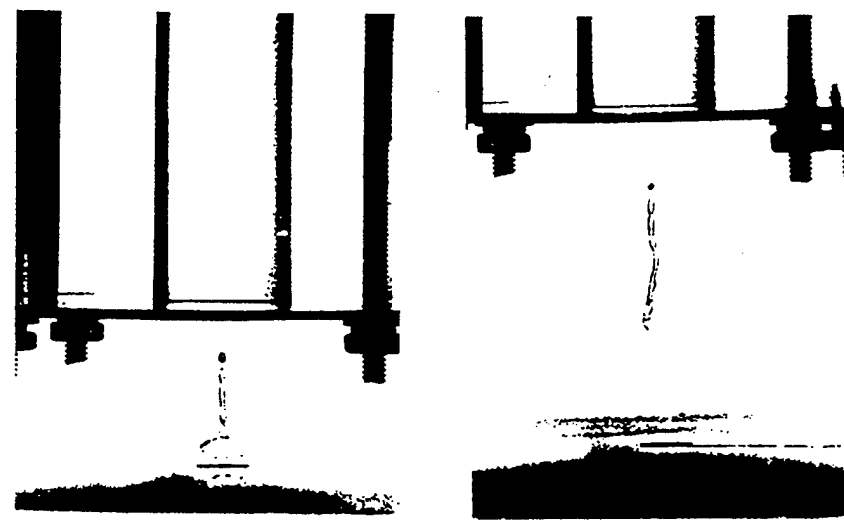


Figure II.14: Cavitation bubble shapes observed at the exit of a vortex tube.

pressure difference. The figures strongly indicate that the bubble behavior depends significantly for a given value of the swirl parameter, Ω , on the normalized core radius \bar{R}_c , ratio of R_c to R_{max} , the maximum radius the bubble would achieve if it was in an infinite medium with an ambient pressure equal to that on the vortex axis. In all cases where the bubble maximum radius, R_{max} is larger than R_c it appears that the bubble tends to adapt to the vortex tube of radius R_c . This could lead to various bubble shapes as shown in the following figures ending up with a very elongated bubble with a wavy surface for large values of R_{max}/R_c .

Figures II.12a – c show bubble contours at various times during growth and collapse for increasing values of the core radius, R_c , and decreasing values of p_i/p_∞ . Also shown are selected 3D shapes of the bubbles at various times which have the advantage of being much more descriptive. It is apparent from these figures, that during the initial phase of the bubble growth, radial velocities are large enough to overcome centrifugal forces and the bubble first grows almost spherically. Later on, the bubble shape starts to depart from spherical and to adapt to the pressure field. The bubble then elongates along the axis of rotation. Once the bubble has exceeded its equilibrium volume, bubble surface portions away from the axis – high pressure areas – start to collapse, or to return rapidly towards the vortex axis. To the contrary, points near the vortex axis do not experience rising pressures during their motion, are not forced back towards their initial position, and continue to elongate along the axis. As a result, a constriction appears in the mid-section of the bubble. The bubble can then separate into two or more tear-shaped bubbles. It is conjectured that this splitting of the bubbles is a main contributor to cavitation inception noise. This behavior is very similar to that observed for bubble growth and collapse between two plates [21], which results in the formation of a vortex line! (see Figure II.13).

Keeping Ω constant while reducing the core size R_c has the effect of steepening the radial pressure gradient along the bubble surface and increasing the rotation speed inside the viscous core. This enhances the deviation of the bubble shape from a sphere, and increases the centrifugal force on the fluid particles closer to the vortex axis. This has the consequence of increasing the elongation rate of the bubble and results in more and more complex dynamic shapes of the elongated bubbles. The bubble can then become subdivided into three, four or more satellite bubbles during the collapse. The elongated and wavy shapes obtained have been observed in unpublished tests that we have conducted on cavitation on the axis of the vortex formed in a vortex tube (see Figure II.14).

5.5 Bubble on vortex axis perpendicular to a wall

The series of Figures II.15a – c show the collapse of a bubble trapped in a line vortex perpendicular to a solid wall at various distances from this wall. The boundary is at $y = 0$ and its distance to the initial bubble center, L , is normalized with R_{max} . The presence of the wall is accounted for by the incorporation of an image bubble. The uneventful growth phase ends with the elongated spheroid shaped contours shown at the center of each figure. Then, the overall bubble behavior appears to be similar to that in absence of the wall; namely, bubble elongation along the axis followed by a splitting into two bubbles. The presence of the wall is felt by an asymmetry between the two secondary bubbles. In all cases, computation was stopped at bubble splitting. A special treatment to the bubble shape discretization needs to be done after that point (panel removal).

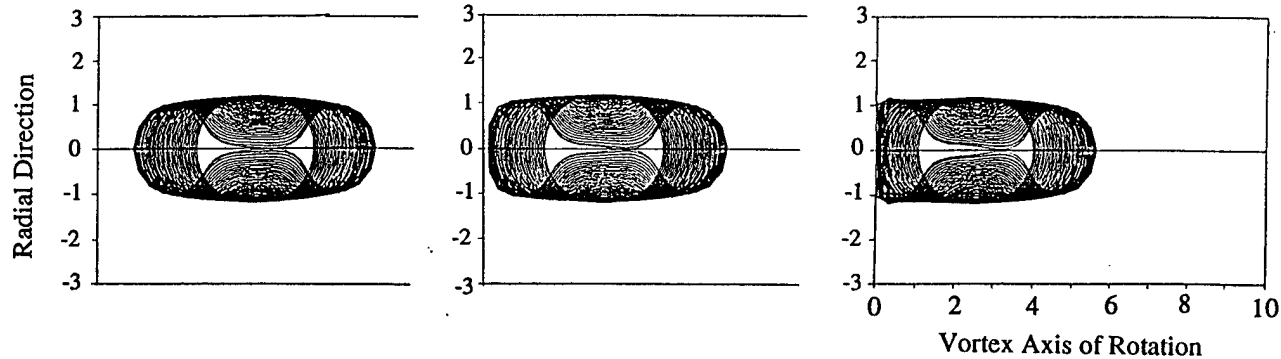


Figure II.15: Influence of solid wall distance on bubble collapse in a line vortex. $\Omega = .475$, $p_i/p_\infty = 584$, $a_c = 1.18$. $L/R_{max} =$ a) 4; b) 3; c) 2.5.

It is speculated, based on previous bubble dynamics observations, that very strong jets bringing back the two pointed tips (in the splitting region) of the two secondary bubbles inside each bubble will be generated. This phenomenon is expected to be stronger for the secondary bubble close to the wall since that bubble has a much more elongated tip.

Figure II.16 shows the influence of the circulation parameter, Ω , on the bubble behavior for fixed values of the core radius and the distance to the wall. This figure contains significant information on the scaling of bubble behavior in a vortex flow. Three characteristic dimensions of the bubble are shown as a function of time. These are the bubble radius along the plane perpendicular to the line vortex, R_n , and the distances between the initial bubble center and the two extreme points on the vortex axis, $Z_n(1)$ and $Z_n(100)$. Figure II.16 shows time variation of these three quantities normalized with R_{max} . Time is normalized with the Rayleigh time based on R_{max} and the pressure difference between P_{go} and the pressure on the vortex axis. It is apparent from this figure that R_n follows the classical Rayleigh model. Variations of Ω between 0.1 and 0.94 modify the normalized bubble period by less than 10 percent. One should notice, however, that bubble period is here defined as the time needed for the bubble to subdivide into two secondary bubbles, and that no bubble surface instability, as described earlier, occurred in that case. Bubble elongation, on the other hand, depends strongly on Ω , as can be seen from the Z_n curves. The elongation of the bubble part close to the wall is seen to be affected for large values of Ω .

6 3D Validation study: bubble/vortex ring interaction

6.1 Experimental study

In order to validate the numerical studies on bubble / vortex interactions, a fundamental experimental and numerical study was conducted. This consisted of the controlled observation of the interaction between a vortex ring and a bubble. The results of the experiment were then compared with those obtained with the 3D free surface dynamics numerical code 3DYNAFS described above

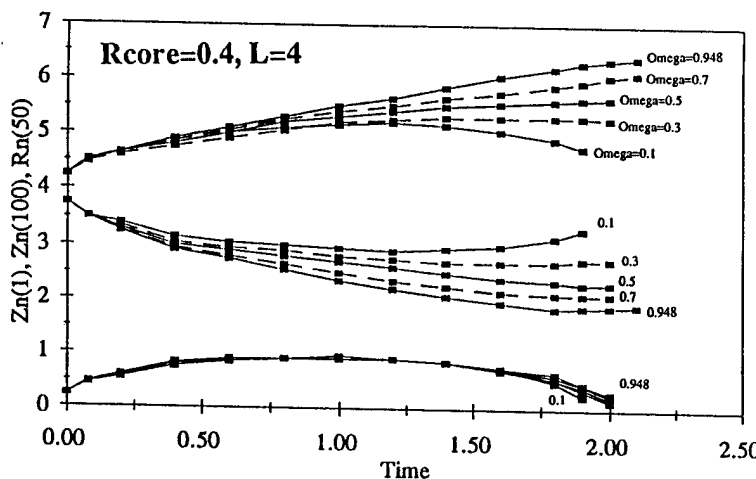


Figure II.16: Influence of Ω on the motion of bubble axial and longitudinal dimensions versus time for a bubble trapped in a line vortex perpendicular to a solid wall. Distances are normalized with R_{max} and times are normalized with Rayleigh time. $p_i/p_\infty = 584$, $a_c/R_{max} = 0.4$, $L/R_{max} = 4$.

[22].

A vortex ring was generated in a Plexiglas tank using a cylinder equipped with a 2.5 cm radius piston. The cylinder has a sharp lip exit to enhance the roll up of the fluid vortex generated at the lip. This results in a vortex ring with a diameter slightly larger than that of the cylinder [23]. The water in the tank is degassed using a vacuum pump and a spark generated bubble is produced using two tungsten electrodes submerged in the tank which can be manipulated from outside the tank to be placed where desired. The spark is produced by discharging during a very short time period ($\simeq 10^{-4}s$) a high voltage (6000 volts) from a series of capacitors. The interaction between the generated ring and bubble was then observed. A spark generating the bubble has the advantage of simulating cavitation bubbles and allowing one to choose precisely when and where the bubble is generated, which is essential to coordinating the positions of the bubble and the ring, and the starting time of a high speed camera. A triggering line allows one to synchronize the departure of the piston and the triggering of the spark generator using pressure transducers to precisely detect the vortex ring motion. As the piston starts to move down, a pressure pulse is created in the tank by the fluid impulsive motion. This is detected by the transducer probe and amplified to trigger a delay generator. The output signal (a very short pulse) then triggers the spark generator. Visualization was performed using a Hycam II high speed camera capable of 11,000 frames per second.

On several of the motion pictures taken very small gas bubbles were present under the piston. The visualization of the motion of these bubbles allows one to observe their trajectory around the vortex ring. The existence of a "viscous core" was apparent from the velocity profile obtained by tracing the microbubbles' motion, whether or not the vortex ring was cavitating. For the cavitating cases, the "viscous core" surrounded the vaporous/gaseous core. A typical trajectory of the small bubbles is shown in Figure II.17. Also shown in this figure is a sketch of a bubble and the particle trajectory line (T). Figure II.17 also shows the geometric characteristics of the bubble/ring positions. D_1 is the distance between the bubble center and the viscous core center

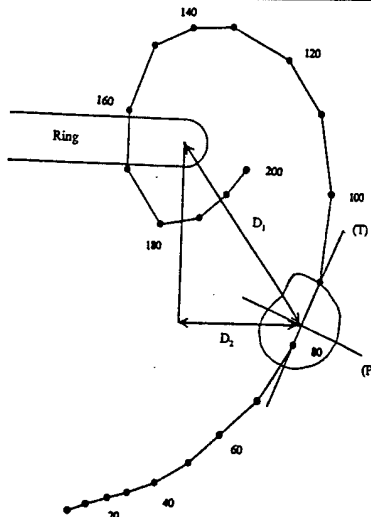


Figure II.17: Particle trajectory around the ring viscous core.

when the bubble is at its maximum volume and has the equivalent maximum radius R_{\max} . D_2 is the horizontal distance between the bubble and the center of the viscous core. The normalized quantities $\overline{D}_1 = D_1/R_{\max}$ and $\overline{D}_2 = D_2/R_{\max}$ characterize the bubble / vortex ring interactions. As expected, it is observed that smaller \overline{D}_1 and \overline{D}_2 correspond to stronger interactions and larger bubble deformations.

Figure II.18a – c drawn in the ring reference frame shows the bubble motion and deformation with time for three selected cases of increasing bubble/shear interaction. The electrodes position shown on each graph is the one at the instant of the spark generation. The vortex ring side view indicates the position of the reference frame.

As can be seen from the pictures in Figure II.19a ($\overline{D}_1 = 2.16$, $\overline{D}_2 = 0$, $V_{ring} = 0.28m/s$) and from the contours in Figure II.20a , the bubble remains practically spherical during its growth. The interaction is weak due to the relatively large distance between the bubble and the ring, and also due to the relatively small circulation of the ring. The first collapse is too fast, and no significant deformation of the bubble is seen until the rebound when a reentrant jet appears on the bottom face of the bubble followed after the rebound by an outgoing jet on the top face. It appears that during the first bubble oscillation period the bubble translation velocity is smaller than the vortex generated fluid velocity. The bubble therefore sees a flow moving upward. The jet direction (including the reentrant and the outside jet) is on a pathline of shear flow, and the bubble motion after the collapse follows a particle path line while oscillating and cutting itself in two.

In Figure II.20b ($\overline{D}_1 = 2.38$, $\overline{D}_2 = 1.5$, $V_{ring} = 0.78m/s$) the bubble first grows spherically, then it starts to stretch into an ovoid shape: the bottom face is less curved and the top face more curved than in the spherical case. Here the distance \overline{D}_1 is not too different from the previous case but the circulation in the vortex ring is about three times larger. When the bubble volume decreases, the stretching due to the shearing action becomes more pronounced and a constriction along the bubble periphery appears along the pathlines (T). The bubble then rebounds with a dumbbell shape.

In Figure II.19c ($\overline{D}_1 = 1.1$, $\overline{D}_2 = 0.37$, $V_{ring} = 0.82m/s$) the bubble appears to be stretched

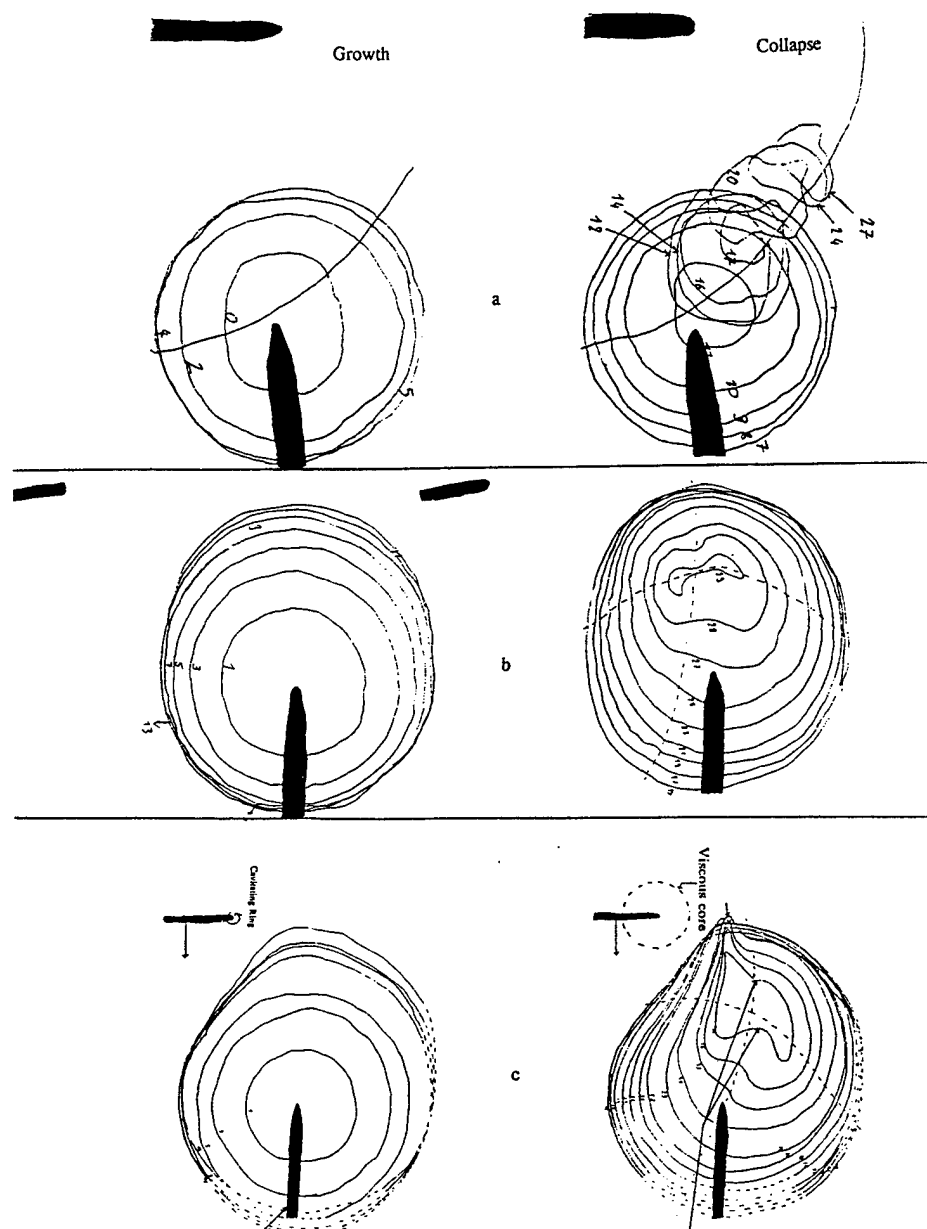


Figure II.18: Bubble contours at various times from High Speed sequences of Figure 19.19. a) $\overline{D_1} = 2.16$, $\overline{D_2} = 0$, $V_{ring} = 0.28m/s$, b) $\overline{D_1} = 2.38$, $\overline{D_2} = 1.5$, $V_{ring} = 0.78m/s$, c) $\overline{D_1} = 1.1$, $\overline{D_2} = 0.37$, $V_{ring} = 0.82m/s$.

more and more in the pathlines' direction during its growth, with the top region more stretched than the bottom one, and the top right part growing more than the left one. When the bubble collapses, its left side continues to be sheared by the flow into a pathline direction and a 'beak' forms at the top left part and becomes more pronounced once the volume of the bubble starts to decrease. Then, there is a constriction all around the bubble which appears first on the top face of the bubble. The bubble then cuts itself in two and rebounds as two side-by-side very distorted bubbles (or bubble clouds). The left one then touches the cavitating ring and splits again into two parts. The deformations of the bubble are more significant in this case than in the two previous cases, because the bubble is closer to the center of the ring core and experiences a strong shear flow. In addition, there appears to be a "venturi effect" between the bubble and the viscous core that further increases the stretching of the left part of the bubble

Within the margin of errors of the measurements, comparison of the time variation of the average radius of each bubble shows no significant effect of the presence of shear on the bubble period. However, indications of a lengthening effect of the bubble period can be seen on the characteristic distances between the bubble 'center' and the two upstream and downstream points along a particle pathline (direction (T)). This effect however seems small in the cases presented here and should be investigated further.

Physical explanations

The observations made above can be qualitatively understood by considering the velocity and pressure fields around the bubble. The motion of each point on the surface of the bubble is the result of the combination of the underlying (shear) fluid velocity and of the velocity due to the bubble growth or collapse. The effect of the underlying fluid flow (whose characteristic speed is about $2m/s$) is minor during initial bubble growth and later bubble collapse phases, but becomes most important at the end of the growth and at the beginning of the collapse where bubble wall velocities reach a minimum. Indeed, right after the spark generation, the speed of each point of the bubble surface is very high (about $40m/s$). It then decreases to zero at about the maximum radius, and then increases during the bubble collapse. For a bubble in a uniform flow, the existence of the flow reflects on the bubble shape by a larger bubble growth in the downstream direction and by a flattening of the bubble shape in the upstream direction. Later on due to inertia, the downstream part that has extended further collapses faster forming a reentrant jet directed upstream in the plane of symmetry of the bubble.

When the flow is not uniform, a similar phenomenon occurs but is stronger on one side of the bubble than on the other due to the typical asymmetry of a shear flow. In addition, the possibility that the underlying shear flow becomes at some point during the bubble history stronger than the bubble wall velocity creates the possibility of a jet generated by the underlying flow, which can be opposite to the one described above and directed downstream. In the case of the figures shown here, the velocity profile seen by the bubble decreases from left to right. When the bubble starts to grow, the speed of each point is much more important than the velocity of the fluid flow: the bubble is therefore almost spherical. Then, when the speed of each point decreases, the influence of the fluid flow increases. The top part of the bubble grows more than without the presence of the basic flow and, due to the shear, the left part grows more than the right one. In addition, the top face is more stretched than the bottom face because on the top face the speeds add up, while

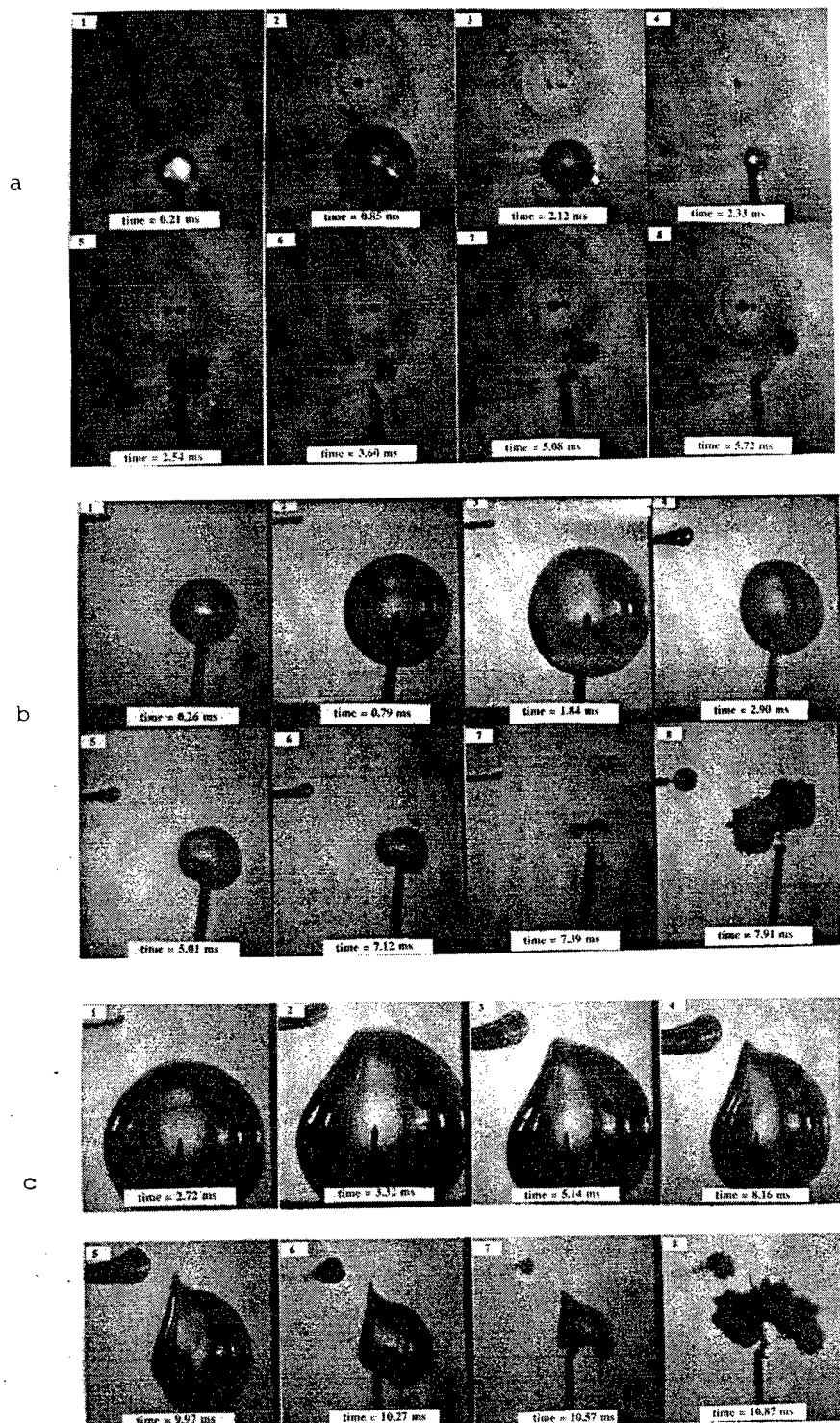


Figure II.19: High Speed Movie sequences of bubble / vortex ring interaction. a) $\overline{D_1} = 2.16$, $\overline{D_2} = 0$, $V_{ring} = 0.28m/s$, b) $\overline{D_1} = 2.38$, $\overline{D_2} = 1.5$, $V_{ring} = 0.78m/s$, c) $\overline{D_1} = 1.1$, $\overline{D_2} = 0.37$, $V_{ring} = 0.82m/s$.

they subtract on the bottom. The opposite is true during the collapse where velocities add up on the bottom part of the bubble and subtract on the top.

As the fluid flow moves upward in the case shown in the figure, the reentrant jet is expected to appear on the top face. However, due to the strong shear, the left part of the bubble is prevented from collapsing forcing a compensating middle of the bubble constriction all along the bubble, with a tendency to form reentrant jets on both ends of the bubble along the pathline. This constricted shape of the bubble is similar to that obtained with a bubble collapsing between two walls.

6.2 Numerical Modeling

In order to model the bubble/shear flow interaction described above, the Boundary Element Method (BEM) code described above, 3DYNAPS, was used. The flow field of the moving vortex ring was modeled using the following classical expression for the velocity potential at the point M produced by a vortex ring (\mathcal{R}):

$$\phi(M) = -\frac{\Gamma}{4\pi} \iint_{S_{\mathcal{R}}} \frac{\mathbf{e}_t \cdot \mathbf{PM}}{|\mathbf{PM}|^2} ds_P, \quad (\text{II.58})$$

where $S_{\mathcal{R}}$ is any surface limited by the ring vortex ring line (\mathcal{R}), and \mathbf{e}_t is the tangential direction along (\mathcal{R}). This enables one to determine the velocity and pressure field outside of the viscous core region of the vortex ring.

6.3 Numerical Results

Figure II.20c shows simulations for these same experimental conditions as in Figure II.19c with $\Gamma = 0.12 m^2/s$, while Figures II.20a and II.20b show the same conditions but for $\Gamma = 0.25 m^2/s$ and $\Gamma = 0.10 m^2/s$. As in the experiment Figure II.20c shows elongation of the left side of the bubble in the shear flow direction. The formation of a beak at the end of the bubble growth is also evident but not as pronounced as in the experiment. Later a constriction in the bubble shape along the fluid pathline is also apparent. The overall comparison between this numerical modeling and the experiment is encouraging. However, the strong shearing effect on the beak preventing the bubble top from collapsing from the left side is not as strongly reproduced in the numerical simulation. This is most probably due to the fact that the simulation neglected the vortex *bubble* ring behavior and did not include any modification of the flow due to the growth of the ring bubble near the spark-generated bubble creating the venturi effect we mentioned earlier.

At the smaller circulations the tendency of the bubble to elongate and then cut itself into two is also clearly apparent as in the experiments.

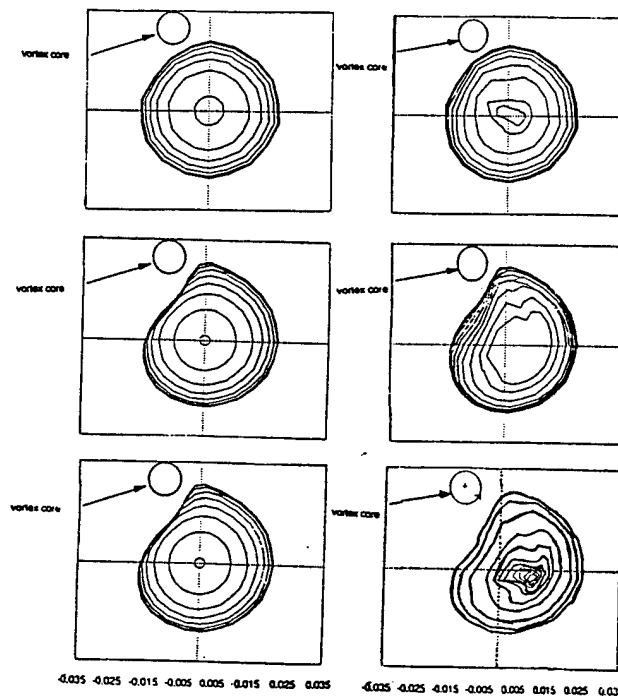


Figure II.20: Numerical simulations of bubble / vortex ring interaction.. $\overline{D_1} = 1.1$, $\overline{D_2} = 0.37$, $V_{ring} = 0.82m/s.; \Gamma =$ a) $0.025m^2/s$; b) $0.10m^2/s$; c) $0.12m^2/s$ which corresponds to Figure c.

Chapter III

CAVITATION INCEPTION ON THE AXIS OF A LINE VORTEX —FULL VISCOUS INTERACTION

1 Introduction

This chapter reconsiders the interaction between a bubble and a vortex line in the case where the bubble is located on the axis of the vortex [2]. Here, we will include viscous effects and determine the conditions for bubble explosive growth. We will consider not only the response of the bubble to the basic flow field, but we also include the influence that the bubble has on the flow. The first part of the study will consider an infinitely elongated bubble on the axis of a Rankine vortex. Due to the symmetry of the problem, a one-dimensional solution is possible, and this gives us the variations along the r -axis in a cylindrical frame of reference. Then, criteria for explosive bubble growth or cavitation inception are deduced. In the last part of the study we consider that the bubble has a finite length along the axis of the vortex. This leads to a two-dimensional problem that we solve using an asymptotic approach.

2 Full Viscous Interaction Between a Cylindrical Bubble and a Line Vortex

A weakness of the numerical approaches presented in Chapter II is the fact that the modification of the flow by the bubble's presence and dynamics was restricted to the case where the "bubble flow" is potential. This restriction will be removed here for the case of a line vortex which has the central part of its viscous core gaseous or vaporous. As illustrated below, such an analysis enables one to determine criteria for unstable bubble growth (cavitation inception), and to describe how the bubble dynamics affects the viscous flow itself. For illustration, we consider the case where, at $t = 0$, the vortex line is a Rankine vortex, and where the elongated bubble is of initial radius a_0 . The vortex then diffuses with time and interacts fully with the axial bubble. The generated flow satisfies the axisymmetric incompressible Navier-Stokes equations in cylindrical coordinates.

With all derivatives with respect to z and θ being null, the continuity and momentum equations reduce to:

$$\frac{1}{r} \frac{\partial}{\partial r} (r \rho u_r) = 0. \quad (\text{III.1})$$

$$\frac{\partial u_r}{\partial t} + u_r \frac{\partial u_r}{\partial r} - \frac{u_\theta^2}{r} = -\frac{1}{\rho} \frac{\partial p}{\partial r} + \nu \frac{\partial}{\partial r} \left[\frac{1}{r} \frac{\partial}{\partial r} (r u_r) \right], \quad (\text{III.2})$$

$$\frac{\partial u_\theta}{\partial t} + u_r \frac{\partial u_\theta}{\partial r} + \frac{u_r u_\theta}{r} = \nu \frac{\partial}{\partial r} \left[\frac{1}{r} \frac{\partial}{\partial r} (r u_\theta) \right], \quad (\text{III.3})$$

Denoting the radius of the bubble as $a(t)$, and its time derivative, $\dot{a}(t)$, the continuity equation leads to:

$$u_r = \frac{a(t) \dot{a}(t)}{r}. \quad (\text{III.4})$$

Replacing u_r by its expression in (III.2) and (III.3) one obtains:

$$\frac{1}{r} \left[a \ddot{a} + \dot{a}^2 - u_\theta^2 - \frac{a^2 \dot{a}^2}{r^2} \right] = -\frac{1}{\rho} \frac{\partial p}{\partial r}, \quad (\text{III.5})$$

$$\frac{\partial u_\theta}{\partial t} + \frac{a \dot{a}}{r} \left(\frac{\partial u_\theta}{\partial r} + \frac{u_\theta}{r} \right) = \nu \frac{\partial}{\partial r} \left[\frac{1}{r} \frac{\partial}{\partial r} (r u_\theta) \right], \quad (\text{III.6})$$

This set of coupled equations allows one to describe both the bubble dynamics and the flow field modification with time accounting for the interaction with the bubble.

2.1 Method of Solution

In order to obtain a differential equation for the bubble radius variations, similar to the Rayleigh Plesset Equation (II.27), Equation (III.5) is integrated between $r = a(t)$ and a very large radial distance $r = R_{inf}$, beyond which the vortex flow is assumed to be inviscid and of vortex circulation Γ . To simplify the numerical solution, the domain of integration is made time independent by using the following variable change:

$$s = \frac{r}{a(t)}. \quad (\text{III.7})$$

The integration region becomes for all times $[1; s_{inf}]$, with $R_{inf}(t) = a(t)s_{inf}$, and Equation (III.5) becomes:

$$\begin{aligned} \bar{a} \ddot{\bar{a}} + \dot{\bar{a}}^2 &= \frac{\dot{\bar{a}}^2}{2 \ln(s_{inf})} \left[-\frac{1}{s_{inf}^2} + 1 \right] + \frac{1}{\ln(s_{inf})} \int_1^{s_{inf}} \frac{\bar{u}_\theta^2}{s} ds + \\ &\quad - \frac{1}{\ln(s_{inf})} \left[1 - \left(\frac{\bar{\Gamma}}{2\pi \bar{a} s_{inf}} \right)^2 - \bar{p}_v + \bar{p}_{go} \left(\frac{1}{\bar{a}} \right)^{2k} - \frac{1}{W_e \bar{a}} - \frac{2 \dot{\bar{a}}}{R_e \bar{a}} \right], \end{aligned} \quad (\text{III.8})$$

with

$$\bar{\Gamma} = \frac{\Gamma}{a_o} \sqrt{\frac{P_\infty}{\rho}}, \quad \bar{p}_v = \frac{p_v}{p_\infty}, \quad \bar{p}_g = \frac{p_g}{p_\infty}, \quad W_e = \frac{a_o P_\infty}{\sigma}. \quad (\text{III.9})$$

With a , \dot{a} known at a given time step through the solution of (III.8), Equation (III.6) becomes:

$$\frac{D\bar{u}_\theta}{Dt} = -\frac{s \ddot{\bar{a}} \partial \bar{u}_\theta}{\bar{a}} - \frac{\ddot{\bar{a}} \partial \bar{u}_\theta}{s \bar{a}} - \frac{\ddot{\bar{a}}}{s^2 \bar{a}} \bar{u}_\theta + \frac{1}{R_e} \frac{1}{\bar{a}^2} \left(\frac{\partial^2 \bar{u}_\theta}{\partial s^2} + \frac{1}{s} \frac{\partial \bar{u}_\theta}{\partial s} - \frac{\bar{u}_\theta}{s^2} \right) \quad (\text{III.10})$$

with

$$\bar{a} = \frac{a}{a_0}, \quad \bar{t} = \frac{t}{a_0} \sqrt{\frac{P_\infty}{\rho}}, \quad \bar{u}_\theta = u_\theta \sqrt{\frac{P_\infty}{\rho}}, \quad R_e = \frac{a_0}{\nu} \sqrt{\frac{P_\infty}{\rho}}, \quad \bar{r} = \frac{r}{a_0}. \quad (\text{III.11})$$

2.2 Initial and Boundary Conditions

The initial conditions considered are as follows. For the bubble,

$$a(0) = a_0, \quad \dot{a}(0) = 0. \quad (\text{III.12})$$

For the line vortex, the equation at $t = 0$, is that of a Rankine vortex with

$$u_r(r, t = 0) = 0. \quad (\text{III.13})$$

The condition of normal stress balance is imposed at the bubble interface:

$$P(a) = p_v + p_{g_0} \left(\frac{a_0}{a} \right)^{2k} - \frac{\sigma}{a} + 2\mu \frac{\partial u_r(a)}{\partial r}, \quad (\text{III.14})$$

where μ is the dynamic viscosity, and the gas compression law is given by:

$$p_g = p_{g_0} \left(\frac{a_0}{a} \right)^{2k}. \quad (\text{III.15})$$

In addition, the following ‘at-infinity’ condition is imposed on the pressure at the distance, R_{inf} :

$$P(R_{inf}) = p_\infty - 2\rho \left(\frac{\Gamma}{2\pi s_{inf} a(t)} \right)^2. \quad (\text{III.16})$$

2.3 Some Preliminary Results

The system of equations (III.8) and (III.10) is solved using a Runge-Kutta procedure for $a(t)$ and a space and time integration of Equation (III.10) which enables one to compute the integral term containing u_θ^2 . This is obtained using a Crank-Nicholson finite difference integration scheme of the partial differential equation (III.6).

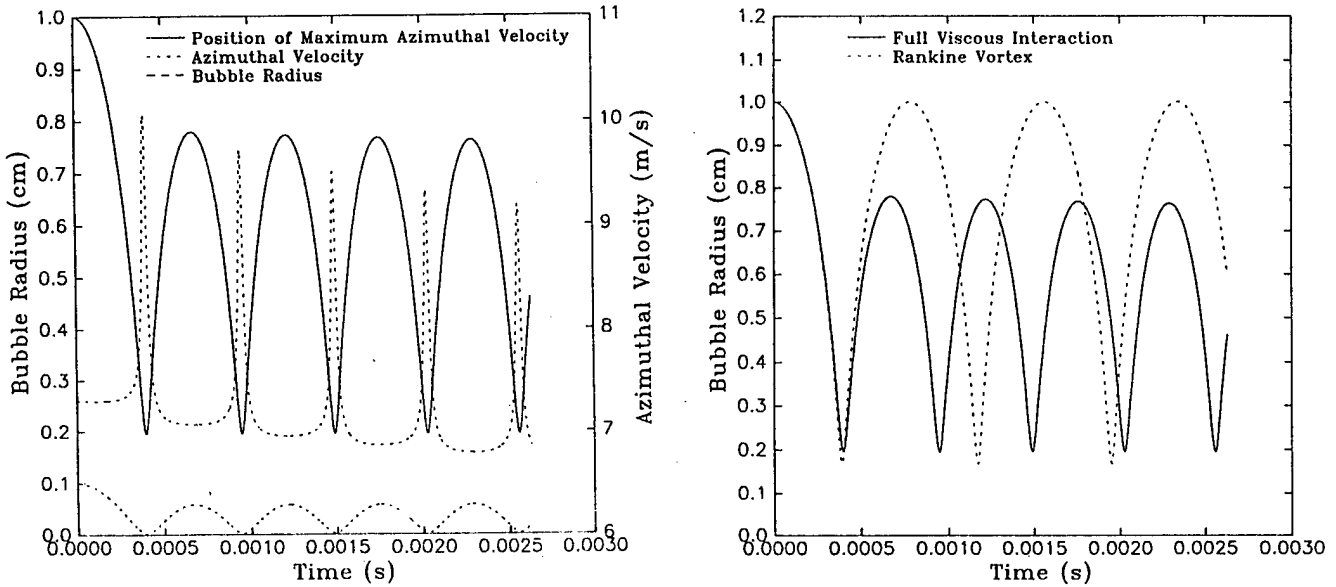


Figure III.1: Dynamics of the interaction between a cylindrical bubble and a line vortex. $\Gamma = 0.5 \text{ m}^2/\text{s}$, $P_{go} = 5 \times 10^3 \text{ Pa}$, $P_\infty = 1.3 \times 10^5 \text{ Pa}$. a) Bubble radius, value of maximum azimuthal velocity $u_{\theta \max}$, and position of $R_{\theta \max}$. b) Bubble radius versus time with and without viscous interaction.

Figures III.1a and III.1b illustrate both the bubble / vortex flow field interaction and a case where there is a need to include this full interaction in the dynamics. In these two figures, the bubble has an initial radius of 1mm, while the viscous core of the vortex has an initial radius of 1cm. The initial circulation in the vortex is $0.5 \text{ m}^2/\text{s}$, and the initial pressure in the bubble is $5 \times 10^3 \text{ Pa}$, while the ambient pressure is $1.3 \times 10^5 \text{ Pa}$. Therefore, the bubble starts its dynamics by collapsing. Figure III.1a shows simultaneously three characteristic quantities of the problem versus time. The first quantity is the bubble radius versus time, while the other two quantities are the radial position, $R_{\theta \max}$, of the maximum azimuthal velocity, $u_{\theta \max}$, and the value of this velocity. In the previous Chapter, these two last quantities remained constant with time. A very important first result very clearly shown in Figure III.1a is that both the position of $R_{\theta \max}$, and the value of $u_{\theta \max}$, depend directly on the variation of $a(t)$. The viscous core (of radius $R_{\theta \max}$) is seen to decrease with the bubble radius during bubble collapse, and to increase with the bubble radius during bubble growth. This tendency of the viscous core to get displaced with the bubble wall, corresponds to intuition, but is proven numerically to our knowledge for the first time in [27, 1].

Viscous effects appear more prominently when following the bubble dynamics over more than a single period of oscillation. Both maximum values of $R_{\theta \max}$ and $u_{\theta \max}$ are seen to decrease with time. Through conservation of momentum, the azimuthal velocity follows an tendency opposite to the core size. As the bubble wall moves inward the viscous core shrinks, simultaneously increasing the tangential velocity to a maximum when the bubble reaches maximum size. As the bubble grows again, the core expands and the tangential velocity decelerates to a minimum at the maximum bubble radius. When the fluid particles are pulled in towards the vortex axis they accelerate tangentially. This is similar to the phenomenon of vortex stretching.

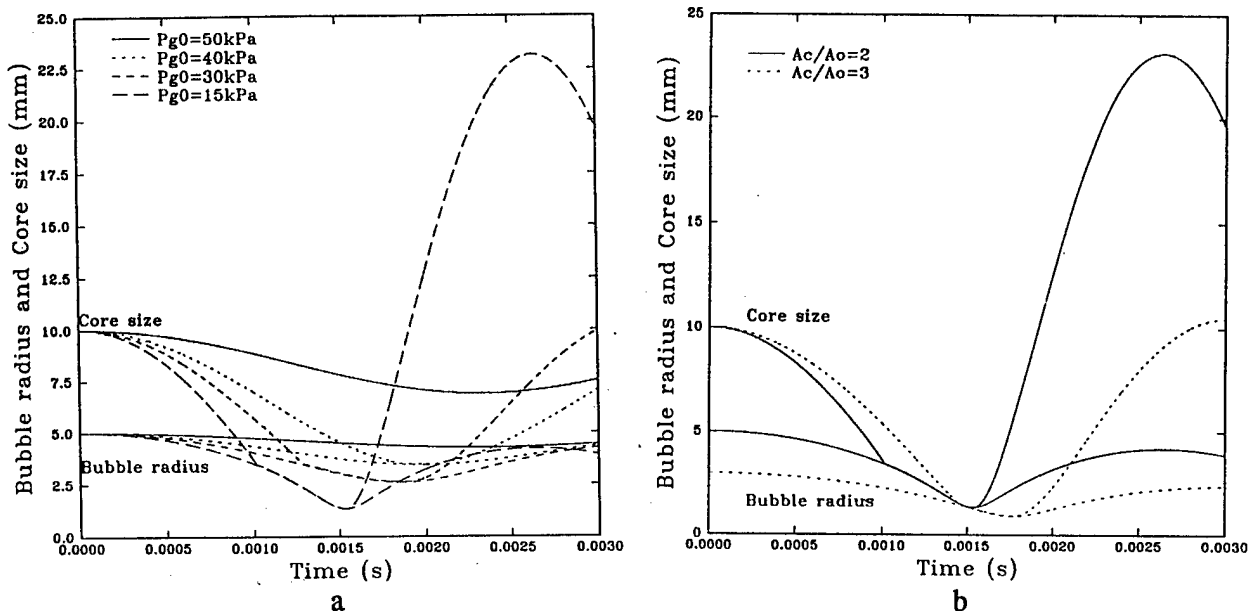


Figure III.2: Dynamics of the interaction between a cylindrical bubble and a line vortex. $P_{axis} = 7 \times 10^5 \text{ Pa}$. a) Influence of the initial bubble pressure, P_{go} , on bubble radius and position of $R_{\theta \max}$. $R_c/a_o = 2$. b) Influence of R_c/a_o on the bubble radius and position of $R_{\theta \max}$. $P_{go} = 1.5 \times 10^5 \text{ Pa}$.

Figure III.1b shows the importance of the inclusion of full viscous flow / bubble interaction in the dynamics. One graph in the figure considers the case where the underlying flow field is forced to remain that of a Rankine vortex. In that case, as apparent in the figure, the bubble oscillations are repeatable with time, and no viscous decay of the amplitude of the oscillations is visible. To the contrary when the underlying flow is modified through viscous diffusion and interaction with the bubble, the bubble radius oscillations decay substantially after the first collapse, and the flow field characteristics are modified as shown in Figure III.1a.

Figures III.2a and III.2b show, respectively, the influence on the dynamics of the initial gas pressure inside the bubble, P_{go} , and the ratio of initial core radius to initial bubble radius, R_c/a_o . For an initial pressure on the vortex axis of $7 \times 10^5 \text{ Pa}$, Figure III.2a shows the dynamics of the bubble and the viscous core size when the initial pressure in the bubble decreases from $5 \times 10^5 \text{ Pa}$ to $1.5 \times 10^5 \text{ Pa}$. For $P_{go} = 5 \times 10^5 \text{ Pa}$ the bubble collapse is very weak, and the core radius is seen to follow the bubble wall oscillations. For all three other larger values of P_{go} starting from $P_{go} = 4 \times 10^5 \text{ Pa}$ the bubble collapse is strong enough to entrain a full collapse of the viscous core which practically disappears (maximum azimuthal velocity at the bubble wall) during the later phases of the bubble collapse. This is followed by a much stronger rebound of the viscous core than the bubble rebound.

Figure III.2b shows a behavior similar to the previous figure when the ratio, R_c/a_o , increases. Here again a strong core collapse and rebound is observed when the initial distance between the bubble wall and the core radius is decreased.

3 Criteria for Cavitation Inception

Present criteria for cavitation inception are based on the dynamics of spherical bubbles in uniform flow fields. This is satisfactory for travelling bubble cavitation inception, but is not necessarily adequate in turbulent flows where nuclei are captured in vortical structures where they explosively grow. In order to consider such cases, we will follow the example of the spherical bubble studies and consider, in a first approach, the static equilibrium equations of an elongated bubble on a vortex line. Then, we will consider the dynamic case and analyze the behavior of the bubble for different variations of the parameters.

3.1 Static Equilibrium

When one considers the static equilibrium conditions, all time derivatives in Equations (III.8) and (III.6) vanish, and these equations degenerate to the following simple forms:

$$\frac{1}{\rho} \frac{\partial p}{\partial r} = \frac{u_\theta^2}{r}, \quad (\text{III.17})$$

$$\frac{\partial}{\partial r} \left(\frac{1}{r} \frac{\partial}{\partial r} (r u_\theta) \right) = 0. \quad (\text{III.18})$$

For a Rankine vortex of core size, a_c , the velocity is given by:

$$\begin{aligned} u_\theta &= \frac{\Gamma}{2\pi a_c^2} r, & r \leq a_c, \\ u_\theta &= \frac{\Gamma}{2\pi r}, & r \geq a_c, \\ u_r &= u_z = 0, \end{aligned} \quad (\text{III.19})$$

which using (III.17) and (III.18) gives the following expressions for the pressure:

$$\begin{aligned} p &= P_\infty - \frac{\rho \Gamma^2}{4\pi^2 a_c^2} \left(1 - \frac{r^2}{2a_c^2} \right), & \text{for } r \leq a_c \\ p &= P_\infty - \frac{\rho \Gamma^2}{8\pi^2 r^2}, & \text{for } r \geq a_c. \end{aligned} \quad (\text{III.20})$$

On the bubble wall, at $r = a$, we have the condition:

$$p(a) = P_v + P_{go} \left(\frac{a_o}{a} \right)^{2k} - \frac{\sigma}{a},$$

where P_{go} is the gas pressure for the bubble of equilibrium radius a_o when the ambient pressure is P_∞ .

Using equation (III.20), we can now write for $r = a < a_c$:

$$P_\infty = P_v + P_{go} \left(\frac{a_o}{a} \right)^{2k} - \frac{\sigma}{a} + \frac{\rho \Gamma^2}{4\pi^2 a_c^2} \left(1 - \frac{a^2}{2a_c^2} \right). \quad (\text{III.21})$$

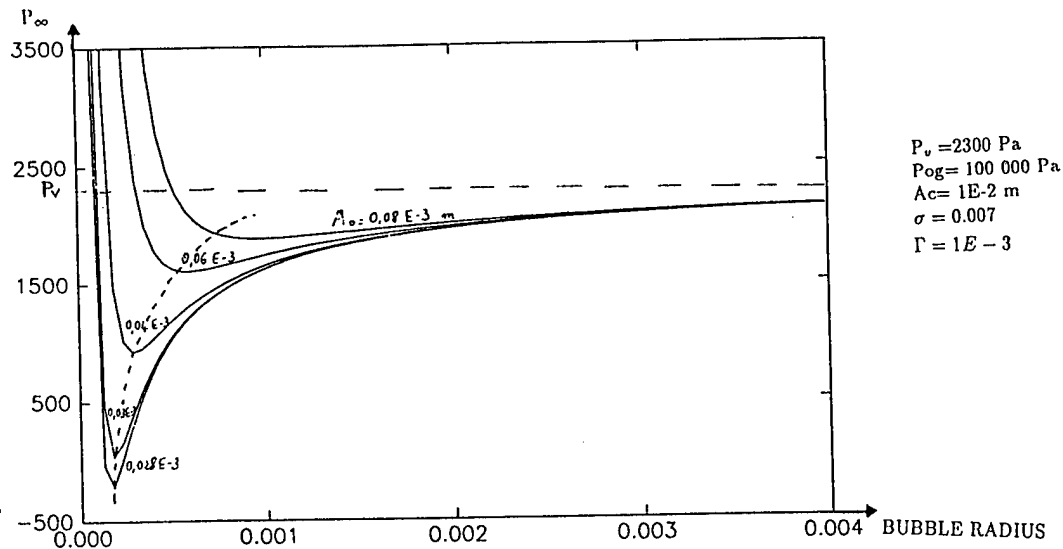


Figure III.3: Cylindrical bubble static equilibrium in a line vortex. Relationship between ambient pressure and bubble radius for different values of a_o .

This expression enables one to plot the curve $P_\infty = f(a)$, (see Figure III.3), which allows one to investigate the bubble stable equilibrium. One can notice, as for spherical bubble equilibrium curves, the existence of a critical radius a_{crit} above which the bubble equilibrium is unstable. All the nuclei, whatever may be their initial size, will grow at a moderate rate, until they reach the radius a_{crit} . Similarly, the pressure in the flow field must drop below the critical pressure P_{crit} , in order to lead to an explosive bubble expansion.

If we consider cases where $a/a_c \ll 1$, we can obtain an expression of a_{crit} by finding the minimum of the curve $P_\infty = f(a)$ as:

$$a_{crit} = \left(\frac{2kP_{go}a_o^{2k}}{\sigma} \right)^{\frac{1}{2k-1}}.$$

By replacing a by a_c in (III.21) one can also obtain the curve P_{crit} as a function of a_o for different values of P_∞ .

Static Equilibrium Examples

Figures III.3 and III.4 illustrate cylindrical bubble equilibrium curves in a line vortex. Figure III.3 shows the relationship between the ambient pressure and the equilibrium bubble radius for different values of a_o . The curves are qualitatively very similar to those obtained for spherical bubbles. We observe the same tendency for the critical pressure to approach p_v for large values of the initial bubble radius. Similarly, the critical pressures can be very small and even negative for small values of a_o . Figure III.4 illustrates the influence of the circulation, Γ , on the critical pressure for various initial bubble radii. As expected, bubble explosive growth occurs for larger ambient pressures when the basic flow circulation is increased.

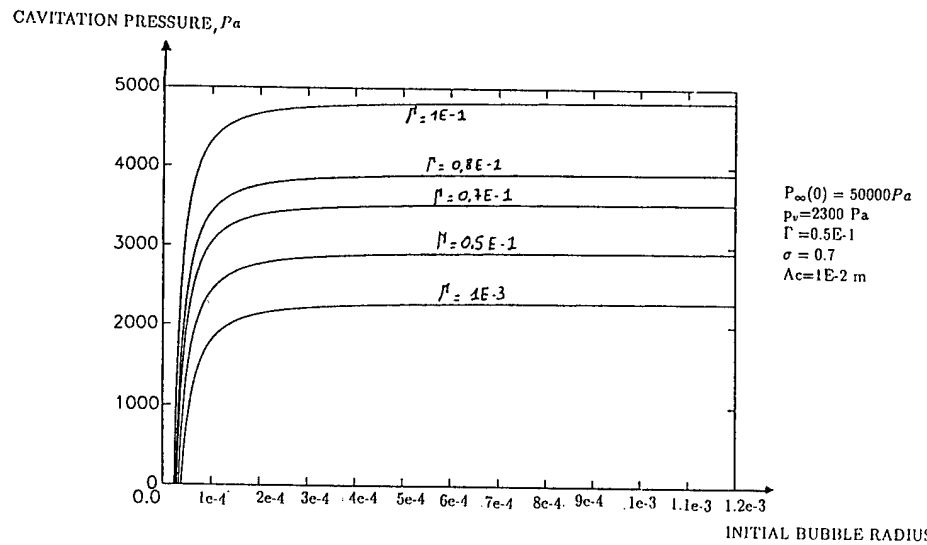


Figure III.4: Influence of the circulation, Γ , on the critical pressure versus the initial bubble radius.

Dynamic Behavior Examples

Solution of the full equations (III.8) and (III.10) provided a dynamic criterion for bubble explosive growth. This is illustrated in Figure III.5 which shows two types of behavior of a bubble of initial radius $60 \mu\text{m}$ and internal gas pressure 10^5 Pascals when the bubble is ‘released’ in a fluid where the ambient pressure, P_{amb} , is either 8000 Pascals or 1850 Pascals. The two types of behavior are dramatically different: in the 8000 Pa case, due to the competing forces of surface tension, viscous forces, circulation and the pressure difference between gas and ambient pressures, the bubble oscillates between its initial value and a maximum value about eight times larger. In the second case, the bubble is typically unstable, and the dynamics is controlled by the pressure difference at the interface that leads to an explosive growth. The value of P_{amb} that indicate the passage between the two type of behavior can be considered as the dynamic equilibrium critical pressure for cavitation. Figure III.6 illustrates again, for another set of initial conditions, the two types of behaviors but in a bubble wall velocity versus bubble radius plot. Such a plot results in a closed shape curve when bubble oscillatory behavior is observed. Instead the curve has an open shape with a continually increasing bubble radius with an almost constant bubble growth rate when the bubble is in an explosive growth mode. Let us note that during oscillations the bubble radius may grow beyond a_c without resulting into explosive bubble growth or cavitation. In comparison with the static equilibrium criteria, P_c was always found in the cases we have studied, lower in the dynamic case than in the static case.

The influence of the circulation Γ on the ambient pressure which results for a given bubble in explosive growth can be seen in Figure III.7. As in the static case, when the circulation Γ increases, bubble explosive growth occurs for larger values of the ambient pressure. The curve III.16 shows the iterative method used to find P_c : the curve P_c is that separating regions of bubble oscillations from bubble explosive growth. Figure III.8 shows similar results for the surface tension parameter γ . Note that for the conditions shown in the figure, a order of magnitude larger values of the

NON-DIMENSIONAL BUBBLE RADIUS

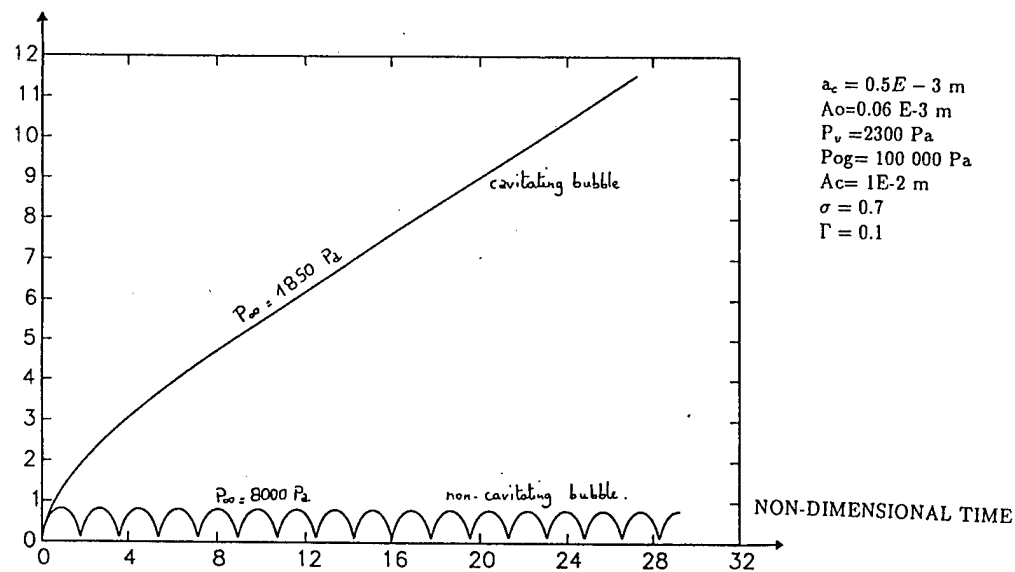


Figure III.5: Bubble radius versus time for two values of the ambient pressure. $a_o = 60 \mu\text{m}$, $P_g o = 1e5 \text{ Pa}$, $a_c = 1e - 2 \text{ m}$, $p_v = 2300 \text{ Pa}$, $\Gamma = 0.1$, $\gamma = 0.7$.

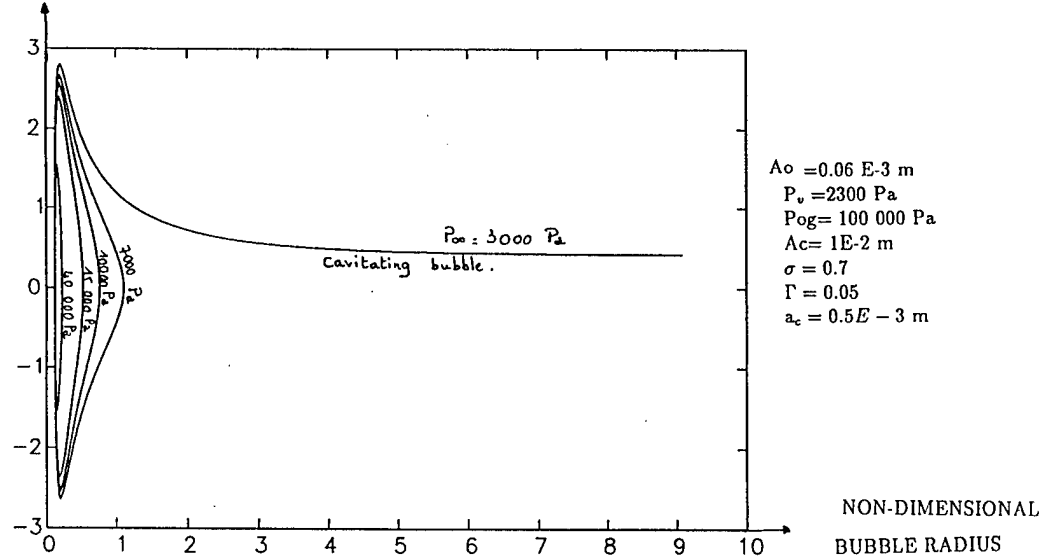
SPEED OF THE BUBBLE WALL \dot{a} 

Figure III.6: Velocity of the bubble wall versus radius of the bubble for different values of P . $a_o = 60 \mu\text{m}$, $P_g o = 1e5 \text{ Pa}$, $a_c = 1e - 2 \text{ m}$, $p_v = 2300 \text{ Pa}$, $\Gamma = 0.05$, $\gamma = 0.7$.

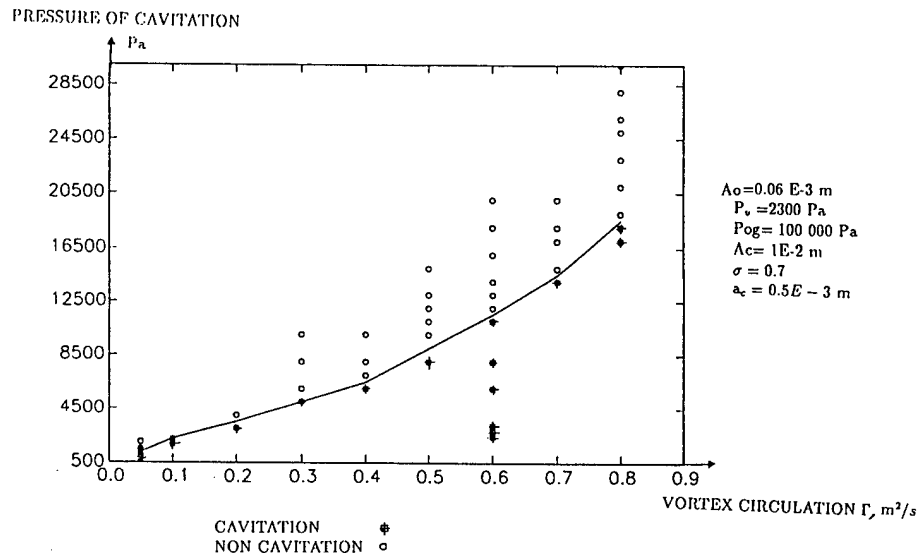


Figure III.7: The influence of the circulation Γ on the ambient pressure which results for a given bubble in an explosive growth. $a_o = 60\mu\text{m}$, $P_{go} = 1\text{e}5\text{Pa}$, $a_c = 1\text{e}-2\text{m}$, $p_v = 2300\text{Pa}$, $\gamma = 0.7$.

surface tension were needed to show a perceptible effect of γ on P_c . An increase in γ opposes bubble growth and therefore cavitation inception.

The study of the dynamic equations enables one to also follow the evolution of the core radius. As illustrated in Figures III.9a and b, the core radius follows the variations of the bubble wall. Two types of behaviors are seen depending on whether the bubble oscillates or grows explosively.

In the case of the oscillating bubble, the growth of the bubble imparts a radial velocity to the different layers of fluid, and the core also expands. When the bubble radius decreases, the opposite phenomenon is observed, however inertia of the fluid leads to a stronger reduction of the core size than of the bubble radius. As shown in Figure III.10, in the case of an explosive growth the ratio between the core radius and the bubble radius remains practically constant. For an oscillating bubble, this ratio is constant during bubble growth but decays strongly during bubble collapse.

4 Two-dimensional Study of a Bubble on the Axis of a Line Vortex

4.1 Presentation of the problem

Let us consider now the case of a bubble of a finite size, located on the axis of a line vortex. The flow in the vortex line is known at $t = 0$ then as it interacts with the bubble it evolves with time. The bubble is assumed to be axisymmetric and the variations of its shape with time is also sought. Its shape equation is:

$$F(r, t, z) = 0 \quad (\text{III.22})$$

It can take one of the following forms.

$$r = a(z, t) = 0, \quad \text{or} \quad z = b(r, t) \quad (\text{III.23})$$

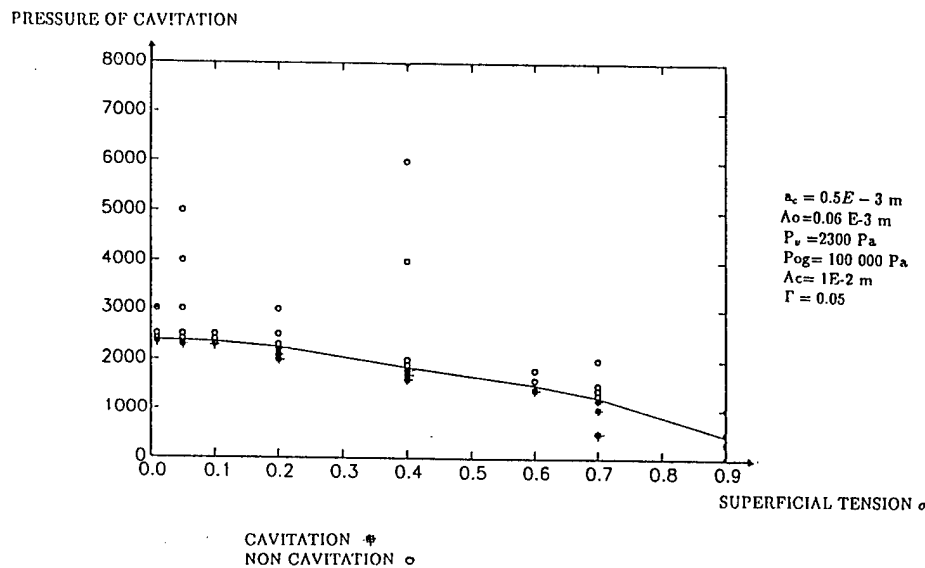


Figure III.8: The influence of the surface tension γ on the ambient pressure which results for a given bubble in an explosive growth. $a_o=60\mu\text{m}$, $P_{go}=1\text{e}5\text{Pa}$, $a_c=1\text{e}-2\text{m}$, $p_v=2300\text{Pa}$, $\Gamma = 0.05$

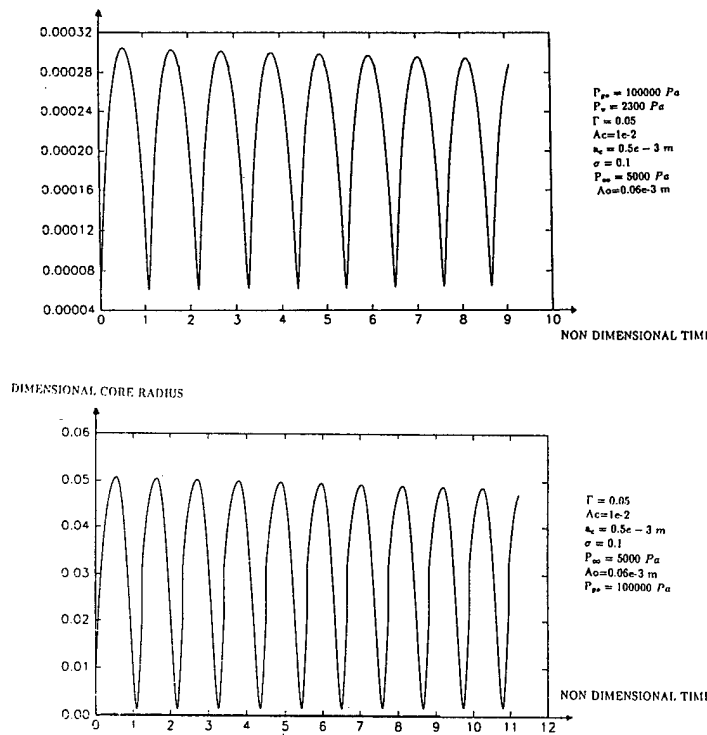


Figure III.9: a)Bubble radius versus time. b) Core radius versus time. $a_o=60\mu\text{m}$, $P_{go}=1\text{e}5\text{Pa}$, $a_c=1\text{e}-2\text{m}$, $p_v=2300\text{Pa}$, $\Gamma = 0.05$, $\gamma = 0.1$.

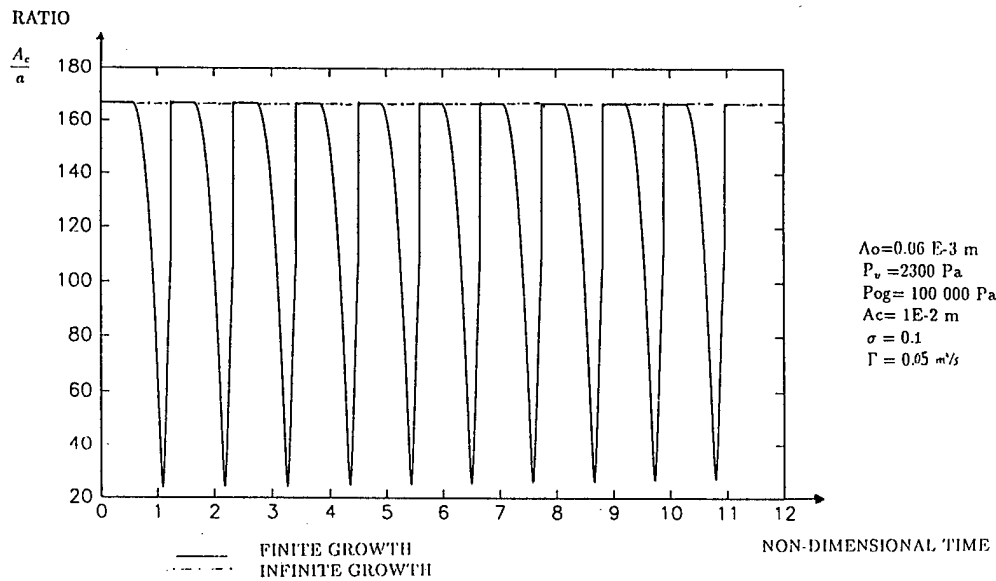


Figure III.10: Ratio between the core radius and the bubble radius. $a_o=60\mu\text{m}$, $P_{go}=1\text{e}5\text{Pa}$, $a_c=1\text{e}-2\text{m}$, $p_v=2300\text{Pa}$, $\Gamma=0.05$, $\gamma=0.1$.

Kinematic condition at the interface

Neglecting any mass exchange between gas and liquid at the interface, the kinematic condition at the interface between the bubble and the liquid is that of a free surface:

$$\left[\frac{DF}{Dt} \right]_S = 0 \Leftrightarrow \frac{\partial a}{\partial t} = u_r(S) - u_z(S) \frac{\partial a}{\partial z}. \quad (\text{III.24})$$

where \mathbf{u} is the velocity of the liquid at the free surface, and S refers to the bubble surface. Another expression of this condition using $b(r, t)$ is:

$$\frac{\partial b}{\partial t} = u_z(S) - u_r(S) \frac{\partial b}{\partial r}. \quad (\text{III.25})$$

Dynamic condition at the interface

The balance of stresses at the interface can be written:

$$\overline{T}_l = \overline{T}_g + \gamma(\nabla \cdot \mathbf{n}), \quad (\text{III.26})$$

where indices l and g refer to the liquid and the gas respectively. \mathbf{n} is the normal vector to the bubble surface and γ is the surface tension. By considering the ratio between the liquid and gas viscosities to be very small ($\mu_g \ll \mu_l$), the gaseous stresses can be neglected:

$$\overline{T}_g = -(p_v + p_g) \bar{I}. \quad (\text{III.27})$$

The projection of the stress balance equation along the bubble yields:

$$p_v + p_g = p_S - 2\mu_l (\overline{D}_w \cdot \mathbf{n}) \cdot \mathbf{n} + \sigma \nabla \cdot \mathbf{n}, \quad (\text{III.28})$$

where \bar{D}_w is the deformation tensor. The projection along the tangential direction, t , also gives:

$$(\bar{D}_w \cdot \mathbf{n}) \cdot \mathbf{t} = 0, \quad (\text{III.29})$$

4.2 Matched asymptotic expansions approach

Problem decomposition

Since an analytical solution of the problem is not presently possible, we will use the following asymptotic approach. The fluid domain of interest is decomposed into three sub-regions, resulting into three sub-problems:

1. **an outer problem** with characteristic length scale given by the viscous core radius, ($R_{out} = a_c$), and characteristic velocity scale related to a_c and the vortex circulation, Γ , ($V_{out} = \Gamma/a_c$), which leads to a characteristic time scale, ($T_{out} = a_c^2/\Gamma$).
2. **an equatorial inner problem** which describes the region near the bubble plane of symmetry. Here the length scale along r is the initial bubble radius, a_o , and the characteristic time scale is that connected to the bubble dynamics, ($T_{in} = a_o \sqrt{\Delta P/\rho}$), where ΔP is the pressure difference between the ambient pressure and the pressure inside the bubble, which drives the bubble dynamics.
3. **an axial inner problem** which describes the region near the bubble poles (near the axis of symmetry). Here the length scale along z is the initial bubble length, l_o , and the characteristic time scale is that connected to the bubble dynamics, T_{in} .

Although the scales of the two sub-problems are identical, their analysis lead to two solutions of the bubble and flow dynamics which are matched by the fact that both problems should give the same bubble volume.

The outer problem is associated with the *macroscopic* behavior of the bubble in a vortex flow. The bubble then appears as a perturbation to the viscous line vortex flow. The inner problems provides the *microscopic* details of the vortex behavior as influenced by the bubble dynamics. In the *neighborhood of the plane of symmetry*, the bubble can be seen as quasi-cylindrical, and the bubble dynamics as that of a cylindrical bubble. On the other hand, *near the axis of symmetry* (i.e. near the bubble top), it appears quasi-flat, and its dynamics as that of a moving piston.

All these problems are inter-connected and provide boundary conditions to each other. To match the different problems, we write that they give the same solution in an intermediary zone.

* *between the inner and the outer problem:*

for $R_{int} \ll (r, z) \ll R_{out}$ we must have

$$p_{inner}(r, z) = p_{outer}(r, z), \quad \mathbf{u}_{inner}(r, z) = \mathbf{u}_{outer}(r, z). \quad (\text{III.30})$$

* *between the two inner problems:*

These are linked through the stress balance equations at the bubble interface, and the assumption of uniform pressure inside the bubble. The identity of the internal pressure and the bubble volume allow matchings between these two subproblems.

Small parameters of the problem.

The main small parameter of the problem is the ratio between the two length scales:

$$\varepsilon = \frac{R_{int}}{R_{out}} = \frac{a_o}{a_c}. \quad (\text{III.31})$$

Another parameter of importance is the ratio between the bubble initial longitudinal and radial dimensions:

$$\alpha = \frac{a_o}{l_o}. \quad (\text{III.32})$$

4.3 The outer problem.**Normalization.**

We normalize the equations of the outer problem using the following scales:

$r = a_c \bar{r}$	a_c , length scale along \mathbf{e}_r .
$z = a_c \bar{z}$	a_c , length scale along \mathbf{e}_z .
$a = a_0 \bar{a}$	a_0 , initial bubble radius.
$u_r = U_{out} \bar{u}_r$	U_{out} , order of magnitude of the velocity along \mathbf{e}_r (unknown a priori).
$u_\theta = V_{out} \bar{u}_\theta$	$V_{out} = \frac{\Gamma}{2\pi a_c}$.
$u_z = W_{out} \bar{u}_z$	W_{out} , order of magnitude of the velocity along \mathbf{e}_z (unknown a priori).
$t = T_{out} \bar{t}$	$T_{out} = a_c^2 / \Gamma$
$p = \Delta P_{out} \bar{p}$	$\Delta P_{out} = \rho V_{out}^2$

This normalization introduces the following physical parameters.

$$\begin{aligned} R_{eo} &= \frac{a_0}{\nu} V_{out} && \text{the Vortex flow Reynolds number} \\ W_e &= \frac{a_0 \Delta P}{\gamma} && \text{the Bubble Weber number} \end{aligned}$$

Basic equations for the outer problem.

Consideration of the normalized continuity equation

$$\frac{U_{out}}{a_o} \frac{1}{\bar{r}} \frac{\partial}{\partial \bar{r}} (\bar{r} \bar{u}_r) + \frac{W_{out}}{l_o} \frac{\partial \bar{u}_z}{\partial \bar{z}} = 0, \quad (\text{III.33})$$

and application of the least degeneracy principle leads to a similar choice for the ratio of the radial and axial velocities:

$$\frac{U_{out}}{W_{out}} \sim \frac{a_o}{l_o} = \alpha. \quad (\text{III.34})$$

With these normalizations the basic equations of the outer problem become:

* Continuity and Navier-Stokes:

$$\begin{aligned} \frac{1}{\bar{r}} \frac{\partial(\bar{r}\bar{u}_r)}{\partial \bar{r}} + \frac{\partial \bar{u}_z}{\partial \bar{z}} &= 0, \\ \alpha \frac{\partial \bar{u}_r}{\partial t} + \alpha^2 \bar{u}_r \frac{\partial \bar{u}_r}{\partial \bar{r}} - \frac{\bar{u}_\theta^2}{\bar{r}} + \alpha \bar{u}_z \frac{\partial \bar{u}_r}{\partial \bar{z}} &= -\frac{\partial \bar{p}}{\partial \bar{r}} + \frac{1}{R_{eo}} \left[\frac{\partial}{\partial \bar{r}} \left(\frac{1}{\bar{r}} \frac{\partial(\bar{r}\bar{u}_r)}{\partial \bar{r}} \right) + \frac{\partial^2 \bar{u}_r}{\partial \bar{z}^2} \right], \\ \frac{\partial \bar{u}_\theta}{\partial t} + \alpha \bar{u}_r \frac{\partial \bar{u}_\theta}{\partial \bar{r}} + \alpha \frac{\bar{u}_r \bar{u}_\theta}{\bar{r}} + \alpha \bar{u}_z \frac{\partial \bar{u}_\theta}{\partial \bar{z}} &= \frac{1}{R_{eo}} \left[\frac{\partial}{\partial \bar{r}} \left(\frac{1}{\bar{r}} \frac{\partial(\bar{r}\bar{u}_\theta)}{\partial \bar{r}} \right) + \frac{\partial^2 \bar{u}_\theta}{\partial \bar{z}^2} \right], \\ \alpha \frac{\partial \bar{u}_z}{\partial t} + \alpha^2 \bar{u}_r \frac{\partial \bar{u}_z}{\partial \bar{r}} + \alpha^2 \bar{u}_z \frac{\partial \bar{u}_z}{\partial \bar{z}} &= -\frac{\partial \bar{p}}{\partial \bar{z}} + \frac{1}{R_{eo}} \left[\frac{1}{\bar{r}} \frac{\partial}{\partial \bar{r}} \left(\frac{\partial \bar{u}_z}{\partial \bar{r}} \right) + \frac{\partial^2 \bar{u}_z}{\partial \bar{z}^2} \right]. \end{aligned} \quad (\text{III.35})$$

* Dynamic conditions at the interface:

$$\begin{aligned} \left[\bar{r} \frac{\partial}{\partial \bar{r}} \left(\frac{\bar{u}_\theta}{\bar{r}} \right) - \varepsilon \frac{\partial \bar{a}}{\partial \bar{z}} \frac{\partial \bar{u}_\theta}{\partial \bar{z}} \right]_S &= 0, \\ \left[\left(\frac{\partial \bar{u}_r}{\partial \bar{z}} + \frac{\partial \bar{u}_z}{\partial \bar{r}} \right) \cdot \left(\varepsilon^2 \left(\frac{\partial \bar{a}}{\partial \bar{z}} \right)^2 - 1 \right) \right]_S &= 2\varepsilon \left[\frac{\partial \bar{a}}{\partial \bar{z}} \cdot \left(\frac{\partial \bar{u}_r}{\partial \bar{r}} - \frac{\partial \bar{u}_z}{\partial \bar{z}} \right) \right]_S, \end{aligned} \quad (\text{III.36})$$

$$\bar{p}_S = \bar{p}_v + \frac{\bar{p}_{go}}{\bar{V}_a^k} + \frac{1}{\left(1 + \varepsilon^2 \left(\frac{\partial \bar{a}}{\partial \bar{z}} \right)^2 \right)} \left\{ \begin{array}{l} \frac{2\alpha}{R_{eo}} \left[\frac{\partial \bar{u}_r}{\partial \bar{r}} - \varepsilon \frac{\partial \bar{a}}{\partial \bar{z}} \left(\frac{\partial \bar{u}_r}{\partial \bar{z}} + \frac{\partial \bar{u}_z}{\partial \bar{r}} \right) + \varepsilon^2 \left(\frac{\partial \bar{a}}{\partial \bar{z}} \right)^2 \frac{\partial \bar{u}_z}{\partial \bar{z}} \right] \\ - \frac{1}{W_e} \left(\frac{1}{\bar{a}} - \frac{\varepsilon^2 \frac{\partial^2 \bar{a}}{\partial \bar{z}^2}}{1 + \varepsilon^2 \left(\frac{\partial \bar{a}}{\partial \bar{z}} \right)^2} \right) \end{array} \right\} \quad (\text{III.37})$$

* Kinematic condition at the interface:

$$\frac{\partial \bar{a}}{\partial t} = \bar{u}_r(a) - \varepsilon \bar{u}_z(a) \frac{\partial \bar{a}}{\partial \bar{z}}. \quad (\text{III.38})$$

Least degeneracy

In order to keep the largest number of terms in the differential equations (principle of least degeneracy) we need to choose $\alpha^2 = \mathcal{O}(\varepsilon)$. The equations then become, written in powers of ε :

* Navier-Stokes:

$$\begin{aligned} \frac{1}{\bar{r}} \frac{\partial(\bar{r}\bar{u}_r)}{\partial \bar{r}} + \frac{\partial \bar{u}_z}{\partial \bar{z}} &= 0, \\ -\frac{\bar{u}_\theta^2}{\bar{r}} + \sqrt{\varepsilon} \frac{\partial \bar{u}_r}{\partial t} + \varepsilon \left(\bar{u}_r \frac{\partial \bar{u}_r}{\partial \bar{r}} + \bar{u}_z \frac{\partial \bar{u}_r}{\partial \bar{z}} \right) &= -\frac{\partial \bar{p}}{\partial \bar{r}} + \frac{\sqrt{\varepsilon}}{R_{eo}} \left[\frac{\partial}{\partial \bar{r}} \left(\frac{1}{\bar{r}} \frac{\partial(\bar{r}\bar{u}_r)}{\partial \bar{r}} \right) + \frac{\partial^2 \bar{u}_r}{\partial \bar{z}^2} \right], \\ \frac{\partial \bar{u}_\theta}{\partial t} + \sqrt{\varepsilon} \left(\bar{u}_r \frac{\partial \bar{u}_\theta}{\partial \bar{r}} + \frac{\bar{u}_r \bar{u}_\theta}{\bar{r}} + \bar{u}_z \frac{\partial \bar{u}_\theta}{\partial \bar{z}} \right) &= \frac{1}{R_{eo}} \left[\frac{\partial}{\partial \bar{r}} \left(\frac{1}{\bar{r}} \frac{\partial(\bar{r}\bar{u}_\theta)}{\partial \bar{r}} \right) + \frac{\partial^2 \bar{u}_\theta}{\partial \bar{z}^2} \right], \\ \sqrt{\varepsilon} \frac{\partial \bar{u}_z}{\partial t} + \varepsilon \left(\bar{u}_r \frac{\partial \bar{u}_z}{\partial \bar{r}} + \bar{u}_z \frac{\partial \bar{u}_z}{\partial \bar{z}} \right) &= -\frac{\partial \bar{p}}{\partial \bar{z}} + \frac{1}{R_{eo}} \sqrt{\varepsilon} \left[\frac{1}{\bar{r}} \frac{\partial}{\partial \bar{r}} \left(\frac{\partial \bar{u}_z}{\partial \bar{r}} \right) + \frac{\partial^2 \bar{u}_z}{\partial \bar{z}^2} \right]. \end{aligned} \quad (\text{III.39})$$

* Dynamic conditions (Boundary conditions at the bubble interface)

$$\left[\bar{r} \frac{\partial}{\partial \bar{r}} \left(\frac{\bar{u}_\theta}{\bar{r}} \right) - \varepsilon \frac{\partial \bar{a}}{\partial \bar{z}} \frac{\partial \bar{u}_\theta}{\partial \bar{z}} \right]_S = 0,$$

$$\left[\left(\frac{\partial \bar{u}_r}{\partial \bar{z}} + \frac{\partial \bar{u}_z}{\partial \bar{r}} \right) \cdot \left(\varepsilon^2 \left(\frac{\partial \bar{a}}{\partial \bar{z}} \right)^2 - 1 \right) \right]_S = 2\varepsilon \left[\frac{\partial \bar{a}}{\partial \bar{z}} \cdot \left(\frac{\partial \bar{u}_r}{\partial \bar{r}} - \frac{\partial \bar{u}_z}{\partial \bar{z}} \right) \right]_S, \quad (\text{III.40})$$

$$\bar{p}_S = \bar{p}_v + \frac{\bar{p}_{go}}{\bar{V}_S^k} + \frac{1}{\left(1 + \varepsilon^2 \left(\frac{\partial \bar{a}}{\partial \bar{z}} \right)^2 \right)} \left\{ \begin{array}{l} \frac{2\sqrt{\varepsilon}}{R_{eo}} \left[\frac{\partial \bar{u}_r}{\partial \bar{r}} - \varepsilon \frac{\partial \bar{a}}{\partial \bar{z}} \left(\frac{\partial \bar{u}_r}{\partial \bar{z}} + \frac{\partial \bar{u}_z}{\partial \bar{r}} \right) + \varepsilon^2 \left(\frac{\partial \bar{a}}{\partial \bar{z}} \right)^2 \frac{\partial \bar{u}_z}{\partial \bar{z}} \right] \\ - \frac{1}{W_e} \left(\frac{1}{\bar{a}} - \frac{\varepsilon^2 \frac{\partial^2 \bar{a}}{\partial \bar{z}^2}}{1 + \varepsilon^2 \left(\frac{\partial \bar{a}}{\partial \bar{z}} \right)^2} \right) \end{array} \right\} \quad (\text{III.41})$$

* Kinematic conditions:

$$\bar{u}_r(S) - \sqrt{\varepsilon} \frac{\partial \bar{a}}{\partial \bar{t}} - \varepsilon \bar{u}_z(S) \frac{\partial \bar{a}}{\partial \bar{z}} = 0. \quad (\text{III.42})$$

4.4 The inner problem.

We nondimensionalize the inner problem equations as follows:

- $r = a_0 \tilde{r}$, a_0 , the initial bubble radius along \mathbf{e}_r .
- $z = l_0 \tilde{z}$, l_0 , the initial bubble radius along \mathbf{e}_z .
- $a = a_0 \tilde{a}$, a_0 , the initial bubble radius along \mathbf{e}_r .
- $b = l_0 \tilde{b}$, l_0 , the initial bubble radius along \mathbf{e}_z .
- $u_r = U_{in} \tilde{u}_r$, U_{in} , order of magnitude for the radial velocity.
- $u_\theta = V_{in} \tilde{u}_\theta$, $V_{in} = \frac{\Gamma}{2\pi a_c^2} a_0$.
- $u_z = W_{in} \tilde{u}_z$, W_{in} , order of magnitude for the axial velocity.
- $p = \Delta P_{in} \tilde{p}$, $\Delta P_{in} = \rho V_{in}^2$
- $t = T_{in} \tilde{t}$, $T_{in} = a_0 \sqrt{\frac{\rho}{\Delta P_{in}}}$, Rayleigh time of a bubble subjected to a pressure variation equal to ΔP_{in} .

This normalization introduces the following physical parameters.

$$\begin{aligned} R_{ei} &= \frac{a_0}{\nu} V_{in} && \text{Cavity Reynolds number} \\ We &= \frac{a_0 \Delta P_{in}}{\sigma} && \text{Cavity Weber number} \end{aligned}$$

We will consider the case where $\alpha = \mathcal{O}(\varepsilon)$ or $l_0 = \mathcal{O}(a_c)$.

The inner sub-problem near the vortex axis.

In this region close to the bubble poles, the radial velocity due to the bubble dynamics is very small ($U_{in} \ll V_{in}$) and can be neglected while both the axial and tangential velocities can be considered of the same order ($U_{in} \sim V_{in}$). Therefore, we will consider the cases where,

$$\frac{U_{in}}{V_{in}} = \varepsilon^2 \quad (\text{III.43})$$

* Navier-Stokes:

$$\begin{aligned} \frac{\varepsilon}{\tilde{r}} \frac{\partial(r\tilde{u}_r)}{\partial\tilde{r}} + \frac{\partial\tilde{u}_z}{\partial\tilde{z}} &= 0, \\ \varepsilon^2 \frac{\partial\tilde{u}_r}{\partial\tilde{t}} + \varepsilon^4 \tilde{u}_r \frac{\partial\tilde{u}_r}{\partial\tilde{r}} - \frac{\tilde{u}_\theta^2}{\tilde{r}} + \varepsilon^3 \tilde{u}_z \frac{\partial\tilde{u}_r}{\partial\tilde{z}} &= -\frac{\partial\tilde{p}}{\partial\tilde{r}} + \frac{\varepsilon^2}{R_{ei}} \left[\frac{\partial}{\partial\tilde{r}} \left(\frac{1}{\tilde{r}} \frac{\partial(r\tilde{u}_r)}{\partial\tilde{r}} \right) + \varepsilon^2 \frac{\partial^2\tilde{u}_r}{\partial\tilde{z}^2} \right], \\ \frac{\partial\tilde{u}_\theta}{\partial\tilde{t}} + \varepsilon^2 \tilde{u}_r \frac{\partial\tilde{u}_\theta}{\partial\tilde{r}} + \varepsilon^2 \frac{\tilde{u}_r \tilde{u}_\theta}{\tilde{r}} + \varepsilon \tilde{u}_z \frac{\partial\tilde{u}_\theta}{\partial\tilde{z}} &= \frac{1}{R_{ei}} \left[\frac{\partial}{\partial\tilde{r}} \left(\frac{1}{\tilde{r}} \frac{\partial(r\tilde{u}_\theta)}{\partial\tilde{r}} \right) + \varepsilon^2 \frac{\partial^2\tilde{u}_\theta}{\partial\tilde{z}^2} \right], \\ \frac{\partial\tilde{u}_z}{\partial\tilde{t}} + \varepsilon^2 \tilde{u}_r \frac{\partial\tilde{u}_z}{\partial\tilde{r}} + \varepsilon \tilde{u}_z \frac{\partial\tilde{u}_z}{\partial\tilde{z}} &= -\varepsilon \frac{\partial\tilde{p}}{\partial\tilde{z}} + \frac{1}{R_{ei}} \left[\frac{1}{\tilde{r}} \frac{\partial}{\partial\tilde{r}} \left(\tilde{r} \frac{\partial\tilde{u}_z}{\partial\tilde{r}} \right) + \varepsilon^2 \frac{\partial^2\tilde{u}_z}{\partial\tilde{z}^2} \right]. \end{aligned} \quad (\text{III.44})$$

* Dynamic conditions:

$$\begin{aligned} \left[\tilde{r} \frac{\partial}{\partial\tilde{r}} \left(\frac{\tilde{u}_\theta}{\tilde{r}} \right) \frac{\partial\tilde{b}}{\partial\tilde{r}} + \varepsilon^2 \frac{\partial\tilde{u}_\theta}{\partial\tilde{z}} \right]_S &= 0, \\ \left[\left(\varepsilon^3 \frac{\partial\tilde{u}_r}{\partial\tilde{z}} + \frac{\partial\tilde{u}_z}{\partial\tilde{r}} \right) \cdot \left(\left(\frac{\partial\tilde{b}}{\partial\tilde{r}} \right)^2 - \varepsilon^2 \right) \right]_S &= 2\varepsilon^2 \left[\frac{\partial\tilde{b}}{\partial\tilde{r}} \cdot \left(\varepsilon \frac{\partial\tilde{u}_r}{\partial\tilde{r}} - \varepsilon^2 \frac{\partial\tilde{u}_z}{\partial\tilde{z}} \right) \right]_S, \end{aligned} \quad (\text{III.45})$$

$$\begin{aligned} \tilde{p}_S = \tilde{p}_v + \tilde{p}_{g_o} \left(\frac{1}{V} \right)^k + \frac{2}{R_{ei} \cdot \left(\varepsilon^2 + \left(\frac{\partial\tilde{b}}{\partial\tilde{r}} \right)^2 \right)} \left[\varepsilon^2 \left(\frac{\partial\tilde{b}}{\partial\tilde{r}} \right)^2 \frac{\partial\tilde{u}_r}{\partial\tilde{r}} + \varepsilon \frac{\partial\tilde{b}}{\partial\tilde{r}} \left(\varepsilon^3 \frac{\partial\tilde{u}_r}{\partial\tilde{z}} + \frac{\partial\tilde{u}_z}{\partial\tilde{r}} \right) + \varepsilon^3 \frac{\partial\tilde{u}_z}{\partial\tilde{z}} \right] + \\ - \frac{1}{W_e \cdot \sqrt{\varepsilon^2 + \left(\frac{\partial\tilde{b}}{\partial\tilde{r}} \right)^2}} \cdot \left(\frac{1}{\tilde{a}} \frac{\partial\tilde{b}}{\partial\tilde{r}} + \frac{\varepsilon^2 \frac{\partial^2\tilde{b}}{\partial\tilde{r}^2}}{\varepsilon^2 + \left(\frac{\partial\tilde{b}}{\partial\tilde{r}} \right)^2} \right). \end{aligned} \quad (\text{III.46})$$

* Kinematic condition:

$$\frac{\partial\tilde{b}}{\partial\tilde{t}} = \tilde{u}_z(S) - \varepsilon \tilde{u}_r(S) \frac{\partial\tilde{b}}{\partial\tilde{r}}. \quad (\text{III.47})$$

The inner sub-problem near the plane of symmetry.

In this region, the bubble is almost cylindrical and the axial velocity is very small. Therefore, the ratio between W_{inn} and U_{inn} is very small. However, we will consider there that $\frac{U_i}{V_i} = \mathcal{O}(1)$. This leads to the following equations:

* Navier-Stokes:

$$\begin{aligned} \frac{1}{\tilde{r}} \frac{\partial(r\tilde{u}_r)}{\partial\tilde{r}} + \varepsilon \frac{\partial\tilde{u}_z}{\partial\tilde{z}} &= 0, \\ \frac{\partial\tilde{u}_r}{\partial\tilde{t}} + \tilde{u}_r \frac{\partial\tilde{u}_r}{\partial\tilde{r}} - \frac{\tilde{u}_\theta^2}{\tilde{r}} + \varepsilon \tilde{u}_z \frac{\partial\tilde{u}_r}{\partial\tilde{z}} &= -\frac{\partial\tilde{p}}{\partial\tilde{r}} + \frac{1}{R_{ei}} \left[\frac{\partial}{\partial\tilde{r}} \left(\frac{1}{\tilde{r}} \frac{\partial(r\tilde{u}_r)}{\partial\tilde{r}} \right) + \varepsilon^2 \frac{\partial^2\tilde{u}_r}{\partial\tilde{z}^2} \right], \\ \frac{\partial\tilde{u}_\theta}{\partial\tilde{t}} + \tilde{u}_r \frac{\partial\tilde{u}_\theta}{\partial\tilde{r}} + \frac{\tilde{u}_r \tilde{u}_\theta}{\tilde{r}} + \varepsilon \tilde{u}_z \frac{\partial\tilde{u}_\theta}{\partial\tilde{z}} &= \frac{1}{R_{ei}} \left[\frac{\partial}{\partial\tilde{r}} \left(\frac{1}{\tilde{r}} \frac{\partial(r\tilde{u}_\theta)}{\partial\tilde{r}} \right) + \varepsilon^2 \frac{\partial^2\tilde{u}_\theta}{\partial\tilde{z}^2} \right], \\ \frac{\partial\tilde{u}_z}{\partial\tilde{t}} + \tilde{u}_r \frac{\partial\tilde{u}_z}{\partial\tilde{r}} + \varepsilon \tilde{u}_z \frac{\partial\tilde{u}_z}{\partial\tilde{z}} &= -\varepsilon \frac{\partial\tilde{p}}{\partial\tilde{z}} + \frac{1}{R_{ei}} \left[\frac{1}{\tilde{r}} \frac{\partial}{\partial\tilde{r}} \left(\tilde{r} \frac{\partial\tilde{u}_z}{\partial\tilde{r}} \right) + \varepsilon^2 \frac{\partial^2\tilde{u}_z}{\partial\tilde{z}^2} \right]. \end{aligned} \quad (\text{III.48})$$

* Dynamic conditions:

$$\begin{aligned} \left[\tilde{r} \frac{\partial}{\partial \tilde{r}} \left(\frac{\tilde{u}_\theta}{\tilde{r}} \right) - \varepsilon^2 \frac{\partial \tilde{a}}{\partial \tilde{z}} \frac{\partial \tilde{u}_\theta}{\partial \tilde{z}} \right]_S &= 0, \\ \left[\left(\varepsilon \frac{\partial \tilde{u}_r}{\partial \tilde{z}} + \frac{\partial \tilde{u}_z}{\partial \tilde{r}} \right) \cdot \left(\varepsilon^2 \left(\frac{\partial \tilde{a}}{\partial \tilde{z}} \right)^2 - 1 \right) \right]_S &= 2\varepsilon \left[\frac{\partial \tilde{a}}{\partial \tilde{z}} \cdot \left(\frac{\partial \tilde{u}_r}{\partial \tilde{r}} - \varepsilon \frac{\partial \tilde{u}_z}{\partial \tilde{z}} \right) \right]_S, \end{aligned} \quad (\text{III.49})$$

$$\begin{aligned} \tilde{p}_S = \tilde{p}_v + \tilde{p}_{g_o} \left(\frac{1}{V_S} \right)^k + \frac{2}{R_{ei} \cdot (1 + \varepsilon^2 \left(\frac{\partial \tilde{a}}{\partial \tilde{z}} \right)^2)} \left[\frac{\partial \tilde{u}_r}{\partial \tilde{r}} - \varepsilon \frac{\partial \tilde{a}}{\partial \tilde{z}} \left(\varepsilon \frac{\partial \tilde{u}_r}{\partial \tilde{z}} + \frac{\partial \tilde{u}_z}{\partial \tilde{r}} \right) + \varepsilon^3 \left(\frac{\partial \tilde{a}}{\partial \tilde{z}} \right)^2 \frac{\partial \tilde{u}_z}{\partial \tilde{z}} \right] + \\ - \frac{1}{W_e \sqrt{1 + \varepsilon^2 \left(\frac{\partial \tilde{a}}{\partial \tilde{z}} \right)^2}} \cdot \left(\frac{1}{\tilde{a}} - \frac{\varepsilon^2 \frac{\partial^2 \tilde{a}}{\partial \tilde{z}^2}}{1 + \varepsilon^2 \left(\frac{\partial \tilde{a}}{\partial \tilde{z}} \right)^2} \right) \end{aligned} \quad (\text{III.50})$$

* Kinematic condition:

$$\frac{\partial \tilde{a}}{\partial \tilde{t}} = \tilde{u}_r(S) - \varepsilon \tilde{u}_z(S) \frac{\partial \tilde{a}}{\partial \tilde{z}}. \quad (\text{III.51})$$

4.5 Resolution at order zero (ε^0).

The outer problem.

At order zero, the equations of the problem degenerate to:

$$\frac{\bar{u}_{\theta_0}^2}{\bar{r}} = \frac{\partial \bar{p}_0}{\partial \bar{r}}, \quad (\text{III.52})$$

$$\frac{\partial \bar{u}_{\theta_0}}{\partial \bar{t}} = \frac{1}{R_{eo}} \left[\frac{\partial}{\partial \bar{r}} \left(\frac{1}{\bar{r}} \frac{\partial (\bar{r} \bar{u}_{\theta_0})}{\partial \bar{r}} \right) + \frac{\partial^2 \bar{u}_{\theta_0}}{\partial \bar{z}^2} \right], \quad (\text{III.53})$$

$$\frac{\partial \bar{p}_0}{\partial \bar{z}} = 0. \quad (\text{III.54})$$

so that $\frac{\partial(\text{III.52})}{\partial z}$ with (III.53) \Rightarrow

$$\frac{\partial \bar{u}_{\theta_0}}{\partial \bar{z}} = 0. \quad (\text{III.55})$$

We must finally solve:

$$\frac{\bar{u}_{\theta_0}^2}{\bar{r}} = \frac{\partial \bar{p}_0}{\partial \bar{r}}, \quad \frac{1}{R_{eo}} \frac{\partial}{\partial \bar{r}} \left(\frac{1}{\bar{r}} \frac{\partial (\bar{r} \bar{u}_{\theta_0})}{\partial \bar{r}} \right) = \frac{\partial \bar{u}_{\theta_0}}{\partial \bar{t}}. \quad (\text{III.56})$$

We can find a self similar solution, $\Psi \left(\frac{\bar{r}^2}{\bar{t}} \right) = \bar{r} \bar{u}_{\theta_0}$. This leads to solve the following equation:

$$\Psi'' + \frac{R_{eo}}{4} \Psi' = 0. \quad (\text{III.57})$$

which can be directly integrated to obtain

$$\bar{u}_{\theta_0} = \frac{1}{\bar{r}} \left(1 - \exp \left(-\frac{R_{eo}}{4} \frac{\bar{r}^2}{\bar{t}} \right) \right), \quad (\text{III.58})$$

which satisfies a decay towards zero for large times, and is a Helmholtz vortex at $t = 0$.

The corresponding pressure expression is:

$$\tilde{p}_0 = \bar{p}_\infty - \frac{1}{2\tilde{r}^2} \left(1 - 2 \exp \left(-\frac{R_{eo}\tilde{r}^2}{4\tilde{t}} \right) + \exp \left(-\frac{R_{eo}\tilde{r}^2}{2\tilde{t}} \right) \right) + \frac{R_{eo}}{4\tilde{t}} E_i \left(\frac{R_{eo}\tilde{r}^2}{4\tilde{t}} \right) - E_i \left(\frac{R_{eo}\tilde{r}^2}{2\tilde{t}} \right), \quad (\text{III.59})$$

where the exponential integral function $E_i(x)$ is defined as :

$$E_i(x) = \int_x^\infty \frac{\exp(-t)}{t} dt. \quad (\text{III.60})$$

A Taylor's series expansion indicates that the solutions are matched with the boundary conditions (see below).

The inner problem in the neighborhood of the axis of symmetry.

The equations are at order zero:

*Navier-Stokes:

$$\begin{aligned} \frac{\partial \tilde{u}_{z_0}}{\partial \tilde{z}} &= 0, & \frac{\tilde{u}_{\theta_0}^2}{\tilde{r}} &= \frac{\partial \tilde{p}_0}{\partial \tilde{r}}, \\ \frac{\partial \tilde{u}_{\theta_0}}{\partial \tilde{t}} &= \frac{1}{R_{ei}} \frac{\partial}{\partial \tilde{r}} \left(\frac{1}{\tilde{r}} \frac{\partial (\tilde{r}\tilde{u}_{\theta_0})}{\partial \tilde{r}} \right), \\ \frac{\partial \tilde{u}_{z_0}}{\partial \tilde{t}} &= \frac{1}{R_{ei}} \frac{1}{\tilde{r}} \frac{\partial}{\partial \tilde{r}} \left(\tilde{r} \frac{\partial \tilde{u}_{z_0}}{\partial \tilde{r}} \right). \end{aligned} \quad (\text{III.61})$$

*Kinematic condition:

$$\frac{\partial \tilde{b}_0}{\partial \tilde{t}} = \tilde{u}_{z_0}(S).$$

Solution of \tilde{u}_{θ_0} . Here also a self similar solution of the form $\Psi_1 \left(\frac{\tilde{r}^2}{\tilde{t}} \right) = \tilde{r}\tilde{u}_{\theta_0}$ can be obtained:

$$\bar{u}_{\theta_0} = \frac{1}{\tilde{r}} \left[1 - \exp \left(-\frac{R_{e2}}{4} \frac{\tilde{r}^2}{\tilde{t}} \right) \right], \quad (\text{III.62})$$

and satisfies a decay towards zero for large times, and is a Helmholtz vortex at $t = 0$.

The resulting pressure equation is:

$$\tilde{p}_0 = \tilde{p}_\infty - \frac{1}{2\tilde{r}^2} \left(1 - 2 \exp \left(-\frac{R_{ei}\tilde{r}^2}{4\tilde{t}} \right) + \exp \left(-\frac{R_{ei}\tilde{r}^2}{2\tilde{t}} \right) \right) - \frac{R_{ei}}{4\tilde{t}} \left(E_i \left(\frac{R_{ei}\tilde{r}^2}{4\tilde{t}} \right) - E_i \left(\frac{R_{ei}\tilde{r}^2}{2\tilde{t}} \right) \right). \quad (\text{III.63})$$

Solution of \tilde{u}_{z_0} . Concerning the equation in \tilde{u}_{z_0} (III.61) we can also find a function Ψ_2 such that $\Psi_2\left(\frac{\tilde{r}^2}{t}\right) = \tilde{t}\tilde{u}_{z_0}$, so that we obtain for \tilde{u}_{z_0} :

$$\tilde{u}_{z_0} = \frac{\beta_1}{\tilde{t}} \exp\left(-\frac{R_{ei}\tilde{r}^2}{4}\right), \quad (\text{III.64})$$

where β_1 is a constant that is not determined at this point. We can also obtain the equation of the bubble $\tilde{b}_0(\tilde{t}, \tilde{r})$ as:

$$\tilde{b}_0 = 1 + \beta_1 \int_{\frac{R_{ei}\tilde{r}^2}{4\tilde{t}}}^{\infty} \frac{\exp(-u)}{u} du. \quad (\text{III.65})$$

Expression of the volume. The boundary conditions on the bubble surface can now be applied. The pressure on the bubble surface at the vortex axis is given by (III.63):

$$\tilde{p}_{\text{along the vortex axis}} = \tilde{p}_{\infty} - \frac{2\delta \ln 2}{\tilde{t}}. \quad (\text{III.66})$$

This leads to a relationship for the bubble volume:

$$\tilde{p}_{\infty} - \frac{2\delta \ln 2}{\tilde{t}} = \tilde{p}_v + \tilde{p}_{g_o} \left(\frac{\tilde{\mathcal{V}}_o}{\tilde{\mathcal{V}}} \right)^k, \quad (\text{III.67})$$

or

$$\left(\frac{\tilde{\mathcal{V}}_o}{\tilde{\mathcal{V}}} \right)^k = \frac{\tilde{p}_{\infty} - \frac{2\delta \ln 2}{\tilde{t}} - \tilde{p}_v}{\tilde{p}_{g_o}} \quad (\text{III.68})$$

The inner problem in the neighborhood of the plane of symmetry.

The equations at order zero become:

**Navier-Stokes:*

$$\begin{aligned} \frac{1}{\tilde{r}} \frac{\partial(r\tilde{u}_{r0})}{\partial\tilde{r}} &= 0, \\ \frac{\partial\tilde{u}_{r0}}{\partial\tilde{t}} + \tilde{u}_{r0} \frac{\partial\tilde{u}_{r0}}{\partial\tilde{r}} - \frac{\tilde{u}_{\theta_0}^2}{\tilde{r}} &= -\frac{\partial\tilde{p}_0}{\partial\tilde{r}} + \frac{1}{R_{ei}} \frac{\partial}{\partial\tilde{r}} \left(\frac{1}{\tilde{r}} \frac{\partial(r\tilde{u}_{r0})}{\partial\tilde{r}} \right), \\ \frac{\partial\tilde{u}_{\theta_0}}{\partial\tilde{t}} + \tilde{u}_{r0} \frac{\partial\tilde{u}_{\theta_0}}{\partial\tilde{r}} + \frac{\tilde{u}_{r0}\tilde{u}_{\theta_0}}{\tilde{r}} &= \frac{1}{R_{ei}} \frac{\partial}{\partial\tilde{r}} \left(\frac{1}{\tilde{r}} \frac{\partial(r\tilde{u}_{\theta_0})}{\partial\tilde{r}} \right), \\ \frac{\partial\tilde{u}_{z_0}}{\partial\tilde{t}} + \tilde{u}_{r0} \frac{\partial\tilde{u}_{z_0}}{\partial\tilde{r}} &= \frac{1}{R_{ei}} \frac{1}{\tilde{r}} \frac{\partial}{\partial\tilde{r}} \left(\tilde{r} \frac{\partial\tilde{u}_{z_0}}{\partial\tilde{r}} \right). \end{aligned} \quad (\text{III.69})$$

**Dynamic conditions:*

$$\tilde{p}_0(\tilde{a}_0) = \tilde{p}_v + \tilde{p}_{g_o} \left(\frac{\tilde{\mathcal{V}}_i}{\tilde{\mathcal{V}}} \right)^k + \frac{2}{R_{ei}} \frac{\partial\tilde{u}_{r0}}{\partial\tilde{r}} - \frac{1}{W_e} \frac{1}{\tilde{a}_0}. \quad (\text{III.70})$$

*Kinematic condition:

$$\frac{\partial \tilde{a}_0}{\partial \tilde{t}} = \tilde{u}_{r_0} (\tilde{a}). \quad (\text{III.71})$$

Integrating the continuity equation over \tilde{r} and replacing in the other equations, we obtain:

$$\begin{aligned} \tilde{u}_{r_0} &= \frac{\tilde{a}_0 \overset{\circ}{\tilde{a}_0}}{\tilde{r}}, \\ \frac{\overset{\circ}{\tilde{a}_0}^2}{\tilde{r}} + \frac{\tilde{a}_0 \overset{\circ}{\tilde{a}_0}}{\tilde{r}} - \frac{\tilde{a}_0^2 \overset{\circ}{\tilde{a}_0}^2}{\tilde{r}^3} - \frac{\tilde{u}_{\theta_0}^2}{\tilde{r}} &= -\frac{\partial \tilde{p}_0}{\partial \tilde{r}}, \\ \frac{\partial \tilde{u}_{\theta_0}}{\partial \tilde{t}} + \frac{\tilde{a}_0 \overset{\circ}{\tilde{a}_0}}{\tilde{r}} \frac{\partial \tilde{u}_{\theta_0}}{\partial \tilde{r}} + \frac{\tilde{a}_0 \overset{\circ}{\tilde{a}_0}}{\tilde{r}^2} \tilde{u}_{\theta_0} &= \frac{1}{R_{ei}} \frac{\partial}{\partial \tilde{r}} \left(\frac{1}{\tilde{r}} \frac{\partial}{\partial \tilde{r}} (\tilde{r} \tilde{u}_{\theta_0}) \right), \\ \frac{\partial \tilde{u}_{z_0}}{\partial \tilde{t}} + \frac{\tilde{a}_0 \overset{\circ}{\tilde{a}_0}}{\tilde{r}} \frac{\partial \tilde{u}_{z_0}}{\partial \tilde{r}} &= \frac{1}{R_{ei}} \frac{1}{\tilde{r}} \frac{\partial}{\partial \tilde{r}} \left(\tilde{r} \frac{\partial \tilde{u}_{z_0}}{\partial \tilde{r}} \right), \end{aligned} \quad (\text{III.72})$$

and at the bubble surface:

$$\tilde{P}_0(\tilde{a}_0) = \tilde{P}_v + \tilde{P}_{go} \left(\frac{\tilde{\mathcal{V}}_o}{\tilde{\mathcal{V}}} \right)^k - \frac{2}{R_{ei}} \frac{\overset{\circ}{\tilde{a}_0}}{\tilde{a}_0} - \frac{1}{W_e \tilde{a}_0} \quad (\text{III.73})$$

Solution for the bubble radius Using a similar approach as in Section III.1, we make the following change of variables to transform the integration domain into a fixed domain:

$$s = \frac{\tilde{r}}{\tilde{a}_0}. \quad (\text{III.74})$$

This leads to the following equation for the evolution of the bubble radius with time.

$$\overset{\circ}{\tilde{a}_0} = -\frac{\overset{\circ}{\tilde{a}_0}^2}{\tilde{a}_0} + \frac{\overset{\circ}{\tilde{a}_0}^2}{\tilde{a}_0 \ln s_{\max}} \left(-\frac{1}{2s_{\max}^2} + \frac{1}{2} \right) + \frac{\int_1^{s_{\max}} \frac{\tilde{u}_{\theta_0}^2}{\xi} d\xi}{\tilde{a}_0 \ln s_{\max}} - \frac{1}{\tilde{a}_0 \ln s_{\max}} (\tilde{p}_0(s_{\max}) - \tilde{p}_0(\tilde{a}_0)), \quad (\text{III.75})$$

where s_{\max} is the cutoff distance far from the bubble wall for the numerical integrations.

This expression is very similar to that obtained for an infinitely long bubble on the vortex axis, (III.8). However, here the value of $\tilde{p}_0(\tilde{a}_0)$ is given by the stress balance equation at the bubble wall which involves the bubble volume, and $\tilde{p}_0(s_{\max})$ is obtained by its limit expression in the outer problem.

In order to solve this equation, we need to use the expression of the volume found at the bubble poles from the previously described inner problem near the vortex axis. This provides a key coupling between the two inner sub-problems.

These equations can be solved numerically using a time and space discretization scheme. Centered differences are used for the space integrations, while a Crank-Nicholson scheme and Runge-Kutta integration are used for the time stepping.

Some example cases and discussion

Because of the nature of the solution of the outer problem, (III.63), it is not possible to start the problem at $t = 0$. (Physically, this is due to the fact that we imposed that at $t = 0$ the vortex line is that in an ideal fluid. Therefore, it is not possible to have a finite bubble at equilibrium on the vortex axis where the pressure is infinitely negative). Therefore, we will start all study cases at a finite time, $t = t_o$. The considered bubble will then be assumed of volume, \mathcal{V}_o , and the rotating flow field will have an Oseen form:

$$u_{\theta_o} = \frac{\Gamma}{2\pi r} \left(1 - \exp \left(-\frac{r^2}{4vt_o} \right) \right). \quad (\text{III.76})$$

The bubble behavior once allowed to interact with the vortex strongly depends on the relationship between \mathcal{V}_o and an equilibrium volume, $\tilde{\mathcal{V}}_{eq}$, defined as follows:

$$\tilde{\mathcal{V}}_{eq} = \left(\frac{\tilde{p}_{g_o}}{\tilde{p}_{\infty} - \tilde{p}_v - \frac{2\delta \ln 2}{t_o}} \right)^{\frac{1}{k}}, \quad (\text{III.77})$$

with $\tilde{\mathcal{V}}_o = 1$, (using \mathcal{V}_o as the volume scale).

1. If $\tilde{\mathcal{V}}_o$ is much greater than $\tilde{\mathcal{V}}_{eq}$, then the bubble undergoes a violent collapse (Figure III.11) with the speed of the bubble wall becoming increasingly negative until touchdown.
2. For smaller values of $\tilde{\mathcal{V}}_o$, but still higher than $\tilde{\mathcal{V}}_{eq}$, the bubble radius begins by dropping, but then the bubble grows back to a large value before violently collapsing (Figure III.12).
3. When $\tilde{\mathcal{V}}_o$ is inferior to $\tilde{\mathcal{V}}_{eq}$, the bubble first grows, and then collapses (Figure III.13) but always in the same violent way. The smaller $\tilde{\mathcal{V}}_o$ is, compared to $\tilde{\mathcal{V}}_{eq}$, the more important is the initial growth of the bubble (Figure III.14).

It is important to notice that in all cases the bubble wall speed become infinite and the radius goes to zero. All attempts to systematically reduce the time step when the radius decreases failed in showing a bubble radius rebound. This illustrates the absence of a restoring force during the collapse of the bubble. This is due to the fact that the variations of the volume in time are in fact very small, which make the influence of compression of the inner gas negligible.

This leads us to the numerical study of the bubble behavior on a vortex axis as described in Chapter II. There it was seen that as the initial pressures in the bubble was higher than that on the vortex axis, the bubble first elongates along that axis and does not encounter any significant resistance in that direction. However, after the bubble has exceeded its equilibrium volume, the portions of its surface farther from the axis start to collapse, i.e. return towards the axis. The points near the axis only experience a very slow pressure increase due to viscous diffusion and, as no force opposes their motion, the bubble continues to elongate. This leads to bubble splitting. As the asymptotic model described in this section give only the bubble position in the plane of symmetry and on the axis, we observe instead of the detailed splitting of the bubble its expression along the two main direction: i.e. increasing elongation along the axis and radial dimension tending to zero.

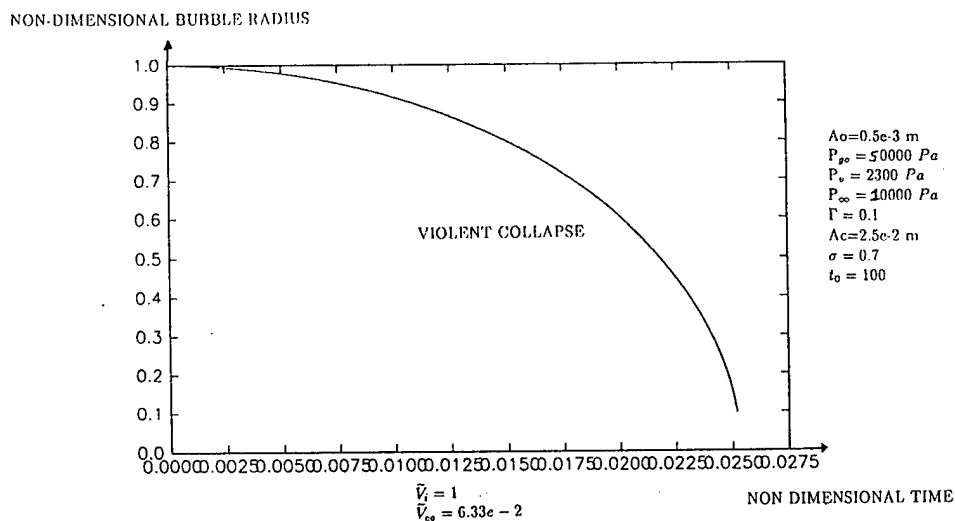


Figure III.11: Bubble radius versus time for an initial bubble volume much larger than the equilibrium volume. $V_{eq}/V_l = 0.063$, $t_0 = 100$, $a_o = 500\mu\text{m}$, $P_{go} = 5.10^5 \text{ Pa}$, $a_c = 0.025\text{m}$, $p_v = 2300 \text{ Pa}$, $\Gamma = 0.1$, $\gamma = 0.7$.

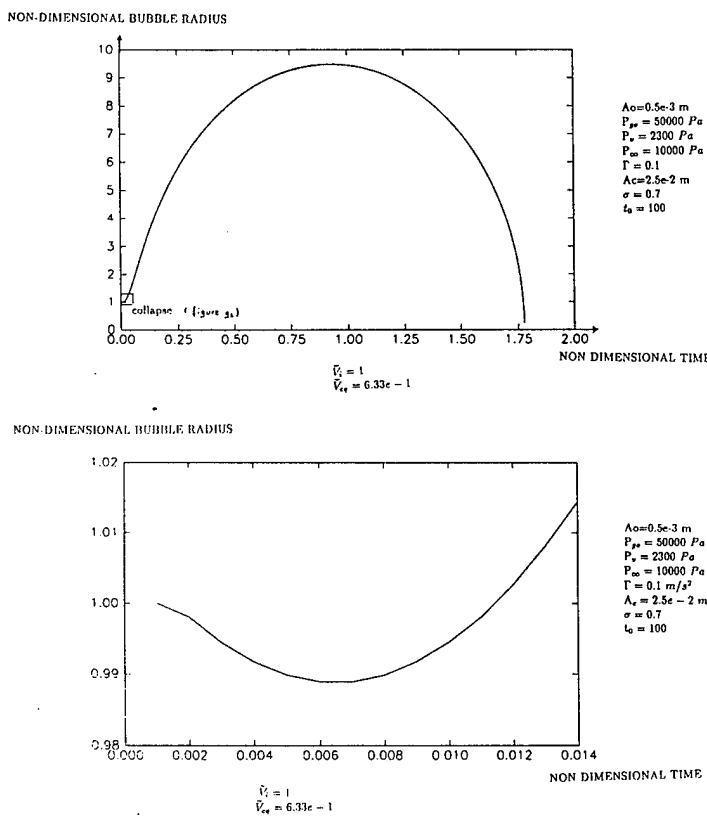


Figure III.12: Bubble radius versus time for an initial bubble volume much larger than equilibrium volume. a. Full curve. b. Blow up of initial region. $V_{eq}/V_l = 0.63$, $t_0 = 100$, $a_o = 500\mu\text{m}$, $P_{go} = 5.10^5 \text{ Pa}$, $t_0 = 100$, $a_c = 0.025\text{m}$, $p_v = 2300 \text{ Pa}$, $\Gamma = 0.1$, $\gamma = 0.7$.

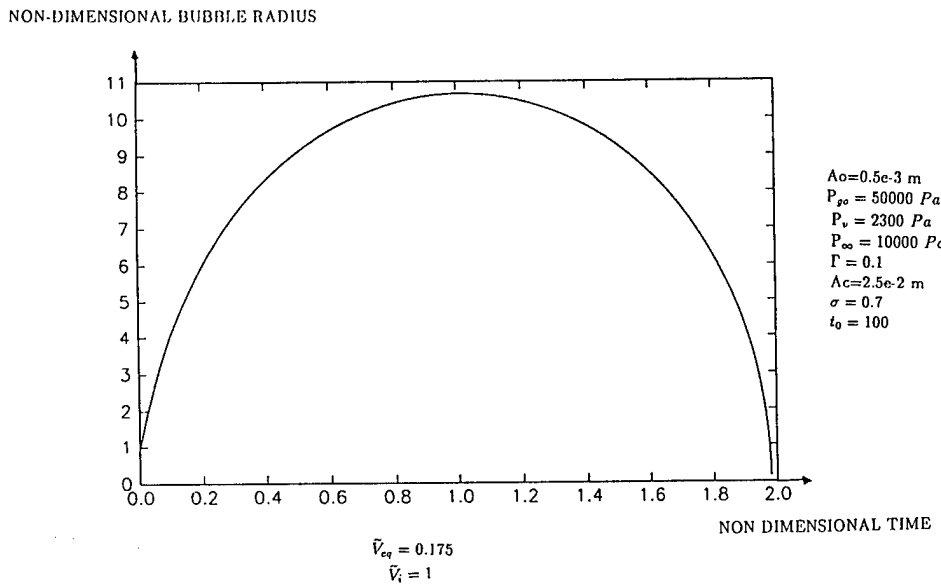


Figure III.13: Bubble radius versus time in the case of bubble growth and collapse. $V_{eq}/V_i = 1.75$, $t_0 = 100$, $a_o = 500\mu\text{m}$, $P_{go} = 5.10^5 \text{ Pa}$, $a_c = 0.025\text{m}$, $p_v = 2300 \text{ Pa}$, $\Gamma = 0.1$, $\gamma = 0.7$.

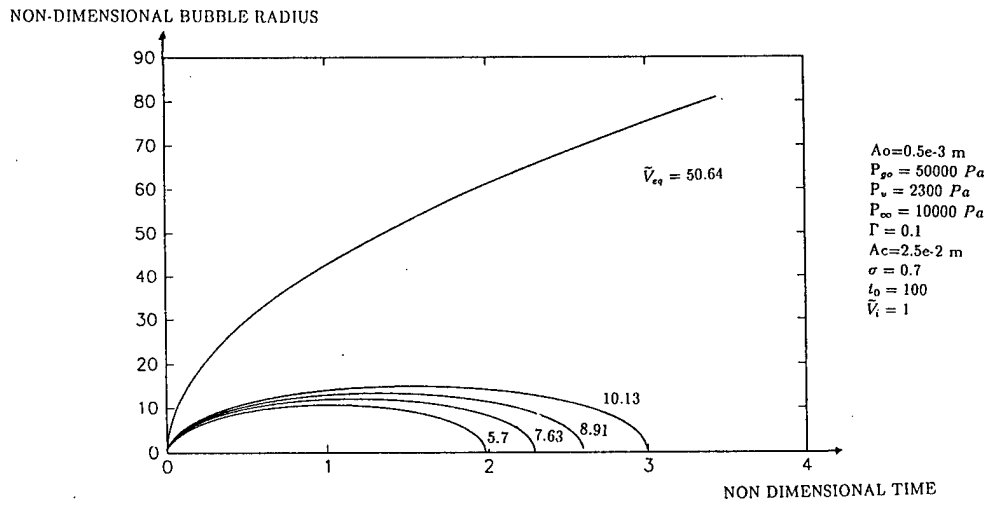


Figure III.14: Bubble radius versus time for various values of the initial bubble volume all smaller than the equilibrium volume. $t_0 = 100$, $a_o = 500\mu\text{m}$, $P_{go} = 5.10^5 \text{ Pa}$, $a_c = 0.025\text{m}$, $p_v = 2300 \text{ Pa}$, $\Gamma = 0.1$, $\gamma = 0.7$.

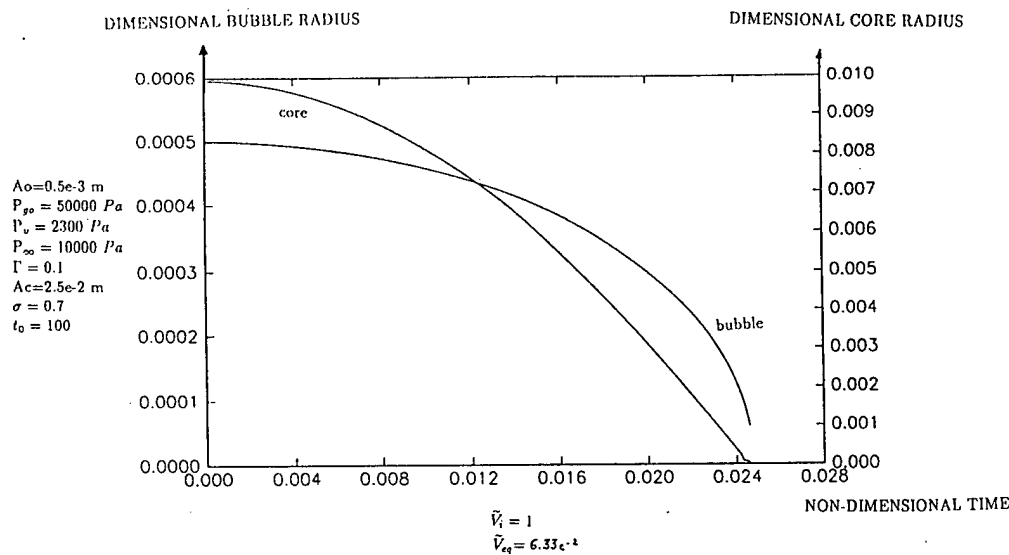


Figure III.15: Bubble radius and viscous core radius versus time in the case of a strong bubble collapse. $V_{eq}/V_t = 0.063$, $t_0 = 100$, $a_o = 500 \mu\text{m}$, $P_{go} = 5.10^5 \text{ Pa}$, $P_\infty = 1.10^4 \text{ Pa}$, $a_c = 0.025 \text{ m}$, $p_v = 2300 \text{ Pa}$, $\Gamma = 0.1$, $\gamma = 0.7$.

Figures III.15, III.16, III.17, illustrate the interactions between the bubble and the flow. In the case of a bubble collapse Figure III.15 shows that the viscous core radius decreases as the bubble radius and even more rapidly. Through conservation of momentum, the tangential velocity follows the opposite tendency to the core size. As the bubble wall contracts, the core shrinks, and the vorticity increases. Both the maximum of the vorticity, $\nabla \times \mathbf{u}$, (Figure III.16), and the maximum of the tangential velocity (Figure III.17) grow exponentially when the bubble collapses violently.

On the contrary, when the bubble has an explosive growth, the core grows in the same way (Figure III.18). It is important to notice that the ratio between the core radius and the bubble radius remains constant. We find here the same result as in the section on cavitation inception using the infinitely elongated bubble approach. The maximum of the tangential velocity (Figure III.19) and the maximum of the vorticity (Figure III.20) drop to asymptotic values very close to zero.

Although these interactions, as well as the tendency of the core radius to get displaced with the bubble wall, correspond to intuition, they are still quite unknown and need to be studied more thoroughly. P_∞

4.6 Resolution at the following orders

The outer problem at the order $\epsilon^{1/2}$.

We collect now all the terms at the following order, here $\epsilon^{1/2}$ for the outer problem.

*Navier-Stokes

$$\begin{aligned} \frac{1}{\bar{r}} \frac{\partial (\bar{r} u_{r1})}{\partial \bar{r}} + \frac{\partial u_{z1}}{\partial \bar{z}} &= 0, \\ \frac{\partial u_{r1}}{\partial \bar{t}} - 2 \frac{\bar{u}_{\theta o} \bar{u}_{\theta 1}}{\bar{r}} &= - \frac{\partial \bar{p}_1}{\partial \bar{r}} + \frac{1}{R_{eo}} \left[\frac{\partial}{\partial \bar{r}} \left(\frac{1}{\bar{r}} \frac{\partial (\bar{r} u_{r1})}{\partial \bar{r}} \right) + \frac{\partial^2 \bar{u}_{r1}}{\partial \bar{z}^2} \right], \end{aligned}$$

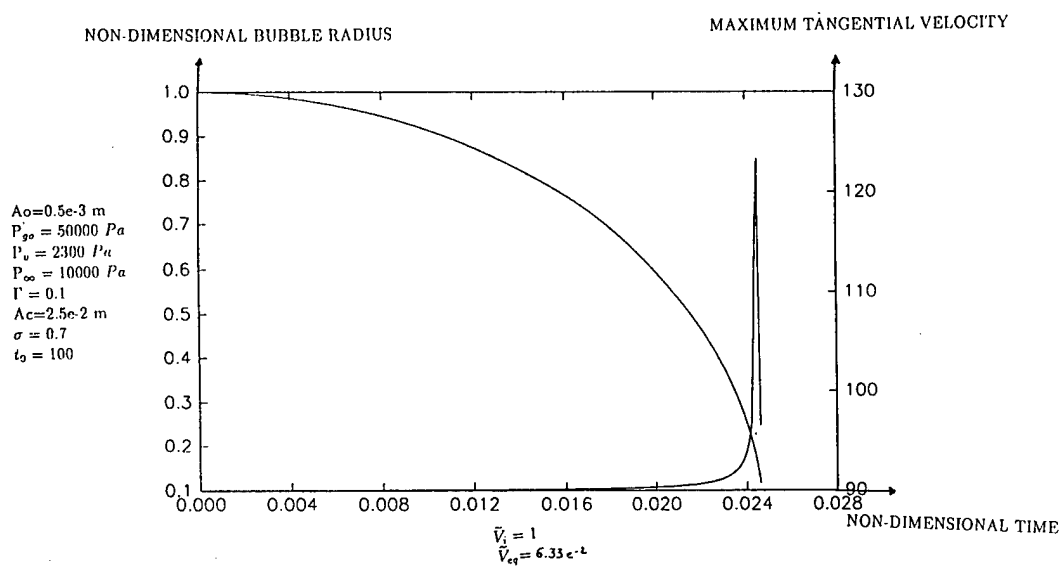


Figure III.16: Bubble radius and maximum tangential velocity versus time in the case of a strong bubble collapse. $V_{eq}/V_i = 0.063$, $t_0 = 100$, $a_o = 500\mu\text{m}$, $P_{go} = 5.10^5 \text{ Pa}$, $P_\infty = 1.10^4 \text{ Pa}$, $a_c = 0.025 \text{ m}$, $p_v = 2300 \text{ Pa}$, $\Gamma = 0.1$, $\gamma = 0.7$.

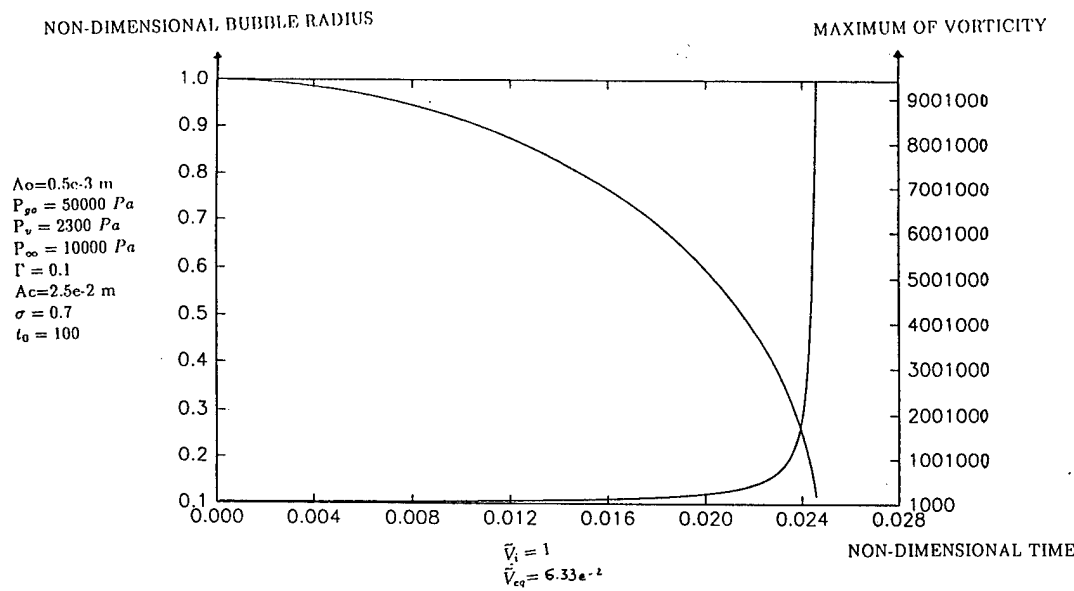


Figure III.17: Bubble radius and maximum vorticity versus time in the case of a strong bubble collapse. $V_{eq}/V_i = 0.063$, $t_0 = 100$, $a_o = 500\mu\text{m}$, $P_{go} = 5.10^5 \text{ Pa}$, $P_\infty = 1.10^4 \text{ Pa}$, $a_c = 0.025 \text{ m}$, $p_v = 2300 \text{ Pa}$, $\Gamma = 0.1$, $\gamma = 0.7$.

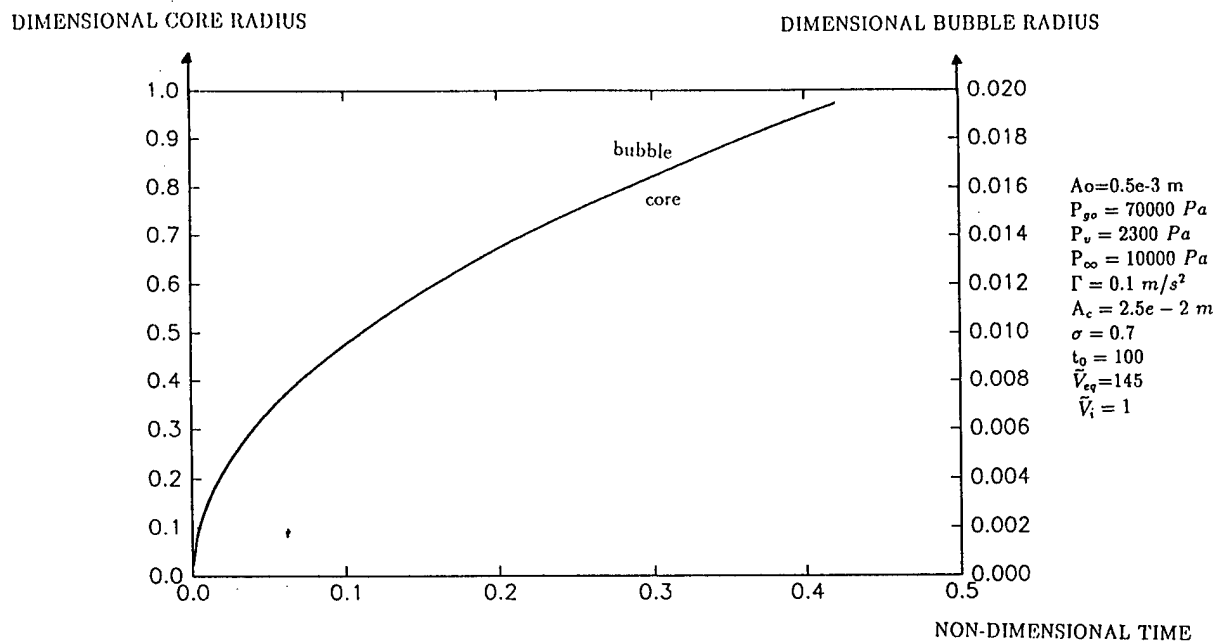


Figure III.18: Bubble radius and viscous core radius versus time in the case of an explosive bubble growth. $\tilde{V}_{eq}/\tilde{V}_i = 145$, $t_0 = 100$, $a_o = 500 \mu\text{m}$, $P_{go} = 7.10^4 \text{ Pa}$, $P_\infty = 1.10^4 \text{ Pa}$, $a_c = 0.025 \text{ m}$, $p_v = 2300 \text{ Pa}$, $\Gamma = 0.1$, $\gamma = 0.7$.

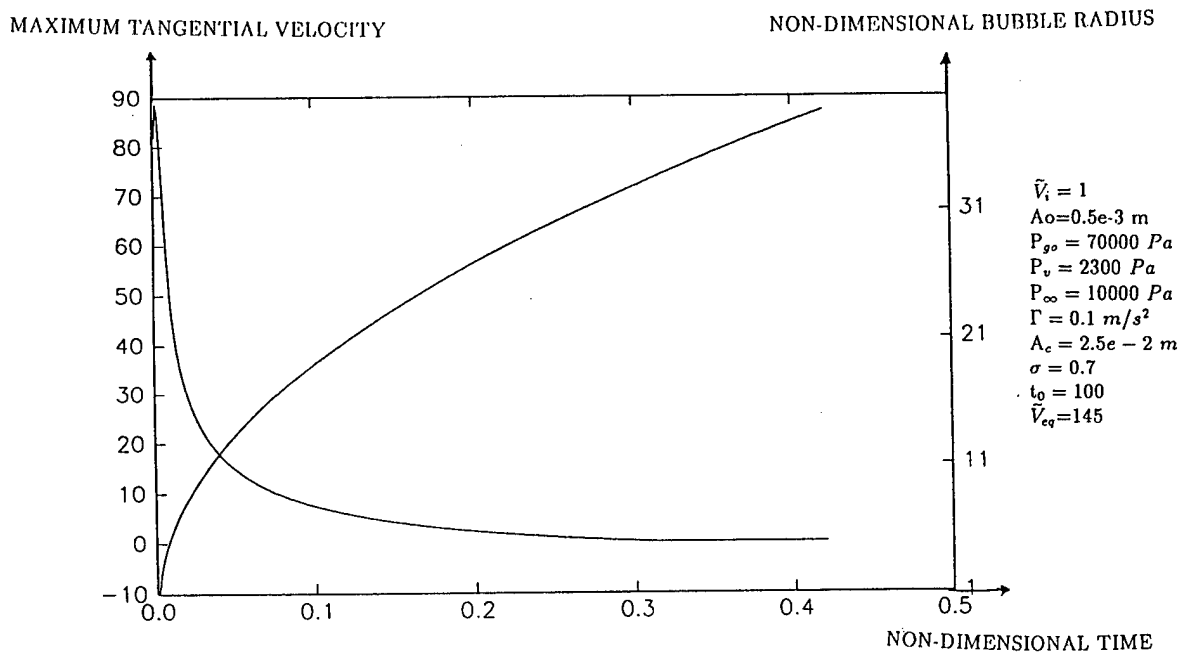


Figure III.19: Bubble radius and maximum tangential velocity versus time in the case of an explosive bubble growth. $\tilde{V}_{eq}/\tilde{V}_i = 145$, $t_0 = 100$, $a_o = 500 \mu\text{m}$, $P_{go} = 7.10^4 \text{ Pa}$, $P_\infty = 1.10^4 \text{ Pa}$, $a_c = 0.025 \text{ m}$, $p_v = 2300 \text{ Pa}$, $\Gamma = 0.1$, $\gamma = 0.7$.

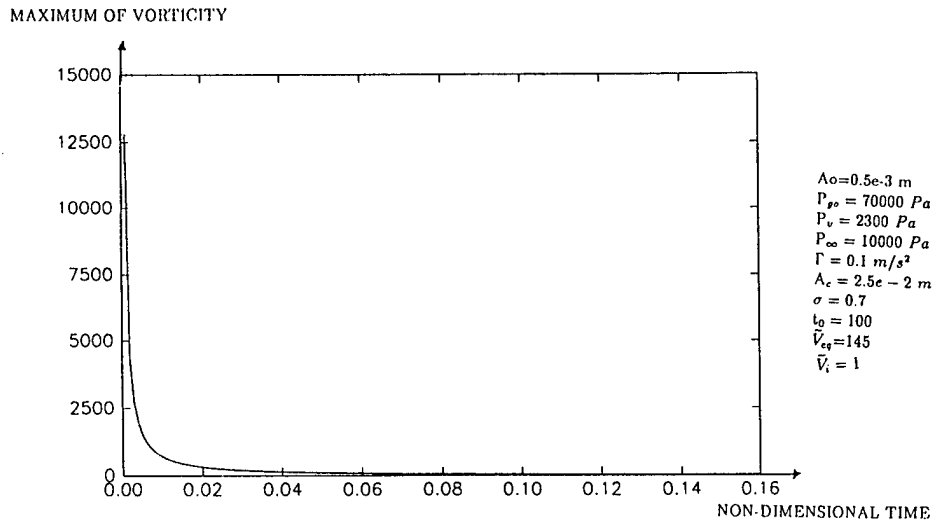


Figure III.20: Bubble radius and maximum vorticity versus time in the case of an explosive bubble growth. $V_{eq}/V_i = 145$, $t_0 = 100$, $a_o = 500 \mu\text{m}$, $P_{go} = 7.10^4 \text{ Pa}$, $P_\infty = 1.10^4 \text{ Pa}$, $a_c = 0.025 \text{ m}$, $p_v = 2300 \text{ Pa}$, $\Gamma = 0.1$, $\gamma = 0.7$.

$$\begin{aligned} \frac{\partial \bar{u}_{\theta_1}}{\partial \bar{t}} + \bar{u}_{r_0} \frac{\partial \bar{u}_{\theta_0}}{\partial \bar{r}} + \frac{\bar{u}_{r_0} \bar{u}_{\theta_0}}{\bar{r}} + \bar{u}_{z_0} \frac{\partial \bar{u}_{\theta_0}}{\partial \bar{z}} &= \frac{1}{R_{eo}} \left[\frac{\partial}{\partial \bar{r}} \left(\frac{1}{\bar{r}} \frac{\partial (\bar{r} \bar{u}_{\theta_1})}{\partial \bar{r}} \right) + \frac{\partial^2 \bar{u}_{\theta_1}}{\partial \bar{z}^2} \right], \\ \frac{\partial \bar{u}_{z_0}}{\partial \bar{t}} &= - \frac{\partial \bar{p}_1}{\partial \bar{z}}. \end{aligned} \quad (\text{III.78})$$

Using the zero order solution, we obtain in a similar fashion for \bar{u}_{θ_1} :

$$\bar{u}_{\theta_1} = \frac{1}{\bar{r}} \left[\alpha + \beta \exp \left(- \frac{R_{eo}}{4} \frac{\bar{r}^2}{\bar{t}} \right) \right], \quad (\text{III.79})$$

where α, β are constants. But, since we need to satisfy ($\bar{u}_{\theta_1} = 0$ when $\bar{t} \rightarrow 0$ and $\bar{t} \rightarrow \infty$), the solution degenerates to $\alpha = \beta = 0$. This, therefore, also gives $p_1 = 0$.

The outer problem at the order ϵ

In order to find the perturbation due to the presence of the bubble on the line vortex flow we have to expand to the second order. We can explore an expression of the radial velocity by analogy with the expression we found near the plane of symmetry at order zero, (i.e. we have a source of intensity $\frac{\partial V_0}{\partial t}$ at the origin). Let us set:

$$\bar{u}_{r_1} = \frac{\partial \bar{V}_0}{\partial \bar{t}} \cdot \frac{\bar{r}}{(\bar{r}^2 + \bar{z}^2)},$$

where the volume \bar{V}_0 is known at the previous order. Using the equation of continuity, the axial velocity at order one is then:

$$\bar{u}_{z_1} = \frac{\partial \bar{V}_0}{\partial \bar{t}} \cdot \frac{\bar{z}}{(\bar{r}^2 + \bar{z}^2)}.$$

The boundary conditions due to the presence of the bubble can now be introduced. This enables one to write an equation with \bar{u}_{θ_2} only:

$$\frac{\partial \bar{u}_{\theta_2}}{\partial t} + \bar{u}_{r_1} \left(\frac{\partial \bar{u}_{\theta_0}}{\partial \tilde{r}} + \frac{\bar{u}_{\theta_0}}{\tilde{r}} \right) = \frac{1}{R_{ei}} \left[\frac{\partial}{\partial \tilde{r}} \left(\frac{1}{\tilde{r}} \frac{\partial (\bar{r} \bar{u}_{\theta_2})}{\partial \tilde{r}} \right) + \frac{\partial^2 \bar{u}_{\theta_2}}{\partial z^2} \right].$$

The inner problem near the axis of symmetry.

At order zero, the bubble appears without geometrical curvature. Now, we will consider the variation according to the two dimensions. The various equations at this order are:

* *Navier-Stokes:*

$$\begin{aligned} \frac{1}{\tilde{r}} \frac{\partial (r \tilde{u}_{r_0})}{\partial \tilde{r}} + \frac{\partial \tilde{u}_{z_1}}{\partial z} &= 0, \\ 2 \frac{\tilde{u}_{\theta_0} \tilde{u}_{\theta_1}}{\tilde{r}} &= \frac{\partial \tilde{p}_1}{\partial \tilde{r}}, \\ \frac{\partial \tilde{u}_{\theta_1}}{\partial \tilde{t}} + \tilde{u}_{z_0} \frac{\partial \tilde{u}_{\theta_0}}{\partial z} &= \frac{1}{R_{ei}} \frac{\partial}{\partial \tilde{r}} \left(\frac{1}{\tilde{r}} \frac{\partial (\tilde{r} \tilde{u}_{\theta_1})}{\partial \tilde{r}} \right), \\ \frac{\partial \tilde{u}_{z_1}}{\partial \tilde{t}} + \tilde{u}_{z_0} \frac{\partial \tilde{u}_{z_0}}{\partial z} &= - \frac{\partial \tilde{p}_0}{\partial z} + \frac{1}{R_{ei}} \frac{1}{\tilde{r}} \frac{\partial}{\partial \tilde{r}} \left(\tilde{r} \frac{\partial \tilde{u}_z}{\partial \tilde{r}} \right). \end{aligned}$$

* *Dynamic conditions:*

$$\begin{aligned} \left[\tilde{r} \frac{\partial}{\partial \tilde{r}} \left(\frac{\tilde{u}_{\theta_0}}{\tilde{r}} \right) \frac{\partial \tilde{b}_1}{\partial \tilde{r}} + \tilde{r} \frac{\partial}{\partial \tilde{r}} \left(\frac{\tilde{u}_{\theta_1}}{\tilde{r}} \right) \frac{\partial \tilde{b}_0}{\partial \tilde{r}} \right]_S &= 0, \\ \left[\frac{\partial \tilde{u}_{z_1}}{\partial \tilde{r}} \cdot \left(\frac{\partial \tilde{b}_0}{\partial \tilde{r}} \right)^2 + 2 \frac{\partial \tilde{u}_{z_0}}{\partial \tilde{r}} \cdot \frac{\partial \tilde{b}_0}{\partial \tilde{r}} \frac{\partial \tilde{b}_1}{\partial \tilde{r}} \right]_S &= 0, \\ \tilde{p}_v + \tilde{p}_{g_o} \left(\frac{1}{\tilde{V}} \right)^k + \frac{2}{R_{ei} \left(\frac{\partial \tilde{b}_0}{\partial \tilde{r}} \right)} \frac{\partial \tilde{u}_{z_0}}{\partial \tilde{r}} - \frac{1}{W_e \left(\frac{\partial \tilde{b}_0}{\partial \tilde{r}} \right)^2} \cdot \left(- \frac{\tilde{a}_1}{\tilde{a}_0^2} \frac{\partial \tilde{b}_0}{\partial \tilde{r}} + \frac{1}{\tilde{a}_0} \frac{\partial \tilde{b}_1}{\partial \tilde{r}} \right) &= \tilde{p}_s. \end{aligned}$$

* *Kinematic condition:*

$$\frac{\partial \tilde{b}_1}{\partial \tilde{t}} = \tilde{u}_{z_1}(S) - \tilde{u}_{r_0}(S) \frac{\partial \tilde{b}_0}{\partial \tilde{r}}.$$

The inner problem near the plane of symmetry.

* *Navier-Stokes:*

$$\begin{aligned} \frac{1}{\tilde{r}} \frac{\partial (r \tilde{u}_{r_1})}{\partial \tilde{r}} + \frac{\partial \tilde{u}_{z_0}}{\partial z} &= 0, \\ \frac{\partial \tilde{u}_{r_1}}{\partial \tilde{t}} + \tilde{u}_{r_1} \frac{\partial \tilde{u}_{r_0}}{\partial \tilde{r}} + \tilde{u}_{r_0} \frac{\partial \tilde{u}_{r_1}}{\partial \tilde{r}} - 2 \frac{\tilde{u}_{\theta_0} \tilde{u}_{\theta_1}}{\tilde{r}} + \tilde{u}_{z_0} \frac{\partial \tilde{u}_{r_0}}{\partial z} &= - \frac{\partial \tilde{p}_1}{\partial \tilde{r}} + \frac{1}{R_{eo}} \frac{\partial}{\partial \tilde{r}} \left(\frac{1}{\tilde{r}} \frac{\partial (r \tilde{u}_{r_1})}{\partial \tilde{r}} \right), \\ \frac{\partial \tilde{u}_{\theta_1}}{\partial \tilde{t}} + \tilde{u}_{r_1} \frac{\partial \tilde{u}_{\theta_0}}{\partial \tilde{r}} + \tilde{u}_{r_0} \frac{\partial \tilde{u}_{\theta_1}}{\partial \tilde{r}} + \frac{\tilde{u}_{r_1} \tilde{u}_{\theta_0}}{\tilde{r}} + \frac{\tilde{u}_{r_1} \tilde{u}_{\theta_0}}{\tilde{r}} + \tilde{u}_{z_0} \frac{\partial \tilde{u}_{\theta_0}}{\partial z} &= \frac{1}{R_{eo}} \frac{\partial}{\partial \tilde{r}} \left(\frac{1}{\tilde{r}} \frac{\partial (r \tilde{u}_{\theta_1})}{\partial \tilde{r}} \right), \end{aligned}$$

$$\frac{\partial \tilde{u}_{z_1}}{\partial \tilde{t}} + \tilde{u}_{r_0} \frac{\partial \tilde{u}_{z_1}}{\partial \tilde{r}} + \tilde{u}_{z_0} \frac{\partial \tilde{u}_{z_0}}{\partial \tilde{z}} = -\frac{\partial \tilde{p}_1}{\partial \tilde{z}} + \frac{1}{R_{eo}} \left[\frac{1}{\tilde{r}} \frac{\partial}{\partial \tilde{r}} \left(\tilde{r} \frac{\partial \tilde{u}_{z_1}}{\partial \tilde{r}} \right) \right].$$

*Dynamic conditions:

$$\left[\tilde{r} \frac{\partial}{\partial \tilde{r}} \left(\frac{\tilde{u}_{r_1}}{\tilde{r}} \right) \right]_S = 0,$$

$$\left[\frac{\partial \tilde{u}_{r_0}}{\partial \tilde{z}} + \frac{\partial \tilde{u}_{z_1}}{\partial \tilde{r}} + 2 \frac{\partial \tilde{a}_0}{\partial \tilde{z}} \frac{\partial \tilde{u}_{r_0}}{\partial \tilde{r}} \right]_S = 0,$$

$$\tilde{p}_v + \tilde{p}_{g_o} \left(\frac{1}{\tilde{V}_S} \right)^k + \frac{2}{R_{eo}} \cdot \left[\frac{\partial \tilde{u}_{r_1}}{\partial \tilde{r}} - \frac{\partial \tilde{a}_0}{\partial \tilde{z}} \frac{\partial \tilde{u}_{z_0}}{\partial \tilde{r}} \right] + \frac{1}{W_e} \frac{\tilde{a}_1}{\tilde{a}_0^2} = \tilde{p}_S$$

*Kinematic condition:

$$\frac{\partial \tilde{a}_1}{\partial \tilde{t}} = \tilde{u}_{r_1}(S) - \tilde{u}_{z_0}(S) \frac{\partial \tilde{a}_0}{\partial \tilde{z}}.$$

These equation can be solved using a finite difference scheme such as the Alternating Direction Implicit (ADI) method.

Chapter IV

THREE-DIMENSIONAL BUBBLE-VORTICAL FLOW INTERACTION — A NUMERICAL STUDY¹

1 Introduction

Simulation of vortical liquid flow fields with free surfaces is important in many fields such as naval hydrodynamics and two-phase flows, and still presents many challenges despite extensive investigations. The simulation requires satisfaction of free surface boundary conditions, incorporation of the vorticity dynamics in the presence of free surfaces, and description of the dynamics of the surface deformation.

In this contribution we present a numerical scheme that we have developed for such three-dimensional vortical flows by coupling a vortex element method (VEM) for the vortical part of the flow with a boundary element method (BEM) for the potential part. We describe this new formulation, and present application of the scheme to some relatively simple cases, where we investigate the bubble deformation due to the flow field, and the effects of the bubble deformation on the flow field.

The BEM has been successfully applied to many inviscid potential flow computations with free boundaries (e.g., bubbles, drops, water waves). The chief advantage of this method is that only the boundary is discretized instead of the complete domain therefore achieving a considerable reduction in the number of unknowns and an increase of accuracy at the free surface. Moreover the movement of the boundary is easily followed in a Lagrangian fashion using the local velocity. The axisymmetric formulation of this method has been widely applied in the literature for the study of bubbles and surface waves,[34], [35], [36], [37]. We have implemented and systematically used both an axisymmetric as well as a three-dimensional boundary element formulation for simulating cavitation and underwater explosion bubbles near solid boundaries and deformable structures, and for studying multi-bubble interaction ([40], [41] &[42], [1], [43]). Similar bubble-bubble interaction

¹This chapter is adapted directly from our publication in Reference [64].

problems were studied by [75] [76] using expansions in special functions.

The vortex element method has also been applied to many free and bounded flow problems ([45], [44]). The modern version of this method pioneered by [49], represents the vorticity field by distributed vortex elements while the induced velocity field is obtained by integration ([46] & [47], [48]). There are three main advantages to this method compared to more traditional methods. First, it eliminates the pressure from the equations with incompressibility automatically satisfied. Second, the dynamics are described by following the movement of the vortex elements, and by solving ordinary differential equations to evaluate their intensities. Finally, only the region in the fluid where the vorticity is nonzero is discretized effecting a substantial saving in computation. Recently, several viscous vortex element schemes have been suggested and successfully implemented in simple geometries making these methods attractive alternatives to more traditional finite difference methods ([49], [50]&[51] , [52] & [53]).

We have coupled the BEM and VEM methods into a numerical scheme that will ultimately be capable of handling general vortical flows with free boundaries while retaining the advantages of the individual methods. In earlier studies of bubbles in a vortical field, the effect of the flow on the bubble was accounted for while neglecting modification due to the bubble of the vortical part of the flow ([1]). The present technique removes this restriction by calculating an evolving vorticity field and incorporating two-way interaction between the bubble dynamics and the vorticity.

The difficulty in implementing the coupled description is the need to compute the pressure on the free surfaces. This difficulty is solved by a formulation with a Poisson equation for a scalar quantity involving the pressure (similar to the expression appearing in the Bernoulli equation), which satisfies a normal derivative boundary condition on the free boundary. The solution of this equation is obtained using a dual reciprocity boundary element method (DRM), ([54]) using the same BEM matrices calculated for the velocity potential. This provides the time derivative of the potential at the bubble nodes and therefore enables computation of the full interaction between the bubble dynamics and the flow.

We describe the mathematical formulation in section 2 and the numerical implementation in section 3. Then in section 4 we apply the method to obtain the dynamics of a bubble in a column vortex flow and a bubble in a vortex ring structure. Conclusions are given in section 5.

2 Mathematical formulation

2.1 Kinematic Equations

In order to proceed with a BEM/VEM mixed approach we use the fact that the velocity field $\mathbf{u}(\mathbf{x})$ can be expressed via the Helmholtz decomposition as the sum of the gradient of a scalar potential ϕ and the curl of a vector potential \mathbf{A} :

$$\mathbf{u}(\mathbf{x}) = \mathbf{u}_b(\mathbf{x}) + \mathbf{u}_\omega(\mathbf{x}) = \nabla\phi(\mathbf{x}) + \nabla \times \mathbf{A}(\mathbf{x}). \quad (\text{IV.1})$$

Restricting our study to the case where the flow is incompressible, we have

$$\nabla^2\phi = 0. \quad (\text{IV.2})$$

Given (IV.2), a boundary element formulation to express ϕ in the fluid domain D is obtained by applying Green's identity

$$a\phi(\mathbf{x}) = \int_S [\phi(\mathbf{x}')\mathbf{n} \cdot \nabla' G(\mathbf{x}, \mathbf{x}') - \mathbf{n} \cdot \nabla' \phi(\mathbf{x}')G(\mathbf{x}, \mathbf{x}')] dS(\mathbf{x}'), \quad (\text{IV.3})$$

where $G(\mathbf{x}, \mathbf{x}') = -[4\pi|\mathbf{x} - \mathbf{x}'|]^{-1}$ is the free space Green's function, a is the solid angle subtended by the fluid at the point \mathbf{x} , normalized by 4π , S is the surface of the boundary delineating the domain D , including wetted and submerged bodies, bubbles and free surfaced; \mathbf{n} is the local outward normal at the surface, and ∇' is the gradient operator in the primed variable.

Taking the curl of (IV.1) we see that \mathbf{A} is related to vorticity $\boldsymbol{\omega}$ by

$$\nabla^2 \mathbf{A} = -\boldsymbol{\omega}, \quad (\text{IV.4})$$

where we have assumed that the vector potential \mathbf{A} is solenoidal ($\nabla \cdot \mathbf{A} = 0$) (For further detail see [30], p. 86). We will seek the field \mathbf{A} , in an unrestricted domain \bar{D} (D is \bar{D} minus the volume of the included body or bubble) with no boundary contribution, since the vorticity field decays sufficiently fast far away. Consequently \mathbf{A} is given by a *volume* integral over the vorticity

$$\mathbf{A}(\mathbf{x}) = - \int_{\bar{D}} G(\mathbf{x}, \mathbf{x}') \boldsymbol{\omega}(\mathbf{x}') dV(\mathbf{x}'). \quad (\text{IV.5})$$

The velocity \mathbf{u}_ω induced by the vorticity is given by the Biot-Savart integral obtained by taking the curl of \mathbf{A}

$$\mathbf{u}_\omega(\mathbf{x}) = -\nabla \times \int_{\bar{D}} G(\mathbf{x}, \mathbf{x}') \boldsymbol{\omega}(\mathbf{x}') dV(\mathbf{x}'). \quad (\text{IV.6})$$

The effect of any boundaries that may be present in the problem will therefore be accounted for by the \mathbf{u}_b term in (IV.1) by (IV.3).

2.2 Dynamic Equations

The evolution of the flow field is governed by the motion of the bounding surfaces as much as by the change in vorticity $\boldsymbol{\omega}$. The change in vorticity field is governed by the vorticity transport equation

$$\frac{D\boldsymbol{\omega}}{Dt} = \boldsymbol{\omega} \cdot \nabla \mathbf{u} + \nu \nabla^2 \boldsymbol{\omega}. \quad (\text{IV.7})$$

where D/Dt represents the material time derivative following the local fluid velocity \mathbf{u} , and ν is the kinematic viscosity.

The potential part of the flow is affected by the movement of any free surface through the boundary conditions. The momentum equation can be written by decomposing \mathbf{u} into its components as in (IV.1):

$$\frac{\partial \mathbf{u}_b}{\partial t} + \frac{\partial \mathbf{u}_\omega}{\partial t} + \boldsymbol{\omega} \times \mathbf{u} + \nabla \left[\frac{1}{2} |\mathbf{u}|^2 \right] = -\frac{\nabla p}{\rho} + \nu \nabla^2 \mathbf{u}. \quad (\text{IV.8})$$

Expressing \mathbf{u}_b in terms of the scalar potential ϕ , a modified Bernoulli type equation can be obtained from (IV.8),

$$\nabla \Psi \equiv \nabla \left(\frac{\partial \phi}{\partial t} + \frac{1}{2} |\mathbf{u}|^2 + \frac{p}{\rho} \right) = -\frac{\partial \mathbf{u}_\omega}{\partial t} - \mathbf{u} \times \boldsymbol{\omega} + \nu \nabla^2 \mathbf{u}. \quad (\text{IV.9})$$

where

$$\Psi = \frac{\partial \phi}{\partial t} + \frac{1}{2} |\mathbf{u}|^2 + \frac{p}{\rho}. \quad (\text{IV.10})$$

By taking the divergence of (IV.9) we obtain the following Poisson equation

$$\nabla^2 \Psi = \nabla \cdot (\mathbf{u} \times \boldsymbol{\omega}) = |\boldsymbol{\omega}|^2 - \mathbf{u} \cdot (\nabla \times \boldsymbol{\omega}) \equiv R, \quad (\text{IV.11})$$

in the entire fluid domain D . We find from (IV.9) that Ψ satisfies on the boundary

$$\mathbf{n} \cdot \nabla \Psi = \mathbf{n} \cdot \left(-\frac{\partial \mathbf{u}_\omega}{\partial t} - \mathbf{u} \times \boldsymbol{\omega} + \nu \nabla^2 \mathbf{u} \right) \equiv Q. \quad (\text{IV.12})$$

In the case where we consider a bubble and vortical field in an infinite medium, ϕ and \mathbf{u} decay to zero at infinity and Ψ tends to p_∞/ρ . Such a Poisson equation with the boundary conditions provides a well-posed problem for the scalar function Ψ . Note that by taking the divergence of the momentum equation and using the incompressibility one may also obtain the familiar Poisson equation for the pressure. However, here we have chosen the above form which is convenient for the numerical solution adopted below.

If the flow field due to the vortical part of the flow is assumed to be steady or to have a predetermined time evolution Equation (IV.8) may be given the form ([1])

$$\nabla \left(\frac{\partial \phi}{\partial t} + \frac{1}{2} |\nabla \phi|^2 + \mathbf{u}_\omega \cdot \nabla \phi + \frac{p - p_\omega}{\rho} \right) = -\nabla \phi \times \boldsymbol{\omega}. \quad (\text{IV.13})$$

This corresponds to assuming that the vortical flow field is not modified by the bubble flow, and that the pressure p_ω due to the vortex field is known beforehand. In that approximation, each field, \mathbf{u}_ω , or \mathbf{u}_b , was assumed to satisfy the momentum equation individually with separate pressure fields p_ω or $p_b (= p - p_\omega)$ associated with them. The right hand side in (IV.13) may be taken to be zero under certain special paths of integration, leading to a Bernoulli integral on the bubble surface

$$\Psi_0 \equiv \frac{\partial \phi}{\partial t} + \frac{1}{2} |\nabla \phi|^2 + \mathbf{u}_\omega \cdot \nabla \phi + \frac{p - p_\omega}{\rho} = \frac{p_\infty - p_\omega(\infty)}{\rho}, \quad (\text{IV.14})$$

where ∞ denotes the value far away. This provides an expression for $\partial \phi / \partial t$ which was used by [1] for updating the values of ϕ at the bubble surface. However the right-hand side of (IV.13) cannot be set to zero for integration of a general evolving vortical flow, and for an interacting vorticity the vortical pressure field p_ω is not generally definable. These issues are satisfactorily resolved here in the new coupled formulation by solving the additional Poisson equation for Ψ . In order to obtain Ψ we apply Green's identity to find

$$a\Psi(\mathbf{x}) = \int_S [\Psi(\mathbf{x}') \mathbf{n} \cdot \nabla' G(\mathbf{x}, \mathbf{x}') - \mathbf{n} \cdot \nabla' \Psi(\mathbf{x}') G(\mathbf{x}, \mathbf{x}')] dS(\mathbf{x}') + \int_D G(\mathbf{x}, \mathbf{x}') R(\mathbf{x}') dV(\mathbf{x}'). \quad (\text{IV.15})$$

Because the right hand side in (IV.11) gives rise to an additional volume term in the corresponding Green's identity (IV.15), Eq. (IV.11) cannot be solved using information only at the boundary and the regular BEM. This can be overcome by applying the so-called "dual reciprocity" boundary element method to solve these equations as shown below. Once we obtain Ψ and the pressure p on the bubble surface from the dynamic boundary condition [see (IV.17) below], (IV.10) provides an expression for $\partial\phi/\partial t$ there. Comparing with regular irrotational flows with free surfaces, we note that the solution for Ψ effectively achieves an integrates the momentum equation similar to arriving at the Bernoulli integral.

2.3 Boundary Conditions

The kinematic boundary condition on the free surface $S(\mathbf{x}) = 0$ is given by

$$\frac{DS}{Dt} = 0, \quad (\text{IV.16})$$

i.e., the points on the free boundary follow the fluid particles.

The dynamic boundary conditions are the balance of normal and tangential stress. In the examples presented below, the fluid motion inside the bubble is neglected. We have also neglected the viscous part of the normal stress which can be included in a straightforward manner. The pressure inside the bubble is then given by the sum of the vapor pressure p_v inside the bubble, and the non-condensable gas pressure p_g , assumed to change by a polytropic process (exponent k) with the bubble volume \mathcal{V} , $p_g \mathcal{V}^k = p_{g0} \mathcal{V}_0^k$ ([40]). The pressure balance at the interface can then be written as

$$p = p_i - \mathcal{C}\gamma = p_v + p_{g0} \left(\frac{\mathcal{V}_0}{\mathcal{V}} \right)^k - \mathcal{C}\gamma. \quad (\text{IV.17})$$

Here p_{g0} and \mathcal{V}_0 are the initial gas pressure and the volume of the bubble, p_i the internal pressure, γ the surface tension, and \mathcal{C} the local surface curvature. Here it was assumed that the internal pressure p_i is spatially uniform, that the time scale of the dynamics is fast enough so that the amount of non-condensable gas remains constant, and that vaporization occurs fast enough to keep the vapor pressure constant at its equilibrium value at the liquid ambient temperature.

3 Numerical Procedure

3.1 Vortex Element Method

The vortex element method starts by representing the vorticity in terms of vortex particles or blobs. As is well known, a point vortex method gives rise to an unbounded velocity when one particle comes close to another ([49], [47]). To remedy this situation [49] suggested a core function that desingularizes the velocity kernel by modifying the near field contribution of the particle. There have been several studies to prove convergence of such methods with various core functions; see [55] for a review. Here we apply the core function suggested by [56] and used among others

by [57] and [58]. The vorticity is discretized introducing overlapping vortex blobs f_Δ of spatial extent Δ at locations $\{\chi_i\}, i = 1, \dots, N$,

$$\omega(\mathbf{x}, t) = \sum_{i=1}^N \omega_i(t) dV_i(t) f_\Delta(\mathbf{x} - \chi_i). \quad (\text{IV.18})$$

If the distributed vortex blobs are aligned along lines as is the case for the examples presented below, we may use the fact that the volume of the blob $dV_i = d\mathbf{A}_i \cdot d\chi_i$, and rewrite (IV.18) as

$$\omega(\mathbf{x}, t) = \sum_{i=1}^N \Gamma_i(t) d\chi_i(t) f_\Delta(\mathbf{x} - \chi_i), \quad (\text{IV.19})$$

where

$$f_\Delta(r) = \frac{3}{4\pi\Delta^3} e^{-(r/\Delta)^3}, \quad (\text{IV.20})$$

$d\chi_i$ is length of the vortex element, $d\mathbf{A}_i$ its area, and $\Gamma_i = \omega_i \cdot d\mathbf{A}_i$ the circulation. Using the circulation Γ_i instead of ω_i eliminates the need for solving the vorticity transport equation (IV.7), if the liquid viscosity is neglected, and therefore when the circulation Γ_i of a fluid particle is conserved. The vortex particles move with the local fluid velocity. Therefore the vorticity dynamics is governed by the advective stretching of the element $d\chi_i$. The vector stream function \mathbf{A} may be found by applying the relation (IV.5). The vorticity induces the velocity field (IV.6), which after performing the volume integration analytically may be written as:

$$\mathbf{u}_\omega(\mathbf{x}, t) = \frac{1}{4\pi} \sum_{i=1}^N \Gamma_i \frac{d\chi_i \times (\mathbf{x} - \chi_i)}{|\mathbf{x} - \chi_i|^3} \kappa\left(\frac{|\mathbf{x} - \chi_i|}{\Delta}\right), \quad (\text{IV.21})$$

where

$$\kappa(r) = 1 - e^{-r^3}. \quad (\text{IV.22})$$

We use overlapping blobs (i.e., $\Delta > h$, h being the separation between neighboring particles) as this choice has been shown to achieve second order accuracy ([56], [55]).

3.2 Boundary Element Method

Discretization of the free surfaces by triangular elements, together with the BEM formulation (IV.3) for ϕ generates a set of linear equations relating ϕ and $\partial\phi/\partial n$ at the nodes,

$$\sum_j \left[A_{ij}(\mathbf{x}_i, \mathbf{x}'_j) \frac{\partial\phi}{\partial n}(\mathbf{x}'_j) - B_{ij}(\mathbf{x}_i, \mathbf{x}'_j) \phi(\mathbf{x}'_j) \right] = 0. \quad (\text{IV.23})$$

Here the functions ϕ and $\partial\phi/\partial n$ are linearly interpolated inside each panel using their values at the nodal points of the panel, namely the vertices of the triangle. A_{ij} and B_{ij} are geometry dependent matrices relating the ‘influence’ of the j -th node at the i -th node. They are obtained by analytically integrating the surface integral in (IV.3) over each panel separately. When the problem has only free surface boundaries as in the examples below, ϕ is known on the free surfaces,

and this set of equations is solved for $\partial\phi/\partial n$ at the boundary. If in addition solid boundaries are present, a mixed formulation is obtained where ϕ is known on the free surface and $\partial\phi/\partial n$ is known on the solid boundaries. The equations are then solved for $\partial\phi/\partial n$ on the free surface and for ϕ on the solid boundaries. The formulation was described in detail previously by [40], and [42].

3.3 Time Integration

The time evolution of the flow is governed by the boundary conditions. We may obtain the updated values of the velocity potential ϕ by integrating

$$\frac{D\phi}{Dt} = \frac{\partial\phi}{\partial t} + \mathbf{u} \cdot \nabla\phi = \Psi - \frac{1}{2}|\mathbf{u}|^2 - \frac{p}{\rho} + \mathbf{u} \cdot \nabla\phi, \quad (\text{IV.24})$$

where the material derivative is used as the surface moves with the fluid. Then, equation (IV.16) is integrated to determine the motion of the bubble surface nodes. The vortex elements follow the fluid velocity

$$\frac{d\chi_i}{dt} = \mathbf{u}(\chi_i, t), \quad (\text{IV.25})$$

while the circulation Γ_i of each element remains the same. These integrations are performed with an explicit Euler scheme. An adaptive time stepping is executed by making the time step proportional to the ratio of the smallest internodal distance to the largest nodal velocity over all nodes.

3.4 Solution of the Poisson Equation for Ψ

To update the nodal values of ϕ at the free surface at successive time steps by (IV.24) we need to solve (IV.11) for Ψ with the boundary condition (IV.12). We note that the inhomogeneity R in (IV.11) is “supported” on the vorticity ω , i.e., the two terms of R involve ω . This indicates that a similar discretization for R and ω may be sufficient to accurately describe their effects. We expand the term R in a way similar to that for ω in (IV.18) using the same core functions and with the same particle positions $\{\chi_i\}$, $i = 1, \dots, N$

$$R(\mathbf{x}) = \sum_{i=1}^N R_i f_\Delta(\mathbf{x} - \chi_i) = \sum_{i=1}^N R_i \nabla^2 g(\mathbf{x} - \chi_i), \quad (\text{IV.26})$$

where

$$\nabla^2 g = f_\Delta = \frac{3}{4\pi\Delta^3} e^{-(r/\Delta)^3}. \quad (\text{IV.27})$$

Upon integration of (IV.27), assuming g to be spherically symmetric (depending only on r) and regular at the origin we obtain the same expression that was used in the discretized Biot-Savart law (IV.21) for the vortex induced velocity

$$\frac{\partial g}{\partial r} = \frac{1}{4\pi r^2} \left(1 - e^{-(r/\Delta)^3} \right) = \frac{1}{4\pi r^2} \kappa \left(\frac{r}{\Delta} \right). \quad (\text{IV.28})$$

We then find the following analytical expression for g ,

$$g = -\frac{1}{4\pi r} \left[1 - e^{-(r/\Delta)^3} + \frac{r}{\Delta} \beta \left(\frac{2}{3}, \frac{r^3}{\Delta^3} \right) \right], \quad (\text{IV.29})$$

where $\beta(m, x)$ is the incomplete Gamma function:

$$\beta(m, x) = \int_x^\infty e^{-y} y^{m-1} dy, \quad m > 0. \quad (\text{IV.30})$$

The constant of integration is obtained by requiring that g vanish at infinity. Therefore the solution to (IV.11) may be written as

$$\begin{aligned} a\Psi(\mathbf{x}) &= \int_S \left[\Psi(\mathbf{x}') \mathbf{n} \cdot \nabla' G(\mathbf{x}, \mathbf{x}') - \mathbf{n} \cdot \nabla' \Psi(\mathbf{x}') G(\mathbf{x}, \mathbf{x}') \right] dS(\mathbf{x}') \\ &\quad + \sum_{i=1}^N R_i \int_D \nabla'^2 g(\mathbf{x}' - \boldsymbol{\chi}_i) G(\mathbf{x}, \mathbf{x}') dV(\mathbf{x}'). \end{aligned} \quad (\text{IV.31})$$

We know $\mathbf{n} \cdot \nabla \Psi(\mathbf{x}')$ from (IV.12). We may hence use this equation for finding $\Psi(\mathbf{x}')$. For the volume integral term, we perform integration by parts twice to obtain

$$\begin{aligned} \int_D \nabla'^2 g(\mathbf{x}' - \boldsymbol{\chi}_i) G(\mathbf{x}, \mathbf{x}') dV(\mathbf{x}') &= ag(\mathbf{x} - \boldsymbol{\chi}_i) \\ &\quad - \int_S \left[g(\mathbf{x}' - \boldsymbol{\chi}_i) \mathbf{n} \cdot \nabla' G(\mathbf{x}, \mathbf{x}') - \mathbf{n} \cdot \nabla' g(\mathbf{x}' - \boldsymbol{\chi}_i) G(\mathbf{x}, \mathbf{x}') \right] dS(\mathbf{x}'), \end{aligned} \quad (\text{IV.32})$$

where

$$\nabla g(\mathbf{x} - \boldsymbol{\chi}_i) = \frac{\partial g}{\partial r_i} \frac{\mathbf{x} - \boldsymbol{\chi}_i}{r_i}, \quad r_i = |\mathbf{x} - \boldsymbol{\chi}_i|. \quad (\text{IV.33})$$

We have thus converted the volume integral into integrals over the surface bounding the domain, here the bubble surface. By collecting similar terms together, it may be seen that using the expansion (IV.26) the Poisson equation (IV.11) has been transformed into the following Laplace equation:

$$\nabla^2 \left[\Psi(\mathbf{x}) - \sum_i R_i g(\mathbf{x} - \boldsymbol{\chi}_i) \right] = 0. \quad (\text{IV.34})$$

Green's identity now involves only the usual surface integrals as in (IV.3). Essentially this is the underlying principle of the dual reciprocity method [54], where basis functions satisfying the relation (IV.27) are applied to solve a Poisson equation by the boundary element method. (Incidentally one could interpret the vortex element method as being based on the same principle which solves the Poisson equation (IV.5) representing the vorticity by the particle core functions.) Now we may use a BEM scheme similar to that for ϕ , and obtain an expression for the field Ψ analogous to (IV.23). The matrix elements A_{ij} , B_{ij} depend only on the geometry, and hence they are the same as before. Also, since we used the same functions g as for the vortex method,

these functions need to be evaluated only once every time step. This makes the present scheme attractive, as it uses the BEM and VEM in an efficient complementary manner.

It is to be noted that the above formulation including the expansion (IV.26) with the coefficients $\{R_i\}$ is implemented at every time step. Our attempts to determine the coefficients by evaluating $R(\mathbf{x})$ at N particle centers $\{\chi_i\}$, and solving a linear system of equations for $\{R_i\}$ (see the method for determining $\{\Gamma_i\}$ in the following section) were not successful to date, and resulted in an ill-conditioned matrix. Therefore we applied the following approximate way to obtain the coefficients. The function $R(\mathbf{x})$ may be written as

$$R(\mathbf{x}) = \int R(\chi) \delta(\mathbf{x} - \chi) dV(\chi) \approx \sum_{i=1}^N R(\chi_i) dV(\chi_i) \delta(\mathbf{x} - \chi_i), \quad (\text{IV.35})$$

giving $R_i(t) = R(\chi_i, t) dV_i$, where we have used the fact that the blob function $f_\Delta(\mathbf{x} - \chi)$ is a smoothed Dirac delta function $\delta(\mathbf{x} - \chi)$, i.e.,

$$\lim_{\Delta \rightarrow 0} f_\Delta(\mathbf{x} - \chi) \rightarrow \delta(\mathbf{x} - \chi). \quad (\text{IV.36})$$

Such approximations have been made in vortex element applications for determining the strengths of the elements (see the discussion in [57]).

To reemphasize the generality of our approach we note that for a viscous implementation, this part of the algorithm involving the normal stress condition at a free boundary would remain largely unchanged. We believe that this mathematical formulation in terms of the Poisson problem is crucial for a full coupling of the potential and the vortical parts of the flow field. More specifically, for a viscous simulation the solution of the vorticity transport equation (IV.7) would have to be implemented in full, as the particle circulation is not conserved. This part has been discussed in detail by various authors and several schemes are available ([50]& [51]; [52] & [53]). However, the Poisson problem for the dynamic pressure Ψ will change only so far as the viscous term in the boundary condition (IV.12) has to be taken into account. It may be computed directly at little extra cost. The dynamic boundary condition will have two parts. The existing pressure condition (IV.17) will be replaced by a normal stress condition where the normal viscous stress has to be added to the fluid part of the equation. The tangential stress condition in the present case, with the motion inside the bubble neglected, will give rise to zero stress on the fluid side. Imposing this condition will necessitate generation of fresh vorticity from the bubble surface, as in [60]. As the vortex fields of interest considered here are relatively large scale structures. e.g., propeller tip vortex, boundary layer hair-pin vortex, or other coherent structures, where the inertial forces dominate the flow and hence fluid viscosity has been justifiably neglected.

4 Numerical Examples

In the following, the method developed is applied to study the interactions between a bubble and the flow fields of a column vortex and of a vortex ring. For each of these cases we performed computations with different discretizations to ensure convergence.

4.1 Bubble Dynamics in a Columnar Vortex

The dynamics of a bubble entrapped in a column vortex can be considered as a simplified model of a cavitation nucleus in the core of a tip vortex (e.g., of a propeller).

Numerical Details

We discretize the column vortex, with initially circular cross-section, as a distribution of line vortices in its core. On each line the vortex elements are distributed equi-spaced along the line. The vorticity distribution, ω_x is chosen to be Gaussian in the cross-sectional plane of the column

$$\omega_x = \frac{\Gamma}{\pi\sigma^2} e^{-(\xi/\sigma)^2}, \quad (\text{IV.37})$$

where ξ is the radial distance from the column vortex axis in the cross-sectional plane, and σ is the physical viscous core of the vortex column (not to be confused with the core Δ , in Eq. (IV.20), of the vortex elements). The total circulation for the column is Γ . The vortex elements on the same line will be of the same circulation Γ_k and

$$\Gamma = \sum \Gamma_k, \quad (\text{IV.38})$$

where the summation is over all the line vortices. The initial discretization is done by choosing the line vortices to be placed in the cross-sectional plane in circular arrays following [57], (see Figure IV.1).

The Γ_k 's are found by solving a set of linear equations, that is obtained by imposing that the vorticity is correctly represented at the vortex nodes according to (IV.18). This procedure is iterated by varying the core radii Δ so that the total circulation value Γ is correctly represented by (IV.38). We also ensure that the particle overlap condition $\Delta > h$ is satisfied, where h is the maximum distance between neighboring particles either along a given line or between two lines. The line vortices, in this case, are extended to infinity in both directions, and the discrete vortex elements are placed only on a finite extent of these infinite lines. This is justified since in reality the vortex lines deviate from being straight only near the bubble. The contribution of the rectilinear vortex lines extending to infinity are computed analytically and added to the contribution of the discrete vortex points. The bubble surface is discretized by triangular elements as described in [40].

Convergence Study

We have chosen an example case of an initial bubble radius of $10 \mu\text{m}$ in a liquid at atmospheric pressure placed in a vortex column. The core of the column $\sigma = 120 \mu\text{m}$. The initial gas pressure inside the bubble $p_{g0} = 5 \times 10^6 \text{ Pa}$, i.e., initial pressure inside the bubble is fifty times the pressure at infinity, P_∞ , and the circulation of the vortex is $0.0015 \text{ m}^2/\text{sec}$. The bubble is initially off-center and located at a distance of $30 \mu\text{m}$ from the center of the column. Figure IV.1 (a) shows the geometry and its discretization, IV.1(b) shows the geometry of the discretized problem at the cross-sectional plane, normal to the column axis and going through the bubble center, and IV.1(c) shows the geometry of the discretized bubble and column at a later time.

The vortex core is discretized, with a single line at the center of the vortex column and a set of circular arrays of line vortices around it. In the cases considered we typically used two circular arrays with 6 and 12 lines, i.e., 19 line vortices in total to represent the column core. Forty vortex elements and two semi-infinite line vortices are used for each line. To reduce the size of the numerical problem advantage is taken of the plane of symmetry that is perpendicular to the line vortices. The bubble is discretized with 41 nodes and 64 panels above the symmetry plane. Extensive convergence results for the boundary element method used have been presented in [42], and [43].

The bubble expands due to the large pressure inside it, exceeds the equilibrium size, and then collapses back towards its initial volume while interacting with the vortex column. A convergence study is performed by varying the number of elements along a line and the number of line vortices used to represent the vortex core. Figure IV.2 shows the bubble equivalent radius R_{eq} (of the sphere giving the same volume) with time. The radius was normalized by the initial bubble radius, R_o , while time was normalized by the Rayleigh time, given by $R_o/\sqrt{p_\infty/\rho}$. The dotted line is the case with 7 vortex lines (1 at the center and 6 in a circular array), and the solid line is that with 19 lines. For the geometry considered here with the bubble inside the core of the vortex the bubble dynamics is strongly coupled with and determined by the spatial vorticity distribution in the column core. Therefore it is expected that a 1 line representation of the column vortex would not be able to represent the bubble collapse. This is shown by the dashed line representing a single vortex line representation, where the bubble experienced unbounded growth. Very close results are seen between the cases with 7 and 19 vortex lines. For studying convergence with varying number of elements along a vortex line, cases were run with 19 vortex lines and 40, 20, and 10 elements in a single line. The results coincide with each other, and are therefore not shown.

Description of the Interaction Between a Bubble and a Vortex Column

Figure IV.3 displays for the same bubble and vortex flow conditions as in Figure IV.2, the time evolution of the bubble shape, and the trace of the line vortices in the plane of symmetry of the problem passing through the center of the bubble. In absence of the bubble the line vortices move around the central line at a fixed velocity dependent on the radial distance. In presence of the oscillating bubble, these circular trajectories are distorted by the bubble growth and collapse indicating one effect of the bubble dynamics on the underlying flow field. The bubble is seen to grow to an oblong shape elongated towards the center of the vortex column where the pressure is the lowest (Figure IV.3a). During collapse (Figure IV.3b), as often is the case with unsteady bubble dynamics ([3], [34]), the part of the bubble that moved the farthest during the growth, forms a reentrant jet during the collapse that moves faster than the rest of the bubble nodes and penetrates the bubble.

The vorticity field is perturbed by the bubble dynamics, with the vortex lines (and the vorticity) pushed away from the bubble during the growth and pulled by it during collapse. This results in non-circular motion of the vortices during the dynamics. These observations are qualitatively similar to those obtained when one-way interactions, namely that of the vortex field on the bubble dynamics, are accounted for ([1]). A vorticity contour plot (component normal to the plane of the cross-section) and the vorticity induced velocity vectors \mathbf{u}_ω (components in the cross-sectional plane) are plotted in Figure IV.4 at six different times, three during growth and three during

collapse. This figure shows that in this case the overall basic flow (vorticity and induced velocity) is little affected in a global sense by the bubble dynamics. A closer look at the change in these quantities shows, however, a different picture.

To bring out the significance of the bubble's presence in the flow field, Figure IV.5 shows the change in the vorticity and in the vortical velocity fields due to the bubble (i.e., the difference in the computed fields with the bubble and without it). We see that near the bubble the vorticity has decreased by as much as 5 % compared to the case without the bubble (shows a negative component in the plot), and that farther away the opposite has happened. This could be expected as the bubble motion moves the vortical fluid away from it. Because of the position of the bubble off-center and in the lower half of the vortex core, its presence and dynamics appear also to have modified the vortical component of the velocity in a fashion leading to the superposition to the basic columnar vortex of two weaker column vortices of opposite signs. This is illustrated by the positive vorticity represented by the yellow color, which has a top-down asymmetry, and appears clearest in the last two frames during the bubble collapse where the secondary vortex structure is clearly visible. It is seen to be rotating in a clock-wise direction, i.e., opposite to the original column. Apart from continual modification of the vortex field by the interacting bubble this result suggests that the bubble could trigger secondary vortex generation by initiating asymmetry in the vorticity field.

To further examine the change in the vorticity field, the normal component of the vorticity along a straight line going through the centers of the bubble and vortex columns at different times is plotted in Figure IV.6. The bubble traces are shown for the corresponding times. The solid, dotted and dashed lines are during growth. The dash and dotted, solid with squares, and dotted with stars lines are during collapse. They are at the same times as in Figure IV.4 and in the same sequence. As expected the vorticity is pushed away from the bubble as the bubble grows and then pulled back into the original configuration as the bubble collapses. Figure IV.7 displays the difference in the vorticity with and without the bubble along the same center line using the same line types as in Figure IV.6. Here we clearly see that the decreases near the bubble during its growth and comes back up during collapse, while a compensating opposite effect is seen away from the bubble.

Analysis of the pressure field shows an overall decrease in pressure during bubble growth and then a large increase during bubble collapse. The pressure field due to the bubble dominates during the violent bubble collapse. It is known that such high pressures associated with cavitation are responsible for damage to nearby solid bodies such as propeller blades.

Parametric Study

To perform a parametric study of the interaction between a bubble and a column vortex we must determine a consistent set of non-dimensional parameters characterizing the motion. In order to do so the bubble dynamics length and time scales are determined using the oscillation of a spherical bubble with the same bubble initial conditions and placed in a quiescent fluid at a pressure corresponding to that in the vortex flow field at the location of the bubble center. This leads to a length scale given by a maximum radius, R_{\max} , and to a time scale given by the Rayleigh time, τ_R , which is the time needed for an empty bubble to collapse from the radius R_{\max} to 0, under the influence of the pressure outside the bubble (Rayleigh 1918).

The flow field in the core of the vortex may be approximated as a solid body rotation, with a core radius R_c , and the same circulation as the discretized vortex. The pressure field inside the vortex core is known as ([1])

$$\bar{p}(\bar{r}) = 1 - \Omega (2 - \bar{r}^2); \quad \frac{\partial \bar{p}}{\partial \bar{r}} = 2\Omega \bar{r}; \quad \bar{r} \leq 1, \quad (\text{IV.39})$$

with

$$\bar{r} = \frac{r}{R_c}; \quad \bar{p}(\bar{r}) = \frac{p(r)}{p_\infty}. \quad (\text{IV.40})$$

and Ω the “swirl parameter”, defined as

$$\Omega = \frac{\frac{1}{2}\rho(\frac{\Gamma}{2\pi R_c})^2}{p_\infty}, \quad (\text{IV.41})$$

which characterizes the intensity of the pressure drop due to the rotation relative to the ambient pressure, p_∞ . Note that the pressure on the vortex axis is $(1 - 2\Omega)$ and goes to zero when Ω approaches 1/2. We define the pressure drop parameter \mathcal{P} as the relative drop in the pressure from the ambient, so that

$$\mathcal{P} = \Omega (2 - \bar{r}^2), \quad (\text{IV.42})$$

and the Rayleigh time is then:

$$\tau_R = R_{\max} \sqrt{\frac{\rho}{p_\infty (1 - \mathcal{P})}}. \quad (\text{IV.43})$$

If a bubble is subjected to such a pressure field, it will experience a higher liquid pressure on its side away from the vortex center than on its side closer to the vortex center, the difference being greater the larger the bubble is. The effect of this pressure difference is to cause the bubble to migrate towards the vortex center. Additionally the bubble is ‘sheared’ since different locations on its surface experience different fluid velocities. As we have seen in the previous section this results in bubble shape deviation from sphericity. The importance of this deviation is a function of the relative orders of magnitude of the pressure gradient, the bubble wall acceleration due to volume change, and surface tension forces.

Results: As the pressure drop parameter, \mathcal{P} , is increased the bubble is in a stronger vortex field, and is entrained further in the vortex. Significant departure from the Rayleigh Plesset behavior is seen, and the bubble deforms and grows further. Figure IV.8 compares the effects of modifying the pressure drop parameter \mathcal{P} by considering 3 different values of the parameter. The bubble equivalent radius is scaled on the Rayleigh-Plesset maximum radius, and the time is normalized with the corresponding Rayleigh time. The effect of increasing \mathcal{P} is seen to cause a slight increase in the maximum radius achieved, and a much larger increase in the bubble period (time to first collapse). This can be explained by considering the fact that the bubble now undergoes motion in the vortical flow-field. Since the collapse occurs on the side of the bubble closer to the center, the collapse speed is reduced the higher \mathcal{P} is, or the lower is the pressure on the reentrant jet side. This fact is demonstrated in Figure IV.9 which presents the scaled bubble cross-sections

in the plane of symmetry. As can be seen the increase in \mathcal{P} is also accompanied by an increase in rotation of the bubble free surface points, and an increased asymmetry in the bubble collapse profile. As we have seen in Figure IV.3, the motion of the bubble significantly affects the motion of the vortex elements. In the last row of Figure IV.9 we show a case where the pressure drop parameter is very large ($\mathcal{P} = 0.8295$). In this case the bubble undergoes significant rotation, and collapses in a highly distorted fashion.

Figure IV.10 shows the influence of the parameter \mathcal{P} on the out of plane vorticity (ω_x) and the in-plane velocities (u_y and u_z) for the cases in Figure IV.9. Here the line vortex is parallel to the x axis, and the bubble is along the y axis, so that initially the velocity u_z is zero. The figure shows these quantities at three different times (corresponding to an initial stage, bubble maximum volume, and the collapse stage). The asymmetry in the bubble shape is directly related to the velocity field induced in the plane. The figures also show contours of the bubble shape at the corresponding time. The maximum vorticity is seen to be reduced further when \mathcal{P} increases during the bubble growth and recovers to its original value following collapse. Deformation of the vortex element by the bubble growth and motion cause a marked change in the vortical velocity field. During bubble growth the change in u_y is positive all along y , while during collapse the shape of the curve is very much affected by the bubble deformation and again reflects the creation of a secondary vortex field. This effect is seen to increase with increasing rotation.

We next present some results on the effects of the variation in the bubble over-pressure p_{g0} normalized by the ambient pressure. Figure IV.11 presents a comparison of the nondimensionalized equivalent bubble radius with time. Increasing the initial bubble overpressure causes the bubble collapse to be sharper. This quicker collapse has an influence on the instant at which the jet formed in the bubble reaches the other side. Contours of bubble growth and collapse for the three cases are shown in Figure IV.12. In the case with the highest pressure the bubble becomes multiply connected at an instant close to the minimum volume of the bubble. In the case with the lowest bubble over-pressure the jet does not reach the other side until the bubble has begun a rebound.

4.2 Bubble Dynamics in a Vortex Ring

A second illustrative example considered is a bubble growing and collapsing in the flow field of a vortex ring. The vorticity distribution in a cross-sectional plane of the ring is given by the same function (IV.37), similar to the column. The vortex discretization is also similar to the column, except that the lines close on themselves. The values of the circulation for each line are obtained by solving a linear system and ensuring that the total circulation is recovered.

Figure IV.13 shows the bubble placed near the ring but outside its core at a distance of 150 μm from the core center. The bubble size is 10 μm , the radius of the ring is 80 μm , whereas the radius of the core of the ring is 30 μm . The circulation is 0.00045 m^2/sec , $P_\infty = 10^5 \text{ Pa}$ and $p_{g0} = 5 \times 10^6 \text{ Pa}$. The ring core is discretized similar to the columnar case with 19 lines vortices. Each line has 40 elements. The bubble is discretized with 66 nodes and 128 panels.

Convergence

In Figure IV.14, we show a convergence study for the discretization of the ring core with 1 (dashed), 7 (dotted), 19 (solid) and 37 (1+6+12+18) line ring vortices (dash-and-dotted) by plotting the equivalent bubble radius R_{eq} nondimensionalized with the initial bubble radius versus time. Fast convergence is seen already while using 7 lines instead of one. Figure IV.15 shows the effects of varying the number of elements along one ring line. We compared the case of the 40 elements with 20 and 100 elements along a line with satisfactory convergence. The cases with 40 (dotted) and 100 elements (solid) coincide, while the one with 20 elements slightly overpredicts the bubble volume.

Description of the Interaction Between a Bubble and a Vortex Ring

Figure IV.16 a and b show in a cross-sectional plane the growth and collapse of the bubble, for the case of Figure IV.13. The movement of the vortex elements in the plane is also shown. During growth, the vortex ring pulls the bubble into a teardrop shape as the ring itself executes its translational motion. This shape is very similar to our experimental observations of the interaction of a spark generated bubble with a travelling vortex ring ([1]), reproduced here in Figure IV.17. During the collapse phase the bubble starts forming re-entering regions. The most extended parts of the bubble form two jets which cut the bubble in two along the trajectory lines as observed experimentally.

Figure IV.18 shows the vorticity field and the induced vortical velocity \mathbf{u}_ω vectors at six different times during growth and collapse. Figure IV.19 shows the difference in the same quantities, namely vorticity and vortical velocity with the bubble and without. As expected the arm of the ring nearer to the bubble is seen to undergo substantial change in its vorticity field. In this region formation of a secondary vortex is clear from the vortical velocity vector plots. Depletion of negative vorticity near the bubble and corresponding enhancement away from the bubble is clearly visible. Here again, one observes the superposition to the basic vortex ring of two ring vortices of opposite signs. Furthermore it is seen that the difference is more pronounced at later times. This is expected as the translational motion of the ring will be cumulatively affected by the bubble.

Parametric Study

The non-dimensional parameters for the bubble dynamics in the vortex ring are obtained by assuming that outside the viscous core, the behavior of the ring may be approximated by that of a potential vortex ring with the same circulation. As before we choose for the length scale the maximum radius the bubble would achieve when subjected in a quiescent liquid to the same pressure, and for the time scale the corresponding Rayleigh time, τ_R . In the cases considered below the bubble is outside the core of the vortex. The velocity potential due to a vortex ring of intensity Γ is given by ([62])

$$\phi^r(r, x) = \text{sgn}(X_0 - x) \frac{\Gamma A_0}{2} \int_0^\infty [\exp(-k|X_0 - x|) J_0(kr) J_1(kA_0)] dk, \quad (\text{IV.44})$$

where, J 's are the Bessel functions, x is the coordinate perpendicular to the plane of the ring, r is the radial coordinate in the plane of the ring, X_0 denotes the x -coordinate of the ring on the axis

of the symmetry, and A_0 denotes the radius of the ring. Calculating the velocities induced at the bubble location, evaluating $\partial\phi^r/\partial t$, and substituting in the Bernoulli equation we can calculate the ambient pressure at the location of the bubble. This pressure is used to compute R_{\max} and the time, τ_R , scale using Eq. (IV.43).

Figure IV.20 shows the effect of varying the pressure drop parameter on the bubble equivalent radius variation with time. Compared to the case of the vortex column, the data for different values of \mathcal{P} scale less well with the Rayleigh non-dimensionalization. We ascribe this to the fact that the pressure and the flow experienced by the bubble changes much more in this case due to the motion of the ring, and the associated flow field.

In Figure IV.21 and IV.22 we present a comparison of the bubble behavior for different initial bubble over-pressure. As the over-pressure increases the bubble collapses in a more violent fashion, and the bubble period is reduced. As shown in Figure IV.22, the bubble gets more distorted at collapse, and the jet gets more pronounced and occurs earlier in the cycle.

Next we consider one case of a bubble inside the core of the vortex ring. The ring geometry and the strength are the same as before. The bubble is made smaller $R_0 = 1 \mu\text{m}$, and the inside gas pressure $p_{g0} = 7.0 \times 10^6 \text{ Pa}$, and is placed inside the left arm of the vortex ring at a distance of $5 \mu\text{m}$ from the center of the section. The growth and the collapse phases in the cross-sectional planes are plotted in Figure IV.23. As expected, the dynamics is very similar to the bubble inside the vortex column, the only difference coming from the curvature of the vortex lines in the ring without formation of a strong reentrant jet. The bubble after executing the collapse shown in the Figure IV.23 (b) started a second growth phase without formation of a re-entering jet. Finally Figure IV.24 shows the modification of the vorticity field and the vertical velocity field due to the presence of the bubble.

5 Summary and Discussions

The boundary element method has been coupled with the vortex element method to handle rotational flow fields containing deformable bubbles. This method accounts for the modification of the vorticity field by the bubbles. The coupling between the two methods is obtained by solving a Poisson equation for the pressure. The Poisson solution is attained efficiently by using a dual reciprocity boundary element method using the same BEM matrix coefficients as those for the velocity potentials, and the same vortex core functions as those used as dual reciprocity basis functions.

The method developed was applied to the cases of a bubble in the field of a column vortex and a vortex ring. The shapes of the bubble during growth and collapse, as well as the evolution of the velocity and vorticity were computed. The analysis has shown that bubble growth and collapse is significantly affected by the presence of the vortical field. The bubble elongates in the direction of the vortex center (direction of lower pressure) and then collapses with a reentrant jet that initiates from the vortex center side and advances through the bubble to the outside of the vortex region. This effect is stronger with increasing vortex circulation and increasing initial gas pressure. Increasing the circulation also has the effect of increasing the bubble rotation in the vortex field and therefore enhances bubble shape distortion. The vortical field is also very much affected in the neighborhood of the bubble. Vorticity is pushed away during bubble growth, and

then sucked in during bubble collapse. In addition the asymmetric flow due to the reentrant jet formation results in the redistribution of the vorticity and its concentration in the reentrant jet region. Including the effect of the bubble on the underlying flow field, which was not previously done, is shown to be relevant in the cases considered. This underscores the need for accurate modeling of *two-way interactions* between bubbles and the flow field in future efforts to describe bubbly flows.

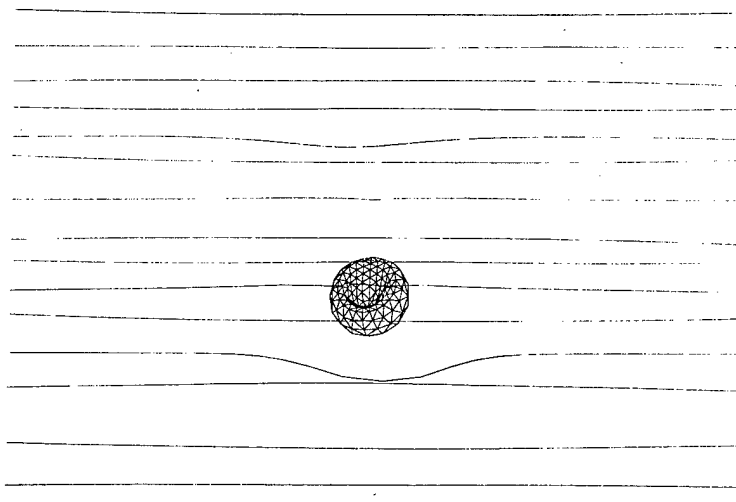
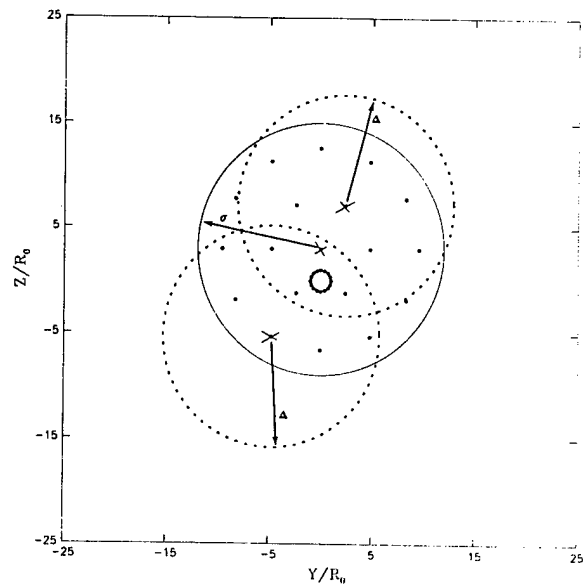
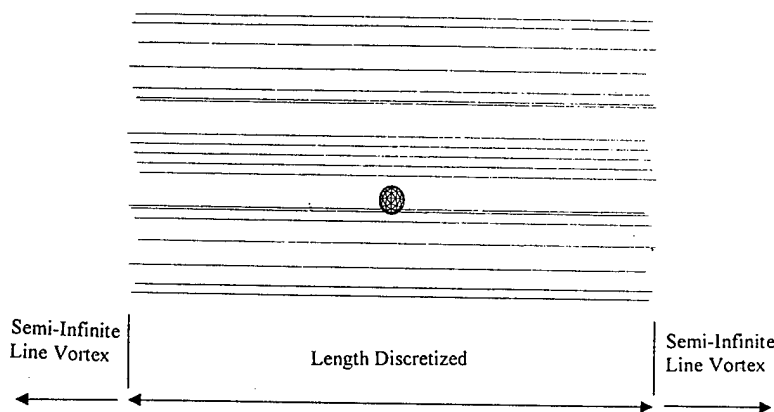


Figure IV.1: a) Geometry of the discretized bubble and column vortex. b) Plot at a cross-sectional plane through the bubble center, the dotted lines represent the core Δ of the cross-marked vortices. c) Geometry of the discretized bubble and column at a later time.

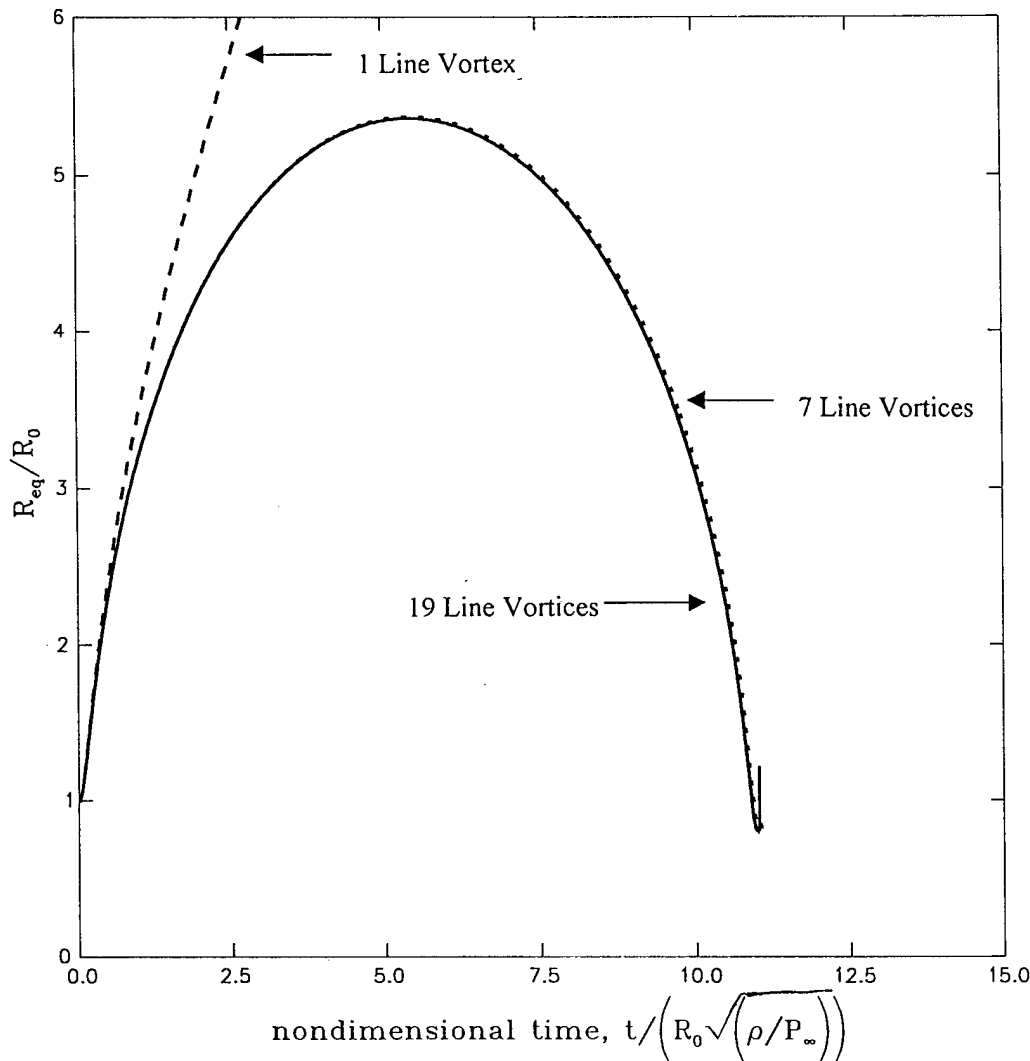


Figure IV.2: Convergence study for different discretization of the core of the vortex column. Time evolution of the equivalent bubble radius R_{eq} for three discretization schemes with 1 line (dashed), 7 line vortices (dotted), 19 line vortices (solid). The curves for different number of elements along a vortex line (10,20 or 40) coincided with each other. Initial bubble radius: $10 \mu\text{m}$, column core radius: $120 \mu\text{m}$, $p_{g0}=5\times 10^6 \text{ Pa}$, $P_\infty = 10^5 \text{ Pa}$, and $\Gamma=0.0015 \text{ m}^2/\text{sec}$.

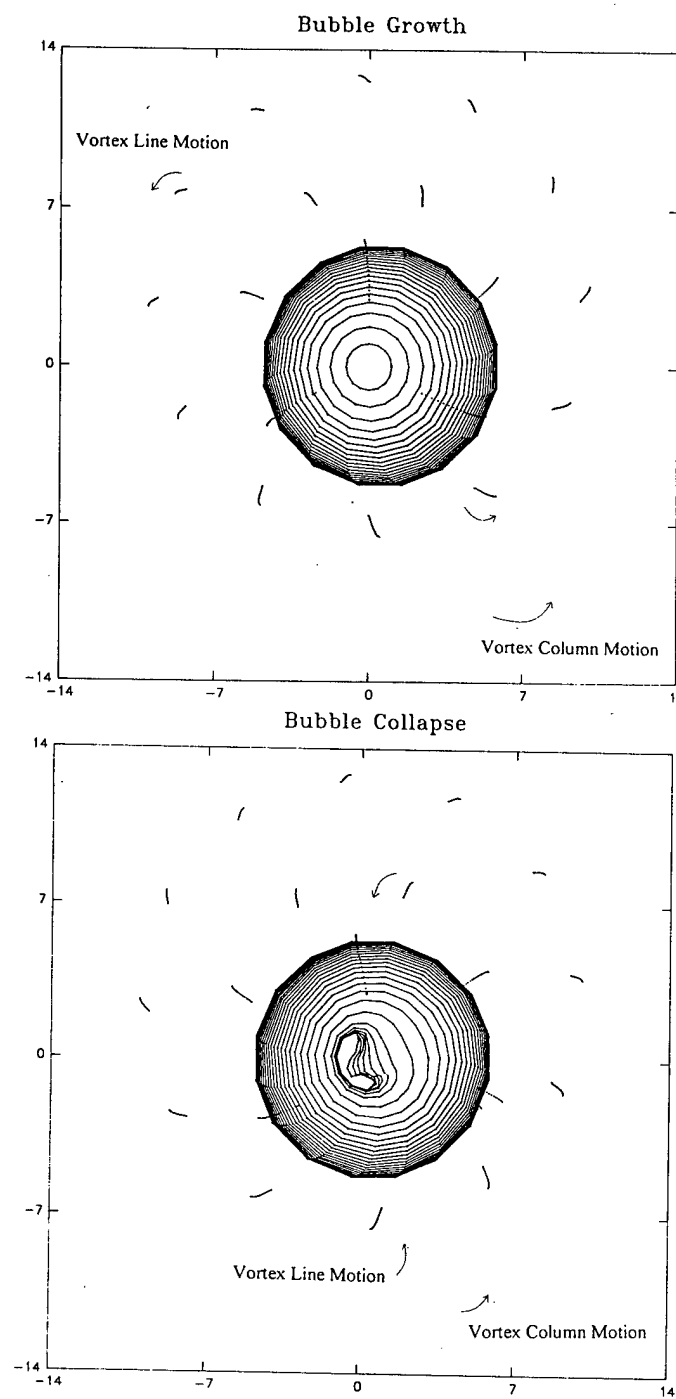


Figure IV.3: Growth (a) and collapse (b) of the bubble in a columnar vortex for the conditions of Figure 2. Time evolution of bubble cross-sections and traces of the vortex lines in the plane of symmetry perpendicular to the vortex axis. The vortex lines move outward during growth, and inward during collapse in an anti-clockwise manner.

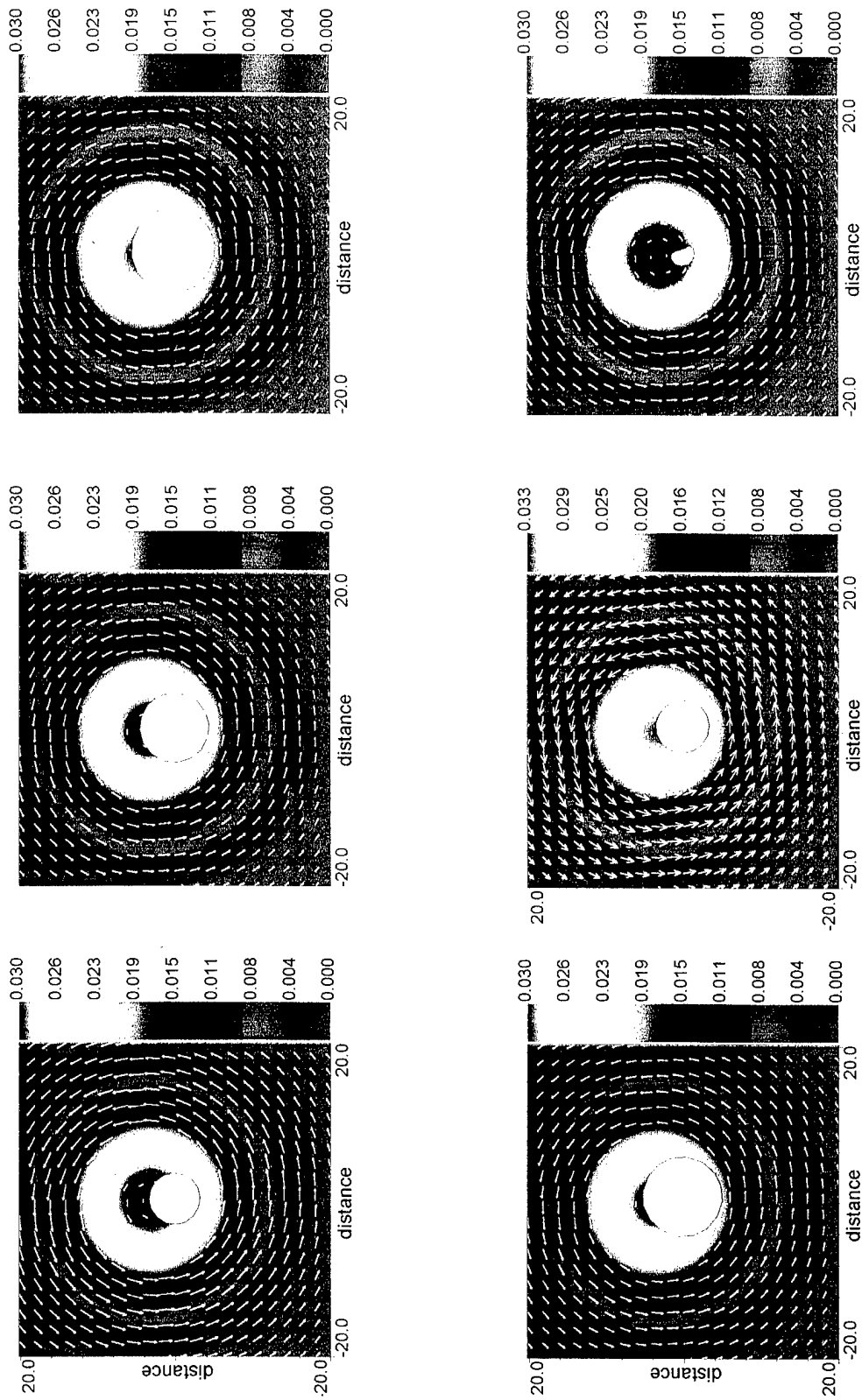


Figure IV.4: The vorticity field ω normal to the plane and the induced vortical velocity vectors \mathbf{u}_ω , i.e., $\mathbf{u} - \mathbf{u}_b$ in a cross-sectional plane at six different times, three during growth at $t=1.03, 2.28, 4.79$, and three during collapse at $t=7.29, 9.78, 10.79$. The conditions are the same as in Figure 2 and 3.

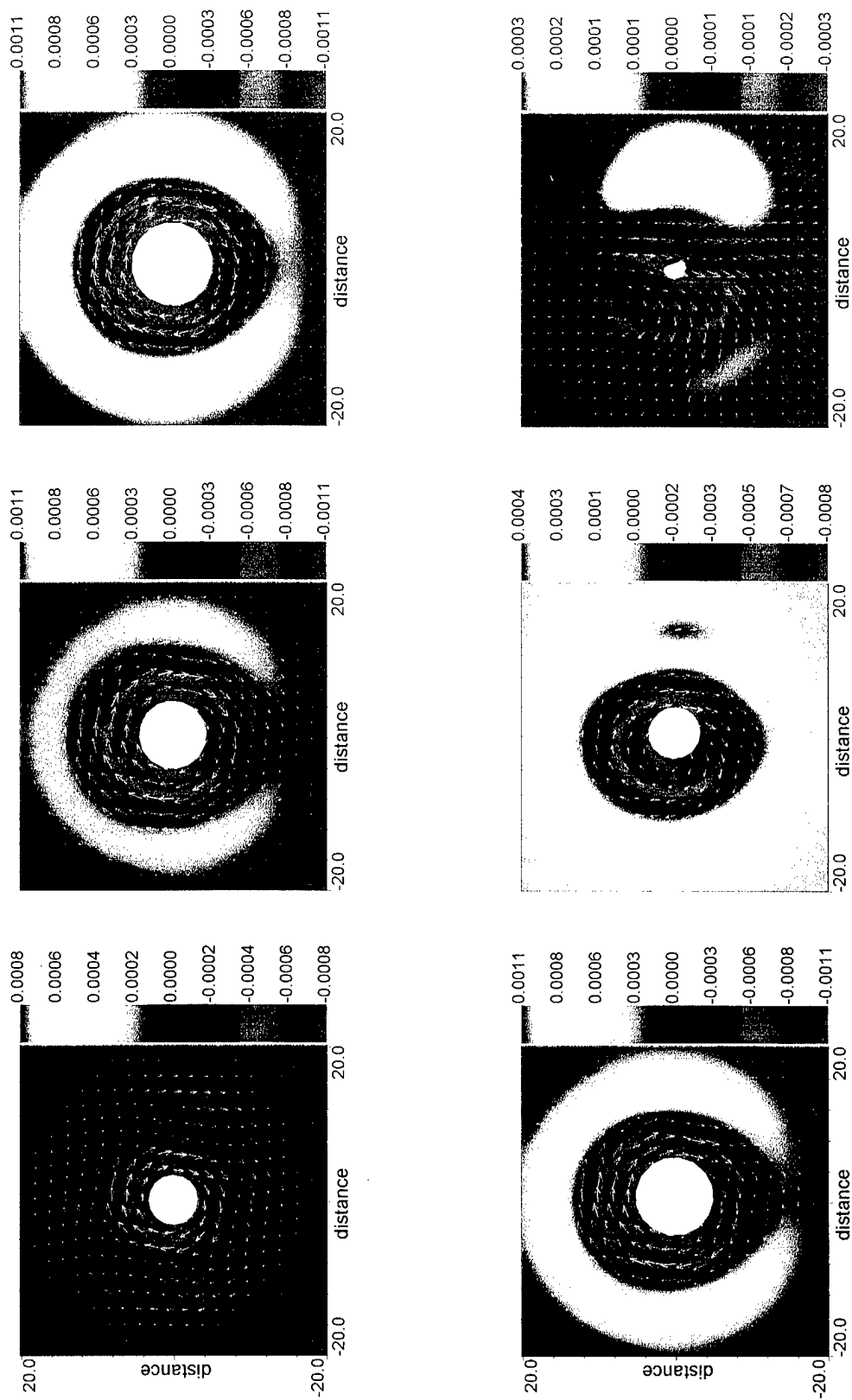


Figure IV.5: The difference in the normal component of the vorticity field ω and in the vortical velocity vectors \mathbf{u}_ω with and without the bubble at the same times and the same cross-sectional plane as in Figure 4.

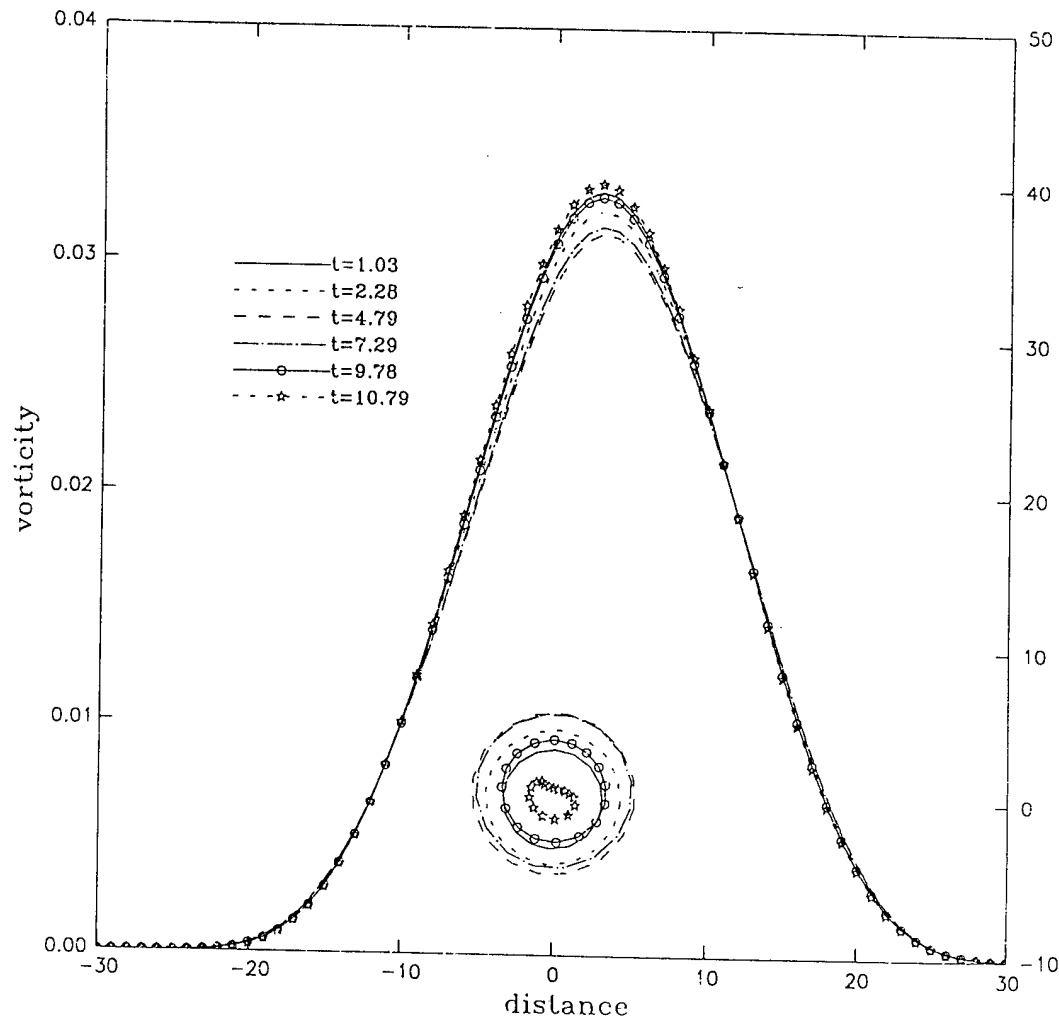


Figure IV.6: The normal component of the vorticity ω along a straight line going through the centers of the bubble and the column core at the same times as in Figure 4. The traces of the bubble at those times are also shown.

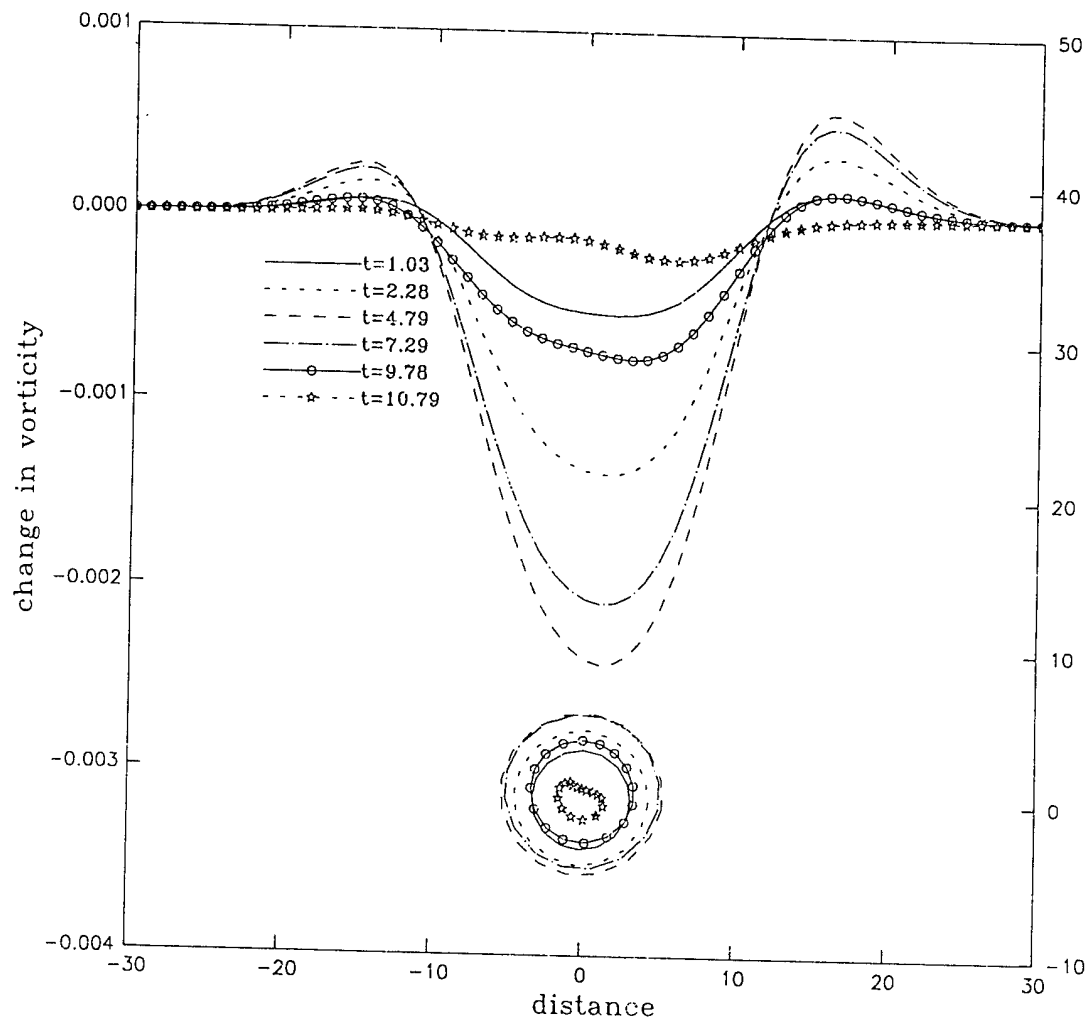


Figure IV.7: The difference in the normal component of the vorticity field ω along the same line as in Figure 6 with and without the bubble.

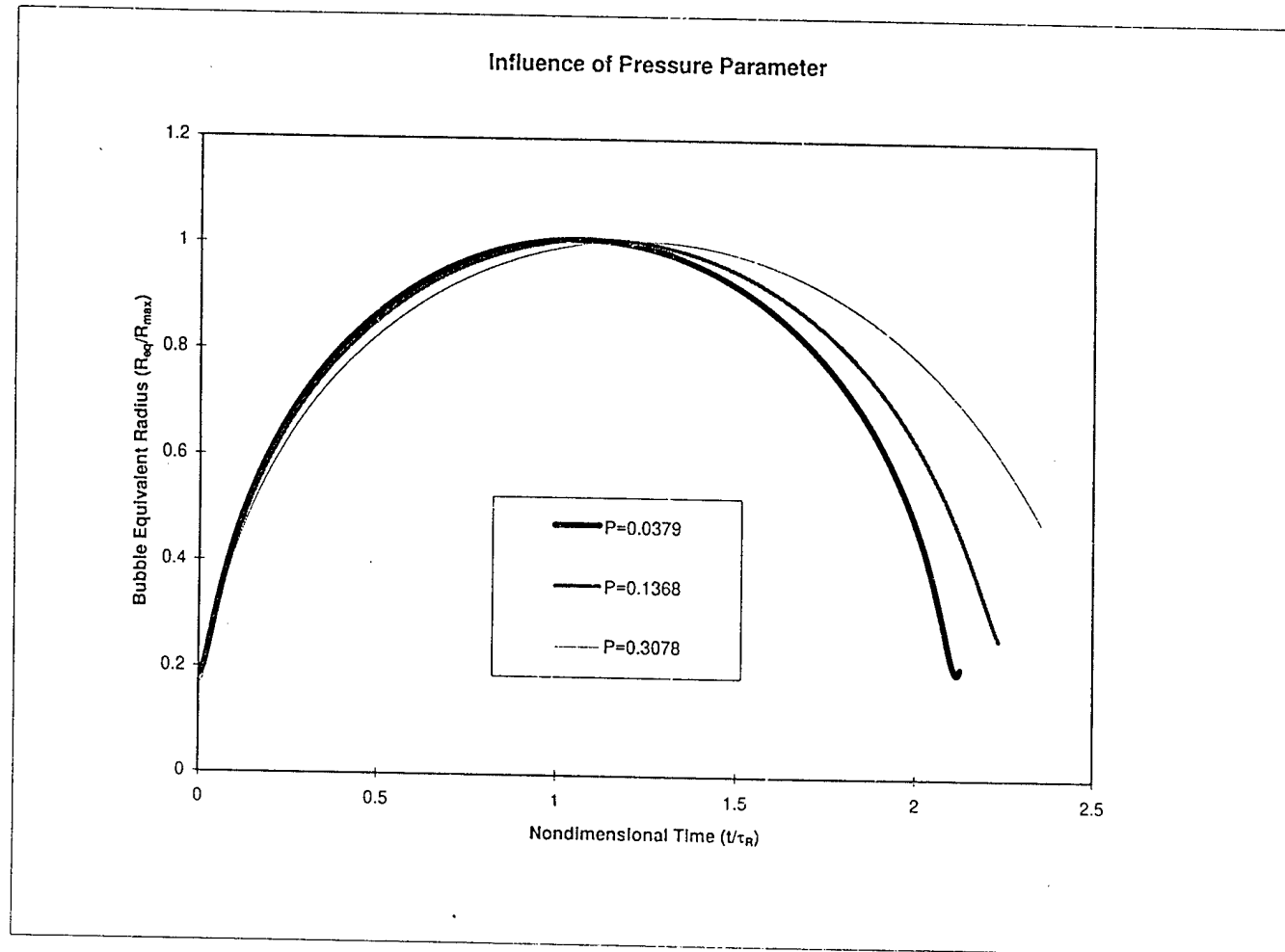


Figure IV.8: Study of the evolution of the non-dimensionalized equivalent bubble radius, R_{eq}/R_{max} , for several values of the pressure drop parameter \mathcal{P} . In each case the bubble initial radius $10 \mu\text{m}$, and the initial gas pressure is $4.742 \times 10^6 \text{ Pa}$, the pressure at infinity is 10^5 Pa , and the bubble is placed $60 \mu\text{m}$ away from the center of a vortex of core size $120 \mu\text{m}$. The circulation, Γ , for the three cases is 0.0015 , 0.003 , and $0.0045 \text{ m}^2/\text{s}$ respectively.

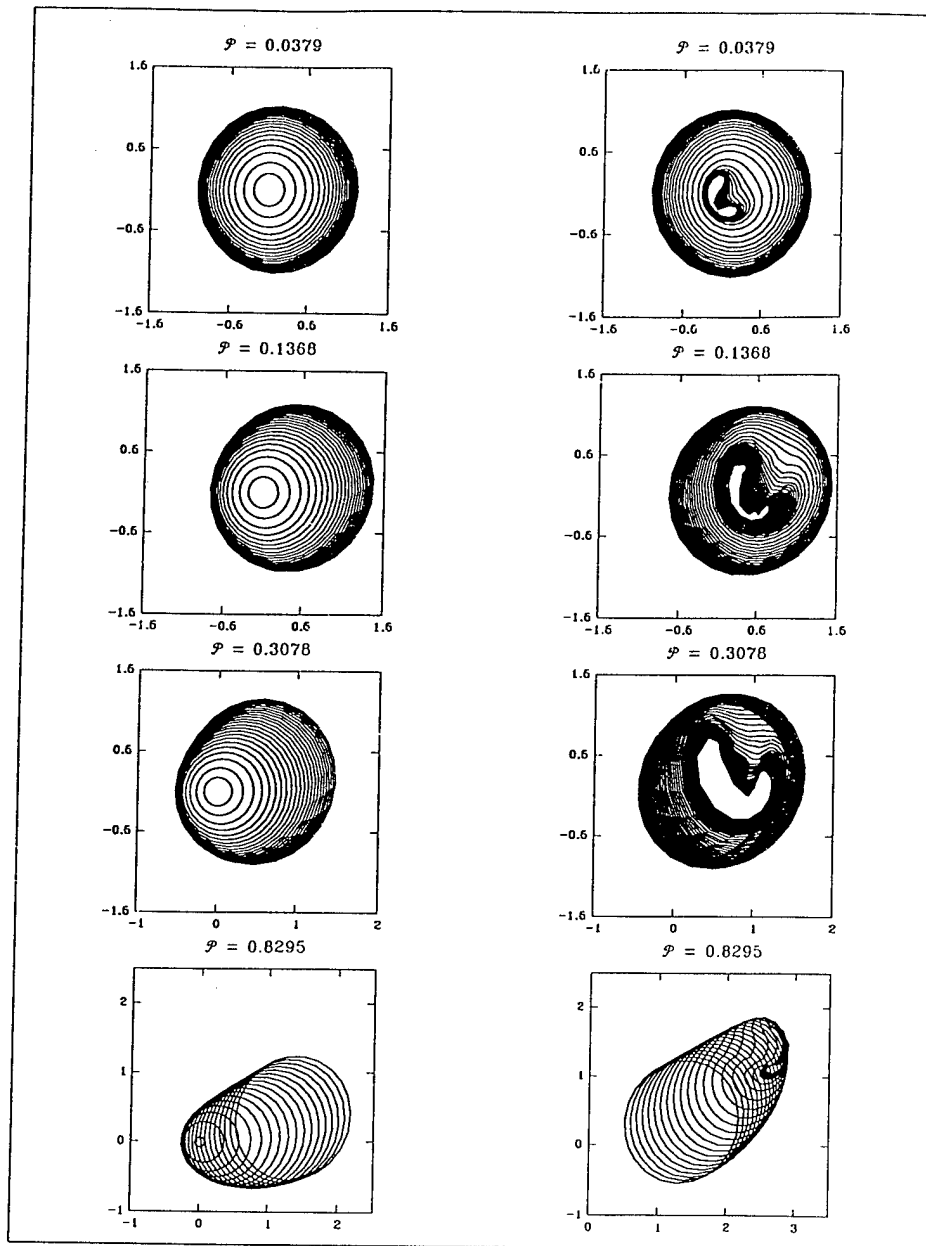
Comparison of growth and collapse contours for four \mathcal{P} 's

Figure IV.9: Contours of bubble growth, and collapse, for four values of the pressure parameter \mathcal{P} . The top three cases correspond to the cases in Figure 8, while the last case is for a higher value of \mathcal{P} .

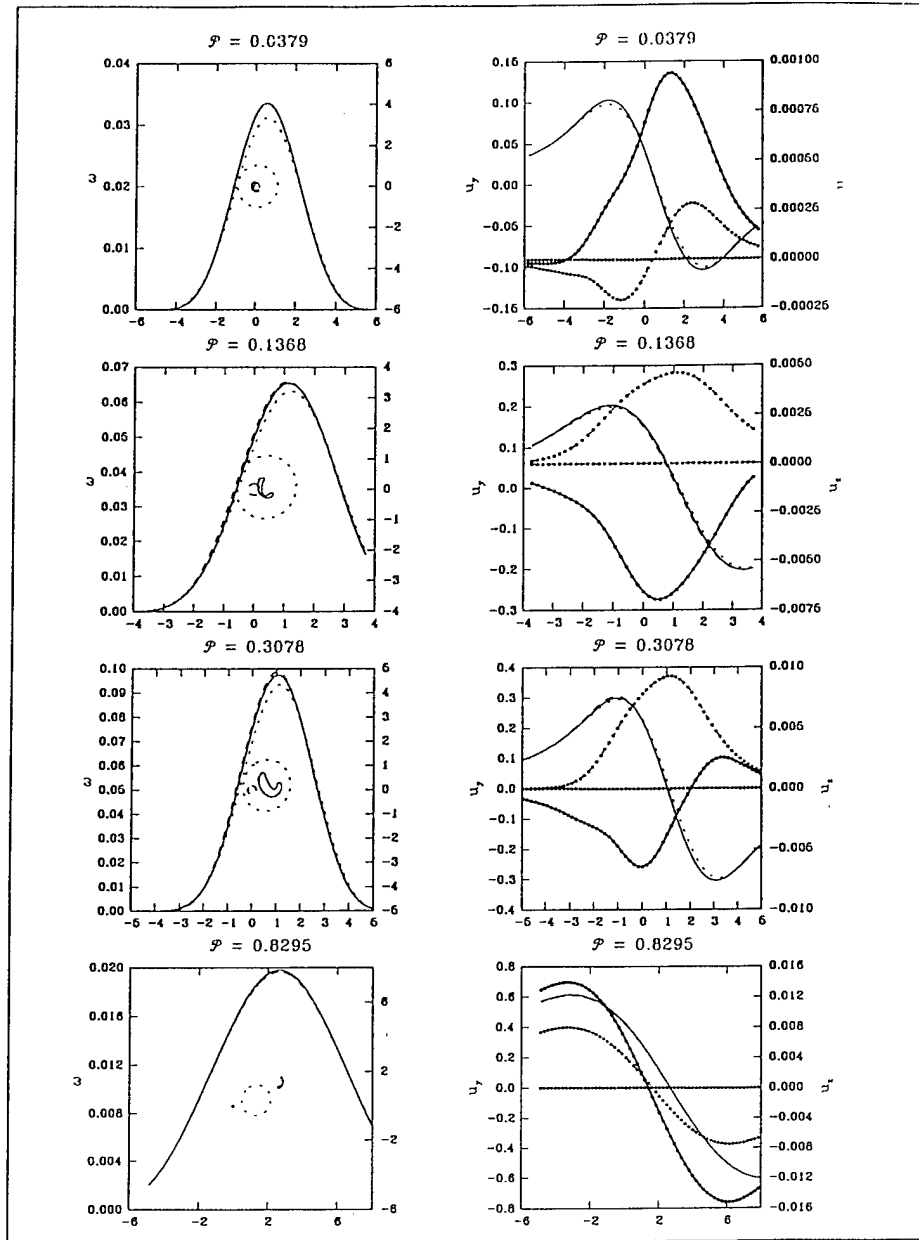
Vorticity and velocity along the y axis for four \mathcal{P} 's

Figure IV.10: The out-of-plane vorticity (left column) and in-plane velocities (right column) along a line joining initial bubble and vortex centers, for the cases of Figure 9. The curves display the value at the initial time (dashed line), at bubble maximum (longer dashes) and at the instant of bubble collapse (solid line). In the velocity plots the component u_z is indicated with lines with circles.

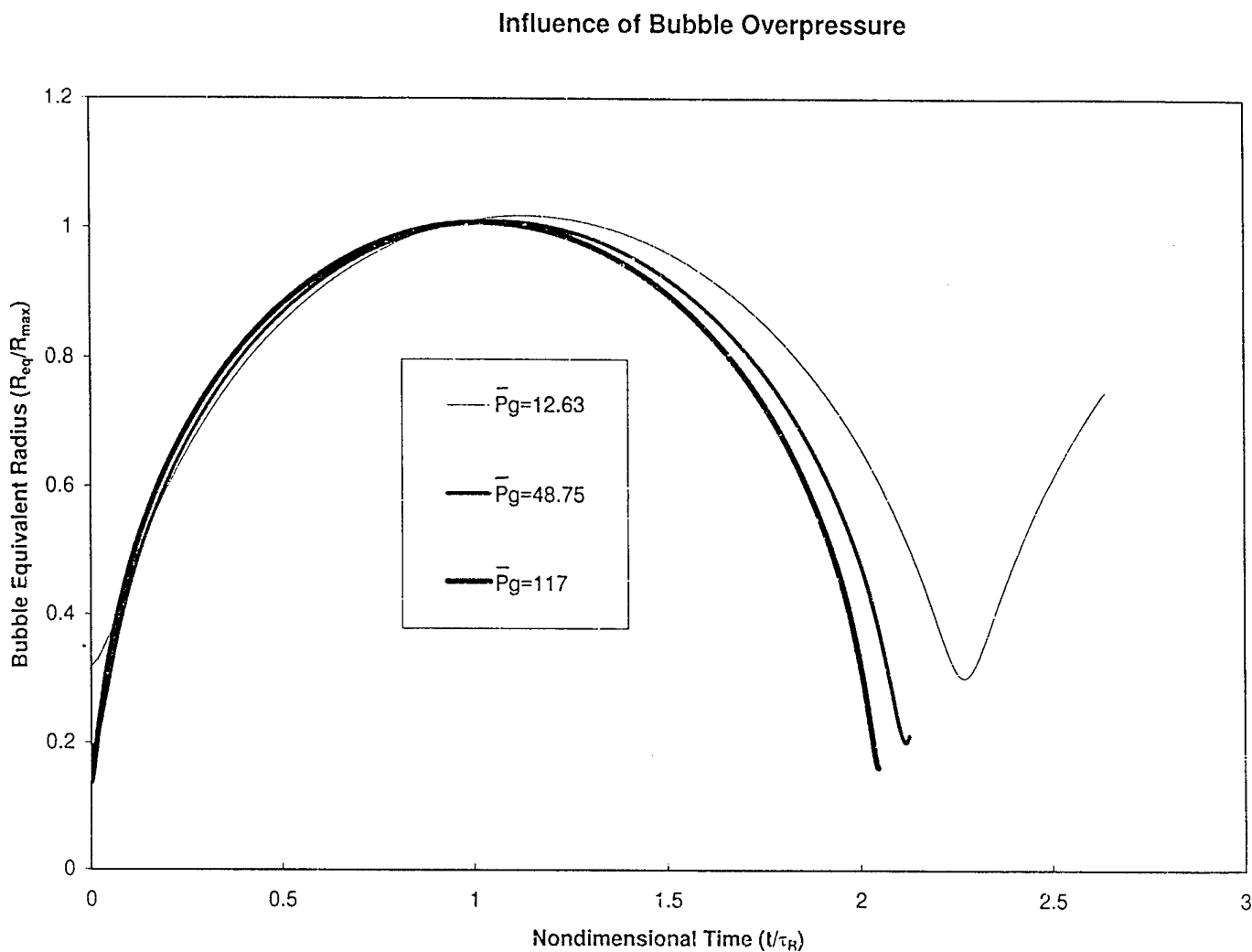


Figure IV.11: Study of the influence of the bubble over-pressure, $\bar{P}_g = P_g/P_\infty$, on the dynamics. The non-dimensionalized equivalent bubble radius, R_{eq}/R_{max} , is plotted versus time for three values of \bar{P}_g . In each case the bubble initial radius is $10 \mu\text{m}$, and is placed $30 \mu\text{m}$ away from the center of a vortex of core size $120 \mu\text{m}$, and circulation $0.0015 \text{ m}^2/\text{s}$. The initial gas pressures are $1.2279 \times 10^6 \text{ Pa}$, $4.7417 \times 10^6 \text{ Pa}$, and $1.138 \times 10^7 \text{ Pa}$, and the pressure at infinity is 10^5 Pa .

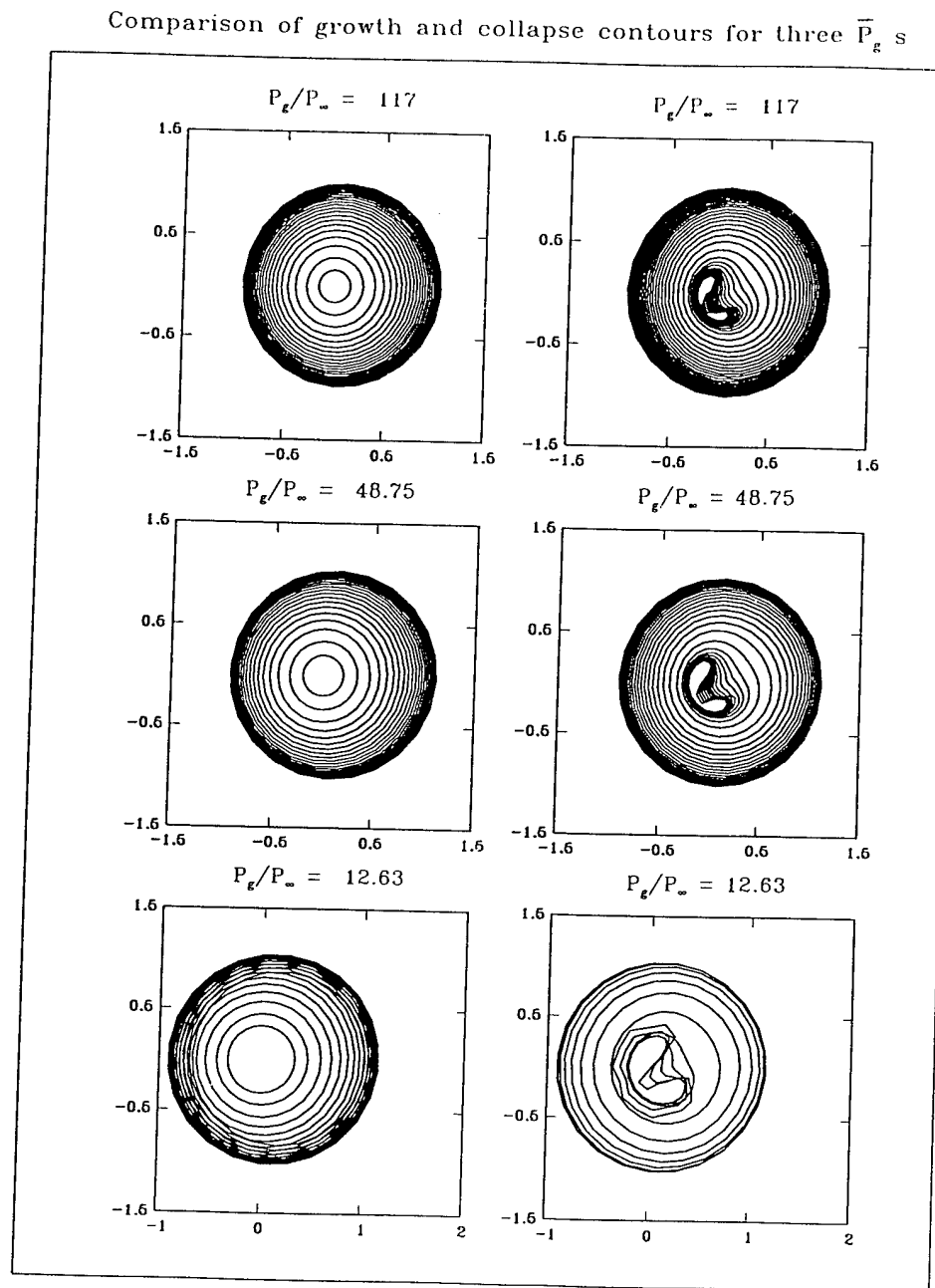


Figure IV.12: Contours of bubble growth (left column) and collapse (right column) for the cases of Figure 11. In the case with the smallest initial pressure, jet formation during rebound can be observed.

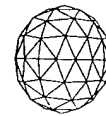
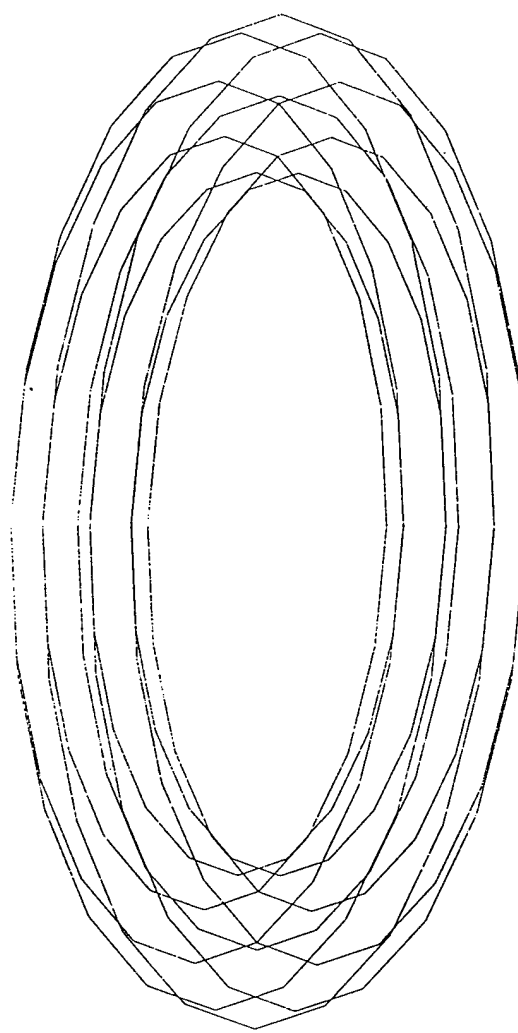


Figure IV.13: Geometry of the discretized bubble and the vortex ring.

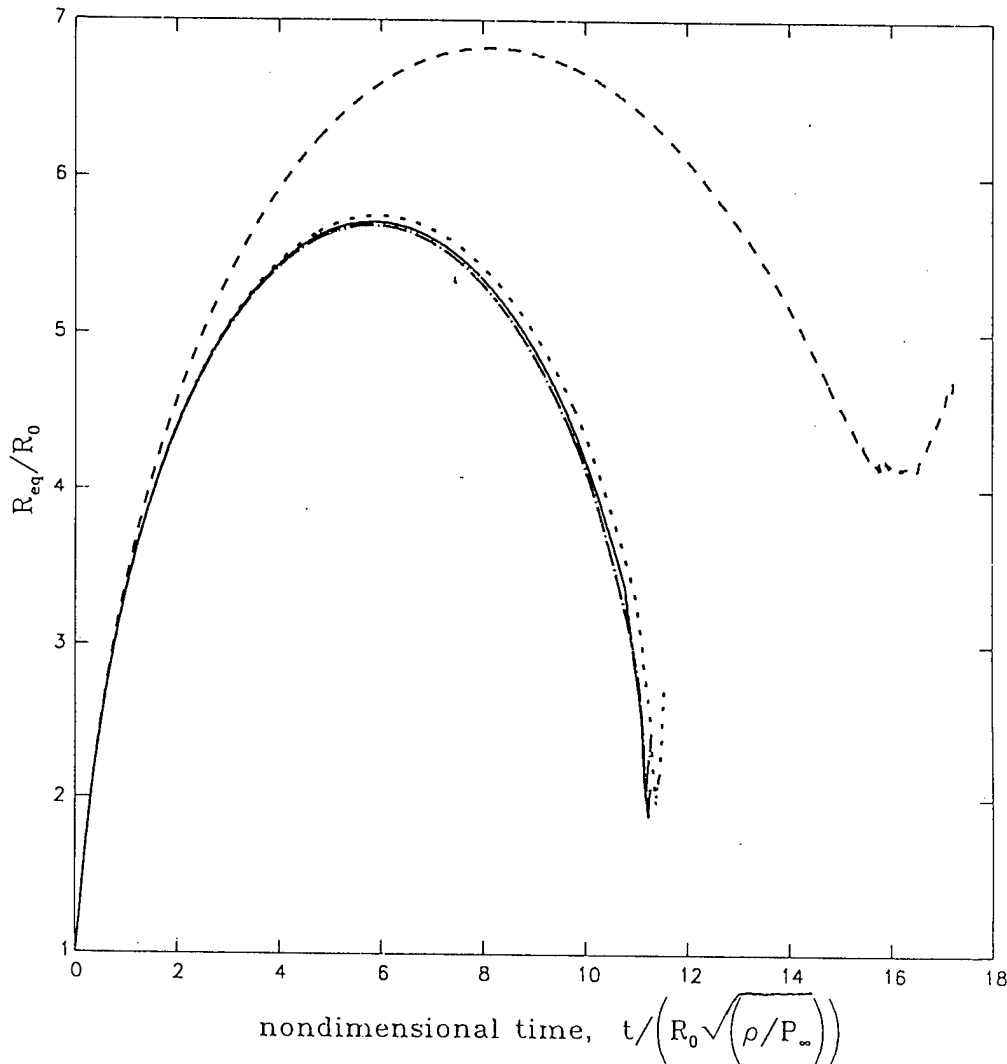


Figure IV.14: A convergence study for the dynamics of a bubble in the flow field of a vortex ring. Four different discretizations, with 1 (dashed), 7 (dotted), 19 (solid), and 37 (dash-and-dotted) lines for the ring core are used. Time evolution of the bubble equivalent radius R_{eq}/R_0 is shown. Initial bubble radius: 10 μm , ring radius: 80 μm , ring core radius: 30 μm , $p_{g0}=5\times 10^6 \text{ Pa}$, and $\Gamma=0.00045 \text{ m}^2/\text{sec}$.

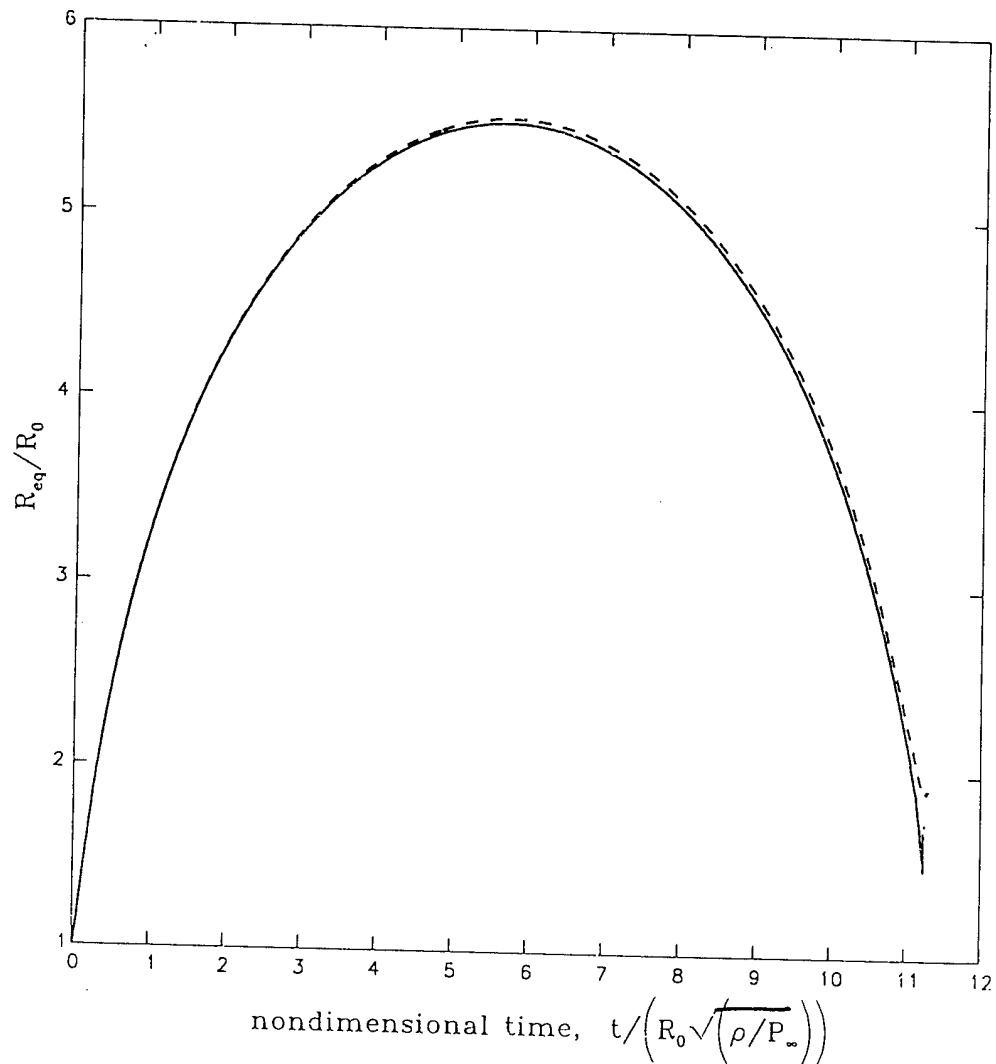


Figure IV.15: A convergence study with respect to the number of elements along a line in the core of the ring: 20 (dashed), 40 (dotted) and 100 (solid) elements are used to discretize a component ring and R_{eq}/R_0 is plotted.

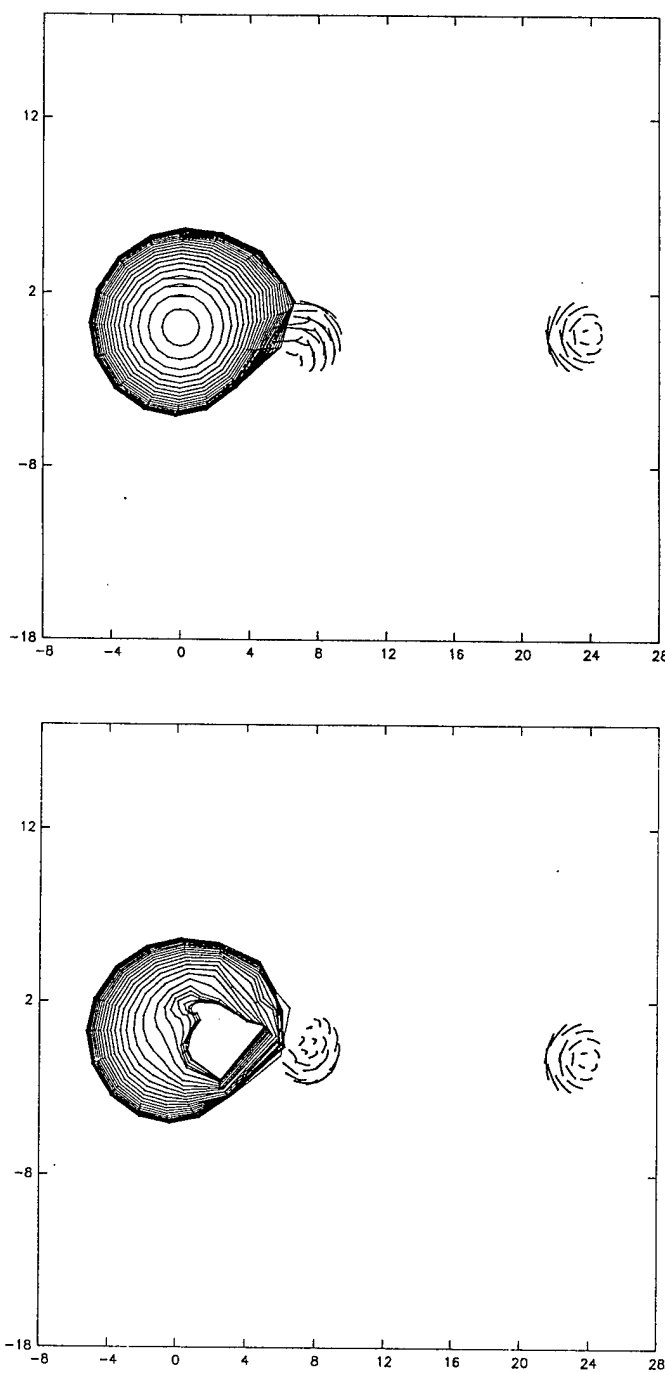


Figure IV.16: Growth (a) and collapse (b) of the bubble in the ring vortex for the conditions of Figure 13. Time evolution of bubble cross-sections and traces of the vortex lines in a plane perpendicular to the column are shown. The scale is non-dimensionalized with the initial bubble radius. The ring is moving downward due to its own induced velocity.

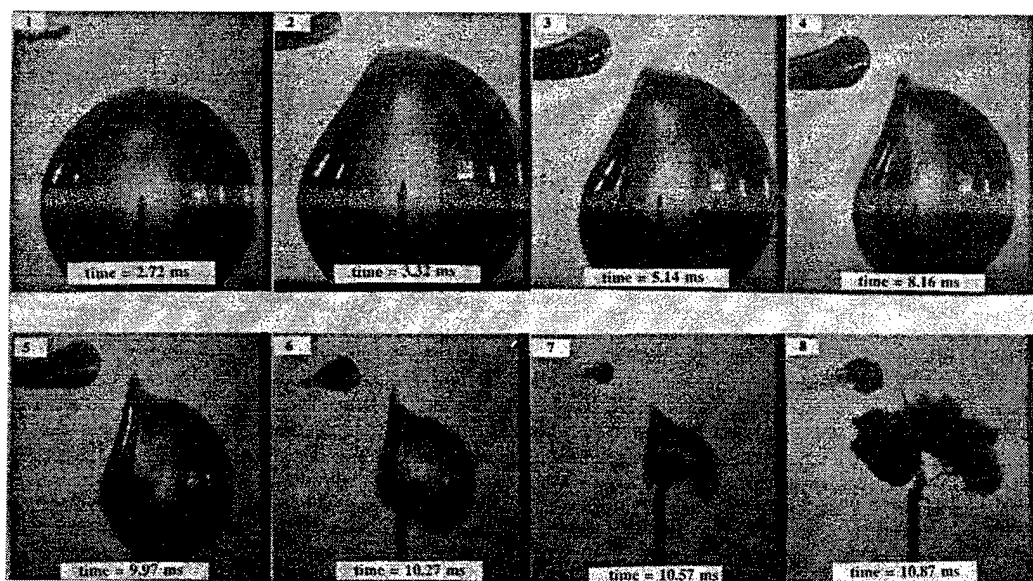


Figure IV.17: Experimental observations of a bubble collapsing in the field of a vortex ring from Chahine (1995). The vortex ring is cavitating and is in the upper left corner of each frame.

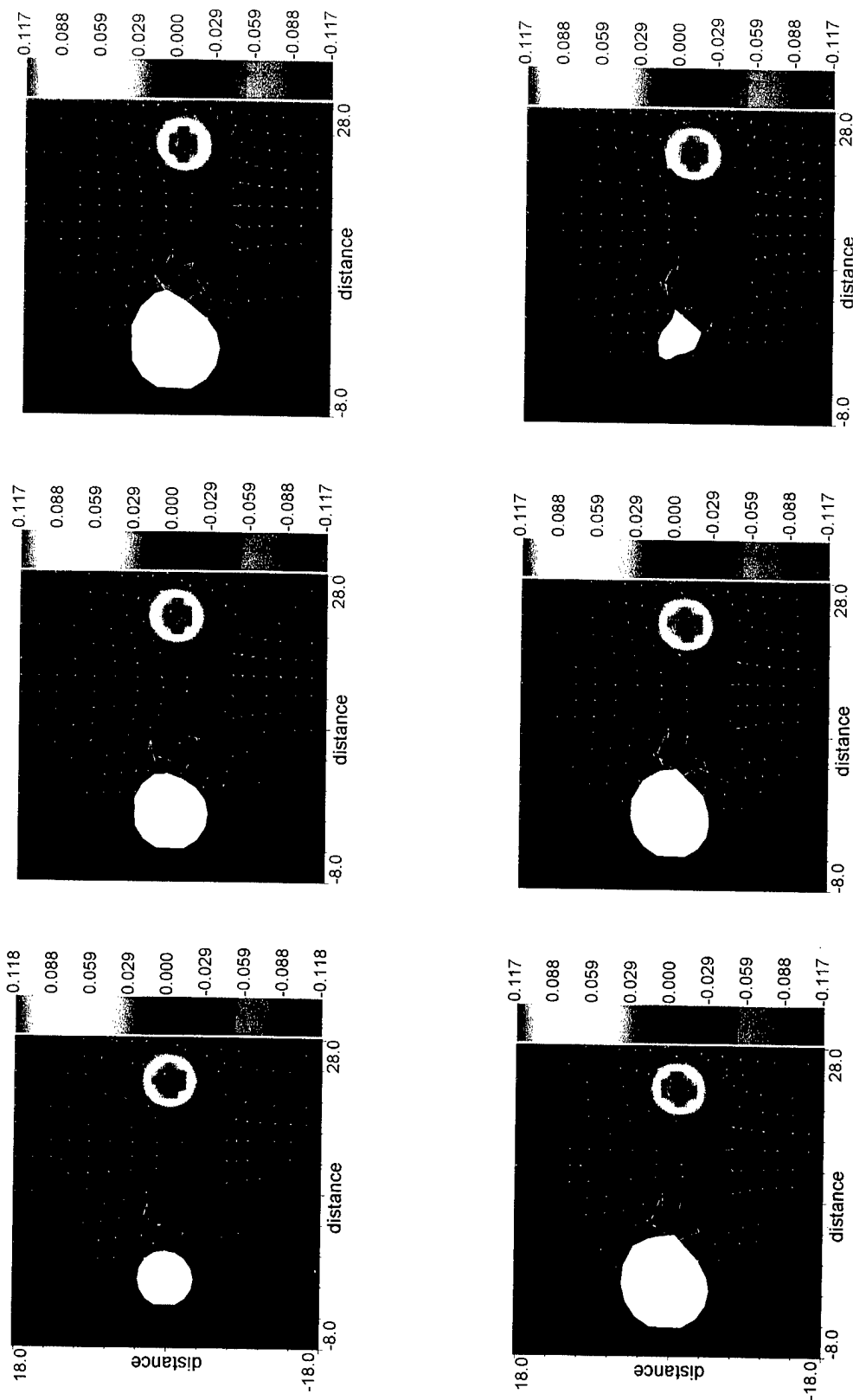


Figure IV.18: The normal component of the vorticity field ω and the tangential components of the induced vortical velocity vectors \mathbf{u}_ω , i.e., $\mathbf{u} - \mathbf{u}_b$ in a cross-sectional plane at six different times, three during growth, $t=1.022, 2.27, 4.77$, and three during collapse, $t=7.27, 8.52, 10.92$. The conditions are the same as in Figure 13.

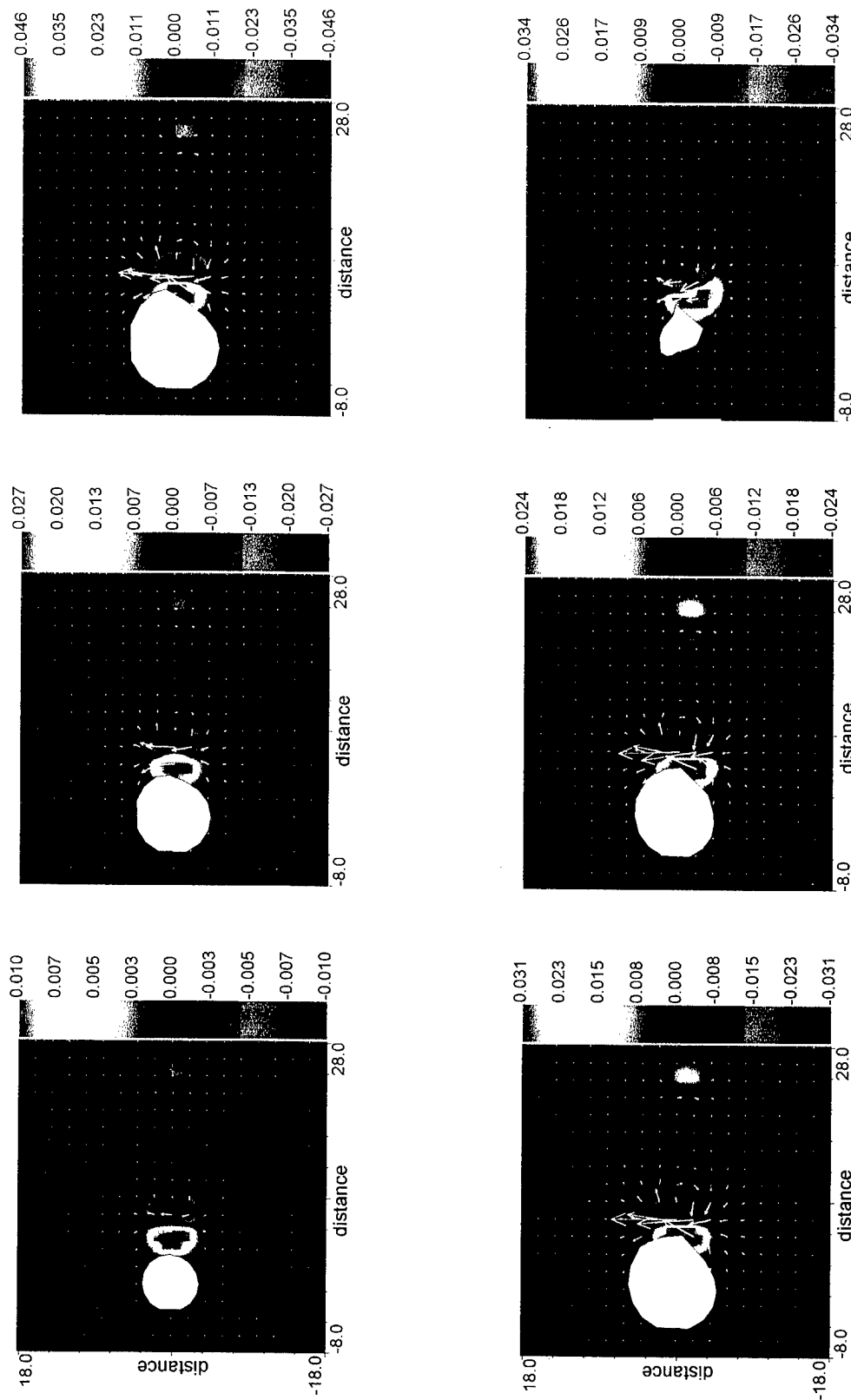


Figure IV.19: The difference in the normal component of the vorticity field ω and the tangential components of the vortical velocity vectors \mathbf{u}_ω with and without the bubble at the same times and the same cross-sectional plane as in Figure 18.

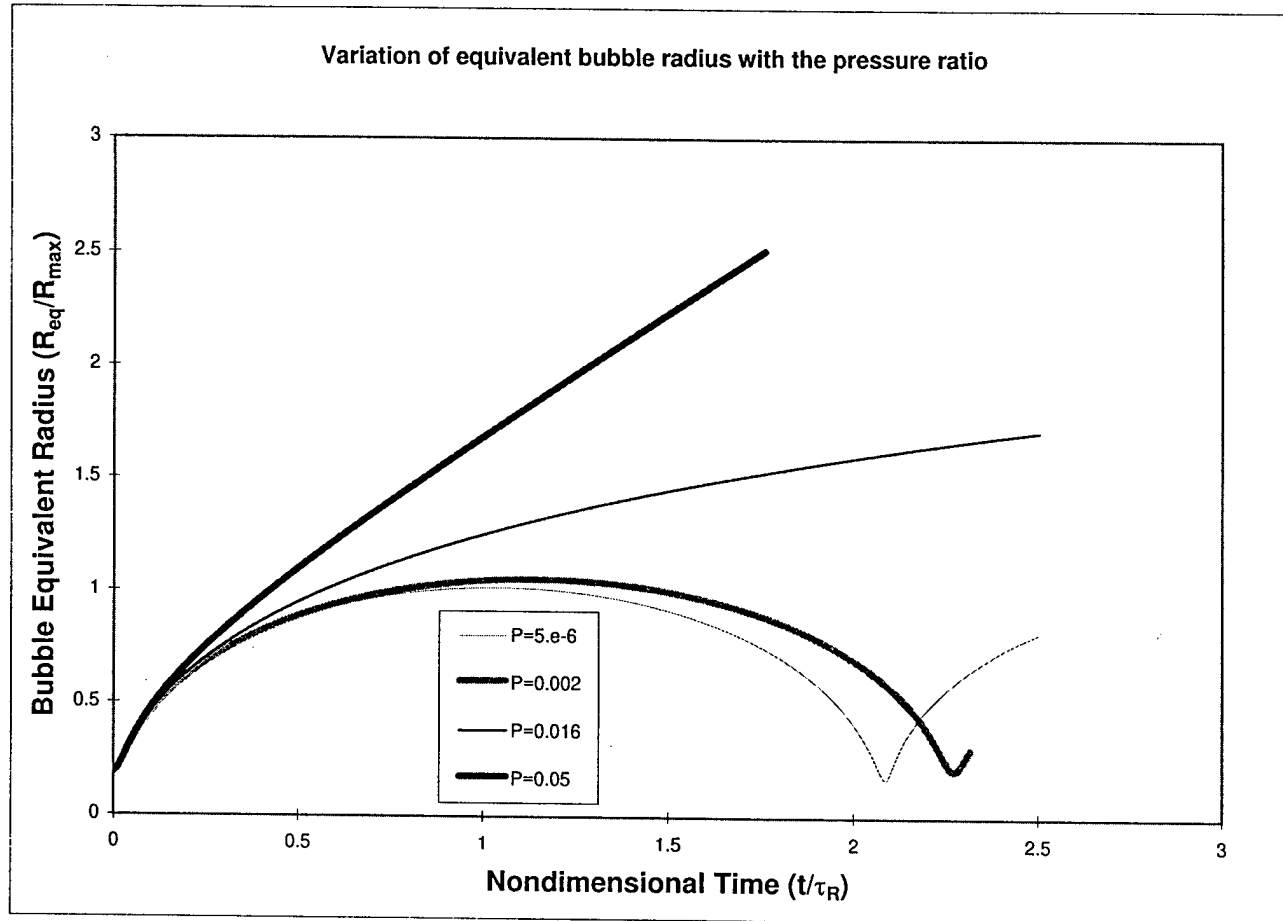


Figure IV.20: Modification of the bubble dynamics with varying vortex ring circulation, as shown by the variation of the bubble equivalent radius, R_{eq}/R_{max} , with time t/τ_R . In each case the bubble initial radius is $10 \mu\text{m}$, and is at an initial pressure of $4.6716 \times 10^6 \text{ Pa}$, and is placed $300 \mu\text{m}$ away from a vortex ring in its plane. The ring has a radius of $80 \mu\text{m}$ and a core radius of $30 \mu\text{m}$. The circulations corresponding to the four cases are respectively 4.5×10^{-5} , 0.0009 , 0.0025 , and $0.0045 \text{ m}^2/\text{s}$.

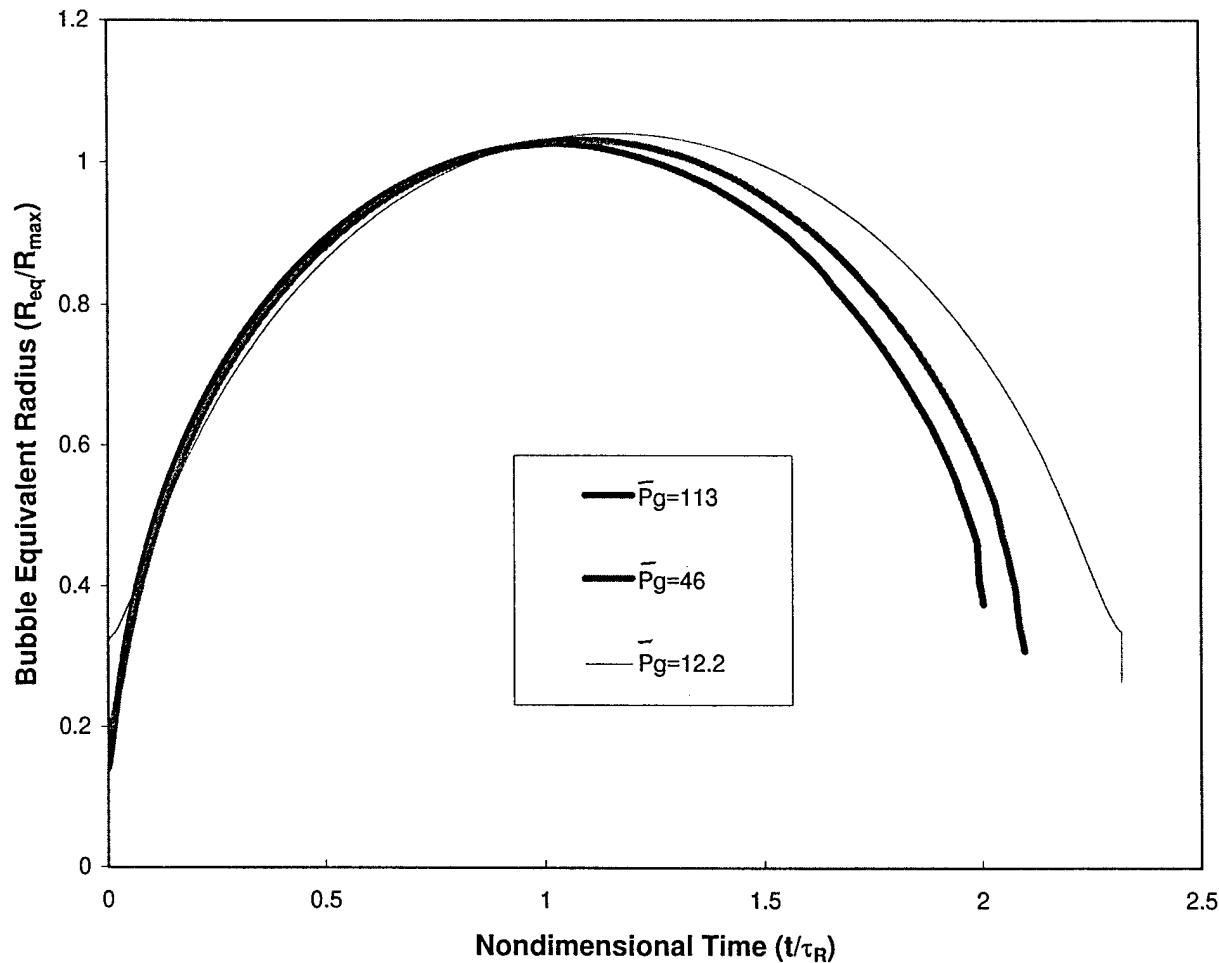
Equivalent radius versus time for different bubble overpressures

Figure IV.21: Modification of the bubble dynamics in a vortex ring flow field with varying initial bubble overpressure, as shown by the variation of the bubble equivalent radius. R_{eq}/R_{max} , with time t/τ_R . In each case the bubble initial radius is $10 \mu\text{m}$, and is placed $150 \mu\text{m}$ away from a vortex ring in its plane. The ring has a radius of $80 \mu\text{m}$, a core radius of $30 \mu\text{m}$, and a circulation of $0.00045 \text{ m}^2/\text{s}$. The initial bubble pressures are $1.2279 \times 10^6 \text{ Pa}$, $4.6716 \times 10^6 \text{ Pa}$, and $1.138 \times 10^7 \text{ Pa}$.

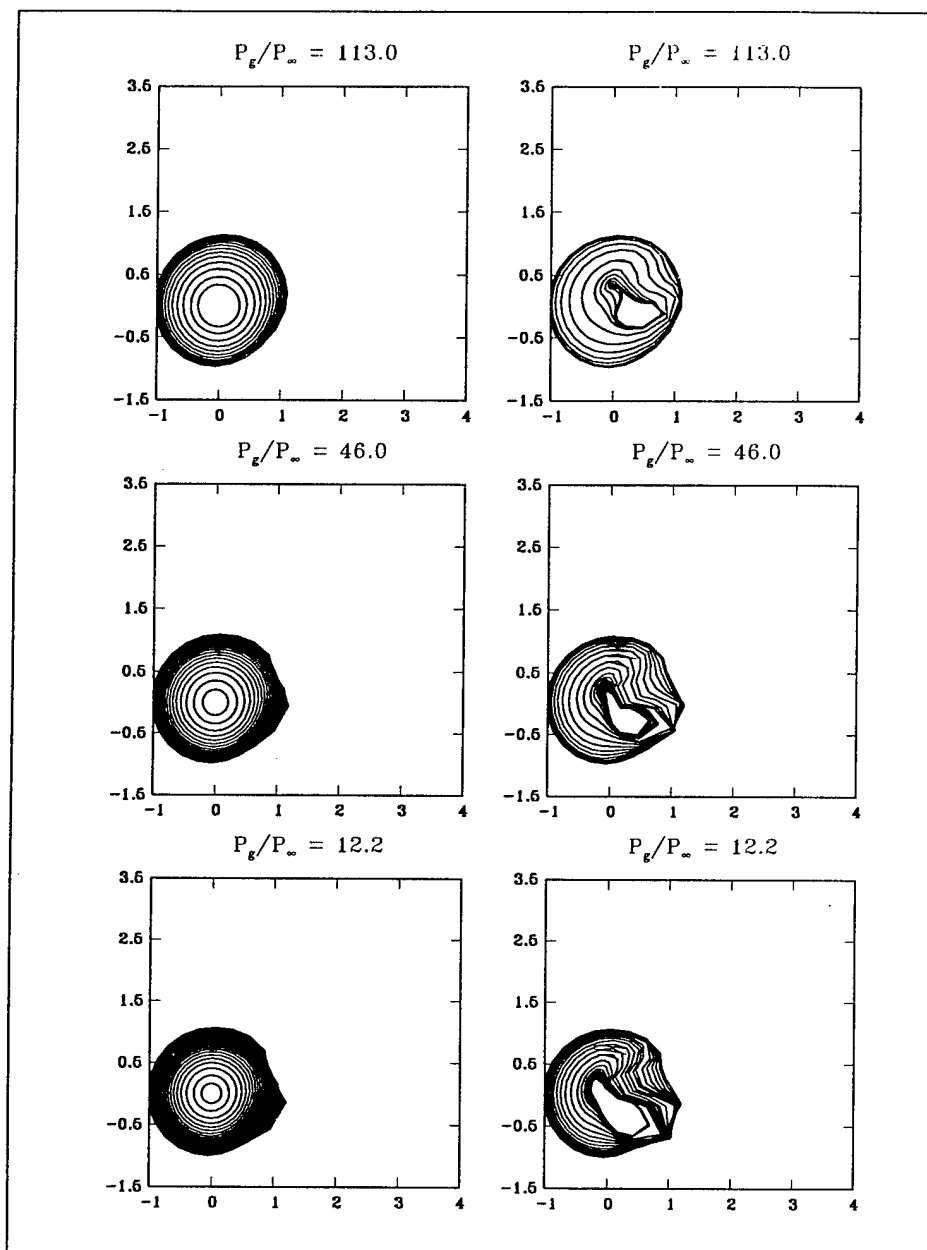
Comparison of growth and collapse contours for three P_g 's

Figure IV.22: Contours of bubble growth (left column) and bubble collapse (right column) for the cases of Figure 21.

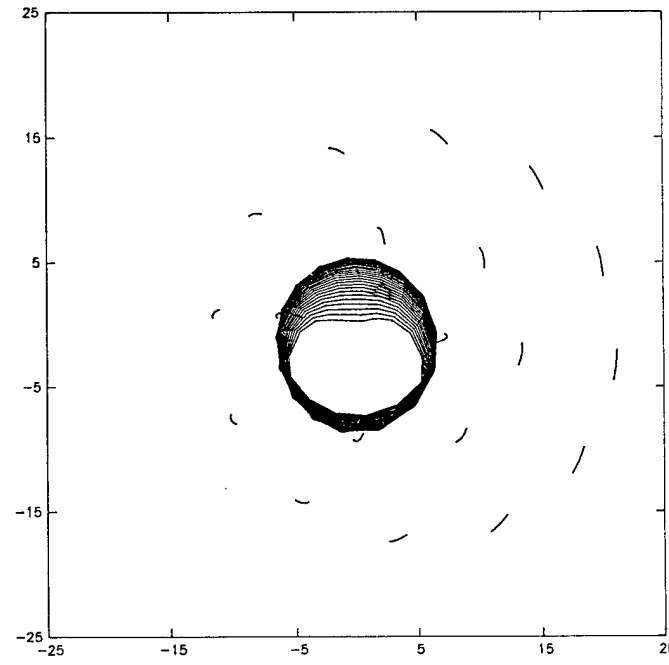
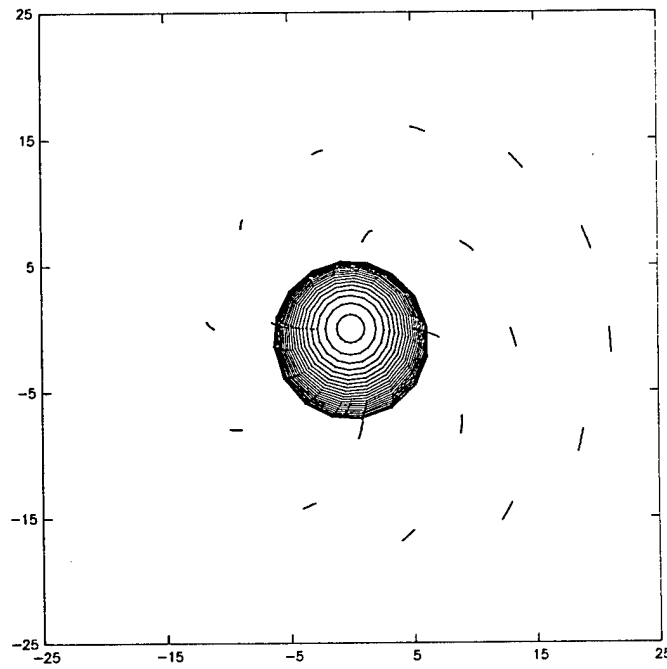


Figure IV.23: Growth (a) and collapse (b) of a bubble placed inside the core of the ring. $R_0 = 1\mu\text{m}$, the inside gas pressure $p_{g0} = 7 \times 10^6 \text{ Pa}$. The vortex parameters are ring radius: $80 \mu\text{m}$, ring core radius: $30 \mu\text{m}$, $p_{g0} = 5 \times 10^6 \text{ Pa}$, $P_\infty = 10^5 \text{ Pa}$ and $\Gamma = 0.00045 \text{ m}^2/\text{sec}$. The bubble is placed $5 \mu\text{m}$ away from the ring core center.

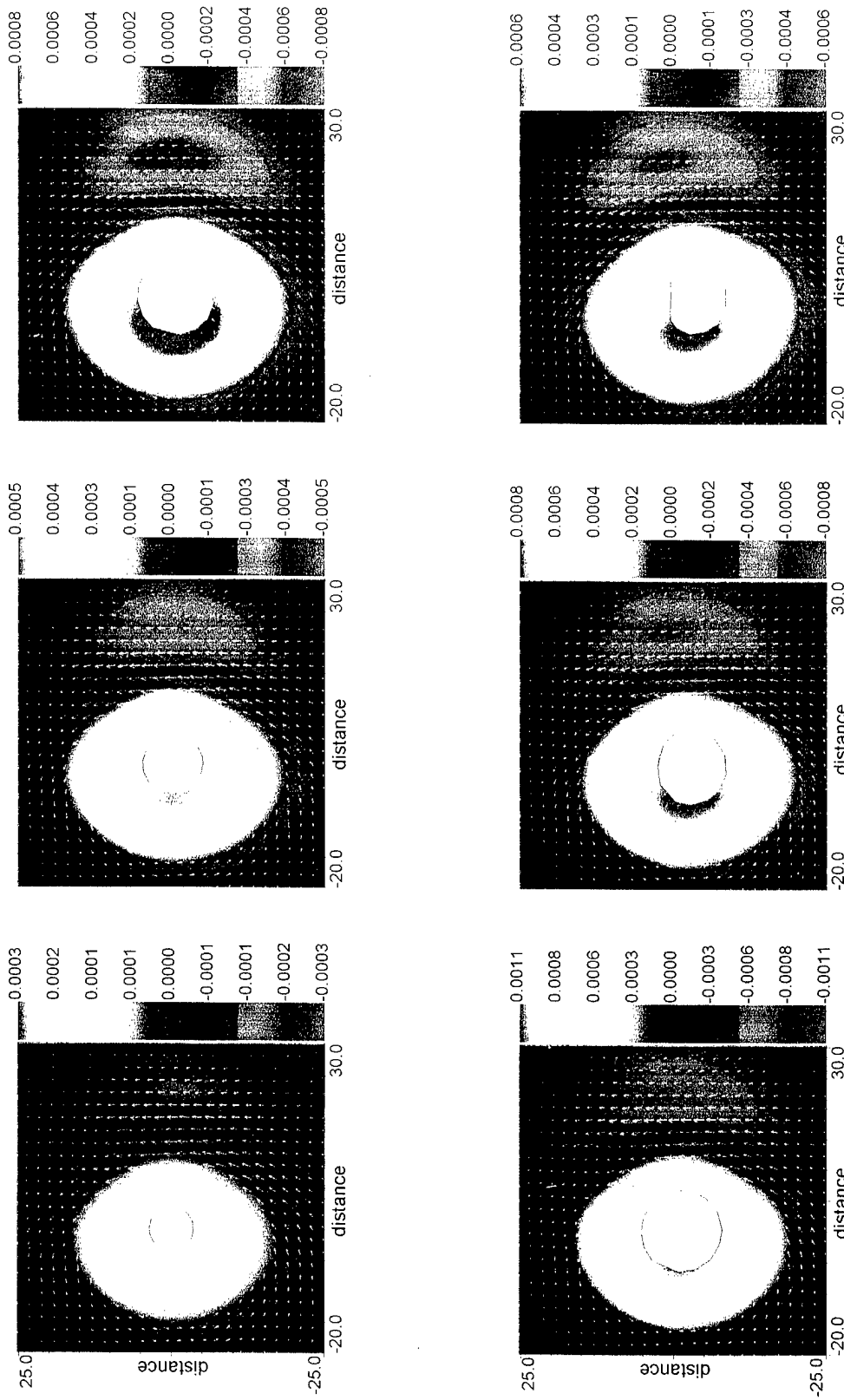


Figure IV.24: The change in the vorticity and the vortical velocity field in the cross-sectional plane for the conditions of Figure 23 at six different times, $t=1.02, 2.27, 4.77$ during growth, and $t=7.27, 11.02, 12.27$ during collapse.

Chapter V

SHEET CAVITATION INCEPTION

1 Introduction

The inception and subsequent dynamics of cavitation on a body moving through the fluid is an important problem that is not yet fully understood. This flow can display a variety of cavitation types for different flow speeds, including travelling bubble cavitation, sheet cavitation, unsteady separated sheet cavitation, cavity break-up into bubbles and bubble clouds. These can be characterized by strong interactions between the intense flow field and the time-dependant moving cavity boundaries.

In this chapter, we present a simulation model for the appearance and the subsequent dynamics of the sheet cavity, that we have implemented in the boundary element codes described in the previous chapters. The code is then exercised to study sheet cavitation on a sphere.

In the first part of the study the flow is considered potential. The model is then extended to include general vortical flows by decomposing the complete flow field into a vortical part and a potential part. The potential part is computed by the boundary element method while the rotational part is modeled by a vortex element method (VEM). The results of the present study will provide guidelines for the future development of a coupled numerical simulation.

2 Mathematical Formulation

2.1 Basic Equations and Boundary Conditions

The relevant equations are those described in the previous chapters. In addition, here we incorporate in the vortex dynamics study the diffusion of vorticity. This requires explicit solution of the transport equation:

$$\frac{D\omega}{Dt} = \omega \cdot \nabla \mathbf{u} + \nu \nabla^2 \omega. \quad (\text{V.1})$$

Furthermore, the tangential component of the no-slip condition on a solid surface and the zero tangential stress condition at the free surface necessitates vorticity creation at those surfaces that has to be addressed.

2.2 Cavity Model

The precise conditions under which a cavity forms on a solid boundary is not yet well understood. Recently in a careful experiment Mrch & Song [61] have shown that a perfect contact between a solid boundary and the liquid cannot exist and that nanoscopic cavities always exist and form potential cavitation regions. We will use this to justify the use of the following model that postulates growth of a cavity when the pressure at the solid surface drops below a critical pressure such as the vapor pressure p_v . If the pressure at any region is below a critical pressure p_c , we make that part of the surface free to move with the pressure thereafter set equal to p_c . This part of the body surface becomes a part of a dynamically behaving cavity.

The cavity surface moves with the local fluid \mathbf{u} . However the cavity surface is obviously not allowed to penetrate the surface of the body. This corresponds to the physical fact that the collapse of the cavity will be hindered by the solid surface underneath. In this case, the nodes in the corresponding cavity region are made solid again.

3 Implementation of the VEM

3.1 Vortex Elements

For three dimensional general body shapes the vorticity of the flow field is modeled by distributing three-dimensional vortex elements in the fluid. The expression of the vorticity field is then

$$\boldsymbol{\omega} = \sum_i \alpha_i f_\Delta(|\mathbf{x} - \boldsymbol{\chi}_i|), \quad (\text{V.2})$$

where α_i is the strength of the i -th element positioned at $\boldsymbol{\chi}_i$, with f_Δ the core function of the element with cut-off length Δ ,

$$f_\Delta(r) = \frac{3}{4\pi\Delta^3} e^{-(r/\Delta)^3}. \quad (\text{V.3})$$

These expressions are similar to those in Chapter 4, except that we have used there a connected filament approach writing the vorticity strengths in terms of circulation of a cylindrical length elements. The velocity due to this vorticity distribution is given by the Biot-Savart law,

$$\mathbf{u}_\omega(\mathbf{x}, t) = \frac{1}{4\pi} \sum_i \frac{\alpha_i \times (\mathbf{x} - \boldsymbol{\chi}_i)}{|\mathbf{x} - \boldsymbol{\chi}_i|^3} \left(1 - e^{-\left(\frac{|\mathbf{x} - \boldsymbol{\chi}_i|}{\Delta}\right)^3} \right). \quad (\text{V.4})$$

and the time evolution of the vorticity field is given by the transport equation

With the expression (V.2), we obtain the following evolution equation for the vortex element strengths

$$\frac{d\alpha_i}{dt} = \alpha_i \cdot \nabla^T \mathbf{u}(\boldsymbol{\chi}_i) + \nu \Delta^3 \nabla^2 \omega(\boldsymbol{\chi}_i), \quad (\text{V.5})$$

where we have chosen the transpose scheme (involves $\nabla^T \mathbf{u}$ in the right-hand-side) as prescribed by Winckelmans & Leonard [48].

In the above equation $\nabla^2\omega$ is computed directly applying Laplace operator to (V.2). The gradient of the vortical velocity \mathbf{u}_ω is computed by applying the gradient operator to the velocity field (V.4). The corresponding gradient for the potential part is obtained by computing ϕ in a grid of points around the location of interest and then fitting a 2nd order polynomial function for ϕ in that region.

3.2 Generation of Vorticity at Solid Boundaries

Vorticity is created at boundaries by viscous effects through the no-slip condition, and diffuses into the body of the fluid. The method described above requires the knowledge of vorticity in all space. This requires inclusion of the generation of vorticity at the boundaries in the model.

Let us consider an initial time t where the no-slip condition holds, and the potential and vortical parts of the flow field are known throughout the domain. We then march the solution from this known stage using a time stepping procedure, to compute the state of the system at time $t + \Delta t$. At a given time step, after the velocity potential has been advanced via the BEM solution, the tangential component of the velocity at the body surface does not satisfy the no-slip condition. The vortical part of the flow field must be modified to ensure that this condition holds. This temporary slip velocity can be expressed as

$$\mathbf{u}_{\text{slip}} = [\nabla\phi + \mathbf{U}]_{\text{tangential}}. \quad (\text{V.6})$$

This slip velocity is spurious, and to cancel it a vortex sheet of strength γ per unit area must be placed on the surface,

$$\gamma = \mathbf{n} \times \mathbf{u}_{\text{slip}}. \quad (\text{V.7})$$

Every time this condition is enforced fresh vorticity is introduced.

In the present vortex element method, the vorticity is approximated using concentrated vortex elements. Generation and diffusion of vorticity in this scheme will be accounted for by a combination of changing the strengths and location of the existing vortex elements, and by introducing new vortex elements to satisfy the boundary condition (V.7).

One possibility is introducing a set of vortex elements from the surface every time step, and letting these elements convect in the fluid at future steps. However, such a scheme soon becomes unwieldy as in every step the number of elements in the approximation (V.2) would increase, and make the method useless. Instead we follow a two step approach to the process.

A set of 3D vortex elements are distributed at a small distance ε away from the surface along the normal at every surface node. In the current code ε is a user-defined parameter, and is the same for every node. These elements are taken to be fixed at this location, and their strength is changed every time step to cancel the spurious slip velocity. The strength of a given element, α_i , will be changed by an amount $\Delta\alpha_i$ in a given time step, with

$$\Delta\alpha_i = \gamma_i \delta A_i \quad (\text{V.8})$$

where δA_i is the area of the surface element on the body surface associated with the given node, and is computed from the total area of the panels surrounding the node divided among the nodes having these panels in common.

While it is true that application of Equation (V.5) would redistribute the vortex strengths, the continuous addition of vorticity to the fixed elements, and the convection of the free elements away from the surface, would cause the strengths of the fixed elements to grow and affect the quality of the approximation (V.2). To avoid this, every Δt_{shed} we introduce Lagrangian vortex elements with the strength of the corresponding bound vortex element are allowed to follow the fluid velocity \mathbf{u} , i.e., they are “free” to move. The strength of the corresponding bound element is set to zero. In this way we control the number of actual moving Lagrangian elements introduced into the fluid. The bound elements only purpose is to represent the correct vorticity field satisfying the no-slip condition in between two shedding events.

3.3 Algorithm Summary

1. Given a flow at infinity solve the BEM satisfying the normal boundary condition at the body surfaces
2. Introduce free vortex elements at each body node with strengths computed from the slip velocity at that node
3. Compute the total velocity at the free vortex elements
4. Compute the total velocity at the body nodes
5. Compute the time derivative of the strengths of the vortex elements using Equation(V.5).
6. Update the positions and strengths of the vortex elements.
7. Update the strengths of “bound” vortex elements at each nodes with strengths computed from the slip velocity at the body surface using Equations (V.7), and (V.8).
8. Update the time to $t + \Delta t$.
9. If t is a multiple of Δt_{shed} shed free vortex elements at each node with the same strengths as the fixed vortex elements and set the strengths of the fixed vortex elements to zero.
10. Solve again the potential part using the BEM.
11. go to step 3 and calculate for the next time step

3.4 Free Surface Time Evolution

The cavity geometry is updated with the local flow velocity. In order to update the value of the potential ϕ we use the dynamic boundary condition or the Bernoulli equation

$$\begin{aligned} \frac{\partial \phi}{\partial t} + \frac{\partial \phi^r}{\partial t} + \frac{1}{2} |\nabla \phi|^2 + \frac{1}{2} |\nabla \phi^r|^2 \\ = -\nabla \phi \cdot \nabla \phi^r - \mathbf{U} \cdot (\nabla \phi + \nabla \phi^r) + \frac{p_\infty - p}{\rho} - g(z - z_\infty), \end{aligned} \quad (\text{V.9})$$

where ϕ^r represent any other potential flow perturbation such as due to the vortex elements. This relation is applied to update the values of ϕ at a moving surface using the material derivative of ϕ :

$$\frac{D\phi}{Dt} = \frac{\partial\phi}{\partial t} + \mathbf{u} \cdot \nabla\phi. \quad (\text{V.10})$$

Upon substitution in (V.9), we obtain

$$\frac{D\phi}{Dt} = -\frac{\partial\phi^r}{\partial t} + \frac{1}{2} [|\nabla\phi|^2 - |\nabla\phi^r|^2] - \nabla\phi^r \cdot \mathbf{U} + \frac{p_\infty - p}{\rho} - g(z - z_\infty). \quad (\text{V.11})$$

The above expression provides the evolution of ϕ at the free surface [11, 39].

Such a Bernoulli relation should be modified for general vortical flow fields. In such a case a Poisson equation is obtained for Ψ

$$\Psi = \frac{\partial\phi}{\partial t} + \frac{1}{2}|\mathbf{u}|^2 + \frac{p}{\rho} + gz. \quad (\text{V.12})$$

The solution procedure of this equation is described in detail in chapter 4.

4 Boundary Element Method

Discretization of the 3D surface by triangular elements, together with the boundary element formulation for ϕ generates a set of linear equations relating ϕ and $\partial\phi/\partial n$ at the nodes,

$$\sum_j \left[A_{ij}(\mathbf{x}_i, \mathbf{x}'_j) \frac{\partial\phi}{\partial n}(\mathbf{x}'_j) - B_{ij}(\mathbf{x}_i, \mathbf{x}'_j) \phi(\mathbf{x}'_j) \right] = 0. \quad (\text{V.13})$$

Here the functions ϕ and $\partial\phi/\partial n$ are linearly interpolated inside each panel by using their values at the vertices of the triangle. A_{ij} and B_{ij} are geometry dependent matrices relating the influence of the j -th node at the i -th node. They are obtained by integrating the surface integrals analytically over each panel separately. In general some region of the boundary is solid while the other is part of a deforming cavity. We solve for ϕ on the solid part knowing $\partial\phi/\partial n$, while we solve for $\partial\phi/\partial n$ on the free surface using the knowledge of ϕ .

5 Axisymmetric Vortex Rings

For the special case of a flow around a sphere we resort to a simpler representation of the vorticity by axisymmetric rings. As a preliminary approach we model this process by satisfying every Δt_{shed} the no-slip condition on the surface of the sphere. Every Δt_{shed} , N vortex rings are emitted at N different locations along the circumference of the sphere. The ring strengths, Γ , are obtained by satisfying the no-slip conditions at those N locations. Once emitted the vortices follow the local fluid velocity and affect the dynamics of the complete flow field. Another simplification in the example is that we will ignore the viscous diffusion and consider inertial forces to be dominant.

The velocity potential due to a vortex ring of intensity Γ is given by a velocity potential outside the ring [62]

$$\phi^r(r, z) = \text{sgn}(Z_0 - z) \frac{\Gamma A_0}{2} \int_0^\infty [\exp(-k|Z_0 - z|) J_0(kr) J_1(kA_0)] dk, \quad (\text{V.14})$$

where, J 's are the Bessel functions, z is the coordinate perpendicular to the plane of the ring, r is the radial coordinate in the plane of the ring, Z_0 denotes the z -coordinate of the ring on the axis of the symmetry, and A_0 denotes the radius of the ring. The velocities induced by the ring at a field point (r, z) are given by

$$u_r = \frac{\Gamma}{2\pi} \frac{Z - z}{r} \left(\frac{1}{r_1} + \frac{1}{r_2} \right) \left(K - \frac{1+m}{1-m} E \right), \quad (\text{V.15})$$

and

$$u_z = \frac{\Gamma}{2\pi} \left[\left(\frac{r - A_0}{r_1} + \frac{r - A_0}{r_2} \right) \left(K - \frac{E}{1-m} \right) - \frac{E\sqrt{m}}{1-m} \left(\frac{r - A_0}{r_1} + \frac{r - A_0}{r_2} \right) \right], \quad (\text{V.16})$$

where

$$m = \left(\frac{r_2 - r_1}{r_2 + r_1} \right)^2, \quad r_{1,2}^2 = (Z - z)^2 + (r \pm A_0)^2. \quad (\text{V.17})$$

The functions K and E are the elliptic integrals. The self propagation velocity of the ring is given by

$$u_z^{\text{self}} = \frac{\Gamma}{4\pi A_0} \left[\log \frac{8A_0}{b} - \frac{1}{4} \right] \quad (\text{V.18})$$

where b is the core radius. The expression for $\partial\phi^r/\partial t$ is obtained as follows:

$$\frac{\partial\phi^r}{\partial t} = -u_z V_z + \frac{\partial\phi^r}{\partial A_0} V_{A_o}, \quad (\text{V.19})$$

where (V_z, V_{A_o}) are the velocities for updating the ring, and

$$\frac{\partial\phi^r}{\partial A_0} = -\frac{\Gamma A_0 |Z - z|}{2\pi r_1^3} \left[K(m) + \frac{E(m)}{1-m} \right]. \quad (\text{V.20})$$

6 Example

The code is used to study the flow around a sphere moving through the water. For a sphere in a steady translational flow with velocity U , it may be shown that the translational velocity has to satisfy the following condition for the inception of cavitation ($p_c = p_v$)

$$U > \sqrt{\frac{8(p_\infty - p_v)}{5\rho}}. \quad (\text{V.21})$$

With $p_\infty = 101230 \text{ Pa}$, $p_v = 2300 \text{ Pa}$, and $\rho = 1000 \text{ kg/m}^3$, the cavitation inception occurs at $U = 12.58 \text{ m/sec}$. We first consider the case of totally irrotational flow outside the sphere, without the vortex emission. The translational basic flow field has $U = 19 \text{ m/sec}$, and $R = 1.0 \text{ m}$ is the sphere radius. Figure V.1 shows a color contour plot of the pressure field around the sphere. The figure shows that the pressure drops below the critical value p_v in the region near the middle part of the sphere where the velocity is highest and correspondingly the pressure is lowest. Figure V.2 shows the dynamics of the resulting cavity obtained with the BEM code 3DynaFS. One can see the trace of the sphere as well as the evolving cavity in a cross-sectional plane through the center of the sphere. The flow is from the left to right. The cavity grows and gets sheared off in the flow direction. In these preliminary runs, the computation could not continue due to the excessive distortion of the mesh where the cavity is sheared by the flow. Clearly remeshing with a significantly larger number of panels in the cavity region is necessary for further simulation. Figure V.3 presents a superposition of the three-dimensional discretization of the sphere and the evolving cavity shapes.

The vortex emission part of the code is then tested first without the cavity part. The time history of the traces of the vortex rings are shown in the Figure V.4. The resulting recirculating zone behind the sphere is clearly visible. The translation velocity of the sphere is $U = 19 \text{ m/sec}$.

We then consider the cavity dynamics with vortex emission. To describe the cavity shape deformation the time stepping needed refinement compared to the case when there were only vortices. In Figure V.5 we present the cavity dynamics with vortices. Here we postponed the cavity initiation until the flow developed with a large number of vortices. After that the surface pressure is checked and the cavity is switched on wherever the pressure went below the critical value. Figure V.5 shows the small cavities and the recirculating region. The near field of the sphere including the cavity is depicted in Figure V.6, where the cavity seems to appear in two disconnected toroidal regions around the sphere. It may seem that the vortex field has substantially modified the pressure field around the sphere to cause such a change of behavior. The case needs to be studied in detail before any rigorous conclusion can be drawn.

7 Conclusions

A simple model has been formulated for separated cavitation on a solid body moving through the water. If the hydrodynamic pressure in the fluid at any part of the body goes below a critical value, say the saturated vapor pressure, a cavity is assumed to initiate and grow there. A boundary element code is used to compute the potential flow around the body and the cavity. Here the code was applied to predict the growth of a cavity over a solid sphere.

The vorticity in the field is modeled by three-dimensional vortex elements. The vorticity generation is linked to the no-slip condition on the solid surface. The vortex element strengths are obtained by solving vorticity transport equation at every time step. For a simpler case of a sphere the vorticity of the field is simulated by axisymmetric vortex rings.

The model was able to describe qualitatively the formation of the cavity in the low-pressure zone. A reliable simulation will need adaptive remeshing capability to resolve the cavity dynamics. This is a preliminary study aiming at creating a complete computational model using coupled BEM-VEM viscous formulation that will address all these shortcomings and accurately predict the cavitation dynamics on an arbitrary body.

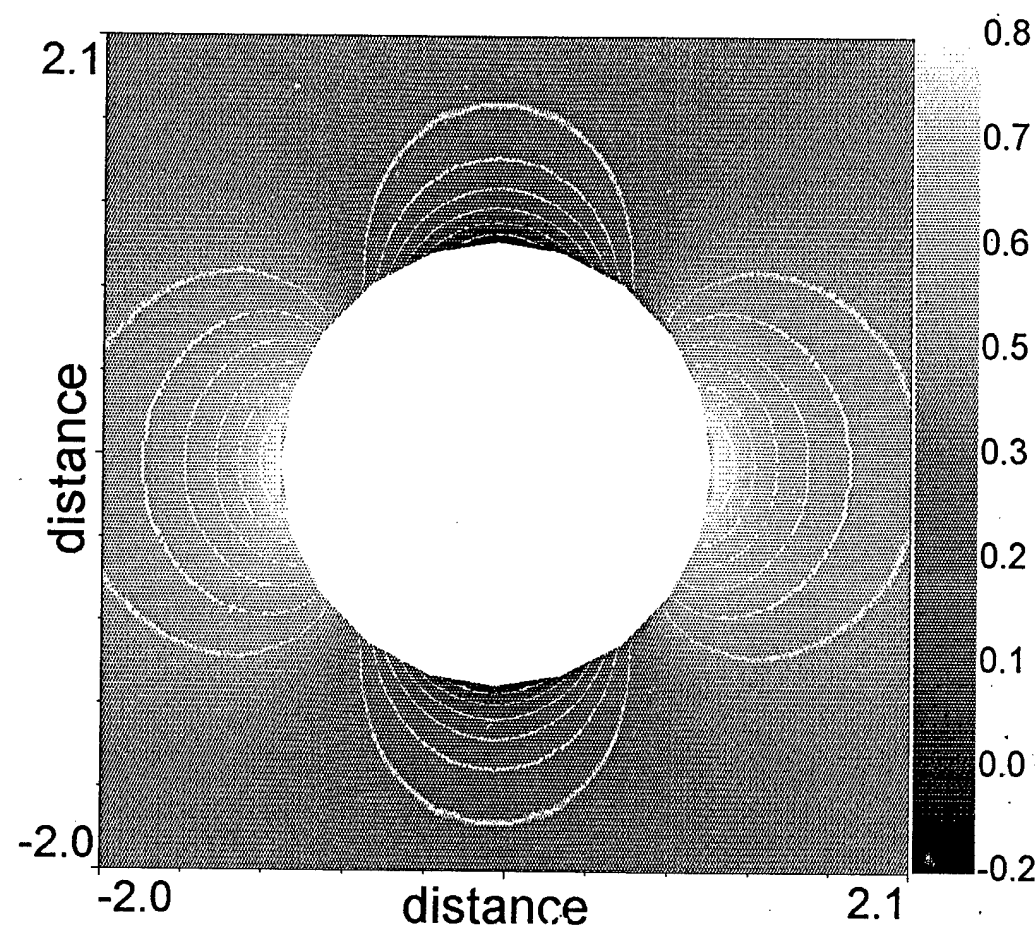


Figure V.1: Pressure field around the sphere: sphere radius $R = 1$ m, pressure at infinity=101230 Pa, and vapor pressure $p_v=2300$ Pa, velocity $U=19$ m/sec.

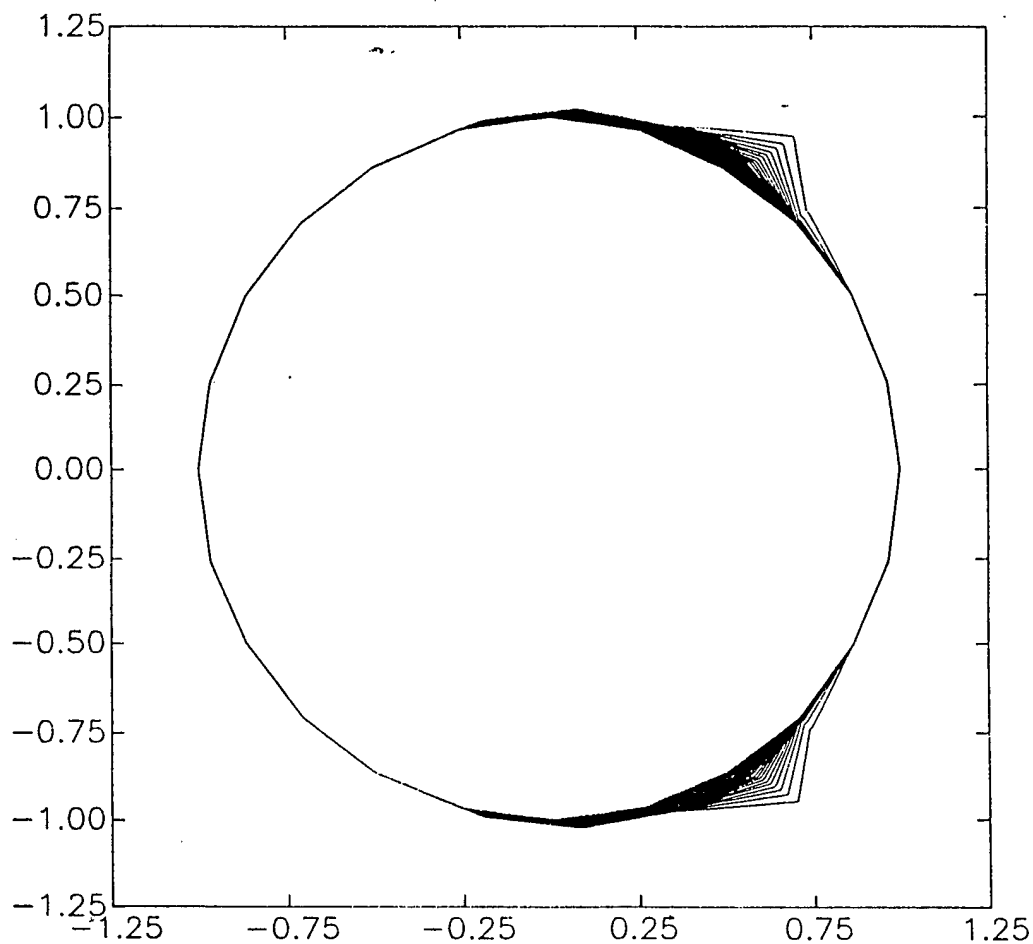


Figure V.2: Dynamics of the cavity in a cross-sectional plane: Different curves represent the shape of the cavity at subsequent times.

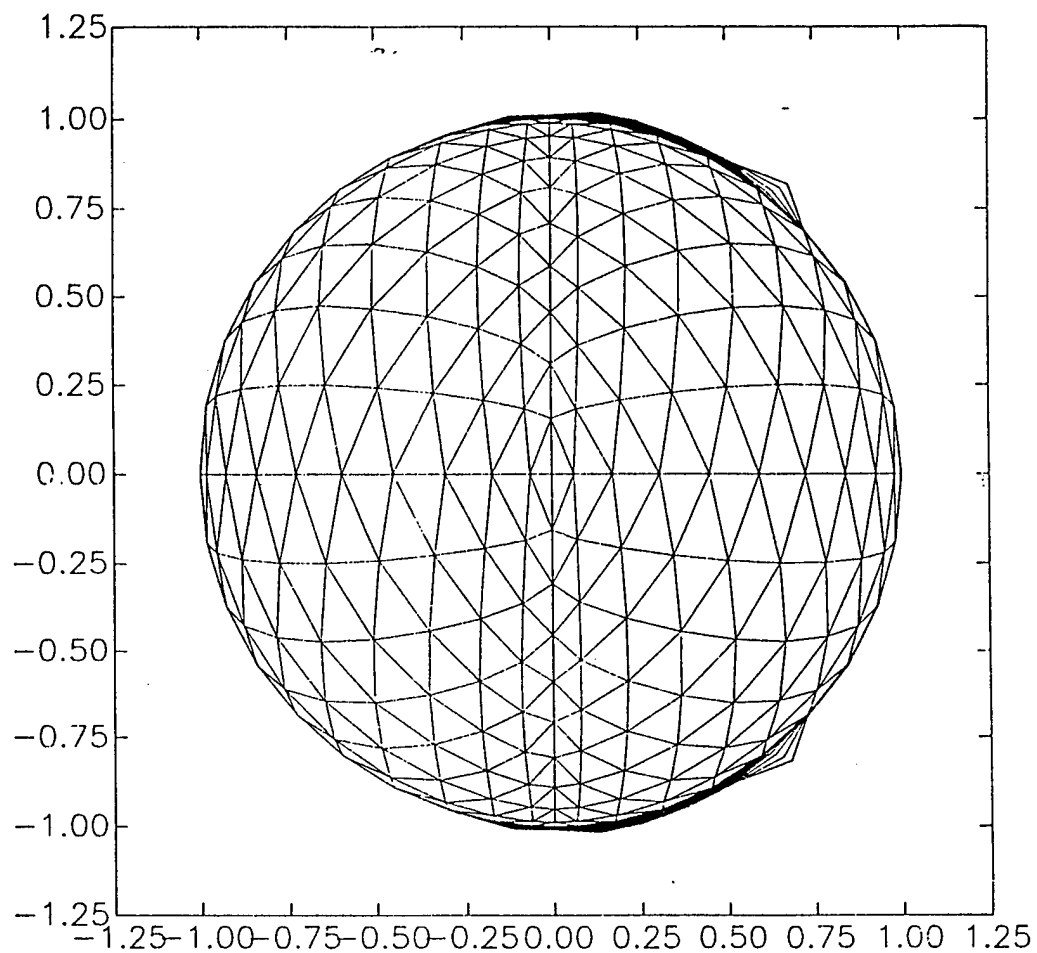


Figure V.3: Three dimensional discretization of the sphere and the cross-sections of cavity at the various times.

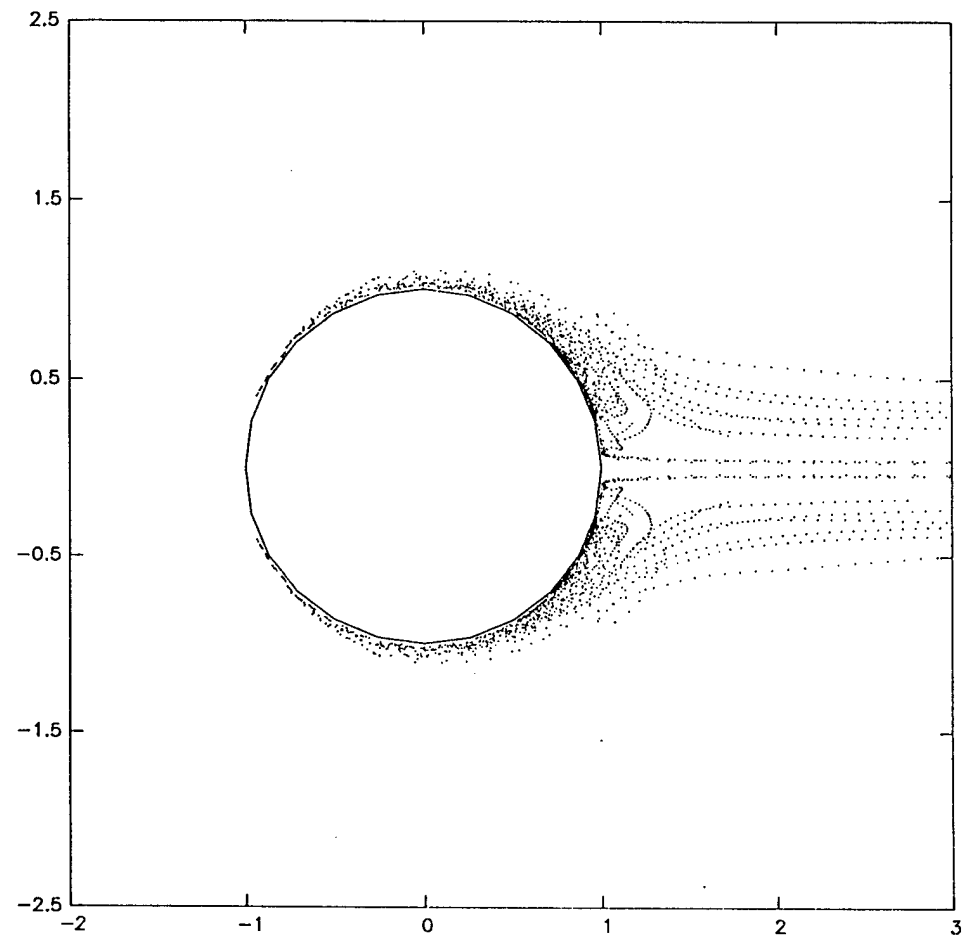


Figure V.4: The vortex structure behind the spher: In the cross-sectional plane the contour of the spher and the time history of the traces of the vortex rings are presented.

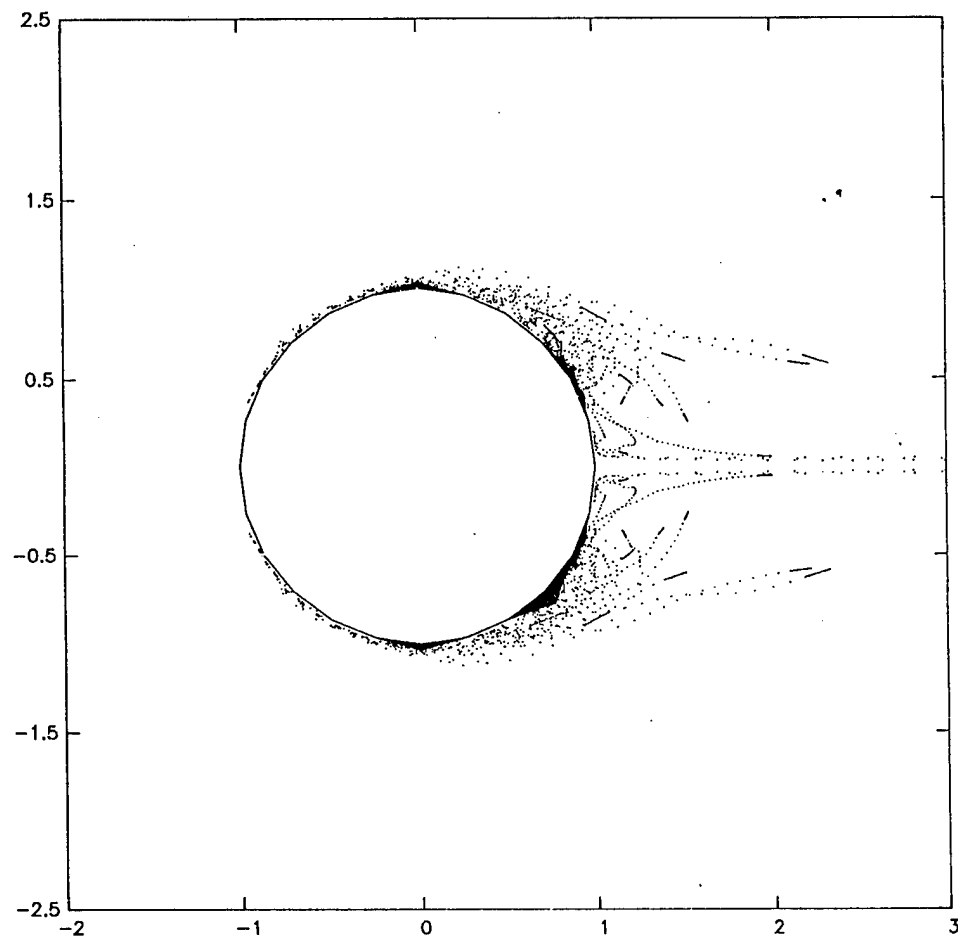


Figure V.5: The time history of the cavity with vortex emission: The cavity computation is started after the vortical flow is developed. The subsequent cavity shapes and the traces of vortex rings are shown.

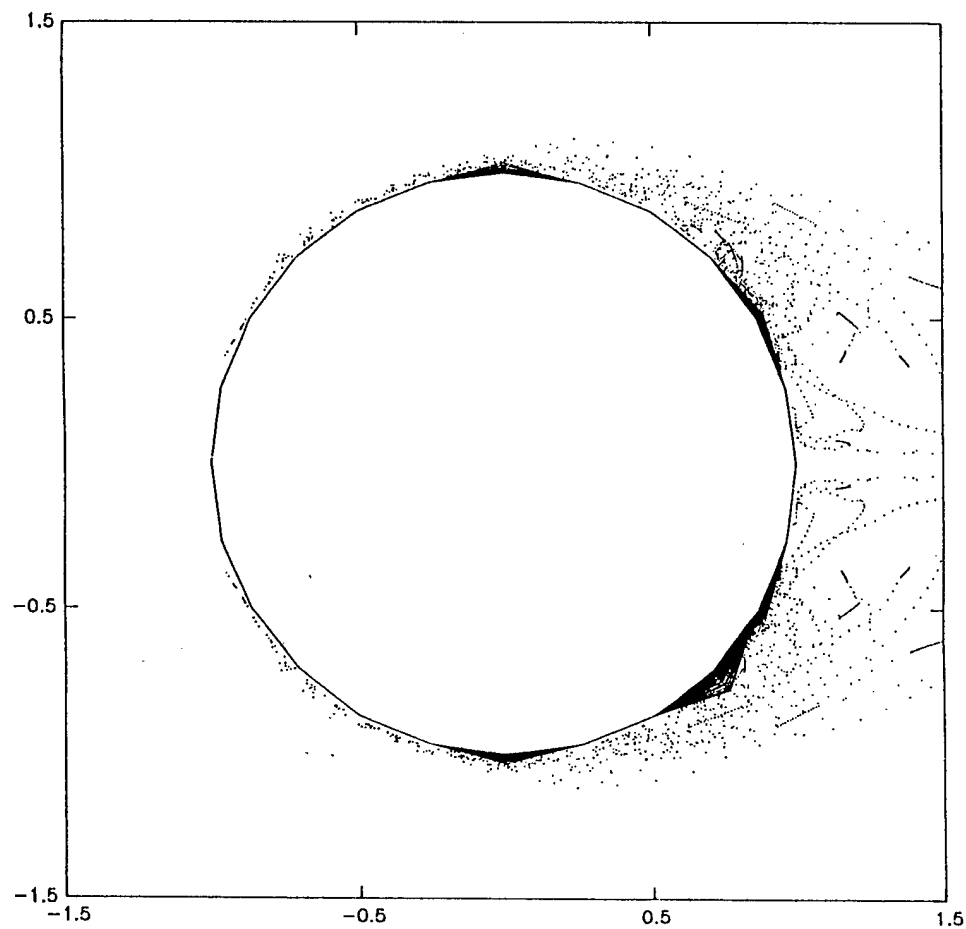


Figure V.6: Near field of the sphere from Figure 6.5 showing detail of the cavity shape.

Chapter VI

CONCLUSIONS

In this study we considered the problem of cavitation dynamics from the standpoints of the dynamics of the interaction between bubbles and nonuniform flow fields and sheet cavitation inception and dynamics. We have considered first the dynamics of the two-way interaction between deforming bubbles and vortical flow fields. Then, we proposed a model for the study of large scale cavitation inception and development on submerged bodies. The models developed and presented here should form a basis for future efforts. These should take advantage of the specialized and efficient nature of the methods we developed for free surface flows, and couple them with powerful but more general methods used to describe the complex flow field around propeller blades, such as hydrocodes and Navier Stokes solvers.

Asymptotic Approach: The dynamics of a bubble captured in the core of a line vortex was studied using asymptotic and numerical approaches. The influence of the vortical flow field on the dynamics of a captured bubble was first studied using an axisymmetric boundary element method. In this case the interaction was one-way in that the effects of the bubble on the vortical component of the flow field were not considered. In a subsequent approach the influence of the dynamics of the captured bubble on the vortical flow field was included using a singular perturbation technique. This was possible in an axisymmetric configuration - that of an axisymmetric bubble located at the center of a line vortex structure - and the viscous flow was modeled using the Navier-Stokes' equations under the assumption that the bubble radial dimension was much smaller than other length scales of the flow. Both approaches indicated that there is a potential for strong interaction, and pointed to the need for more sophisticated modeling to include these interactions.

Numerical Approach: To address the problem in a more general and three-dimensional fashion, and to describe more fully the two-way interaction between bubble dynamics and vortical flow fields, we used a numerical approach. We implemented a Lagrangian vortex element method that modeled the time evolving vorticity field and coupled it with our boundary element method code 3DYNAFS.

In the time stepping procedure, the coupling between the two methods was achieved through matching the velocity and pressure fields used to update at successive time steps the position of the free surfaces and the vortices.

A potential flow representation of the vorticity outside the vortical region was used and allowed application of a modified Bernoulli equation to compute the pressure field due to the vorticity. In the coupled formulation the dynamic pressure at a field point satisfies a Poisson type equation

which is solved again with the BEM method with the right-hand-side handled by the so-called *dual reciprocity* method. This right hand side is represented as the sum of basis functions (here the same as those used to represent the vorticity field) which satisfy the Laplace equation. This results in the transformation of the domain terms in Green's equation into surface integrals. This results in a modified but still efficient boundary element method. Such complementary usage of the same basis functions results in a very efficient computational code and retains the advantages of both boundary element and vortex element methods.

The developed model was applied to the investigation of the interaction of bubbles and the viscous / vortical flow fields due to a line vortex and a vortex ring. The results showed potential for significant effects of the bubbles on the vortex field and vice versa. These effects can have significant implications for applications where cavitation occurs and where the bubbles find themselves in intense time varying vortical regions.

Sheet cavitation: In the last part of the report, we presented the first steps of the modeling of the inception of a leading edge cavity on a submerged body interacting with a two phase medium (stream of traveling nuclei) flowing near it. The coupled vortex element boundary element code described above is used to model the corresponding flow. The main components of the model are as follows:

- The flow is decomposed into a potential and a vortical part.
- The potential part of the flow around the submerged body and the attached sheet cavity is described using the boundary element method.
- The vorticity field, shear and boundary layer around the body is modeled by distributed vortex elements in the flow region. Their subsequent evolution is determined by the vortex element method.
- The freely traveling bubbles are modeled by singularity distributions and by an asymptotic multipole expansion scheme.

This effort is our attempt to model the unsteady three-dimensional flow around airfoil with sheet and traveling bubble cavitation and the breakup of the sheet into bubble clouds at the end of the cavity. Some limited examples were presented concerning the development of such cavities around a sphere. We are presently actively pursuing the study of this aspect of the problem.

Appendix A

INCLUSION OF NUCLEI DYNAMICS

1 Introduction

This appendix describes how the presence of nuclei in the flow field can be accounted for in the codes we have developed. This method has been implemented as an option in the codes, and is presently being tested for accuracy and computational efficiency.

2 Problem considered

Let us consider the case where the liquid contains M microbubbles or nuclei distributed in the flow field. To account for the motion and volume oscillations of these nuclei without resorting to a detailed description of their shape oscillations via the BEM method, we consider them as moving singularities with properties to be determined by the solution. We decompose the velocity potential component of the flow, ϕ , into that due to boundaries, submerged bodies and finely described cavities, ϕ_b , and a potential ϕ_n due to the nuclei dynamics. The presence of a vortical component would be handled as in the previous chapter. To account for the presence of the nuclei as isolated point singularities with specified source and dipole strengths, m_j and \mathbf{d}_j , the equation for ϕ is modified to:

$$\nabla^2 \phi = 4\pi m_j \sum_{j=1}^M \delta(\mathbf{x} - \mathbf{x}_j) + d_{jk} \sum_{j=1}^M \frac{\mathbf{x} - \mathbf{x}_j}{|\mathbf{x} - \mathbf{x}_j|} \frac{\partial \delta(\mathbf{x} - \mathbf{x}_j)}{\partial x_k}, \quad k = 1, 2, 3, \quad (\text{A.1})$$

where \mathbf{x}_j indicates the location of the microbubble. A model for providing the singularities strengths is needed to close the system, and is provided below.

On the surface of the body we require the normal derivative of the total potential, ϕ , to vanish. Accordingly, ϕ_n should satisfy

$$\frac{\partial \phi_n}{\partial n} = -\frac{\partial \phi_b}{\partial n}. \quad (\text{A.2})$$

Let us denote the fundamental solution to Laplace's equation by G , so that

$$\nabla^2 G(\mathbf{x}, \mathbf{y}) = 4\pi \delta(\mathbf{x} - \mathbf{y}), \quad \text{where} \quad G = -|\mathbf{x} - \mathbf{y}|^{-1} \quad (\text{A.3})$$

Green's identity is :

$$a\pi\phi(\mathbf{x}) = \int_{V_y} \nabla^2\phi(\mathbf{y})G(\mathbf{x},\mathbf{y})dV_y + \int_S \mathbf{n}_y \cdot [\phi(\mathbf{y})\nabla G(\mathbf{x},\mathbf{y}) - G(\mathbf{x},\mathbf{y})\nabla\phi(\mathbf{y})] dS_y. \quad (\text{A.4})$$

Equations (A.1) can be reformulated as

$$\begin{aligned} a\pi\phi(\mathbf{x}) &= \sum_{j=1}^M \int_V G(\mathbf{x},\mathbf{y}) \left[4\pi m_j \delta(\mathbf{y} - \mathbf{x}_j) + d_{jk} \frac{\partial \delta}{\partial x_k}(\mathbf{y} - \mathbf{x}_j) \right] dV_y + \int_S \mathbf{n}_y \cdot [\phi\nabla G - G\nabla\phi] dS_y \\ &= \sum_{j=1}^M \left[4\pi m_j G(\mathbf{x}, \mathbf{x}_j) - d_{jk} \frac{\partial G}{\partial x_k}(\mathbf{x}, \mathbf{x}_j) \right] + \int_S \mathbf{n}_y \cdot [\phi(\mathbf{y})\nabla G(\mathbf{x},\mathbf{y}) - G(\mathbf{x},\mathbf{y})\nabla\phi(\mathbf{y})]. \end{aligned} \quad (\text{AS5})$$

The dipole term can be explicitly evaluated as

$$\frac{\partial G}{\partial x_k} = -\frac{\partial}{\partial x_k} \frac{1}{|\mathbf{x} - \mathbf{x}^j|} = \frac{(\mathbf{x}_k - \mathbf{x}_k^j)}{|\mathbf{x} - \mathbf{x}^j|^3}. \quad (\text{A.6})$$

Following a collocation approach, by selecting the points \mathbf{x} to be the nodes on S , a linear system of equations of the form

$$\mathbf{A} \frac{\partial \phi}{\partial \mathbf{n}} + \mathbf{r} = \mathbf{B} \phi \quad (\text{A.7})$$

results. Here \mathbf{A} and \mathbf{B} are matrices corresponding to the discretization and integration with the Green's function and its derivative, while \mathbf{r} is the vector obtained by evaluating the source and dipole terms at the collocation points.

3 Nuclei local model

With R_j being the instantaneous radius of the j th bubble, the source term is given by

$$m_j = R_j^2 \dot{R}_j, \quad (\text{A.8})$$

where the dot superscript indicates time differentiation.

The dipole terms are given by

$$d_{jk} = -\frac{R_j^3}{2} \mathbf{V}^j \cdot \mathbf{e}_k, \quad k = 1, 2, 3. \quad (\text{A.9})$$

where \mathbf{V}^j is the slip velocity between the liquid and the bubble center, and \mathbf{e}_k is the unit vector in the k direction.

Thus if we have evolution equations which provide the variation of (m_j, d_{jk}, x_k^j) with time we in terms of the other variables of the problem we can close the system of equations.

3.1 Evolution of the source term

Dynamic Evolution

The spherical bubble oscillations and radius variations with time can be obtained using the Rayleigh Plesset equation:

$$R_j \ddot{R}_j + \frac{3}{2} \dot{R}_j^2 = \frac{P_l - P(\mathbf{x}_j)}{\rho}, \quad (\text{A.10})$$

where $P(\mathbf{x}_j)$ is the pressure in the liquid at the nuclei center location in its absence. P_l is the pressure in the liquid at the surface of the bubble. It is connected by the continuity of normal pressures to the partial pressures of gas and vapor inside the bubble, $p_g^j + p_v$, and to the surface tension:

$$P_l = p_g^j + p_v - \frac{2\sigma}{R_j}. \quad (\text{A.11})$$

Quasi Static Bubble Model

In practice, the above bubble model causes numerical difficulties due to the large differences in time scales between the nuclei dynamics characteristic time and the overall flow characteristic time. This would result in an enormous amount of small time steps to integrate the Rayleigh Plesset equations along the path of the nuclei. Most of this time would be in fact wasted in minute bubble oscillations around the bubble equilibrium value. Instead, a simple static equilibrium model should be used as long as the liquid pressure does not drop below the nuclei corresponding critical pressure. To do this we use the static equilibrium equation:

$$P_l - p_v = \frac{p_{go}^j R_{jo}^3}{R_j^3} - \frac{2\sigma}{R_j},$$

where R_{jo} and p_{go}^j are a reference (initial) radius and gas pressure of the bubble. We can solve this equation for a given P_l using a Newton method and rejecting radius values larger than the critical bubble radius, R_c

$$R_c = \left[\frac{3R_j^3}{2\sigma} \left(P' - p_v + \frac{2\sigma}{R_j} \right) \right].$$

When the bubble radius approaches the critical radius we switch to solving the Rayleigh Plesset equation.

3.2 Evolution of the dipole term

The dipole is that due to the relative motion of a sphere of the same radius as the bubble. If along the x direction the liquid velocity is U , and the bubble of radius a moves at a velocity v , the corresponding velocity potential is:

$$\phi_0 = - \frac{a^3 (U - v) x}{(x^2 + y^2 + z^2)^{3/2}}, \quad (\text{A.12})$$

when we take the center of the bubble as the origin of coordinates. The strength of the corresponding dipole is:

$$d = a^3 (U - v). \quad (\text{A.13})$$

To determine the bubble velocity we have to solve an equation of motion of the bubble. This can be written using a classical formation [77] as:

$$\begin{aligned} \frac{d\mathbf{v}^j}{dt} &= \frac{3}{2\pi\rho R_j^3} \left[\frac{1}{2}\rho C_D \pi R_j^2 |\mathbf{u}' - \mathbf{v}^j| (\mathbf{u}' - \mathbf{v}^j) - 2\pi R_j^3 \nabla P + 2\pi\rho (\mathbf{u}' - \mathbf{v}^j) R_j^2 \dot{R}_j \right] \\ &= \left[\frac{3}{4} C_D \frac{|\mathbf{u}' - \mathbf{v}^j|}{R_j} (\mathbf{u}' - \mathbf{v}^j) - \frac{3}{\rho} \nabla P + 3 (\mathbf{u}' - \mathbf{v}^j) \frac{\dot{R}_j}{R_j} \right], \end{aligned} \quad (\text{A.14})$$

where C_D is a drag coefficient and \mathbf{u}' is the liquid velocity at the nucleus center location if the nucleus were not present.

The pressure to which the bubble is subjected, P' is given by:

$$P' = P_\infty - \rho \left(\frac{\partial \phi'}{\partial t} + \frac{1}{2} \mathbf{u}' \cdot \mathbf{u}' \right), \quad (\text{A.15})$$

where primes denotes quantities computed at the corresponding nuclei center in its absence. Finally:

$$\frac{d\mathbf{x}_j}{dt} = \mathbf{v}_j. \quad (\text{A.16})$$

To compute the time derivative by finite differences at the microbubble location, we need to account for the microbubble motion

$$\begin{aligned} \frac{\partial \phi'}{\partial t} &= \frac{\phi'(x, t) - \phi'(x, t-h)}{h} = \frac{\phi'(x, t) - [\phi'(x-\delta, t-h) + \partial \phi'/\partial x|_{x-\delta, t-h} \delta]}{h} \\ &= h^{-1} [\phi'(x, t) - \phi'(x-\delta, t-h) - \mathbf{u}'^j \cdot \delta^j] \\ &= h^{-1} [\phi'(x, t) - \phi'(x-\delta, t-h) - \mathbf{u}'^j \cdot \mathbf{V}^j h] \\ &= h^{-1} (\phi'(x, t) - \Phi(x-\delta, t-h)), \text{ where } \Phi = \phi'(x-\delta, t-h) + h \mathbf{u}'^j \cdot \mathbf{V}^j \end{aligned} \quad (\text{A.17})$$

4 Code organization

(a) Given

- flow at infinity;
- location of body;
- location, radius, radial and translational velocity of microbubbles

(a) Compute source and dipole strengths

(b) Compute \mathbf{A} and \mathbf{B}

(c) Compute rhs due to boundary conditions

- (d) Add to rhs the term \mathbf{r} due to the sources and dipoles
- (e) Solve and get ϕ on the surface
- (f) Get pressures on the surface
- (g) If below vapor pressure convert to free surface for future steps
- (h) Evaluate ϕ' on the microbubbles
- (i) Evaluate \mathbf{u}' at the bubbles using finite-differences in space
- (j) Get $\partial\phi'/\partial t$ at the bubbles using finite-differences in time
- (k) Get pressure at the bubble location
- (l) Get static radius of the bubbles and check for near criticality
- (m) Get $\nabla P'$ at the bubble location using finite-differences in space
- (n) Time step the radius
- (o) Time step the velocity
- (p) Time step the bubble location
- (q) Time step free surface locations
- (r) Goto step 2 and repeat

5 Analytical Solutions to check the code

Consider a flow with potential ϕ_0 . One can determine the potential for the perturbed flow caused by introduction of a fixed sphere of radius a at the origin by using the sphere theorem [17]:

$$\phi = \phi_0 + \frac{a}{r} \phi_0 \left(\frac{a^2}{r^2} \mathbf{x} \right) - \frac{2}{ar} \int_0^a \lambda \phi_0 \left(\frac{\lambda^2}{r^2} \mathbf{x} \right) d\lambda. \quad (\text{A.18})$$

Here we develop the solutions for a uniform flow, source and dipole for comparison with the numerical code. The developed code was found to be successful in recovering the analytical solution in each case.

Consider the velocity potential of a uniform flow

$$\phi_0 = Ux. \quad (\text{A.19})$$

Using Equation (A.18) the corresponding potential, ϕ , in the presence of a sphere of radius a at the origin is

$$\phi = U \left(x + \frac{a^2 x}{r^2} \right) - \frac{2}{ar} \int_0^a \frac{\lambda^3}{r^2} U x d\lambda = Ux \left(1 + \frac{a^2}{r^2} - \frac{1}{2} \frac{a^3}{r^3} \right). \quad (\text{A.20})$$

In the case of a source of strength q located at $(-x_0, 0, 0)$ the potential ϕ_0 is

$$\phi_0 = -\frac{q}{\sqrt{(x + x_0)^2 + y^2 + z^2}}. \quad (\text{A.21})$$

Using Equation (A.18) the corresponding ϕ is

$$\phi = -q \left(\frac{1}{\sqrt{r^2 + 2xx_0 + x_0^2}} + \frac{r}{\sqrt{a^4 + 2xx_0a^2 + r^2x_0^2}} - \frac{1}{a} \ln \frac{a^2 + xx_0 + \sqrt{(a^4 + r^2x_0^2 + 2xx_0a^2)}}{(x+r)x_0} \right). \quad (\text{A.22})$$

In the case of a dipole of strength Λ directed along the x axis and located at $(-x_0, 0, 0)$ the potential ϕ_0 is

$$\phi_0 = -\frac{\Lambda(x+x_0)}{\left((x+x_0)^2 + y^2 + z^2\right)^{3/2}}. \quad (\text{A.23})$$

Using Equation (A.18) the corresponding ϕ is

$$\phi = -\Lambda \left(\frac{(x+x_0)}{\left((x+x_0)^2 + y^2 + z^2\right)^{3/2}} + \frac{a(a^2x + r^2x_0)}{\left(a^4 + 2a^2xx_0 + x_0^2r^2\right)^{3/2}} - \frac{a/x_0}{\sqrt{(a^4 + r^2x_0^2 + 2xx_0a^2)}} \right). \quad (\text{A.24})$$

Bibliography

- [1] CHAHINE, G. L., 1995, "Bubble Interactions with Vortices," chapter XVIII in Vortex Flows Ed. S. Green, Kluwer Academic.
- [2] CHAHINE, G. L., 1993, "Strong Bubble/Bubble and Bubble/Flow Interactions," Bubble Dynamics and Interface Phenomena, Proceedings of an IUTAM Symposium, Birmingham, U.K., Ed. J. R. Blake, J. M. Boulton-Stone, and N. H. Thomas, Kluwer Academic, Boston.
- [3] Chahine, G. L., (1982) "Experimental and Asymptotic Study of Nonspherical Bubble Collapse," *Appl. Scient. Res.* 38, 187-197.
- [4] BILLARD, J. Y. 1995, Personal Communications.
- [5] HAMMITT, F.G., 1980, "Cavitation and Multiphase Flow Phenomena," McGraw-Hill Inc. N.Y.
- [6] BOVIS, A., 1980 , "Etude Asymptotique du Phénomène de Cavitation: Cavités Non Sphériques," Thèse de Docteur-Ingénieur, Université de Pierre et Marie Curie, Paris.
- [7] BOVIS, A.G., 1980, "Asymptotic Study of Tip Vortex Cavitation," ASME Cavitation and Polyphase Flow Forum, New Orleans, pp. 19-21.
- [8] LATORRE, R., 1982, "TVC Noise Envelope - An approach to Tip Vortex Cavitation Noise Scaling," Journal of Ship Research, Vol. 26, No. 1, pp. 65-75.
- [9] LIGNEUL, P. , 1989 , "Theoretical Tip Vortex Cavitation Inception Threshold," European Journal of Mechanics, B/Fluids, Vol.8, Number 6.
- [10] LIGNEUL, P. AND LATORRE R., 1989, "Study of the Capture and Noise of Spherical Nuclei in the Presence of the Tip Vortex of Hydrofoils and Propellers," Acustica Vol. 68.
- [11] CHAHINE, G. L., 1990 , "Nonspherical Bubble Dynamics in a Line Vortex," Proceedings of ASME Cavitation and Multiphase Flow Forum, Toronto 1990,(ed. O. Furuya) ASME, pp 121-126
- [12] HIGUCHI, H., ARNDT, R.E.A. AND ROGERS, M.F., 1989, "Characteristics of Tip Vortex Cavitation Noise," Journal of Fluids Engineering, Vol. 111, No 4, pp. 495-502.
- [13] MAINES, B.H., AND ARNDT, R.E.A., 1993, "Bubble Dynamics of Cavitation Inception in a Wing Tip Vortex," ASME Cavitation and Multiphase Flow Forum, Washington D.C., FED-Vol 153, pp. 93-99.

- [14] RAYLEIGH, LORD., 1918, "On the Pressure Developed in a Liquid during collapse of a Spherical Cavity," Phil. Mag., 34, 94-98.
- [15] LATORRE, R., 1980, "Study of Tip Vortex Cavitation Noise from Foils," International Shipbuilding Progress, 676-685.
- [16] DURAISWAMI, R., CHAHINE, G. L. , 1992 , " Analytical Study of a Gas Bubble in the Flow Field of a Line Vortex," ASME Cavitation and Multiphase Flow Forum, Los Angeles.
- [17] MILNE-THOMSON, 1968, "Theoretical Hydrodynamics," 5th Edition, the McMillan company, New York.
- [18] JOHNSON, V.E., JR. AND HSIEH, T.,1966, "The influence of Trajectories of Gas Nuclei on Cavitation Inception," Proc. 6th Symposium of Naval Hydrodynamics, pp. 163-179.
- [19] VAN WIJNGAARDEN, L., 1980, "Sound and Shock Waves in Bubbly Liquids," in Cavitation and Inhomogeneities in Underwater Acoustics, Ed. W. Lauterborn, Springer-Verlag, Berlin. pp. 127-140.
- [20] PLESSET, M.S., 1948, "Dynamics of Cavitation Bubbles," Journal of Applied Mechanics, Trans. ASME, 16, 228-231.
- [21] CHAHINE, G.L., 1989, "A Numerical Model for Three-Dimensional Bubble Dynamics in Complex Configurations," 22nd. American Towing Tank Conference, St. Johns, Newfoundland, Canada.
- [22] CHAHINE, G.L., DELEPOULE, E., AND HAUWAERT, P., 1993, "Study of the Interaction Between a Bubble and a Vortical Structure," 1993 ASME Cavitation and Multiphase Flow Forum, Washington D.C., FED-Vol 153, pp. 39-47.
- [23] KALUMUCK, K. M. AND CHAHINE, G.L., 1990, "Cavitating Vortex Ring Formation and Dynamics," ASME Cavitation and Multiphase Flow Forum, Toronto, FED, Vol 98, pp.43-49.
- [24] CHAHINE, G.L., AND GENOUX, PH., 1983, "Collapse of a Cavitating Vortex Ring," Journal of Fluids Engineering, Vol. 105, 400-405.
- [25] GENOUX, PH., AND CHAHINE, G.L., 1983, "Collapse of a Toroidal Bubble near a Solid Wall," ASME Cavitation and Multiphase Flow Forum, New Orleans, pp. 69-72.
- [26] CHAHINE, G.L., AND KALUMUCK, K.M., FREDERICK, G.S., AND WATSON, R.E., 1988, "Development of a Directed Underwater Destructive Vortex Bubble Ring," Tracor Hydronautics Inc. Technical Report, 88018-1.
- [27] DESGREES DU LOU, G., SARAZIN, T., AND CHAHINE, G. L., 1993 , " Viscous Interaction Between Bubble and Line Vortex," DYNAFLOW, INC. Technical Report 6.002_15
- [28] MORGAN, M., ROQUELET, D., AND CHAHINE, G.L., 1992, "Cavitation Bubble Behavior in Vortical Structures," DYNAFLOW, INC. Technical Report 6.002_17.

- [29] CHAHINE, G.L., 1984, "Pressures Generated by a Bubble Cloud Collapse," Chemical Engineering Communications, Vol. 28, No. 4-6, pp. 355-364.
- [30] BATCHELOR, G. K., 1967 , " An Introduction to Fluid Dynamics, " Cambridge University Press.
- [31] DARROZES, J. S., CHAHINE, G. L. , 1983 , " Les Recherches sur les Phénomènes de Cavitation," Extrait de Sciences et Techniques de l'Armement, Mémorial de l'Artillerie française.
- [32] DUGUÉ, C., 1989 , "Des Bulles et des Tubes dans un Tourbillon," Rapport de D.E.A., E.N.S.T.A., Groupe Phénomènes d'Interface.
- [33] GUERRI, L., LUCCA, G. AND PROSPERETTI, A., 1981 , " A Numerical Method for the Dynamics of Non-Spherical Cavitation Bubbles," Proceedings 2nd International Colloquium on Drops and Bubbles, JPL Publication.
- [34] BLAKE, J. R, AND GIBSON, D. C., 1987, "Cavitation Bubbles Near Boundaries, " Annual Review Fluid Mechanics., Vol. 19, pp. 99-123.
- [35] OĞUZ, H. N., AND PROSPERETTI, A., 1990, "Bubble Entrainment by the Impact of Drops on Liquid Surfaces," J. Fluid Mech., 219, 143-179.
- [36] TRYGGVASON, G., UNVERDI S. O., AND SONG, M., 1991, "Interaction of Vortices with a Free Surface and Density Interfaces," Lectures in Applied Math., 28, Vortex Dynamics and Vortex Methods, Ed. Anderson, C. R., and Greengard, C., AMS, 679-701.
- [37] TSAI, AND YUE, D. K., 1993, "Interactions Between a Free Surface and a Vortex Sheet Shed in the Wake of a Surface-Piercing Plate," J. Fluid Mech., 257, 691-721
- [38] CHAHINE, G. L., 1990, "Numerical Modeling of the Dynamic Behavior of Bubbles in Non-uniform Flow Fields," ASME Symposium on Numerical Methods for Multiphase Flows, Toronto, FED-91, 57-65.
- [39] CHAHINE, G. L., 1994, "Bubble Dynamics and Cavitation Inception in Non-uniform Flow Fields," Proc. of the Twentieth Symposium of Naval Hydrodynamics, Santa Barbara.
- [40] CHAHINE, G. L., AND PERDUE, T. O., 1989, "Simulation of the Three-Dimensional Behavior of an Unsteady Large Bubble Near a Structure," in Drops and Bubbles Ed. T. G. Wang, A.I.P. Conference Proceedings, 197, 169-187.
- [41] CHAHINE, G. L., AND DURAIWAMI, R., 1992, "Dynamical Interactions in a Multi-Bubble Cloud," ASME, J. Fluids Engg. 114, 680-686.
- [42] CHAHINE, G. L., AND DURAIWAMI, R., 1994, "Boundary Element Method for Calculating 2D and 3D Underwater Explosion Bubble Behavior in Free Water and Near Structures," Naval Surface Warfare Center Report NSWCDD/TR-93/44.
- [43] KALUMUCK, K. M, DURAIWAMI, R., AND CHAHINE, G. L., "Bubble Dynamics Fluid-Structure Interaction Simulation by Coupling Fluid BEM and Structure FEM Codes," J. Fluids Struct., 9, 861-883.

- [44] GUSTAFSON, K.E., AND SETHIAN, J. A., 1991, "Vortex Methods and Vortex Motion," SIAM, Philadelphia.
- [45] SARPKAYA, T., 1989, "Computational Methods with Vortices — The 1988 Freeman Scholar Lecture," J. Fluids Engg., 111, 5-52.
- [46] LEONARD, A., 1980, "Vortex Methods for Flow Simulation," J. Comp. Phys., 37, 289-335.
- [47] LEONARD, A., 1985, "Computing Three-Dimensional Incompressible Flows with Vortex Elements," Ann. Rev. Fluid Mech., 17, 523-559.
- [48] WINCKELMANS, G. S., AND LEONARD, A., 1993, "Contributions to Vortex Particle Methods for Computation of Three-Dimensional Incompressible Flows," J. Comp. Phys., 109, 247-273.
- [49] CHORIN, A.J., 1973, "Numerical Study of Slightly Viscous Flow," J. Fluid Mech., 57, 785-796.
- [50] CHORIN, A.J., 1978 "Vortex Sheet Approximation of Boundary Layers," J. Comp. Phys. 27, 428-442.
- [51] CHORIN, A.J., 1980, "Vortex Models and Boundary Layer Instability," SIAM J. Sci. Stat. Comp. 1, 1-21.
- [52] FISHELOV, D., 1990, "A New Vortex Scheme for Viscous Flows," J. Comp. Phys., 86, 211-224.
- [53] FISHELOV, D., 1994, "Simulation of Three-Dimensional Turbulent Flow in Non-Cartesian Geometry," J. Comp. Phys., 115, 249-266.
- [54] PATRIDGE, P. W., BREBBIA C. A., AND WROBEL, L. C., 1991, "The Dual Reciprocity Boundary Element Method," Computational Mechanics Publications, Southampton, and Elsivier, London.
- [55] ANDERSON, C., AND GREENGARD, C., 1985 "On Vortex Methods," SIAM J. Num. Anal. 22, 413-440.
- [56] BEALE, J. T., AND MAJDA, A., 1985, "Higher Order Accurate Vortex Methods with Explicit Velocity Kernels," J. Comp. Phys., 58, 188-208.
- [57] KNIO, O. M., AND GHONIEM, A. F., 1990, "Numerical Study of a Three-Dimensional Vortex Method," J. Comp. Phys., 86, 75-106.
- [58] GHONIEM, A. H., AND KNIO, O. M., 1991, "The Development and Application of the Transport Element Method to Three Dimensional Reacting Shear Layers" in Lectures in Applied Mathematics, 28, Vortex Dynamics and Vortex Methods Ed. Anderson, C. R., and Greengard, C., AMS, 165-218.
- [59] BERGER, S. A., TALBOT, L., AND YAO, L.-S., 1983, "Flow in Curved Pipes," Ann. Rev. Fluid Mech., 15, 461-512.
- [60] KOUMOUTSAKOS, P., AND LEONARD, A., 1995, "High-Resolution Simulations of the Flow around an Impulsively Started Cylinder Using Vortex Method," J. Fluid Mech., 296, 1-38.

- [61] MORCH, K. A., AND SONG, J. P., 1992, "Cavitation Nuclei at Solid-Liquid Interfaces," Cavitation: Proceedings of the Institution of Mechanical Engineers, 1-7.
- [62] LAMB, H., 1932, "Hydrodynamics," Cambridge University Press, Cambridge.
- [63] SARKAR, K., DURAISWAMI, R., AND CHAHINE, G. L., 1995, "Three Dimensional Numerical Simulation of Bubble-Vortical Flow Interaction," ASME Cavitation and Multiphase Flow Forum, Hilton Head, South Carolina.
- [64] SARKAR, K., CHAHINE, G. L., AND DURAISWAMI, R., 1996, "Three Dimensional Bubble-Vortical Flow Interaction -A Numerical Study," submitted to J. Fluid Mech.
- [65] BLAKE, J. R., TAIB, B.B. AND DOHERTY, G., 1986, "Transient Cavities Near Boundaries. Part I. Rigid Boundary," Journal of Fluid Mechanics, vol. 170, pp. 479-497.
- [66] CHAHINE, G.L., PERDUE, T.O., AND TUCKER, C.B., 1988, "Interaction Between an Underwater Explosion and a Solid Submerged Structure," DYNAFLOW, INC. Technical Report 89001-1.
- [67] CHAHINE, G.L., 1991, "Dynamics of the Interaction of Non-Spherical Cavities," in "Mathematical Approaches in Hydrodynamics," ed. T. Miloh, SIAM, Philadelphia.
- [68] CHAHINE, G.L., FREDERICK, G.F., AND BATEMAN, R.D., 1993b, "Propeller Tip Vortex Cavitation Suppression Using Selective Polymer Injection," Journal of Fluids Engineering, Vol. 115, pp. 497-504.
- [69] CRESPO A., CASTRO F., MANUEL, F., AND HERNANDEZ J., 1990, "Dynamics of an Elongated Bubble During Collapse," Journal of Fluids Engineering, Vol 112, 232-237.
- [70] GREEN, S.I., "Correlating Single Phase Flow Measurements with Observations of Trailing Vortex Cavitation," Journal of Fluids Engineering, Vol. 113, No 1, pp. 125-130.
- [71] KEZIOS, P. AND SCHOWALTER, W.R., 1986, "Rapid Growth and Collapse of single Bubbles in Polymer Solutions Undergoing Shear," Phys. Fluids 29 (10), 3172-3181.
- [72] BOULON, O., 1996, "Etude Experimentale de la Cavitation de Tourbillon Marginal: Effets Instationnaires, de germes et de confinement," Ph.D. Thesis (in French), Institut National Polytechnique de Grenoble.
- [73] TAIB, B.B., 1985, "Boundary Integral Method Applied to Cavitation Bubble Dynamics," Ph. D. Thesis, University of Wollongong, Australia.
- [74] WILKERSON, S., 1989, "Boundary Integral Technique for Explosion Bubble Collapse Analysis," ASME Energy Sources Technology Conference and Exhibition, Houston Tx.
- [75] PELEKASIS, N. A., AND TSAMOPOULOS, J. A. (1993a), "Bjerknes forces between two bubbles. Part 1. Response to a step change in pressure," J. Fluid Mech., 254, 467-500.
- [76] PELEKASIS, N. A., AND TSAMOPOULOS, J. A. (1993b), "Bjerknes forces between two bubbles. Part 2. Response to an oscillatory pressure field," J. Fluid Mech., 254, 501-530.

- [77] SRIDHAR, G. AND KATZ, J. (1993), "*Lift and drag forces on bubbles entrained by a vortex ring,*" Proceedings Cavitation and Multiphase Flow Forum, O. Furuya, ed., FED Vol 153, ASME, New York, 165-170.